Stochastic Modelling and Analysis for Bridges under Spatially Varying Ground Motions

by

Deyi Zhang

A thesis
presented to the University of Waterloo
in fulfilment of the
thesis requirement for the degree of
Doctor of Philosophy
in
Civil Engineering

Waterloo, Ontario, Canada, 2013

Author's Declaration

I hereby declare that I am the sole author of this thesis. This is a true copy of the thesis, including any required final revisions, as accepted by my examiners.

I understand that my thesis may be made electronically available to the public.

Abstract

Earthquake is undoubtedly one of the greatest natural disasters that can induce serious structural damage and huge losses of properties and lives. The resulting destructive consequences not only have made structural seismic analysis and design much more important but have impelled the necessity of more realistic representation of ground motions, such as inclusion of ground motion spatial variations in earthquake modelling and seismic analysis and design of structures.

Recorded seismic ground motions exhibit spatial variations in their amplitudes and phases, and the spatial variabilities have an important effect on the responses of structures extended in space, such as long span bridges. Because of the multi-parametric nature and the complexity of the problems, the development of specific design provisions on spatial variabilities of ground motions in modern seismic codes has been impeded. Eurocode 8 is currently the only seismic standard worldwide that gives a set of detailed guidelines to explicitly tackle spatial variabilities of ground motions in bridge design, providing both a simplified design scheme and an analytical approach. However, there is gap between the code-specified provisions in Eurocode 8 and the realistic representation of spatially varying ground motions (SVGM) and the corresponding stochastic vibration analysis (SVA) approaches. This study is devoted to bridge this gap on modelling of SVGM and development of SVA approaches for structures extended in space under SVGM.

A complete and realistic SVGM representation approach is developed by accounting for the incoherence effect, wave-passage effect, site-response effect, ground motion nonstationarity, tridirectionality, and spectra-compatibility. This effort brings together various aspects regarding rational seismic scenarios determination, comprehensive methods of accounting for varying site effects, conditional modelling of SVGM nonstationarity, and code-specified ground motion spectra-compatibility.

A comprehensive, systematic, and efficient SVA methodology is derived for long span structures under tridirectional nonstationary SVGM. An absolute-response-oriented scheme of pseudo-excitation method and an improved high precision direct integration method are proposed to reduce the enormous computational effort of conventional nonstationary SVA.

A scheme accounting for tridirectional varying site-response effect is incorporated in the nonstationary SVA scheme systematically. The proposed highly efficient and accurate SVA approach is implemented and verified in a general finite element analysis platform to make it readily applicable in SVA of complex structures. Based on the proposed SVA approach, parametric studies of two practical long span bridges under SVGM are conducted.

To account for spatial randomness and variability of soil properties in soil-structure interaction analysis of structures under SVGM, a meshfree-Galerkin approach is proposed within the Karhunen-Loève expansion scheme for representation of spatial soil properties modelled as a random field. The meshfree shape functions are proposed as a set of basis functions in the Galerkin scheme to solve integral equation of Karhunen-Loève expansion, with a proposed optimization scheme in treating the compatibility between the target and analytical covariance models. The accuracy and validity of the meshfree-Galerkin scheme are assessed and demonstrated by representation of covariance models for various homogeneous and nonhomogeneous spatial fields.

The developed modelling approaches of SVGM and the derived analytical SVA approaches can be applied to provide more refined solutions for quantitatively assessing code-specified design provisions and developing new design provisions. The proposed meshfree-Galerkin approach can be used to account for spatial randomness and variability of soil properties in soil-structure interaction analysis.

Acknowledgments

I would like to express my deep and sincere gratitude to my supervisors, Professor Wei-Chau Xie and Professor Mahesh D. Pandey, for their valuable guidance and constant support throughout the preparation of this thesis.

I would like to thank my thesis committee members, Professors Hanping Hong, Jeffrey S. West, Scott Walbridge, Sriram Narasimhan, and Xinzhi Liu, for their insightful comments for my research.

I would also like to extend my sincere gratitude to Dr. Binh-Le Ly and Mr. Wei Liu for their enlightening discussions, invaluable suggestions, and continuous support during my work at Candu Energy Inc. Thanks are also given to Mr. Xue-Ming Han, Mr. Sudip Adhikari, Dr. Zhi-Hua Chen, Mrs. Yi-Ming Jiang, Mr. Jim Liu, Dr. Yu-Xin Liu, and Dr. Tarek S. Aziz of Candu Energy Inc. and Dr. Aman Usmani of AMEC NSS for their kind help and support.

I am specially indebted to my sincere friends Dr. Hong-Yu Jia of Southwest Jiaotong University and Mr. Xi Li of Beijing University of Technology for their strong motivations, great talents, and hard-working during our research cooperations. Furthermore, I would like to sincerely thank my previous supervisors, Professor Jin-Guang Teng of Hong Kong Polytechnic University and Professor Hui Li of Harbin Institute of Technology, for their rigorous training and excellent supervision, which benefit me very much for my Ph.D. study.

My special thanks are given to my wife Qian Hao, my parents, my parents-in-law, and my sister and brother for their constant love and inspiration over the years. Without their support, I could not have done it.

I am indebted to my colleagues, Dr. Tian-Jin Cheng, Dr. Dong-Liang Lu, Dr. Shun-Hao Ni, Dr. Jian Deng, Dr. Xu-Fang Zhang, Bo Li, Zhao-Liang Wang, Xiao-Li Yuan, Shuo Yu, Wei Jiang, and Sen Long, for all their help and friendship.

Finally, the financial support from the Natural Sciences and Engineering Research Council of Canada and the University Network of Excellence in Nuclear Engineering is gratefully acknowledged.

TO

My Wife Grace

Contents

List of Figures

Nomenclature

CFST	Concrete-Filled Steel Tubular
CPT	Cone Penetration Test
DOF	Degree-Of-Freedom
DSHA	Deterministic Seismic Hazard Analysis
FEA	Finite Element Analysis
FTF	Frequency Transfer Function
GPCE	Generalized Polynomial Chaos Expansion
HHT	Hilbert-Huang Transform
HPDIM	High Precision Direct Integration Method
I-HPDIM	Improved High Precision Direct Integration Method
IM	Intensity Measure
K-L	Karhunen-Loeve
MLS	Moving Least Squares
MRD	Mean Rate Density
NEHRP	National Earthquake Hazard Reduction Program
NGA	Next Generation Attenuation
PBEE	Performance-Based Earthquake Engineering
PDS	Phase Difference Spectrum
PEM	Pseudo-Excitation Method
PGA	Peak Ground Acceleration
PGD	Peak Ground Displacement
PSD	Power Spectral Density

PSHA	Probabilistic Seismic Hazard Analysis
RF	Random Field
RHA	Response History Analysis
RSA	Response Spectrum Approach
RSD	Required Separation Distance
SD	Standard Deviation
SH	Shear Horizontal
SHD	Seismic Hazard Deaggregation
SRM	Spectral Representation Method
SRSS	Square Root Of The Sum Of Squares
SSI	Soil-Structure Interaction
SV	Shear Vertical
SVA	Stochastic Vibration Analysis
SVGM	Spatially Varying Ground Motion
UHS	Uniform Hazard Spectrum
VPSHA	Vector-Valued Probabilistic Seismic Hazard Analysis
VSHD	Vector-Valued Seismic Hazard Deaggregation
VST	Vanes Shear Test
WNA	Western North America

CHAPTER 1

Introduction

Earthquake is undoubtedly regarded as one of the greatest destructive natural disasters that can induce serious damage of structures, thereby causing huge economic losses, including lives and properties. The spatial variation of seismic ground motions has an important effect on the response of long structures, e.g., long span bridges (Zerva, 2009). Thus, structural seismic analysis and design, as the most effective approach in mitigating the consequences of earthquakes, become much more crucial for these long structures (Housner and Jennings, 1977).

In Section 1.1, a general overview of this thesis is presented, along with the scope and motivation of this study. Following the background introduced in Sections 1.1, the objectives of this study are presented in Section 1.2, and the organization of this thesis is then described in Section 1.3.

1.1 Motivation and Background

In the past several decades, a large number of destructive earthquakes have caused catastrophical damage to bridge structures and tremendous losses of casualties and property (see Figure 1.1), such as 1906 San Francisco, 1976 Tangshan, 1979 Imperial Valley, 1994 Northridge, 1995 Kobe, 1999 Chi-Chi, 2008 Sichuan, 2010 Haiti, and 2011 Tohoku earthquakes. These earthquakes not only have made structural seismic analysis and design much more essential, but impelled the necessity of more realistic representation of ground

motions, e.g., inclusion of ground motion spatial variations in earthquake modelling and seismic analysis and design of structures.

(a) 1994 Northridge

(b) 1995 Kobe

(c) 1999 Chi-Chi

(d) 2008 Sichuan

Figure 1.1 Collapse of bridges in the past earthquakes

1.1.1 Spatially Varying Ground Motions (SVGM)

Observations from past earthquakes demonstrated that the seismic ground motions recorded exhibit spatial differences in their amplitude and phases (i.e., spatial variations of ground motions), such as the El Centro differential array that was installed to record the 1979 Imperial Valley earthquake (Spudich and Cranswick, 1984), the Strong Motion Array in Taiwan-Phase 1 (SMART-1) and Lotung Large Scale Seismic Test (LSST) array in Lotung, Taiwan (Bolt *et al.*, 1982), and the dense array in the Parkway Valley, Wainuiomata, New Zealand (Zerva and Stephenson, 2011).

There are three phenomena that mainly give rise to the spatial variability of ground motions (Somerville *et al.*, 1991; Der Kiureghian, 1996)

- The wave-passage effect, which results from difference in the arrival times of seismic waves at separate stations due to finite velocity of travelling waves.
- The incoherence effect, which arises from random differences in the amplitudes and phases of seismic waves due to their multiple reflections and refractions in the heterogeneous medium (scattering effect) and their differential superposition when arriving from an extended source (extend source effect).
- The site-response effect, which is attributed to differences of the surface motions owing to propagation of seismic waves through different site conditions.

Ground motion spatial variations significantly affect the responses of large dimensional structures, such as pipelines, tunnels, dams, bridges, and structures with large rigid foundation, e.g., nuclear power plants (Zerva, 2009). Because these long or large structures extend over large distance, their supports will undergo different ground motion during an earthquake. For example, spatial variations of seismic motion may result in pounding or even collapse of adjacent bridge decks owing to the large out-of-phase responses, which were observed and reported from almost all the past major earthquakes, e.g., the 1994 Northridge, 1999 Chi-Chi, and 2008 Sichuan earthquakes (Moehle and Eberhard, 2000). Thus, it is necessary to account for the spatial variations in ground motion modelling and seismic response analysis and design of bridges.

In performance-based earthquake engineering (PBEE), response history analysis (RHA) is required to account for nonlinear behaviors of structures, where the specified time histories of ground motions at supports of the structure must be provided. Due to the scarcity of earthquake time histories recorded at closely spaced seismographic stations and wide ranges of practical structure dimensions, nonlinear RHA of multiply supported structures must rely on synthetic ground motions. Therefore, the generation of synthetic SVGM is of great importance and much more necessary than ground motion synthesis for a single location, which prompted the study on modelling of SVGM in this thesis.

1.1.2 Modelling of SVGM

Existing methods in synthesizing earthquake wave motions include the classical wave propagation methods, stochastic-based methods, and other signal processing techniques, such as the wavelet and Hilbert-Huang Transform (HHT) methods. In the wave propagation methods, ground motions are normally obtained by solving equations of waves prorogating through elastic and stratified medium using all the available information about the source, path, and site characteristics (Wang, 1999). The stochastic methods modulate the generic Gaussian white noise by an envelope function to obtain the synthetic time histories (Boore, 1983). The wavelet and HHT methods are usually used to model nonstationarity of ground motions (Wen and Gu, 2004).

Almost all of the techniques of simulating SVGM, including the unconditional simulation (Shinozuka and Deodatis, 1988; Hao *et al.*, 1989; Conte *et al.*, 1992; Deodatis, 1996) and conditional simulation (Vanmarcke *et al.*, 1993; Heredia-Zavoni and Santa-Cruz, 2000; Hu *et al.*, 2012), can be generally grouped as spectral representation method (SRM), which involves the decomposition of cross power spectral density (PSD) matrix. This is because that, in practice, all of the parametric modellings of spatially correlated earthquake motions are described by the coherence function (a measure of spatial seismic motion coherency in frequency domain), where the SRM becomes conceptually and theoretically consistent with the existing coherence model.

For the PSD model used in SRM, a physically consistent and refined model using seismological spectra, which can account for effects of the fault rupture and the transmission of waves from the fault through the media to the ground surface (Brune, 1970), is preferred. In combination with the stochastic representation method, seismological spectra have been widely used to simulate the physical processes responsible for the ground shaking (Boore, 2003a; Campbell, 2003), but have been rarely used to synthesize ground motions used for structural RHA. The stochastic representation method, combined with seismological spectra model, is extended to simulate SVGM in Chapter 2.

In determining the seismological spectra, seismological parameters of the earthquake scenarios, such as earthquake magnitude and source-site distance, are required. In addi-

tion, the seismic hazard of these seismic scenarios should be consistent with the design response spectra, e.g., uniform hazard spectra (UHS), since the design seismic loads specified by regulatory agencies are usually prescribed in the form of response spectra. The determination of seismic hazard for earthquake scenarios can be accomplished through the seismic hazard deaggregation (SHD). Atkinson (2009) utilized this scheme to generate earthquakes compatible with UHS, but it requires a number of ground motions to be simulated for RHA, since different hazard deaggregation results of spectral acceleration on UHS are resulted by scalar SHD at each vibration period. This leads to enormous efforts in RHA, especially for structures with complex geometric or constitutive properties. Chapter 2 adopts the vector-valued seismic hazard deaggregation (VSHD) approach, instead of the scalar SHD, to determine the earthquake scenarios, which can contribute seismic hazard to spectral accelerations at multiple periods simultaneously.

Among spatial variations of seismic motions, the site-response effect can significantly affect responses of structures extended in space, since ground motions propagating from the base rock have significant spatial variability. Furthermore, different site amplifications and filtering induced by non-uniform (varying) sites tend to increase the quasi-static responses of structures under SVGM. Most of the existing studies in addressing the topic of simulations of random processes and random fields fail to (Shinozuka and Deodatis, 1988; Hao *et al.*, 1989; Conte *et al.*, 1992), or only partially and simplistically, account for amplification and filtering effect of local site condition, e.g., those using different soil parameters in the Clough-Penzien spectrum to represent different soil conditions at structural supports (Deodatis, 1996; Ates *et al.*, 2006; Dumanoglu and Soyluk, 2003), or those simply incorporating local site conditions as a linear soil column subjected to a vertically propagating S-wave (Konakli and Der Kiureghian, 2011b). Specifically, using different soil parameters in Clough-Penzien spectrum can consider only one peak corresponding to the fundamental vibration mode of the site, but cannot consider various vibration modes of the site where local soil conditions will amplify and filter the incoming seismic waves. The approach in Konakli and Der Kiureghian (2011b) fails to provide tridirectional site responses (as a result of the incoming P and S seismic waves towards the site with incident angles), which are of prime significance in tridirectional SVGM simulation and tridirectional structural re-

sponse analysis including site-response effect. Moreover, these approaches cannot account for the randomness and uncertainties of dynamic properties of site conditions and site irregularities for structures supported in canyon sites.

In Chapter 2, a site response scheme is derived and incorporated into the SRM to model SVGM at varying site conditions, which can capture the multiple vibration modes of local site, provide tridirectional site response results, account for randomness and uncertainties of local site conditions, and consider effect of site irregularities. It is believed to be an approach that can realistically simulate the tridirectional SVGM at varying site conditions. Moreover, the site analysis approach is futher incorporated into the stochastic vibration analysis (SVA) methodology in Chapter 4 for structural seismic analysis including tridirectional site effect.

Besides local site effect, synthetic ground motions should have a good approximation of nonstationary characteristics of real time histories, which is critical in seismic analysis of hysteretic structures in PBEE. Methods in modelling nonstationarity of ground motions in SRM usually requires the specification of an evolutionary PSD model (Cacciola and Deodatis, 2011; Hu *et al.*, 2012), whose analytical expression is very difficult to be established to reflect ground motion nonstationarity induced by the source, path, and local site effect, since very limited information is available on the spectral characteristics of propagating seismic waves. Other methods, such as the wavelet and HHT methods, are usually used to model nonstationarity of ground motions; however, they are limited to ground motion simulation for a single location, due to the lack of available spatial correlation model derived from the wavelet and HHT bases (Zeldin and Spanos, 1996; Wen and Gu, 2004).

The conditional simulation methods have been used as an alternative approach to simulate nonstationary SVGM that are compatible with prescribed real records. Based on the stationary simulation techniques, ground motion fields are generated by conditional simulation of the Fourier coefficients in the frequency domain (Kameda and Morikawa, 1994), which cannot well preserve the nonstationary nature of ground motions. Hence, these conditional approaches are then improved by dividing the time duration into a sequence of time windows, to which different spectral properties are attributed (Vanmarcke *et al.*, 1993; Heredia-Zavoni and Santa-Cruz, 2000; Liao and Zerva, 2006; Konakli and Der Kiureghian, 2012); however, it is difficult to choose the appropriate time windows and their respective

properties. Furthermore, these conditional simulation approaches are limited to the case of uniform soil conditions that fail to account for the non-uniformity of site conditions.

In Chapter 3, a conditional simulation scheme is developed to model nonstationarity of SVGM at canyon sites using phase difference spectrum (PDS), which preserves ground motion nonstationarity in both time and frequency domains and provides good estimations of the ground motions using only a few model parameters (magnitude and distance). Besides, ground motion nonstationarity has also been included in Chapters 4 to 6 in structural stochastic seismic analysis under SVGM.

Besides spatial variations and nonstationarity of SVGM, the dimensionality is also studied in this thesis, since the combined responses of structures with complex geometries (e.g., long span bridges) under tridirectional ground motions, especially tridirectional SVGM, are important to be considered in seismic assessment. In addition, engineers have long recognized that synthetic SVGM should be compatible with target design response spectra, which are usually prescribed as the design seismic loads by regulatory agencies. However, modelling of tridirectional SVGM that are compatible with design response spectra and considering the multidimensional characteristics of SVGM in structural response analysis and design have not been adequately studied. A simulation scheme of SVGM that accounts for both ground motion tridirectionality and response spectra compatibility is presented in Chapter 3. Tridirectionality of SVGM has also been included in the nonstationary SVA scheme presented in Chapters 4 to 6.

1.1.3 Stochastic Seismic Analysis of Structures under SVGM

Seismic response analysis of structures under SVGM is often performed through linear/nonlinear RHA with design earthquake time histories, SVA with design PSD model, and response spectrum approach (RSA) with design response spectra input. During the past two decades, responses of bridges to SVGM have been studied extensively using RHA (Price and Eberhard, 1998; Saxena, 2000; Kim and Feng, 2003; Zanardo *et al.*, 2002; Lou and Zerva, 2005; Lupoi *et al.*, 2005; Chouw and Hao, 2008; Bi and Hao, 2013), SVA (Zerva, 1990; Hao, 1993; Heredia-Zavoni and Vanmarcke, 1994; Harichandran *et al.*, 1996; Dumanoglu and Soyluk, 2003; Lin *et al.*, 2004a; Soyluk, 2004a; Ates *et al.*, 2006; Zhang *et al.*, 2009; Bi *et al.*,

2011), or RSA (Berrah and Kausel, 1992; Der Kiureghian and Neuenhofer, 1992; Konakli and Der Kiureghian, 2011a).

Because earthquakes are in essence random and RHA usually leads to biased estimations of structural responses owning to uncertainty and intrinsic randomness of ground motions, stochastic vibration based aseismic analysis of structures has been gradually accepted by bridge seismic design standards (CEN, 2005b; MCPRC, 2008). CEN (2005b) and MCPRC (2008) have recommended SVA as one of three common structural analysis approaches for bridges, along with RHA and RSA, since SVA is a theoretically advanced spectral tool that can provide stable, reliable, and physically compliant structural seismic responses, especially for bridge structures under SVGM. This prompts the necessity and significance of developing SVA approaches in this thesis for long structures under SVGM.

As discussed in Section 1.1.2, seismic analysis of bridge structures should account for the incoherence effect, wave-passage effect, local site effect, nonstationarity, and tridirectionality of SVGM. However, considering ground motion nonstationarity in SVA, i.e., nonstationary SVA, for structures subjected to SVGM is too complicated and difficult to be widely used in general engineering computations (in spite of its recognized importance), due to which most of existing works are limited to stationary SVA. In particular, for structures having a large number of DoF and dozens of spatial supports, or the input nonuniformly modulated nonstationary ground motions being spatially correlated and tridirectional, their stochastic response formulas are rather complex and involve a great deal of multiple integration and summation operations, e.g., the Riemann-Stieltjes integration, requiring considerable computational effort.

To reduce the large computational effort involved in the conventional nonstationary stochastic analysis, a time domain method, such as pseudo-excitation method (PEM), is used in this study to improve the computational efficiency (Lin *et al.*, 1997a), in conjunction with the high precision direct integration method (HPDIM), which can further enhance computational efficiency of the direct time domain integration within PEM scheme (Zhong and Williams, 1994). PEM (along with HPDIM) is an accurate and efficient method that can transform both stationary and nonstationary stochastic analyses in frequency domain to deterministic dynamic response problems in time domain, making structural stochas-

tic analysis very simple yet accurate. Time domain analyses make PEM more adaptable for implementation in the general finite element analysis (FEA) platforms, making PEM particularly attractive for engineering purposes.

However, HPDIM still suffers from the bottle-neck problem that the time step has to be small enough to simulate recursively varying pseudo loadings properly, especially for nonuniformly modulated nonstationary pseudo loadings. In Chapter 6, an improved high precision direct integration method (I-HPDIM) is proposed to resolve these shortcomings.

Moreover, the conventional indirect approach solves equations of motion of structures under SVGM by treating the total responses as a linear superposition of a quasi-static and a dynamic components, where massive computations on static influence matrix and inverse of structure stiffness matrix are required. Moreover, the linear superposition treatment has prevented the conventional indirect approach from possible extension to the nonlinear SVA used for PBEE (Der Kiureghian and Fujimura, 2009). To resolve these shortcomings, an absolute-response-oriented scheme within the PEM framework is derived in Chapter 4.

In Chapter 6, the absolute-response-oriented scheme of PEM and I-HPDIM, which can greatly improve the computational efficiencies of both PEM and conventional HPDIM, are combined and implemented in general FEA platform, which becomes more attractive for engineering purposes, particularly in SVA of large complex structures under tridirectional nonstationary SVGM.

1.1.4 Random Field (RF) Representation of Spatial Soil Profiles

Besides wave-passage, incoherence, and site-response effects, seismic motions can be further modified by the soil surrounding structural foundations or piles, known as soil-structure interaction (SSI) effect. SSI is well-recognized to significantly affect structural responses through the coupling between structures and the surrounding soil domain (Wolf, 1985), but has not been adequately considered for structures under SVGM. In SSI analysis, modelling of soil profiles is a fundamental issue, where inherent spatial variability and uncertainty of soil should be accounted for, since, unlike some artificial materials, soil exhibits great spatial variation and uncertainty that may exert a dominant influence in SSI (Lumb, 1966). This impels the study of representing spatial soil profiles for SSI analysis.

Soil properties vary from point to point in space that it is natural to describe them as random fields (RF), where the probability distributions and correlation structures of these soil properties are required (Vanmarcke, 1977). However, due to the lack of relevant experimental data, RF are usually assumed to have finite second order statistics and are usually categorized into Gaussian and non-Gaussian fields (homogeneous or nonhomogeneous). SRM is widely used in conjunction with the transformed field to simulate non-Gaussian RF, but it usually requires an iterative procedure between the underlying Gaussian field and the target non-Gaussian field, where the existence of the underlying Gaussian field cannot be ensured. Furthermore, SRM fails to represent the nonhomogeneity of RF satisfactorily (Li *et al.*, 2007), although most of soil properties exhibit strong nonhomogeneity in reality.

Alternatively, the Karhunen-Loève (K-L) expansion offers a unified framework for the simulation of homogeneous and nonhomogeneous RF that can effectively represent their covariance kernels (Phoon *et al.*, 2002b). However, the implementation of K-L expansion is often hindered by the difficulty encountered in solving the Fredholm integral equation (Ghanem and Spanos, 1991), where the numerical Galerkin method is often used relying on the trigonometric, polynomial, or wavelet basis functions (Phoon *et al.*, 2002a). These basis-function-based methods may not be effective or applicable to a domain of arbitrary shape associated with a general covariance function (Rahman and Xu, 2005).

To resolve these problems, in Chapter 7, a meshfree-Galerkin method is developed within the K-L expansion scheme for modelling and synthesizing spatial soil properties, where meshfree shape functions are employed as a set of complete basis functions within the Galerkin scheme to solve Fredholm integral equation.

1.2 Objectives of This Study

In reviewing the existing standards in dealing with spatial variabilities of ground motions in bridge design, it is found that CEN (2005b) is currently the only seismic code worldwide that gives a detailed set of guidelines to explicitly tackle this problem, since the development of specific design provisions in modern seismic codes has been impeded by the multiparametric nature and the complexity of the problem (Sextos and Kappos, 2009). Specifically, the US

and Japanese bridge design guidelines account for ground motion spatial variabilities solely on the basis of seating length provisions (AASHTO, 2002; ATC/MCEER, 2003; FEMA, 2010; JRA, 2002), the Canadian bridge code fails to account for ground motion spatial variations in its design specifications (CSA, 2006), and the Chinese bridge design code recommends SVA as a preferred analysis approach to account for ground motion spatial variations on bridge responses but fails to provide the simplified design schemes or detailed and explicit analysis approaches (see Section 6.6 of the Commentary) (MCPRC, 2008). CEN (2005b) provides both a simplified design scheme (see Section 3.3) and an analytical approach (see Annex D) in dealing with the problem.

In the simplified scheme, the dynamic (inertia) responses of the entire bridge should be accounted for by the uniform excitation analysis (dynamic analysis, RSA or RHA), while the pseudo-static responses can be calculated using the Set A and Set B deformation displacements imposed at the supports of the bridge (static analysis). The total responses are then obtained by combining the dynamic and pseudo-static responses through square root of the sum of squares (SRSS) rule. In the analytical approach, specific provisions are presented on both the simulation of SVGM by SRM (see Sections D.1 and D.2) and the linear SVA of bridges under SVGM (see Section D.3.2).

However, in modelling of SVGM, CEN (2005b) fails to (a) provide a site-response approach that can both provide the tridirectional response results at varying sites and account for soil randomness and uncertainties; (b) include a more reasonable approach in modelling ground motion nonstationarity (its suggested envelope modulation method within SRM scheme cannot represent ground motion nonstationarity well); (c) model ground motion multidimensionality; and (d) consider response spectra compatibility (only PSD compatibility is specified). As discussed in Section 1.1.2, these effects are of prime importance in generating SVGM used for RHA. Moreover, CEN (2005b) also fails to present explicit and detailed provisions or recommended commentaries on SVA of bridges under SVGM, e.g., to include varying site effect, ground motion nonstationary, and tridirectionality in SVA, along with some high-efficient schemes in nonstationary SVA for the complex bridge structures. Therefore, there is gap between the code-specified provisions and the realistic SVGM representation and the corresponding SVA approaches.

To bridge this gap, the objectives of this study are to develop a complete and realistic SVGM representation approach and a comprehensive, systematic, and efficient SVA methodology in dealing with spatial variability of seismic ground motions for bridge structures. The results of this study aim to provide more refined solutions for quantitatively assessing the code-specified design provisions and developing new design provisions.

1.3 Organization of This Study

Following the motivations and discussions in Section 1.1 and the objectives in Section 1.2, the organization of this study is presented below.

Chapters 2 and 3 develop a complete and realistic representation approach for SVGM, where wave-passage effect, incoherence effect, varying site effect, ground motion nonstationarity, tridirectionality, and response spectra compatibility are considered. Firstly, the scheme of SRM combined with seismological spectra is derived to simulate SVGM, where the earthquake scenarios are determined through VSHD. Secondly, a comprehensive method of accounting for local site effect in synthesizing SVGM is proposed, including consideration of spatial-random-variable soil profiles, the effect of water saturation, and combining P wave, shear vertical (SV) wave, and shear horizontal (SH) wave motions to result in tridirectional site responses. Thirdly, a conditional simulation scheme is established to model nonstationarity of SVGM at canyon sites using PDS method. Finally, both ground motion tridirectionality and response spectra compatibility are included in the representation approach.

Chapter 4 provides a comprehensive, systematic, and efficient SVA methodology for structures under tridirectional nonstationary SVGM at varying site conditions. The absolute-response-oriented scheme of PEM is established and implemented in the general FEA platform. Site analysis approach is also incorporated into the SVA methodology for structural seismic analysis including tridirectional site effect. Relying on the theoretical basis of Chapter 4, two practical bridges, a concrete-filled steel tubular (CFST) arch bridge and a high-pier railway bridge, are analyzed in detail in Chapter 5. The conclusions of these

examples can be considered as some specifications for seismic design and analysis of the CFST arch bridges and high-pier railway bridges in seismic design guidelines.

In Chapter 6, the I-HPDIM scheme is proposed to improve the computational efficiencies of the theoretical methodology in Chapter 4 for nonstationary SVA of complex long structures. The I-HPDIM scheme is then implemented in general FEA platform for engineering purposes. Effects of local site conditions on required separation distance (RSD) of adjacent segments of a high-pier railway bridge have been studied to avoid bridge seismic pounding.

To account for soil inherent spatial variability and uncertainty in SSI analysis, a meshfree-Galerkin method is developed in Chapter 7 within the K-L expansion scheme for modelling and synthesizing spatial soil properties modelled as random fields, along with an proposed optimization scheme used for treating the compatibility between the target and analytical covariance models. The accuracy and validity of the meshfree-Galerkin scheme is then assessed and demonstrated through the modelling and synthesis of the spatial field models, inferred from the field measurements, of soil properties.

A summary of conclusions from this study and some suggestions for future research are presented in Chapter 8.

C H A P T E R 2

Modelling of SVGM: (I) Seismic Scenarios Determination and Varying Site Effect

The recorded seismic ground motions are observed to exhibit spatial variations because of the incoherence, wave-passage, and site-response effects. Due to the scarcity of these earthquakes recorded at closely spaced seismographic stations and wide ranges of practical structure dimensions, response history analysis (RHA) of multiply supported structures must rely on the synthetic spatially varying ground motions (SVGM). In this chapter, the seismic scenarios determination and local site effect in simulating SVGM are studied.

2.1 Introduction

As discussed in Section 1.1.2, almost all of the techniques of simulating SVGM can be generally grouped as spectral representation method (SRM), where the approximate ground motion "power" models, e.g., the empirical Kanai-Tajimi spectrum or Clough-Penzien spectrum, are usually used. However, these approximate spectrum fail to accurately account for wave motions transmitted from the earthquake source through the medium. Hence, a physically consistent and refined model using seismological spectra, which can account for effects of the fault rupture and the transmission of waves from the fault through the media to the ground surface, is desired. Furthermore, seismic hazard of these seismic

scenarios in seismological spectra should be consistent with the design response spectra and determined by the seismic hazard deaggregation (SHD), which is adopted by Atkinson (2009) to generate earthquakes compatible with uniform hazard spectra (UHS), but requires a number of ground motions to be simulated.

The site-response effect can significantly affect responses of structures extended in space. Most of the existing studies in simulating SVGM fail to, or only partially and simplistically, account for amplification and filtering effect of local site condition (Hao *et al.*, 1989; Deodatis, 1996; Dumanoglu and Soyluk, 2003; Konakli and Der Kiureghian, 2011b). These approaches also fail to provide tridirectional site responses and do not account for the randomness and uncertainties of dynamic properties of site conditions and site irregularities for structures supported in canyon sites.

To resolve these problems, a comprehensive and rational approach of synthesizing SVGM is developed. The scheme of modelling SVGM at varying site conditions is presented in Section 2.2. The physically compliant seismological spectra are determined by the results from vector-valued seismic hazard deaggregation (VSHD) in Sections 2.3.1 and 2.3.2, based on which a simulation framework is proposed to resolve the problem that a number of simulations need to be carried out for ground motion generation based on UHS. The combined coherence model, utilizing different coherence models to describe the SVGM, is proposed in Section 2.3.3. A comprehensive approach of accounting for local site effect in simulating SVGM is presented in Section 2.4, including consideration of random and spatially variable soil profiles, combined P-wave, shear horizontal (SH)-wave and shear vertical (SV)-wave motions for simulating tridirectional SVGM. Following the numerical examples presented in Section 2.5, some conclusions are drawn in Section 2.6.

2.2 Modelling of Spatially Correlated Ground Motions at Varying Site Conditions

Consider the spatial points i-i', j-j', and k-k' with different site properties at a canyon site as shown in Figure 2.1, spatially correlated ground motions need to be synthesized to account for the varying site effect.

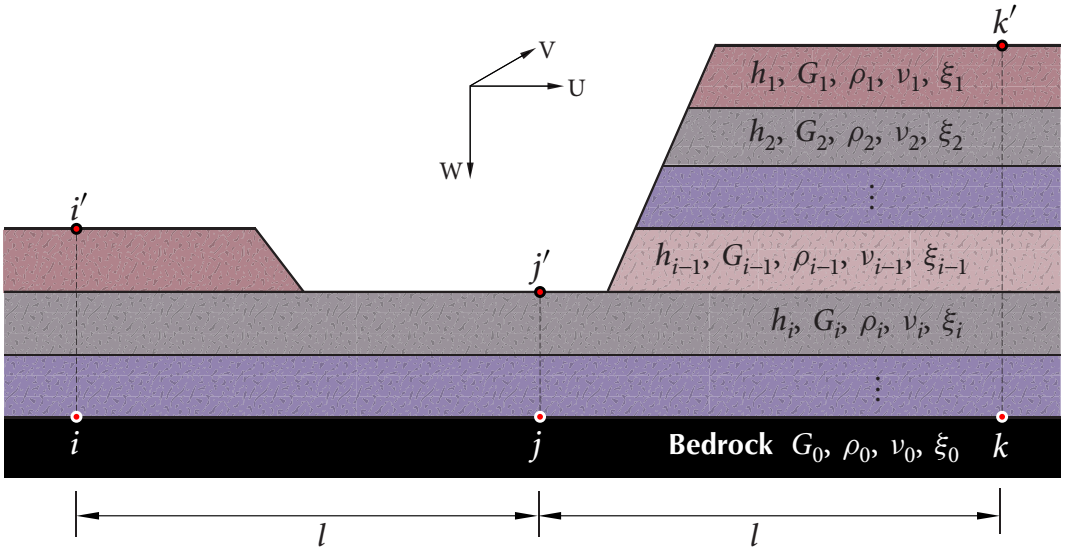

Figure 2.1 Spatially distributed points with varying site conditions

It is assumed that spatial ground motions on the base rock are stationary random processes with zero mean values and have the same power spectral density (PSD) function, which is reasonable since the source-to-site distance is usually much larger than the dimensions of the structure. The cross-PSD function of ground motions at n bedrock locations is

$$\mathbf{S}_{\text{bedrock}}(\mathrm{i}\omega) = \begin{bmatrix} S_{11}(\mathrm{i}\omega) & S_{12}(\mathrm{i}\omega) & \cdots & S_{1n}(\mathrm{i}\omega) \\ S_{21}(\mathrm{i}\omega) & S_{22}(\mathrm{i}\omega) & \cdots & S_{2n}(\mathrm{i}\omega) \\ \vdots & \vdots & \cdots & \vdots \\ S_{n1}(\mathrm{i}\omega) & S_{n2}(\mathrm{i}\omega) & \cdots & S_{nn}(\mathrm{i}\omega) \end{bmatrix}_{n\times n}, \tag{2.2.1}$$

where $S_{ii}(\omega)$ is the auto-PSD function at the ith location, $S_{ij}(\mathrm{i}\omega)$ is the cross-PSD function for ground motions at locations i and j given by

$$S_{ij}(\mathrm{i}\omega) = \sqrt{S_{ii}(\omega)S_{jj}(\omega)}\,\gamma_{ij}(\mathrm{i}\omega) = \sqrt{S_{ii}(\omega)S_{jj}(\omega)}\,\left|\gamma_{ij}(\mathrm{i}\omega)\right|\exp\left(-\mathrm{i}\,\frac{\omega\, d_{ij}}{v_{\text{app}}(\omega)}\right), \tag{2.2.2}$$

where $\gamma_{ij}(\mathrm{i}\omega)$ is the spatial coherence function at the bedrock, which is combined with the lagged coherency value $\left|\gamma_{ij}(\mathrm{i}\omega)\right|$ and the wave-passage effect as $\exp\left\{-\mathrm{i}\,\omega\, d_{ij}/v_{\text{app}}(\omega)\right\}$, d_{ij} is the spatial distance from point i to point j, and $v_{\text{app}}(\omega)$ is the wave apparent velocity.

To obtain the cross-PSD matrix of ground motions at ground surface, the following equation gives cross-PSD functions between the bedrock spatial points and ground surface points as

$$S_{i'j'}(\mathrm{i}\omega) = H_i(\mathrm{i}\omega)\, H_j^*(\mathrm{i}\omega)\, S_{ij}(\omega), \tag{2.2.3}$$

in which $H_i(\mathrm{i}\omega)$ and $H_j(\mathrm{i}\omega)$ are frequency transfer functions (FTF) between points *i*-*i*′ and *j*-*j*′ shown in Figure 2.1, and they can be obtained based on the site amplification method presented in Section 2.4.1. Then the cross-PSD matrix of ground motions at ground surface can be written as

$$\mathbf{S}_{\text{surface}}(\mathrm{i}\omega) = \left[S_{i'j'}(\mathrm{i}\omega)\right]_{n\times n}. \tag{2.2.4}$$

Matrix $\mathbf{S}_{\text{surface}}(\mathrm{i}\omega)$ is Hermitian and positive definite; it can be decomposed into the product of a complex lower triangular matrix $\mathbf{L}(\mathrm{i}\omega)$ and its Hermitian $\mathbf{L}^H(\mathrm{i}\omega)$ using the Cholesky decomposition as

$$\mathbf{S}_{\text{surface}}(\mathrm{i}\omega) = \mathbf{L}(\mathrm{i}\omega)\, \mathbf{L}^H(\mathrm{i}\omega), \tag{2.2.5}$$

where $\mathbf{L}(\mathrm{i}\omega)$ is given by

$$\mathbf{L}(\mathrm{i}\omega) = \begin{bmatrix} l_{1'1'}(\mathrm{i}\omega) & 0 & \cdots & 0 \\ l_{2'1'}(\mathrm{i}\omega) & l_{2'2'}(\mathrm{i}\omega) & \cdots & 0 \\ \vdots & \vdots & \ddots & \vdots \\ l_{n'1'}(\mathrm{i}\omega) & l_{n'2'}(\mathrm{i}\omega) & \cdots & l_{n'n'}(\mathrm{i}\omega) \end{bmatrix}_{n\times n}, \tag{2.2.6}$$

in which

$$\begin{aligned} l_{i'i'}(\omega) &= \left[S_{i'i'}(\omega) - \sum_{k'=1}^{i'-1} S_{i'k'}(\mathrm{i}\omega) S_{i'k'}^*(\mathrm{i}\omega)\right]^{\frac{1}{2}}, \quad i' = 1', 2', \ldots, n', \\ l_{i'j'}(\mathrm{i}\omega) &= \frac{S_{i'j'}(\mathrm{i}\omega) - \sum_{k'=1}^{i'-1} S_{j'k'}(\mathrm{i}\omega) S_{i'k'}^*(\mathrm{i}\omega)}{S_{j'j'}(\omega)}, \quad j' = 1', 2', \ldots, i'. \end{aligned} \tag{2.2.7}$$

As seen from equation (2.2.7), caculation of square roots is required in the Cholesky decomposition in equation (2.2.6). If the matrix being factorized is positive definite as

required, the numbers under the square roots are always positive in exact arithmetic. Unfortunately, sometime the numbers can become negative because of round-off errors caused by the caculation of square roots, in which case the algorithm cannot continue. An alternative way avoiding extracting square roots is to use the LDL decomposition, which can be found in detail from Krishnamoorthy and Menon (2011).

Then the stochastic process $u_{j'}(t)$ can be simulated using the following expression (Hao *et al.*, 1989)

$$u_{j'}(t) = \sum_{m'=1}^{j'} \sum_{l=1}^{N_f} a_{j'm'}(\omega_l) \cos\left[\omega_l t - \theta_{j'm'}(\omega, t) + \varphi_{m'l}\right], \tag{2.2.8}$$

where

$$a_{j'm'}(\omega_l) = \left|l_{j'm'}(\mathrm{i}\omega_l)\right| \sqrt{4\,\Delta\omega}, \quad \theta_{j'm'}(\omega_l) = \tan^{-1}\left[\frac{\Im\left(l_{j'm'}(\mathrm{i}\omega_l)\right)}{\Re\left(l_{j'm'}(\mathrm{i}\omega_l)\right)}\right], \tag{2.2.9}$$

are the amplitudes and phase angles of the simulated time histories, $\Delta\omega$ is the resolution in the frequency domain, N_f is number of discrete points of frequency, and $\omega_l = l\Delta\omega$ is the lth discrete frequency. $\varphi_{m'l}$ is the random phase angle, which is often assumed to be uniformly distributed over $[0, 2\pi]$, resulting in stochastic process $u_j(t)$ being stationary. The nonstationary ground motions may be obtained by using the time-domain amplitude modulating function (Deodatis, 1996; Hao *et al.*, 1989).

2.3 VSHD-based Seismological Spectra and the Combined Coherence Model

It is well known that a UHS cannot represent a spectrum induced by a single earthquake event, and the simulation scheme presented by Atkinson (2009) is a time-consuming procedure, since a number of simulations are required. Similar to SHD in scalar probabilistic seismic hazard analysis (PSHA) (presented in Appendix A.1.1), VSHD, which is based on vector-valued probabilistic seismic hazard analysis (VPSHA) (Bazzurro and Park, 2011; Ni *et al.*, 2012; Zhang *et al.*, 2013c) can be used more appropriately to select earthquake records or to determine the seismological spectra, rather than using the SHD values on UHS.

2.3.1 Vector-Valued Seismic Hazard Deaggregation

It is well recognized that a vector of ground motion intensity measures (IM) can give more accurate and stable results for structural seismic response analysis. The VPSHA, provided in detail in Appendix A.1.2, is usually employed because it can provide a multivariate probability exceedence model of the joint shaking hazards when many ground motion parameters are of interest for structural analysis (Bazzurro and Cornell, 1999). The joint hazards provided in VPSHA can be deaggregated through the VSHD as follows.

For a vector of spectral accelerations at multiple vibration periods $\{S_a(T_1), S_a(T_2), \ldots, S_a(T_n)\}$, the mean rate density (MRD), contributed by all (m, r)-pairs, can be expressed as

$$\lambda_{s^*} = \sum_{i=1}^{N} \nu_i \Big\{ \sum_{j=1}^{N_m} \sum_{k=1}^{N_r} \bar{P}\left\{S_a(T_1) > s_1^*,\ S_a(T_2) > s_2^*,\ \ldots,\ S_a(T_n) > s_n^* \,\middle|\, m_j, r_k\right\} \bar{P}_M(m_j) \bar{P}_R(r_k) \Big\}_i, \tag{2.3.1}$$

and the MRD contributed by (m_j, r_k)-pair is given by

$$\lambda_{s^*}(m_j, r_k) = \sum_{i=1}^{N} \nu_i \Big\{ \bar{P}\left\{S_a(T_1) > s_1^*,\ S_a(T_2) > s_2^*,\ \ldots,\ S_a(T_n) > s_n^* \,\middle|\, m_j, r_k\right\} \bar{P}_M(m_j) \bar{P}_R(r_k) \Big\}_i, \tag{2.3.2}$$

in which N is the number of seismic sources of interest in the VPSHA, ν_i is the mean rate of occurrence of the ith seismic source, N_m and N_r are the numbers of discrete points of magnitude and site-to-source distance, respectively. $\mathbf{s}^* = \{s_1^*, s_2^*, \ldots, s_n^*\}$ is the vector containing spectral acceleration thresholds with respect to MRD, $\bar{P}\{S_a(T_1) > s_1^*,\ S_a(T_2) > s_2^*,\ \ldots,\ S_a(T_n) > s_n^* \,|\, m, r\}$ is the complementary cumulative probability distribution function corresponding to the multivariate lognormal distribution conditional on (m, r)-pair, $\bar{P}_M(m)$ and $\bar{P}_R(r)$ are the probability mass functions of earthquake magnitude and site-to-source distance, respectively (Bazzurro and Cornell, 1999).

Similar to the SHD in PSHA, the joint hazard provided in VPSHA can be deaggregated to all the (m_j, r_k)-pair; the dominant (the most likely) pair $(m_{\max}, r_{\max})$ or the mean pair, denoted as (m_β, r_β), can be obtained based on the maximum or average contribution to the

total mean exceedence rate p_{jk} given by

$$p_{jk} = \frac{\lambda_{s^*}(m_j, r_k)}{\lambda_{s^*}}. \tag{2.3.3}$$

The VSHD presented in this section is performed using the seismic sources shown in Figure 2.2, in which $M_{\min}$ and $M_{\max}$ are the minimum and maximum earthquake magnitudes considered in the VPSHA, ν denotes the annual mean rate of exceedence for a given seismic source, and d is the depth of the seismic source. These seismicity parameters are given in Figure 2.2, and Abrahamson and Silva's predictive equation is used (Abrahamson and Silva, 1997). Eight vibration periods, namely $T = \{0.01, 0.02, 0.05, 0.1, 0.3, 0.5, 1, 5\}$ (sec) are selected, and the VSHD result at $p^* = 4 \times 10^{-5}$ is shown in Figure 2.3, where p^* is the joint probability of exceedence of spectral accelerations at periods T (Zhang *et al.*, 2012b).

2.3.2 Physically Compliant Seismological Spectra

The seismological spectrum at a site $Y(M_0, R, f)$ can be expressed as the contribution from earthquake source (E), path (P), site (G), and instrument or type of the motion (I) (Boore, 2003a)

$$\begin{aligned} Y(M_0, R, f) &= E(M_0, f)P(R, f)G(f)I(f) \\ &= \frac{R_{\Theta\Phi}VF}{4\pi\rho_s\beta_s^3 R_0} \frac{1}{1 + (f/f_0)^2} \cdot Z(R) \exp\left(-\frac{\pi f R}{Q(f)c_Q}\right) \cdot A(f) \exp(-\pi\kappa_0 f) \cdot I(f), \end{aligned} \tag{2.3.4}$$

where M_0 is the seismic moment measuring the earthquake size, R is the site-to-source distance, $R_{\Theta\Phi}$ is the radiation pattern, V is the partition of total shear-wave energy into horizontal components, F represents the effect of the free surface, ρ_s and β_s are the density and shear-wave velocity in the vicinity of the source, R_0 is a reference distance which is usually set as 1 km, c_Q is the seismic velocity, $Z(R)$ is the geometric spreading function, $A(f)$ is a function of shear-wave velocity versus depth, κ_0 is the diminution parameters, and f_0 is the corner frequency given by

$$f_0 = 4.9 \times 10^6 \beta_s \left(\frac{\triangle\sigma}{M_0}\right)^{\frac{1}{3}}, \tag{2.3.5}$$

in which $\triangle\sigma$ is called stress drop with unit in bars.

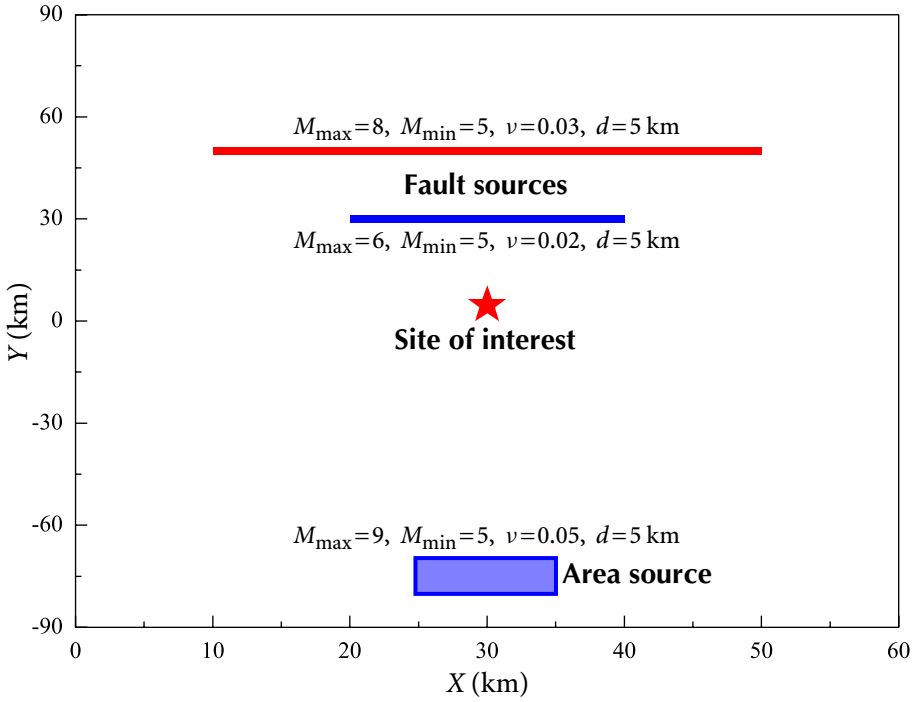

Figure 2.2 Seismic source

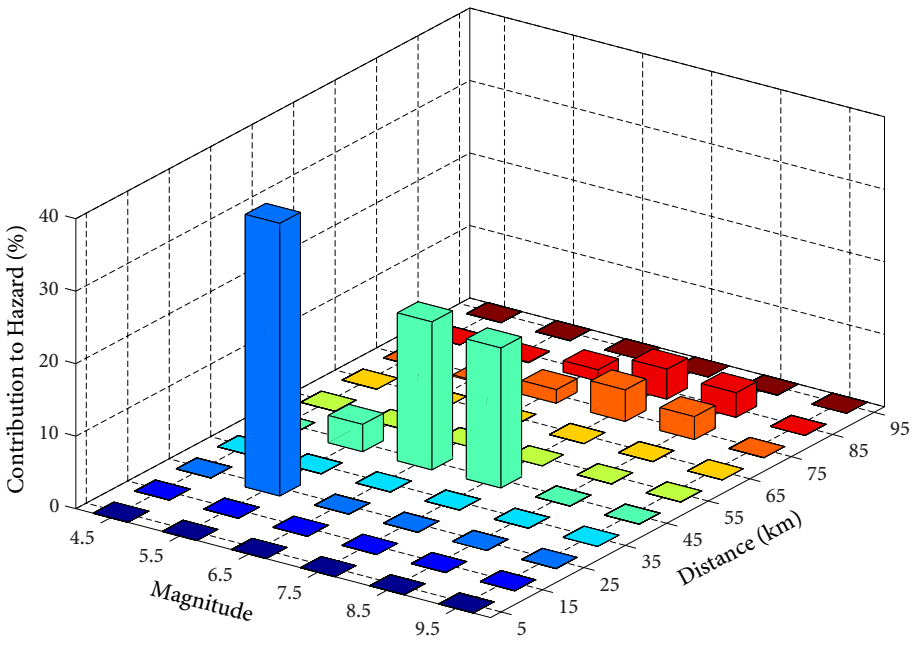

Figure 2.3 Result of vector-valued seismic hazard deaggregation

It is seen, in equation (2.3.4), that the shape and amplitude of semiological spectrum can be uniquely determined by an earthquake event, i.e., an (m, r)-pair. However, the problem is how to reasonably determine an (m, r)-pair to obtain a specific seismological spectrum. One of the most appropriate ways of obtaining (m, r)-pair is based on PSHA. Atkinson (2009) used the hazard deaggragation results on UHS to obtain the (m, r)-pair in simulating earthquake time histories; however, it is a time-consuming procedure because a number of simulations are required.

On the other hand, VPSHA can provide the joint probability information for spectral accelerations at multiple vibration periods, and the joint hazard can be deaggregated through VSHD to obtain an earthquake event containing the joint information of these spectral accelerations. Thus, the physically compliant seismological spectrum is properly related to the deaggregated results from VSHD for the simulation of SVGM.

It is noted that simulation schemes using the seismological spectra in conjunction with the stochastic approach are widely used in the simulation of earthquake rupture processes, but are rarely used in ground motion synthesis for structural RHA. One approach proposed by Atkinson (2009) is for ground motion synthesis for a single site. However, none of the existing work is for the generation of SVGM.

It should also be noted that an (m, r)-pair may not completely represent a single earthquake, and other earthquake features, such as duration of ground motion, peak ground motions, and local site effects, should also be incorporated to comprehensively determine a single earthquake. However, it is well recognized that the (m, r)-pair is the most important and most frequently used parameters in defining an earthquake scenario; all other features, such as duration of ground motion, peak ground motions, and ground motion near-fault effect, can be predicted through the (m, r)-pair (Datta, 2010; Shahi and Baker, 2011), and these predicted features can be incorporated in the proposed approach. Other earthquake features, such as the local site effects, in determining an earthquake event are accounted for in details for ground motion simulation in Section 2.4.

It is assumed that the earthquake magnitude and hypocentral site-to-source distance derived from VSHD are $m = 7.0$ and $r = \sqrt{b^2 + h^2} = 31.6$ km, where $h = 10$ km is the depth of the source and $b = 30$ km is the epicentral distance. The seismological spectra of Western

North America (WNA) with this (m, r)-pair as shown in Figure 2.4 are used. Parameters of the seismological spectra are from Campbell (2003) in verifying the ground motion predictive models of Next Generation Attenuation (NGA).

Besides the ground motion "power" model, Section 2.3.3 introduces the combined coherence model in modelling spatially correlated earthquake motions.

2.3.3 The Combined Spatial Coherence Model

As mentioned in Section 1.1.2, the coherence function is expressed in the frequency domain to model the ground motion spatial variability. The coherence of ground motions at points k and l is obtained from the smoothed cross-PSD that is normalized with respect to the corresponding auto-PSD given by

$$\gamma_{kl}(\omega, d_{kl}) = \frac{S_{kl}(\omega, d_{kl})}{\sqrt{S_{kk}(\omega) S_{ll}(\omega)}}. \tag{2.3.6}$$

Because the coherence value is a complex number, equation (2.3.6) can be written as

$$\gamma_{kl}(\omega, d_{kl}) = \left|\gamma_{kl}(\omega, d_{kl})\right| \exp\left[\mathrm{i}\,\theta_{kl}(\omega, d_{kl})\right], \quad \theta_{kl}(\omega, d_{kl}) = \tan^{-1} \frac{\Im S_{kl}(\omega, d_{kl})}{\Re S_{kl}(\omega, d_{kl})}, \tag{2.3.7}$$

where $0 < \left|\gamma_{kl}(\omega, d_{kl})\right| < 1$ is called the lagged coherence, and d_{kl} is the spatial distance between points k and l.

Der Kiureghian (1996) presented a theoretical study to account for incoherence effect, wave-passage effect, attenuation effect, and site-response effect. These effects are accounted for separately in the wave coherence function model as

$$\begin{aligned} \gamma_{kl}(\omega)^{\text{combined}} &= \gamma_{kl}(\omega)^{\text{incoherence}} \gamma_{kl}(\omega)^{\text{wave-passage}} \gamma_{kl}(\omega)^{\text{site}} \\ &= \cos\left[\beta(d_{kl}, \omega)\right] \cdot \exp\left[-\frac{1}{2}\alpha^2(d_{kl}, \omega)\right] \cdot \exp\left[-\mathrm{i}\frac{\omega d_{kl}^L}{v_{\text{app}}(\omega)}\right] \cdot \exp\left[\mathrm{i}\,\theta_{kl}\right], \end{aligned} \tag{2.3.8}$$

in which d_{kl}^L is the spatial distance, in the propagating direction of apparent wave motions, between points k and l, $\gamma_{kl}(\omega)^{\text{incoherence}}$ is modelled by accounting for the randomness of the medium and is the lagged coherence, $\gamma_{kl}(\omega)^{\text{wave-passage}}$ and $\gamma_{kl}(\omega)^{\text{site}}$ are used to reflect the phase effects of coherence model induced by wave-passage effect and local site effect, and parameter θ_{kl} in the local site effect can be obtained through the FTF of layered soil profiles.

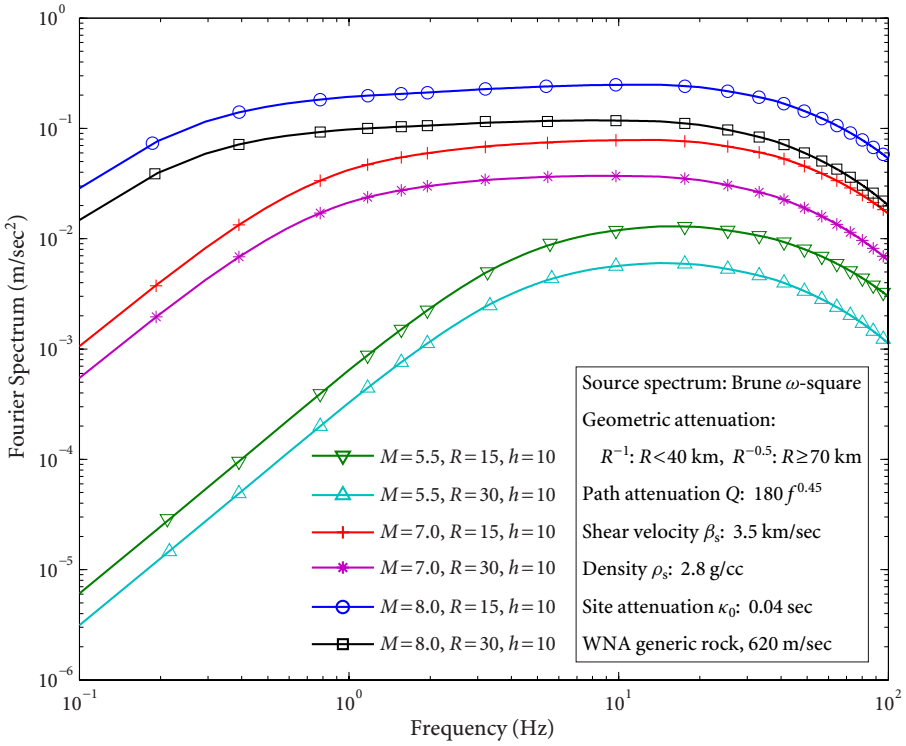

Figure 2.4 Seismological spectra

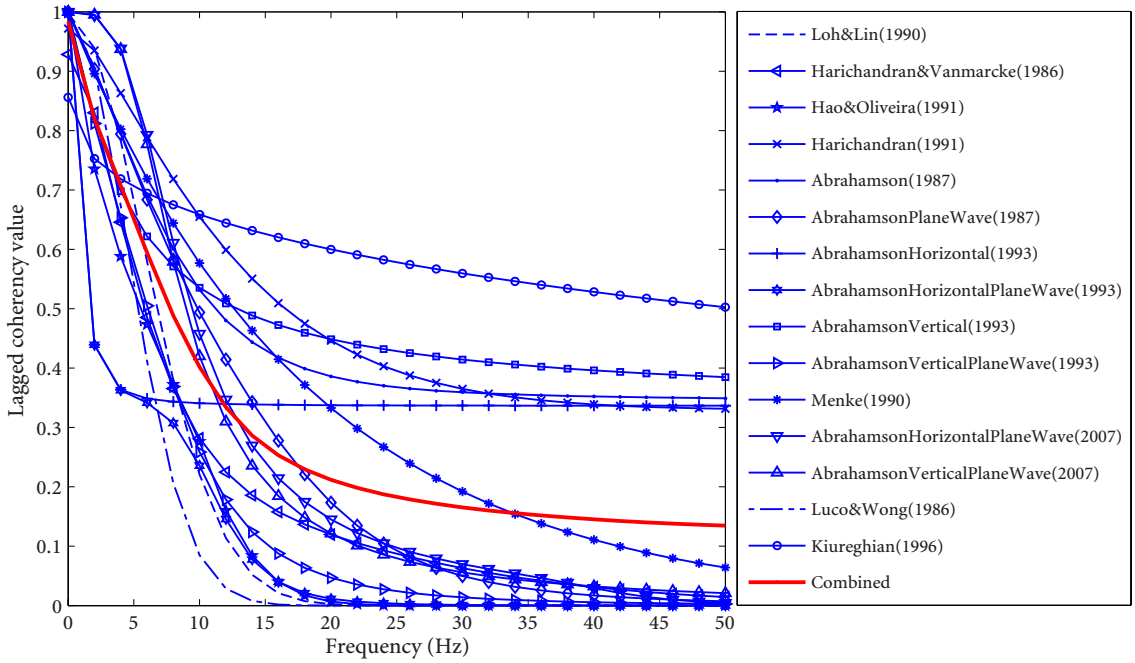

Figure 2.5 Combined coherence model

The existing coherence models are mostly regressed from the spatially implemented dense arrays; they vary from one to another due to the dependence of the array data used and even signal analysis techniques. In reality, it is difficult to obtain a theoretically accurate coherence model because of the difficulty in studying wave propagation through highly variable and complex soil media. It is well-known that a more refined model can be obtained through a more advanced analysis of wave motion transmitting through an practically modeled medium, e.g., considering the 2-D/3-D soil domains or the heterogeneity of soil profiles. However, most of these works fail to obtain an explicit analytical expression of the coherence function that is needed for synthesis of SVGM.

Furthermore, in the theoretical wave coherence model by Der Kiureghian (1996), only the randomness of rock was accounted for approximately in the incoherence effect, which is assumed to affect the lagged coherency value only, and the local site effects is assumed to have an influence on the phase only. However, in practice, the local soil exhibits greater randomness and variation than the rock, which can also affect the lagged coherency value (Bi and Hao, 2011). Unfortunately, how the local soil profile influences the lagged coherence value, besides affecting the phase part of coherence model, is unknown.

Because of these reasons and the importance of selecting the coherency function for seismic analysis of structures extended in space under SVGM, a more plausible and viable approach would be to use various coherence models to obtain a weighted combined model in describing the SVGM, which is similar to the logic tree method in combining various ground motion predictive models in the PSHA. In this study, almost all the existing wave coherence models, including theoretical, semi-analytical, and empirical models, are selected; a total of 15 coherence models are collected (Loh and Lin, 1990; Harichandran and Vanmarcke, 1986; Oliveira *et al.*, 1991; Harichandran, 1991; Tsai, 1987; Menke, 1990; Luco and Wong, 1986; Der Kiureghian, 1996). These models are combined with equal weighting coefficient to yield the combined coherence function. The combined coherence model ($d = 100$ m) is shown in Figure 2.5.

It is admitted that choosing the weighting coefficient for each model is subjective; however, it has combined information of all the current models and would be an appropriate way to account for complicated wave coherence effect as discussed above. Further studies

should be conducted on the treatment of epistemic uncertainty of coherence models in a more rigorous manner for the spatial ground motion simulation. For example, analogous to the logic tree method in combining various ground motion prediction models in scalar PSHA and VPSHA, the viability of coherence models can be reflected in the cross-PSD in equation (2.3.6), which determines the simulated spatial earthquake motions. A family of cross-PSD outputs, corresponding to each logic tree thread, can be obtained (like hazard curves). The variability of coherence model can be calibrated and accounted for by using a group of cross-PSD curves.

2.4 Tridirectional Local Site Amplification Approach Accounting for Random Soil Profiles

As discussed in Section 1.1.2, the local site condition can strongly influence the responses of structures extended in space, and the one-dimensional site response analysis is perhaps the most used technique in accounting for the local site effect and is adopted in several design standards (ASCE, 1998). It is admitted that the results obtained from 2-D or 3-D analysis with accurate local soil modelling are preferred; however, these results are not readily applicable in engineering practices due to the complexity of site response analysis.

In reality, spatial variations and uncertainties of soil properties always exist, which are caused by the inherent heterogeneity or variability of soils, the limited availability of information about internal conditions, and sometimes the measurement errors. Soil properties can also be affected by underground water, such as the water saturation effect. As a result, soil, which is spatially variable, random, heterogeneous, and nonlinear, becomes a natural material that is difficult to characterize accurately; none of the existing works, to the best knowledge of the author, presented detailed study in accounting for the local site effect in synthesis of SVGM.

2.4.1 Site Amplification of In-plane and Out-of-plane Wave Motions

Consider a canyon site with horizontal infinitely-extended multiple linear elastic soil layers on a half space (base rock), as shown in Figure 2.1, in which h_i, G_i, ρ_i, ν_i, ξ_i are the depth,

shear modulus, mass density, Poisson's ratio, and damping ratio of layer *i*. The spatially varying base rock motions are assumed to consist of out-of-plane SH-wave and in-plane combined P-SV-waves propagating into a site with assumed incident angles. It is assumed that the amplitude of the vertical motion is 2/3 of that of the horizontal components for the incoming waves consisting of SH-wave and combined P-SV-waves. The incident motions at different locations on the base rock are assumed to have the same PSD. This assumption is reasonable, since the source to site distance is usually much larger than the dimension of the structure.

Specifically, for two pairs of points k-k' and l-l' located on the bedrock and ground surface, their cross-PSD is

$$G_{a_{k'}a_{l'}}(\omega, d_{k'l'}) = H_{kk'}(\omega)\, H_{ll'}(-\omega)\, G_{a_k a_l}(\omega, d_{kl}), \tag{2.4.1}$$

in which $H_{kk'}(\omega)$ and $H_{ll'}(\omega)$ are the FTFs between points k-k' and l-l', and

$$G_{a_k a_l}(\omega, d_{kl}) = \gamma_{kl}(\omega, d_{kl}) \sqrt{G_{a_k a_k}(\omega) G_{a_l a_l}(\omega)}, \tag{2.4.2}$$

where $G_{a_k a_k}(\omega) = G_{a_l a_l}(\omega)$, and $\gamma_{kl}(\omega, d_{kl})$ is the coherence function for spatial points at the bedrock.

To obtain the FTFs $H_{kk'}(\omega)$ and $H_{ll'}(\omega)$ in equation (2.4.1), equations of wave motion in volumetric strain e and in rotation strain vector $\mathbf{\Omega}$ are

$$\nabla^2 e = -\frac{\omega^2}{c_p^2} e, \qquad \nabla^2 \mathbf{\Omega} = -\frac{\omega^2}{c_s^2} \mathbf{\Omega}. \tag{2.4.3}$$

The dynamic equations can be expressed in the frequency domain for the SH-wave and P-SV-wave as

$$\mathbf{K}_{\text{SH}} \mathbf{X}_{\text{SH}} = \mathbf{P}_{\text{SH}}, \qquad \mathbf{K}_{\text{P-SV}} \mathbf{X}_{\text{P-SV}} = \mathbf{P}_{\text{P-SV}}, \tag{2.4.4}$$

where $\mathbf{X}_{\text{SH}}$, $\mathbf{P}_{\text{SH}}$ and $\mathbf{X}_{\text{P-SV}}$, $\mathbf{P}_{\text{P-SV}}$ are the displacement and load vectors corresponding to the incident SH-wave and combined P-SV-wave. The stiffness matrices $\mathbf{K}_{\text{SH}}$ and $\mathbf{K}_{\text{P-SV}}$ are dependent on the soil properties, incident wave type, incident angle, and circular frequency ω. The dynamic load vectors $\mathbf{P}_{\text{SH}}$ and $\mathbf{P}_{\text{P-SV}}$ depend on the incident wave type, bedrock properties, incident wave frequency and amplitude. The site transfer functions in the out-of-plane and in-plane directions can be estimated by solving equations (2.4.4) in the frequency

domain at every discrete frequency (Wolf, 1985). Detailed information on solving equation (2.4.4) is provided in Appendix A.2.

It should be noted that, based on equations (2.4.4), tridirectional SVGM (SH wave motions in the horizontal direction and P-SV-wave motions in the horizontal and vertical directions) can be obtained, which is of prime importance for structural seismic analysis under tridirectional ground motions.

2.4.2 Spatial Random Field Theory

Due to the inherent spatial variation and uncertainty of historically accumulated soil profiles, the random field theory is one of the most appropriate approaches to describe the variability of soil properties, which is introduced briefly in the following (Vanmarcke, 1977).

For a one-dimensional random field $x(z)$, with the mean value $\overline{x}$ and the standard deviation σ_x, the mean and variance of its local average process $x_Z(z)$ are given by

$$\mathrm{E}[x_Z(z)] = \overline{x}(z), \quad \sigma[x_Z(z)] = \lambda(Z)\sigma_x^2, \tag{2.4.5}$$

in which $\lambda(Z)$ is the variance reduction parameter of $x(z)$ that measures the reduction of point variance σ_x^2 under the local average, and it can be derived by the auto-correlation function $\rho_x(\triangle z)$ as follows

$$\lambda(Z) = \frac{2}{Z}\int_0^Z \left(1 - \frac{\triangle z}{Z}\right)\rho_x(\triangle z)\mathrm{d}(\triangle z). \tag{2.4.6}$$

By using the exponential auto-correlation function, the variance reduction function can be expressed as

$$\lambda(Z) = \frac{1}{2(Z/r_x)^2}\left[2(Z/r_x) + \mathrm{e}^{-2(Z/r_x)} - 1\right], \tag{2.4.7}$$

in which r_x is the spatial correlation distance, which measures the correlation level or persistence of the property from one point to another at a site; small values of r_x suggest rapid fluctuation about the average, whereas large values of r_x imply that a slowly varying component is superimposed on the average value $\overline{x}$.

In the one-dimensional case, introducing correlation distance of a random property results in a reduction of its standard deviation, i.e., the reduced variance for process $x(z)$ is $\lambda(Z)\sigma_x^2$ (Vanmarcke, 1977).

2.4.3 Water Saturation Effect

For water saturation induced site amplification, Yang and Sato (2000) stated that the degree of water saturation of a site has a significant influence on its Poisson's ratio and P-wave propagation, but does not affect the S-wave propagation at the site. The interactions between the solid skeleton and pore fluid were modelled using the macroscopic laws of mechanics, based on which the Poisson's ratio accounting for water saturation is given by

$$\nu = \frac{1}{2}\frac{\alpha^2 M/G + 2\nu'/(1-2\nu')}{\alpha^2 M/G + 1/(1-2\nu')}, \tag{2.4.8}$$

where ν' is Poisson's ratio of soil skeleton, α and M are

$$\nu' = \frac{\lambda}{2(\lambda+G)}, \quad \alpha = 1 - \frac{K_b}{K_s}, \quad M = \frac{K_s^2}{K_d - K_b}, \tag{2.4.9}$$

in which K_s and K_b are bulk moduli of solid grains and skeleton, respectively, and

$$K_d = K_s\left[1 + n\left(\frac{K_s}{K_f} - 1\right)\right], \quad K_f = \frac{1}{\dfrac{1}{K_w} + \dfrac{1-S_r}{P_a}}, \quad n = \frac{V_v}{V_t}, \quad S_r = \frac{V_w}{V_v}, \tag{2.4.10}$$

where n is the porosity, S_r is the degree of saturation, K_f is the bulk modulus of homogeneous fluid, V_v, V_w, and V_t are the volumes of pores, pore-water, and total volume, respectively, K_w is the bulk modulus of water, and P_a is the absolute fluid pressure.

It is noted that spatial variability model of soil properties given in Section 2.4.2 and water saturation effect model presented in Section 2.4.3 are reflected in equation (2.4.4) to obtain the site transfer function. Furthermore, practical soil properties also exhibit great randomness, which is accounted for by the Monte Carlo simulation. The stiffness matrix in equation (2.4.4) is defined by site soil properties, such as the shear modulus, damping ratio, and mass density. To model the random variability of these properties, Monte Carlo simulation is used to estimate the mean and standard deviation

A different approach in considering the local site effect is the conditional simulation (Vanmarcke *et al.*, 1993), which assumes that ground motions at several spatial points are conditional on the selected real earthquake records having similar site conditions to the sites where these spatial points are located. However, a problem arises on how to reasonably choose these records for structures with various dimensions.

Thus, a more appropriate approach is perhaps to take a comprehensive and detailed site response analysis that can account for the soil effects, which is also recommended in several standards on site response analysis (ASCE, 1998).

Combining the VSHD-based semiological spectra given in Section 2.3.2 and the combined coherence model presented in Section 2.3.3, a numerical example is presented in Section 2.5, considering the incoherence effect, wave-passage effect, and local site effects.

2.5 Numerical Example

A local soil condition with heterogeneous soil profiles given in Figure 2.6 is used and the soil properties are given in the attached table. Four pairs of equally spaced points (i-i', j-j', m-m', n-n') located on the bedrock and the ground surface with spatial distance 100 m are considered. The ground water level is assumed to be in the 3rd layer initially, and the WNA generic rock site with bedrock wave velocity 620 m/sec is selected as the bedrock of soil profiles (Campbell, 2003).

Using VSHD results in Figure 2.3, the VSHD-based seismological spectra of WNA in Figure 2.4 are used, and the combined coherence model in Figure 2.5 is used for the four points located at the bedrock level in Figure 2.6. The site response approach, presented in Section 2.4, is adopted to account for the local site effect in simulation of SVGM by the multi-variate stochastic vector process given in Section 2.2 (Deodatis, 1996; Hao *et al.*, 1989). The duration, sampling frequency of generated time histories, and the length of Fourier transformation are chosen as 40.96 sec, 50 Hz, and 2048, respectively. Jenning's envelope function is used to obtain the nonstationary ground motions. In determining the wave-passage effect, the apparent velocity at the bedrock is given as $v_{\text{app}} = 1240$ m/sec. The initial wave motion incident angle beneath the bedrock is assumed to be $\alpha_{\text{SH}} = \alpha_P = 60^\circ$.

2.5.1 Local Site Effects on the Loss of Motion Coherency

Assuming that all properties of soil profiles shown in Figure 2.6 are deterministic, SVGM on the bedrock and ground surface are simulated to study the influence of local site condition on the wave motion coherency. Figure 2.7 presents the lagged coherency of generated

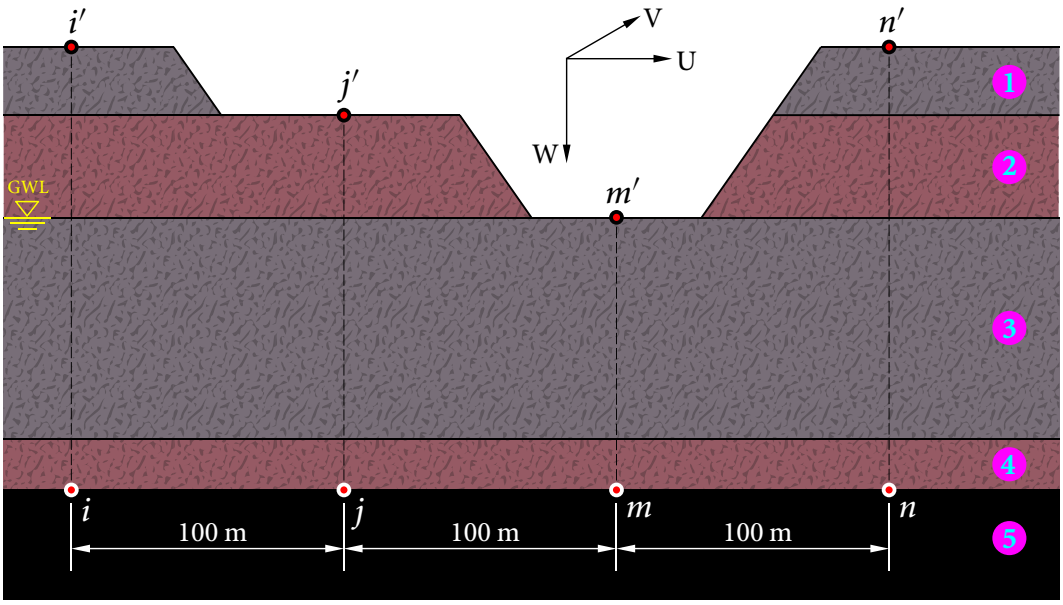

Layer	Property	h (m)	G (MPa)	ρ (kN/m^3)	ν	ξ
1	Silty Clay	3.6	17.89	16.80	0.35	0.05
2	Clay	13.8	18.30	20.36	0.35	0.05
3	Silty Clay	6.8	19.33	16.00	0.32	0.05
4	Fine Sandy Clay	4.4	20.35	20.06	0.30	0.05
5	Rock	—	1153.20	29.40	0.25	0.05

Figure 2.6 Schematic view of the local site condition with different soil profiles

bedrock motions and the corresponding targets between points *i*-*j* and *j*-*n*, where the lagged coherency of generated wave motions is chosen as the mean value of 100 simulated lagged coherency values from the Monte Carlo simulation. As shown, the lagged coherency values of bedrock motions agree well with their targets and they will converge as the number of simulated samples increases, which further indicates the consistency of generated spatially correlated bedrock wave motions.

Figure 2.8 shows the mean values of 100 simulated lagged coherency functions of spatial in-plane and out-of-plane surface motions for points i'-j', i'-m', and i'-n', and the lagged coherency functions between bedrock motions at sites *i*-*j*, *i*-*m*, and *i*-*n* are also presented. It reveals that the coherency values between surface ground motions are significantly different from those between the bedrock motions. The lagged coherency values of surface ground

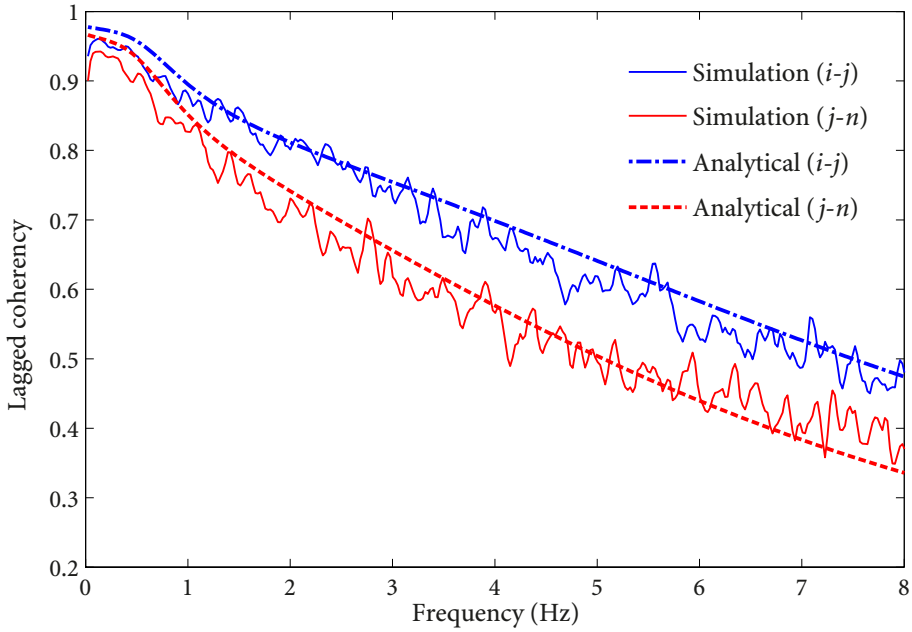

Figure 2.7 Lagged coherency of ground motions at bedrock

motions are smaller at all frequencies than those on the bedrock level, and the coherency between bedrock motions is the upper bound of that on the ground surface. These phenomena indicate that the local site condition can cause reduction of cross correlation of spatial bedrock motions. These observations are consistent with those obtained by Liao and Li (2002) and Bi and Hao (2011).

In Figure 2.8, it is observed that there are many obvious peaks and troughs in the coherency function of surface ground motions, and these peaks and troughs are related to the modulus of spectral ratio $|H_{k'}(\mathrm{i}\omega)|/|H_{l'}(\mathrm{i}\omega)|$ shown in the same figure. For example, six minima can be observed around frequencies 1.00, 2.70, 4.80, 6.17, 6.90, and 7.80 Hz in the coherency function of horizontal in-plane motions between points i' and j', and these minima correspond to the six peaks and troughs of the spectral ratio in Figure 2.8. Similar results can also be observed for the out-of-plane and in-plane ground motions between points i' and m' in Figure 2.8. This is because that the site amplification results are different at certain frequencies for the two local sites, which results in the loss of coherency of surface motions at these frequencies. These conclusions are in good agreement with observations

obtained from real records, such as El Centro array in California, the SMART-1 strong motion array in Taiwan, and the array in the Parkway Valley, New Zealand (Zerva, 2009).

Furthermore, the local site effect remains a minor factor on the loss of lagged coherency of spatial locations with the same or very similar site conditions, such as site i-i' and site n-n' in Figure 2.6, in which the loss of lagged coherency is caused mainly by the incoherence effect and wave-passage effect. This conclusion can be observed from lagged coherency of in-plane and out-of-plane surface motions between points i' and n' in Figure 2.8, where wave propagation through the two sites does not significantly cause the loss of coherency of these spatial bedrock motions. It should be noted that these observations also reveal that the site effect can affect the modulus of coherency function, i.e., the lagged coherency function; the conclusion that site effect can only cause the phase difference of coherency function by Der Kiureghian (1996) is not appropriate .

2.5.2 Simulation of Spatially Correlated Ground Motions

The simulated spatially correlated ground motions, accounting for the randomness and variability of soil properties, wave motions and water saturation level, are presented in this section. For soil properties, the layer thickness d, shear modulus G, density ρ, damping ratio ξ, and Poisson's ratio ν are regarded as random variables. Their specific distributions are not considered herein, but the variations are accounted for by the coefficients of variation $\text{cov} = \sigma/\mu$, with $\text{cov}_d = 0.2$, $\text{cov}_G = 0.4$, $\text{cov}_\rho = 0.2$, $\text{cov}_\xi = 0.4$, and $\text{cov}_\nu = 0.2$. The randomness of water saturation level is accounted for by the variation of Poisson's ratio ν, and the randomness in wave motions is accounted for by the wave incident angle α with $\text{cov}_\alpha = 0.4$ (Wang and Hao, 2002). The spatial correlation distance is chosen as 1.2 times of the thickness of each soil layer (Vanmarcke, 1977), and reductions of the standard deviations of random properties (d, G, ρ, ξ, and ν) have been considered based on one-dimensional random field theory in Section 2.4.2. Parameters related to the water saturation are given as $K_w = 2$ GPa, $n = 0.37$, $P_a = 100$ kPa, and $S_r = 0.98$ for each layer (Yang and Sato, 2000).

The scheme presented in Section 2.4.1 is used to obtain the site amplification functions for every local soil profiles, and the Monte Carlo simulation method is applied to compute the mean and standard deviation of those amplification functions. Figure 2.9 shows part

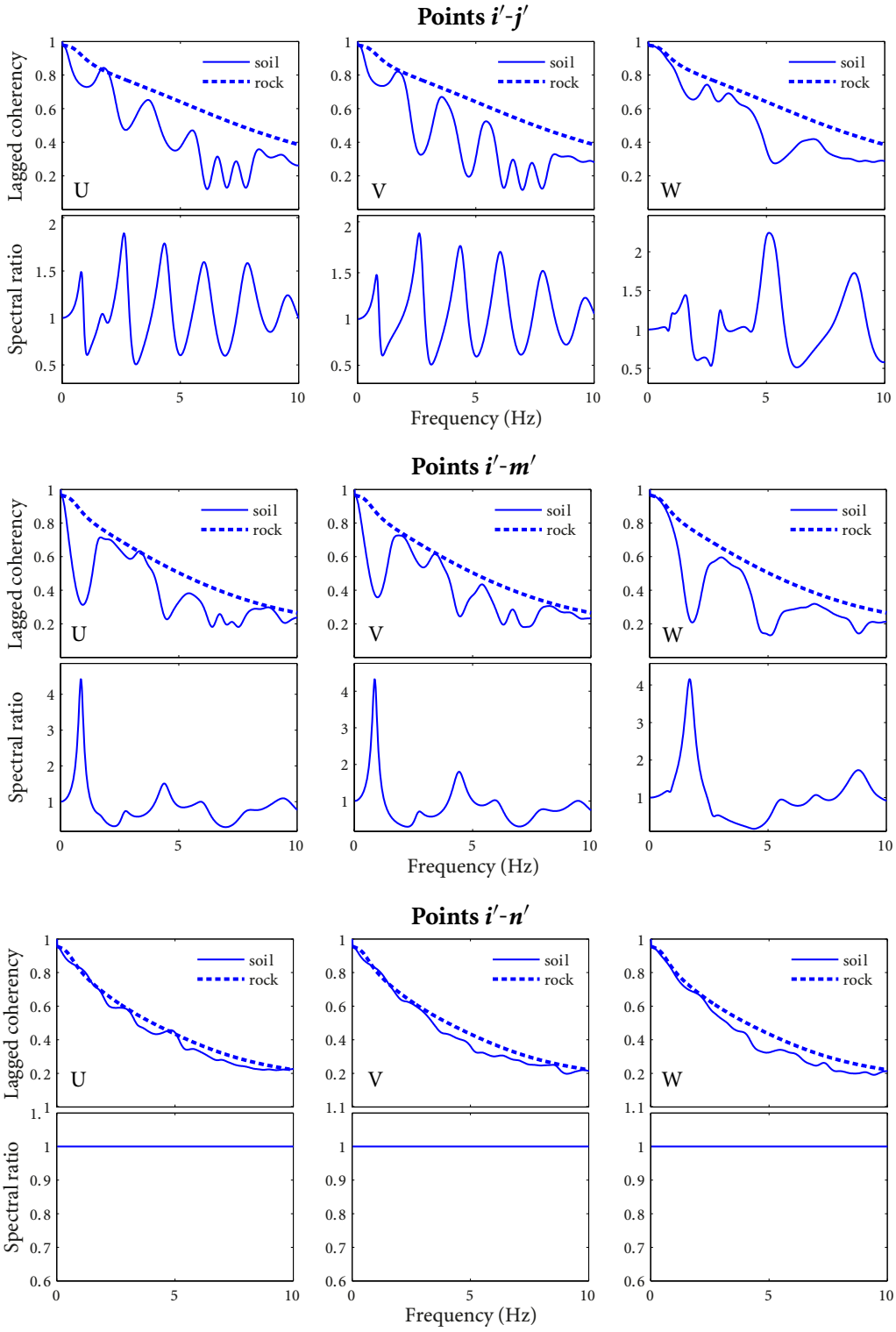

Figure 2.8 Lagged coherency of ground motions at ground surface

of the simulated samples, the estimated mean, mean-plus-one-SD, and mean-minus-one-SD, for points *i*-*i*′ in the horizontal direction U of the in-plane wave motion, for points *j*-*j*′ in the horizontal direction V of the out-of-plane wave motion, and points *m*-*m*′ in the vertical direction W of the in-plane wave motion. Figure 2.10 presents the corresponding phase spectra. It is seen from Figures 2.9 and 2.10 that the variability of soil properties, incident wave motions, and water saturate level can result in variation of amplitude of site amplification functions, shifts of natural frequencies of soil columns and phase spectrum of site amplification functions, especially at high frequency bands. In this study, the values of mean-plus-one-SD of site amplification amplitudes are chosen to account for the local site amplification, and the mean value of phase spectrum is selected to account for the effect of random phase variation of local soil profiles on the ground response.

It should be noted that the extent of variation of site amplification results is largely dependent on the modelling of soil properties. It is observed that variations of site amplification results become much larger as soil profiles are modelled to be much more nonlinear, where these variations closely depend on both the randomness of soil properties, and randomness and uncertainties of earthquake motions beneath soil profiles (Rathje *et al.*, 2010; Li and Assimaki, 2010). In this study, the soil profiles are assumed to be linear in the site amplification analysis. Advanced modellings of soil profiles, e.g., soil dynamic viscoelasto-plastic constitutive model, for the site response analysis are out of the scope of this study; however, the proposed scheme is still applicable and site amplification results obtained from the advanced site response analysis can be directly adopted in this scheme. Furthermore, it is also indicated that the estimated surface motions differ substantially when the random variations of soil properties are taken into account (Rathje *et al.*, 2010; Li and Assimaki, 2010). At the same time, the calibration of the variability of ground motions is dependent on the soil modelling, randomness and uncertainties of earthquake motions. Thus, future studies should be conducted on the calibration of surface ground motion by simultaneously considering soil nonlinearity, randomness and uncertainties of earthquake motions beneath soil profiles.

The tridirectional SVGM on the ground surface and SVGM on the bedrock are generated. Only in-plane horizontal wave motions, including accelerations and displacements, are

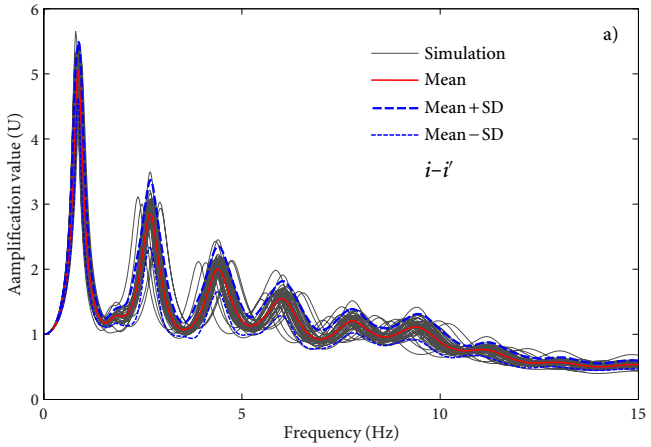

(a) Points *i*-*i*′ in U direction

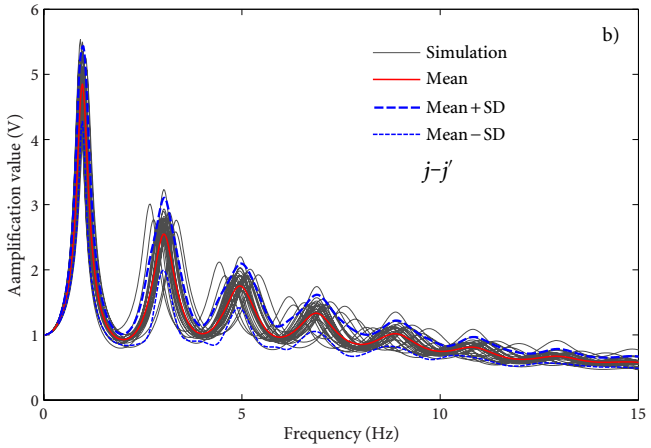

(b) Points *j*-*j*′ in V direction

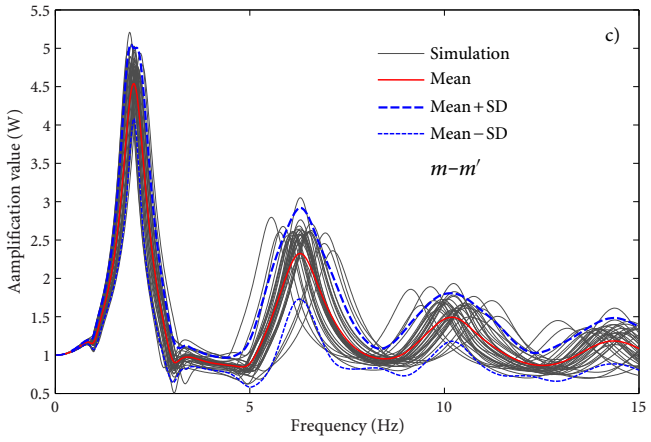

(c) Points *m*-*m*′ in W direction

Figure 2.9 FTFs for in-plane and out-of-plane wave motions

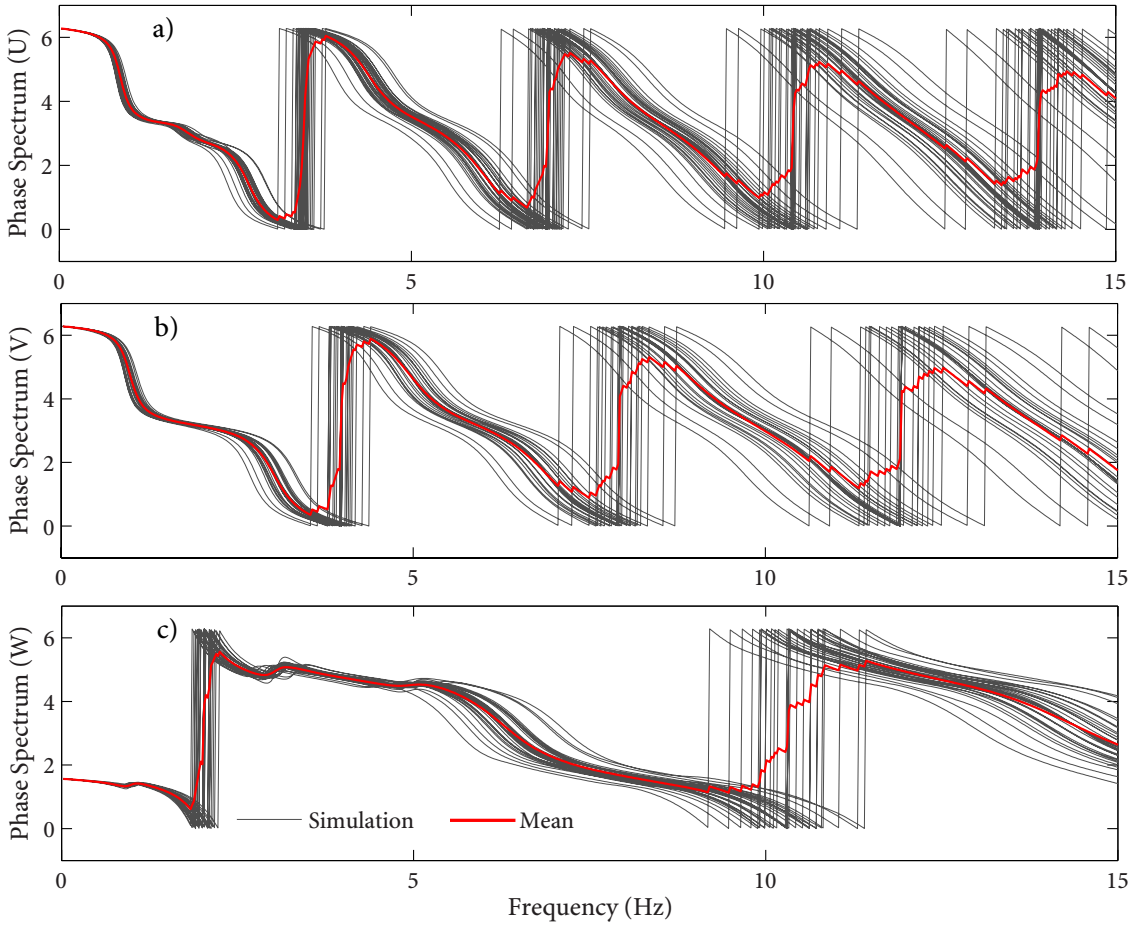

Figure 2.10 The phase spectrum for in-plane and out-of-plane wave motions

shown in Figure 2.11. As shown, the peak ground accelerations (PGA) and displacements (PGD) for bedrock points i, j, m, n are 0.094 g, 0.109 g, 0.115 g, 0.092 g, and 0.098 m, 0.094 m, 0.101 m, 0.098 m, respectively, which are in good agreement with the predicted peak ground motion acceleration and displacement of 0.104 g and 0.097 m (Vanmarcke, 1972). More importantly, it is clearly observed that local soil profiles significantly amplify and filter earthquake bedrock accelerations in the entire duration of ground motions, e.g., PGA at bedrock are amplified as 0.178 g, 0.171 g, 0.185 g, 0.192 g for ground surface points i', j', m', n'. Similar observations are also obtained for the PGD.

The response spectra for ground motions at surface and bedrock points j-j', m-m', and n-n' are shown in Figure 2.12 to illustrate site amplification in the frequency domain. It

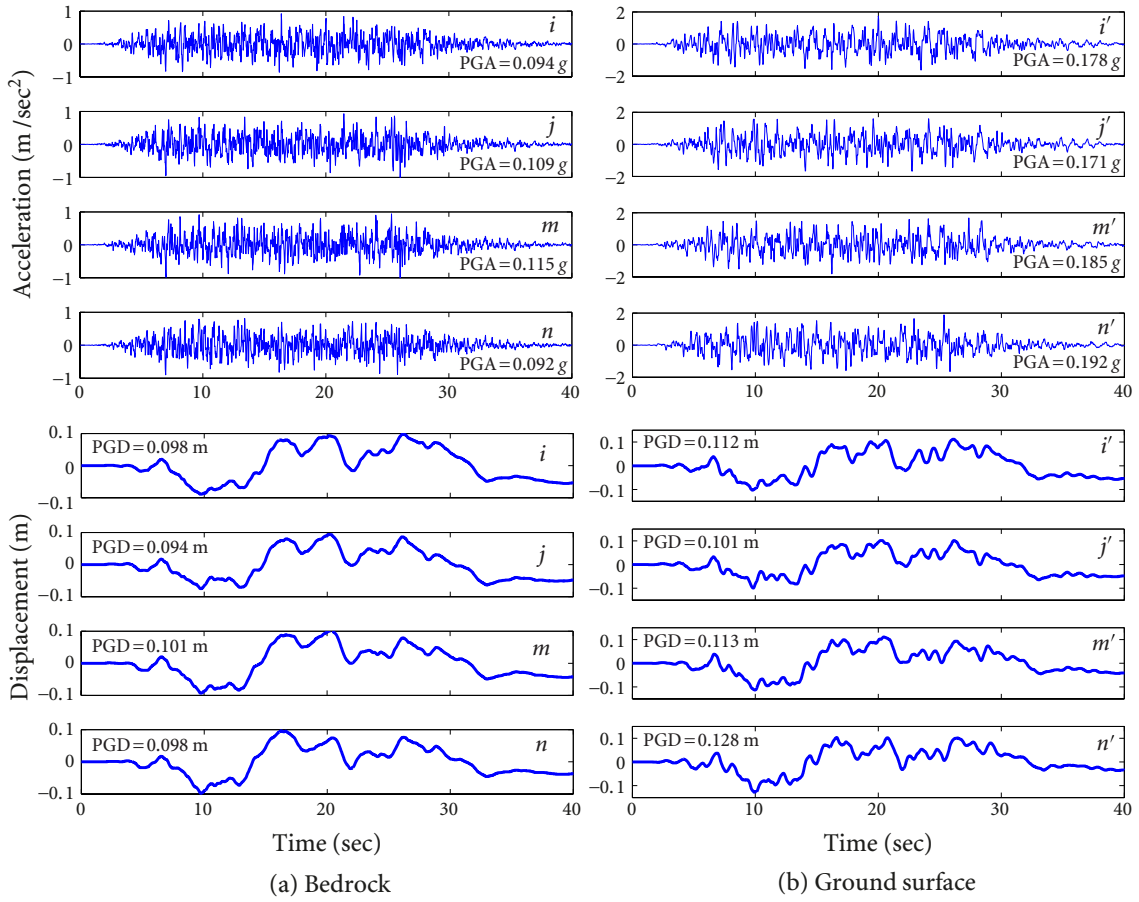

Figure 2.11 The generated earthquake histories at the bedrock and ground surface (in-plane horizontal)

is seen that spectra of bedrock motions are significantly amplified in certain frequencies, e.g., at 1.12 Hz, 3.03 Hz, and 7.69 Hz with spectral amplification values 3.96, 3.36, and 1.46 for ground motions at points *i*-*i*′, and those frequencies are directly related to the natural vibration modes of the site. It is also observed that ground motions obtained on the ground surface are concentrated at a few frequencies corresponding to the various vibration modes of the site, which indicates the importance of considering multiple modes of a local soil site in the estimation of site amplification. Moreover, these conclusions and observations regarding the site amplification, reflected in the time and frequency domains, further show the importance and necessity of considering the local site effect in the ground motion simulation.

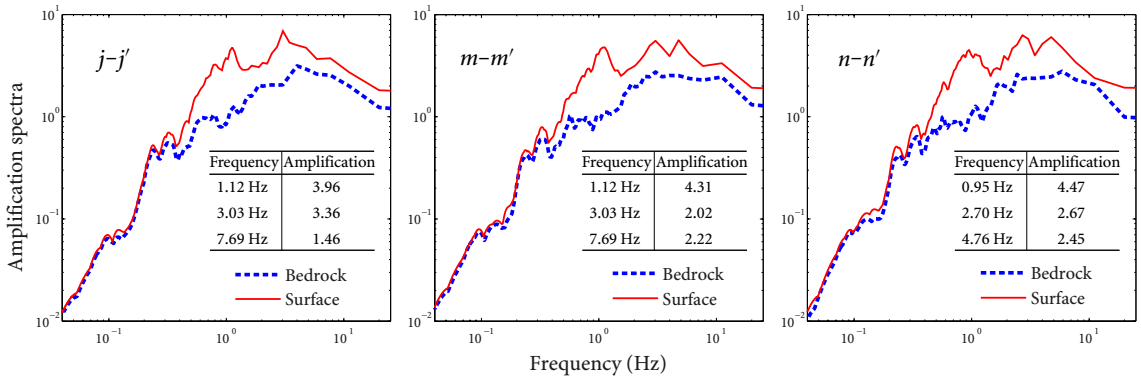

Figure 2.12 Response spectra for horizontal bedrock and in-plane surface motions (U)

Compatibility of the PSD and coherence function of the generated ground motion with the target PSD and the coherence function can be used to check the goodness of the generated SVGM. Figure 2.13 shows PSD for generated bedrock motions at points *j*, *m*, *n* for the horizontal motions. Figure 2.14 presents PSD of generated surface motions at points i', j', and m' for both in-plane (U, W) and out-of-plane (V) wave motions. It is clearly seen that the generated motions at the bedrock and ground surface agree well with their targets. Good agreements are also observed in Figure 2.15 of lagged coherence functions between bedrock points *i*-*j*, *j*-*m*, and *i*-*n* for horizontal wave motions, and in Figure 2.16 of transfer functions between generated bedrock motions and in-plane and out-of-plane ground surface motions. These compatibilities of generated ground motions again show the appropriateness of the synthesized spatially correlated earthquake motions.

It is noteworthy that, in simulation of tridirectional SVGM, the horizontal VSHD-based seismological spectra (in Section 2.3.2) and combined coherence model (in Section 2.3.3) are also assumed to be appropriate in modelling of SVGM in vertical direction for simplicity, although seismological spectra and coherence model of the vertical SVGM sometime differ from those of the horizontal in practice. However, the simulation scheme in this study is not limited to any specific "power" model or coherence model, and these vertical seismological spectra and coherence models can be incorporated directly in this simulation scheme.

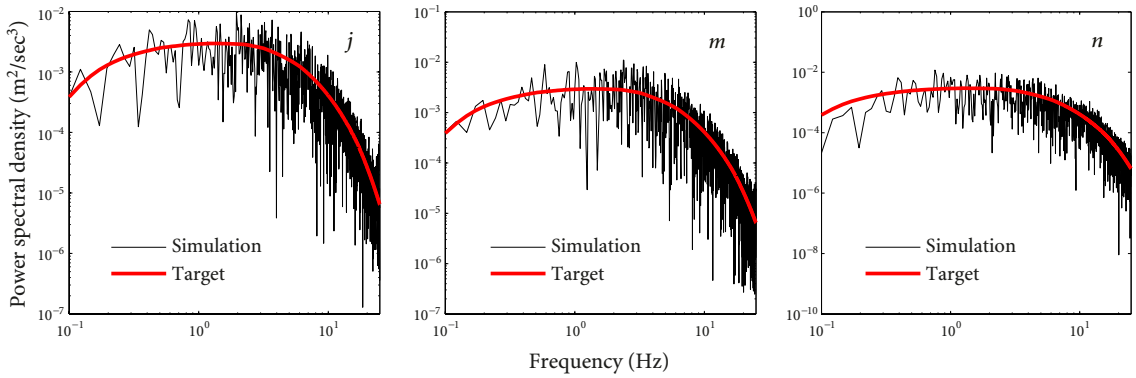

Figure 2.13 PSD functions with targets for generated horizontal bedrock motions

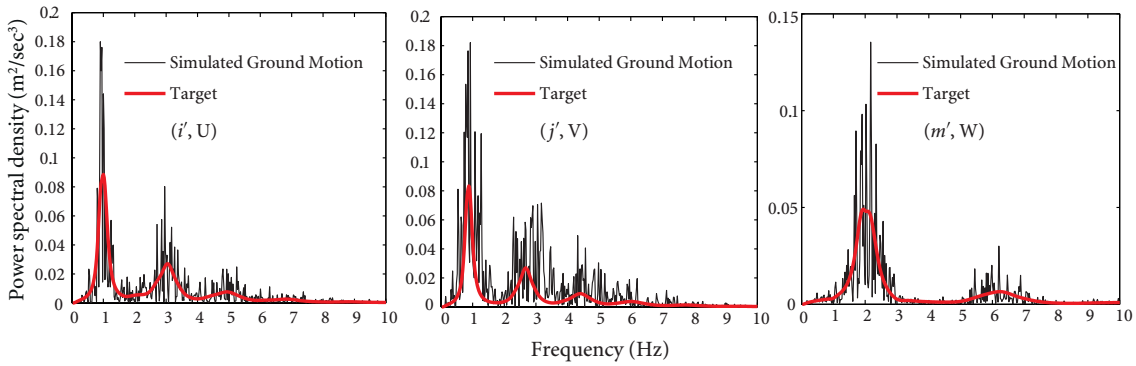

Figure 2.14 PSD functions with targets for generated surface motions

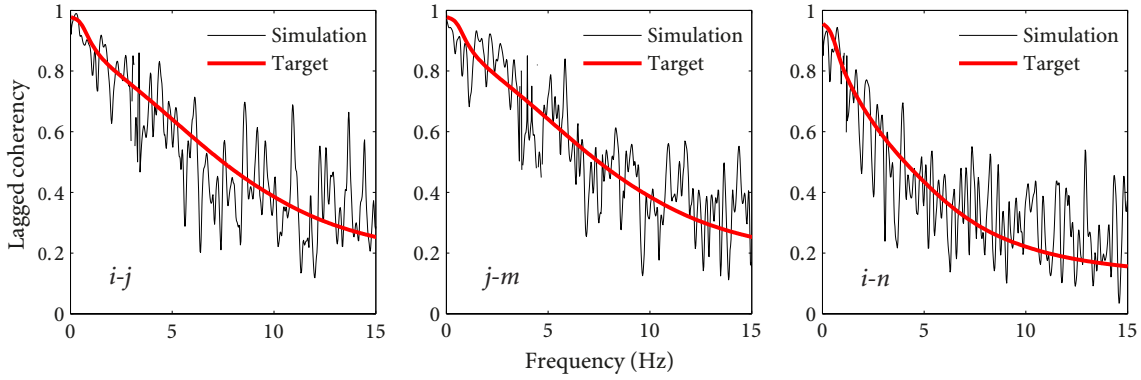

Figure 2.15 The coherency functions with targets for generated horizontal bedrock motions

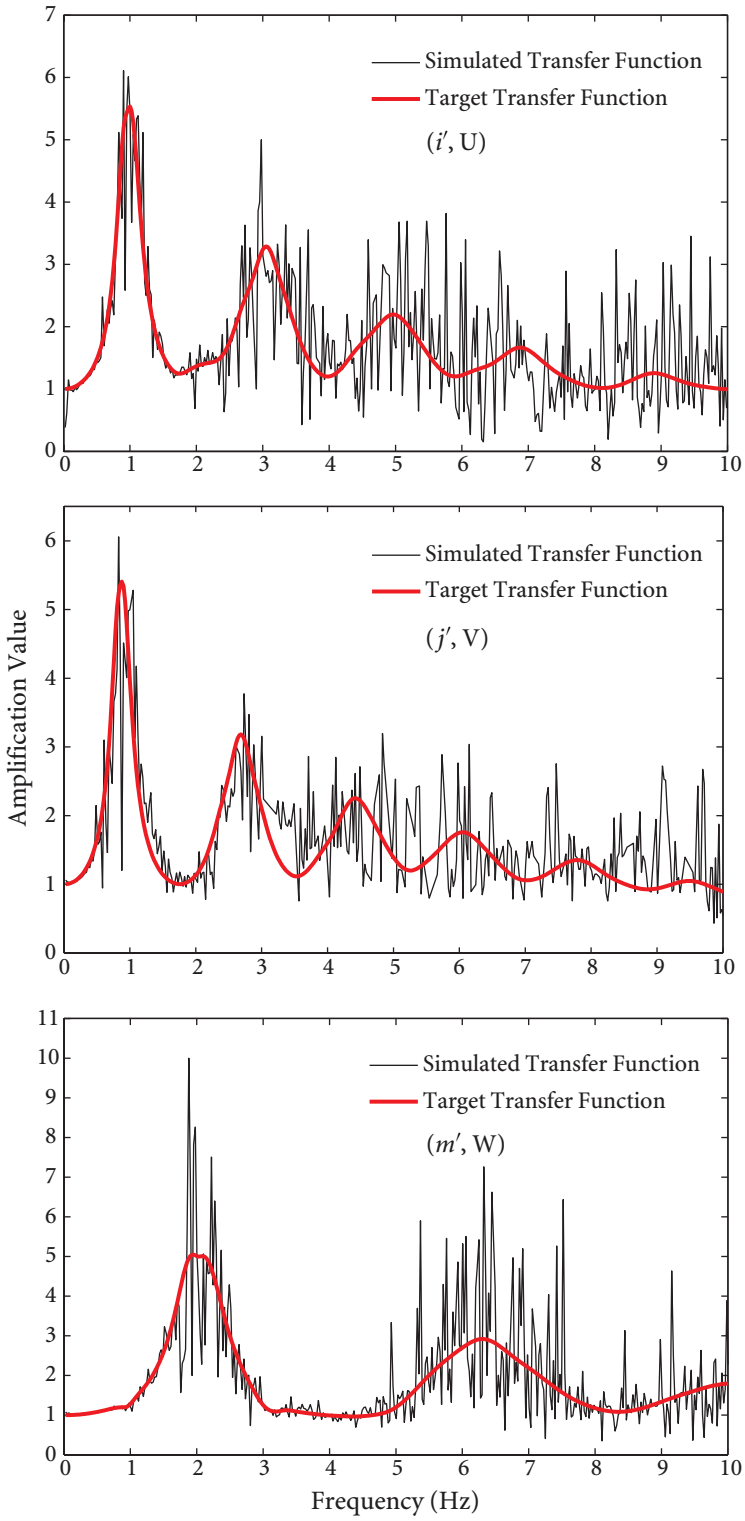

Figure 2.16 Transfer functions with targets for generated ground motions

It should also be noted that the topography effect on site response results (in Figure 2.6, induced by the alluvial valleys) is not considered in this study for simplicity, and it can be investigated more accurately by 2-D or 3-D site response analysis.

2.6 Summary and Conclusions

In this chapter, a comprehensive approach of synthesizing SVGM is proposed, which includes

1. The physically compliant seismological spectra is employed to synthesize SVGM and their earthquake scenarios are determined by VSHD, based on which a simulation framework is proposed to resolve the problem that a number of simulations need to be carried out for the UHS-based ground motion generation.
2. A comprehensive method of accounting for varying site effects in synthesizing SVGM is proposed, including consideration of spatial-random-variable soil profiles, effect of water saturation, effect of varying site conditions, and combining P-wave, SV-wave, and SH-wave motions to simulate tridirectional SVGM.
3. A canyon site is selected to synthesize the spatially correlated earthquake ground motions by considering the wave incoherence effect, wave-passage effect, and site-response effect. Study of local site effects on the loss of motion coherency shows that the local site can significantly reduce the lagged coherency at certain frequencies, and they can not only cause the phase difference of coherency function but also affect the modulus of coherency function.
4. Further studies should be conducted on the treatment of epistemic uncertainty of coherence models using the logic-tree method, and calibration of the variability of surface ground motions induced by soil variability.

C H A P T E R 3

Modelling of SVGM: (II) Nonstationarity and Spectra-compatibility

The synthetic spatially varying ground motions (SVGM), used in response history analysis (RHA), are usually desired to be spatially correlated, site reflected, nonstationary, and compatible with target design response spectra. In addition to seismic scenarios determination and varying site effect considered in Chapter 2, modelling of SVGM nonstationarity and spectra-compatibility are studied in this chapter.

3.1 Introduction

Studies have revealed that nonstationarity of a specific ground motion, with proper dispersive characteristics and realistic wave arrival times, is largely determined by its phase difference spectrum (PDS) (Trifunac, 1971; Ohsaki, 1979). The PDS method has been used to capture nonstationarity of a time history. Most of the stochastic modelling procedures of strong motions still assume phase angles to be independent and uniformly distributed, from which only the stationary ground motions can be obtained. Nonstationary ground motions can be simulated using phase contents of ground motions that are uniquely obtained through phase difference model. Several statistical distributions were proposed to fit phase differences using Fourier analysis or wavelet technique (Montaldo *et al.*, 2003;

Thrainsson and Kiremidjian, 2003); these models are frequently used in the ground motion simulation at a single location, but have rarely been used for modelling nonstationary spatial ground motions.

Compared to traditional geophysical or statistical approaches, the phase difference method provides good estimations of the ground motions using only a few model parameters (magnitude and distance), and it enables the generation of nonstationary synthetic strong motions without employing any specific modulation function (Montaldo *et al.*, 2003; Thrainsson and Kiremidjian, 2003). Moreover, the phase difference content of a ground motion can determine the starting time and length of its stronger part, and the simulated ground motion exhibits nonstationarity in both time and frequency domains. This chapter uses the phase spectrum model by Thrainsson and Kiremidjian (2003) to model the nonstationarity of spatially correlated ground motions.

Furthermore, the conditional simulation methods have been proposed to generate nonstationary spatial seismic motions that are compatible with prescribed real records (Vanmarcke *et al.*, 1993). Among these approaches, the envelope and frequency modulate functions used in spectral representation method (SRM) are often used with the Kriging method to generate the nonstationary space-time fields (Vanmarcke *et al.*, 1993; Heredia-Zavoni and Santa-Cruz, 2000; Hu *et al.*, 2012). In this aspect, adopting phase difference model in simulating nonstationarity of spatial motions can also be taken as a conditional simulation, because the phase difference models used are derived from the real earthquake records; as a result, the simulated motions exhibit similar nonstationarity. For example, one or several phase difference models can be obtained from one or several prescribed spatial real records, and the models can then be directly used to model the nonstationarity of the simulated spatial motions at the respective spatial points.

Besides nonstationarity of seismic motions, the dimensionality is also included in this chapter and Chapter 2, since the combined responses of structures with complex geometries (e.g., long span bridges) under tridirectional ground motions are important to be considered in seismic assessment. It is particularly important to study bridge structures under tridirectional SVGM, since spatial variability of ground motions tend to induce different dominant modes of bridges in comparison with the uniform earthquake motions; as a re-

sult, substantially different structural responses would be induced under tridirectional or bidirectional ground motions compared to those under unidirectional ground motions. In addition, engineers have long recognized that synthetic SVGM should be compatible with target design response spectra, which are usually prescribed as the design seismic loads by regulatory agencies. However, modelling of tridirectional SVGM that are compatible with target design spectra and considering the multidimensional characteristics of SVGM in structural response analysis and design have not been adequately studied.

In this chapter, a method is presented for simulating SVGM considering the nonstationarity, local site effect, and compatibility of response spectra. Principles and examples of PDS in conditional modelling of SVGM nonstationarity are presented in Section 3.2. The approach for transforming response spectrum at bedrock to the ground surface, using the site amplification method of Section 2.4.1, is given in Section 3.3.1, and modelling of SVGM nonstationarity and spectra-compatibility in the SRM is introduced in Section 3.3.2. The proposed scheme is then demonstrated with numerical examples in Section 3.4 for simulating nonstationary SVGM compatible with the bedrock and ground surface response spectra. Some conclusions are drawn in Section 3.5.

3.2 Conditional Modelling of Nonstationarity of SVGM using Phase Difference Spectrum

As discussed in Section 1.1.2, modelling of the nonstationarity characteristics of ground motions is very important and phase difference content of ground motions can model the characteristic of nonstationarity very well (Trifunac, 1971; Ohsaki, 1979; Zhang *et al.*, 2013b). Thus, the PDS method is adopted in this section for the simulation of SVGM with nonstationarity. In this section, the principle of the underlying PDS in determining ground motion's nonstationarity is illustrated first, in conjunction with an example for additional explanations that are provided behind the illustration.

3.2.1 Principles of Phase Difference Spectrum in Determining Ground Motion's Nonstationarity

The PDS is defined as (Ohsaki, 1979; Sato *et al.*, 2002)

$$\Delta\varphi(\omega_k) = \begin{cases} \varphi_{k+1} - \varphi_k + 2\pi, & -2\pi \leqslant \varphi_{k+1} - \varphi_k < 0, \\ \varphi_{k+1} - \varphi_k, & 0 < \varphi_{k+1} - \varphi_k \leqslant 2\pi, \end{cases} \quad \varphi_{k+1},\ \varphi_k,\ \Delta\varphi(\omega_k) \in [0, 2\pi], \tag{3.2.1}$$

where $k = 0, 1, 2, \ldots, N_0/2 - 1, N_0$ is the length of Fourier transformation, and φ_{k+1} and φ_k are phase angles. Equation (3.2.1) can be expressed in a different form as

$$\Delta\varphi(\omega_k) = \frac{2\pi}{N_0 \Delta t} \cdot \frac{\Delta\varphi(\omega_k)}{\Delta\omega} \quad \text{or} \quad \frac{2\pi}{N_0 \Delta t} \cdot \frac{\mathrm{d}\varphi(\omega)}{\mathrm{d}\omega}, \tag{3.2.2}$$

in which Δt is the time step, $\Delta\omega$ is the resolution of circular frequency, $\mathrm{d}\varphi(\omega)/\mathrm{d}\omega$ is called phase derivative or group delay time (Boore, 2003b), which is defined for the continuous time series $f(t)$ as

$$\frac{\mathrm{d}\varphi(\omega)}{\mathrm{d}\omega} = \Re\left(\frac{R_G + \mathrm{i} I_G}{R_F + \mathrm{i} I_F}\right) = \frac{R_G R_F + I_G I_F}{R_F^2 + I_F^2}, \tag{3.2.3}$$

where R_F, R_G, I_F, and I_G are the real and imaginary parts of Fourier spectrum $F(\omega)$ and $G(\omega)$, respectively, $F(\omega)$ and $G(\omega)$ are the Fourier spectrum of time histories $f(t)$ and $t \cdot f(t)$.

Equation (3.2.2) indicates that the phase difference varies linearly with the group delay time; as a result, ground delay time can be directly reflected in the phase difference. The group delay time is an important tool in revealing nonstationary characteristics of ground motions, which can be rewritten as

$$\frac{\mathrm{d}\varphi(\omega)}{\mathrm{d}\omega} = \Re\left(\frac{G(\omega)\, F^*(\omega)}{F(\omega)\, F^*(\omega)}\right) = \Re\left(\frac{S_{FG}}{S_{FF}}\right), \tag{3.2.4}$$

where S_{FF} and S_{FG} are the functions of Fourier transform of time histories $f(t)$ and $t \cdot f(t)$, given by

$$S_{FF} = \frac{1}{2\pi} \int_{-\infty}^{\infty} \mathrm{E}\left[f(t) f(t+\tau)\right] \mathrm{e}^{-\mathrm{i}\omega\tau} \mathrm{d}\tau, \quad S_{FG} = \frac{1}{2\pi} \int_{-\infty}^{\infty} \mathrm{E}\left[t \cdot f(t) f(t+\tau)\right] \mathrm{e}^{-\mathrm{i}\omega\tau} \mathrm{d}\tau. \tag{3.2.5}$$

Substituting equation (3.2.5) into equation (3.2.4) gives

$$\frac{\mathrm{d}\varphi(\omega)}{\mathrm{d}\omega} = \Re\left(\frac{\int_{-\infty}^{\infty} \mathrm{E}\left[t\cdot f(t)f(t+\tau)\right]\ \mathrm{e}^{-\mathrm{i}\omega\tau}\mathrm{d}\tau}{\int_{-\infty}^{\infty} \mathrm{E}\left[f(t)f(t+\tau)\right]\ \mathrm{e}^{-\mathrm{i}\omega\tau}\mathrm{d}\tau}\right), \tag{3.2.6}$$

where it is evident that $\mathrm{d}\varphi(\omega)/\mathrm{d}\omega$ denotes the arrival time of ground motion energy concentrated at circular frequency ω. Because actual recorded ground motions have energy content from every frequency, the mean and variance of group delay time are given by

$$\mu = \frac{1}{N_0}\sum_{i=1}^{N_0} \frac{\mathrm{d}\varphi(\omega)}{\mathrm{d}\omega}\Big|_{\omega=\omega_i}, \quad \sigma^2 = \frac{1}{N_0-1}\sum_{i=1}^{N_0}\left[\frac{\mathrm{d}\varphi(\omega)}{\mathrm{d}\omega}\Big|_{\omega=\omega_i}\right]^2. \tag{3.2.7}$$

In equation (3.2.7), the mean μ is the centroid of the total energy of time history in the time axis, while the variance σ^2 denotes the degree of dispersion of the distribution of the total energy.

The centroids of the total energy of most recorded motions lie within their stronger portions in the time domain, because most of the ground motion energy is concentrated in the stronger part. If the variance is small, the arrival of energy at each frequency becomes more concentrated, which means that most of the energy is scattered over a smaller time interval, thereby the duration of stronger part of ground motion becames shorter. On the contrary, the larger the variance, the more dispersive of the ground motions, and the longer the stronger parts. This is the basis that phase difference can determine the nonstationarity and time-domain pattern of a time history, and these conclusions will be shown in the examples in Section 3.2.2.

3.2.2 Examples of Phase Difference Spectrum in Simulating Ground Motion's Nonstationarity

The phase difference model by Thrainsson and Kiremidjian (2003), originally developed from approximately 300 uniformly processed California strong ground motion data, is used for simulating ground motion's nonstationarity.

In this model, the Fourier phase differences are modeled conditional on the Fourier amplitudes, which are classified into categories of small, intermediate, and large (Thrainsson

and Kiremidjian, 2003). Therefore, three types of phase difference models have been derived for the small, intermediate, and large categories, respectively.

A Beta distribution for the large and intermediate categories $f_x^{l,i}$, and a combination of a Beta distribution and a uniform distribution f_x^s for the small group are defined for the phase differences (Thrainsson and Kiremidjian, 2003). These distribution functions are given as

$$f_x^{l,i} = \frac{x^{p-1}(1-x)^{q-1}}{\beta(p,\ q)},\ \ f_x^s = w + (1-w)\,\frac{x^{p-1}(1-x)^{q-1}}{\beta(p,q)},\ \ 0 \leqslant x < 1, \tag{3.2.8}$$

where x is the random variable of phase difference that is normalized to the interval [0, 1], p and q are the statistical parameters of Beta distribution, $\beta(p,q) = \int_0^1 t^{p-1}(1-t)^{q-1}\mathrm{d}t$ is the Beta function, w is the weight coefficient of the uniform distribution. Subsequently, Montaldo *et al.* (2003) applied this method in two areas with different tectonic patterns in North-Eastern and central Italy.

Parameters of distribution functions in equation (3.2.8) are estimated for different site conditions specified in National Earthquake Hazard Reduction Program (NEHRP) (FEMA, 2010; Thrainsson and Kiremidjian, 2003). The site conditions specified in NEHRP include

- #A: hard rock, $V_s > 1524$ m/s,
- #B: rock, 762 m/s $< V_s <$ 1524 m/s,
- #C: very dense soil and soft rock, 366 m/s $< V_s <$ 762 m/s,
- #D: stiff soil, 183 m/s $< V_s <$ 366 m/s.

Thus, this phase difference method can model nonstationarity of ground motions recorded at site conditions ranging from stiff soil to hard rock.

Figure 3.1 presents the target distribution functions and simulated histogram of phase differences for each of the small, intermediate, and large categories. It is seen that variance values at site #A&#B are about three times larger than those for sites #C and #D, which indicates that the durations of stronger parts of ground motions at site #A&#B are larger. This result can be clearly seen in Figure 3.2, which shows the generated spatially correlated ground motions at three equally spaced spatial points located at site #A&#B, site #C, and site #D, respectively. The synthetic ground motions at sites #C and #D are concentrated in a smaller time interval, while time history at site #A&#B stretches over a longer time period.

In addition, the peak ground acceleration (PGA) recorded at harder sites are smaller than those at softer ones, e.g., PGA at site #A&#B, #C, and #D are, respectively, 0.116 g, 0.210 g, and 0.252 g. The mean values of phase differences at harder site are around 1.1 larger than those at softer sites, which results in that the occurring time of the strongest parts of ground motions at every site is close to each other, and the centroid of the total energy of synthetic ground motions at every site condition lies within its stronger portion in the time domain.

These results are in good agreement with observations of real wave motions recorded at hard and soft sites (Thrainsson and Kiremidjian, 2003; Kramer, 1996), which indicates that it is reasonable to model nonstationarity of spatially correlated ground motions using phase difference method.

3.3 Response Spectrum at Varying Site Surface and Spectra-compatibility of Spatial Motions

Besides ground motion nonstationarity, as specified in seismic design code for response history analysis of structures extended in space, synthetic spatially correlated ground motions are required to account for the local site effect (CEN, 2005b; MCPRC, 2008). Moreover, the generated ground motion at both single location and multiple spatial points should be compatible with the target design response spectrum (ASCE, 1998; NCC, 2010; NBCC, 2010; FEMA, 2010).

3.3.1 Response Spectrum at Varying Site Surface

To obtain the power spectral density (PSD) functions at the ground surface $S^i_{\text{surface}}(\omega)$, the frequency transfer function (FTF) of a given site $H(\mathrm{i}\omega)$ is required in this relation $S^i_{\text{surface}}(\omega) = \left|H(\mathrm{i}\omega)\right|^2 S_{\text{bedrock}}(\omega)$. The site FTF $H(\mathrm{i}\omega)$ is obtained in Section 2.4.1.

The approach by Park (1992, 1995), requiring no numerical iterations, is used to directly convert a target response spectrum to an equivalent PSD function $S_{\text{bedrock}}(\omega)$. The unknown PSD function of a target acceleration response spectrum $R_t(\omega, \xi)$ is discretized at circular frequencies ω_j and expressed as the sum of a series of discretized power components p_j, and the target response spectrum can also be approximated by a superposition of

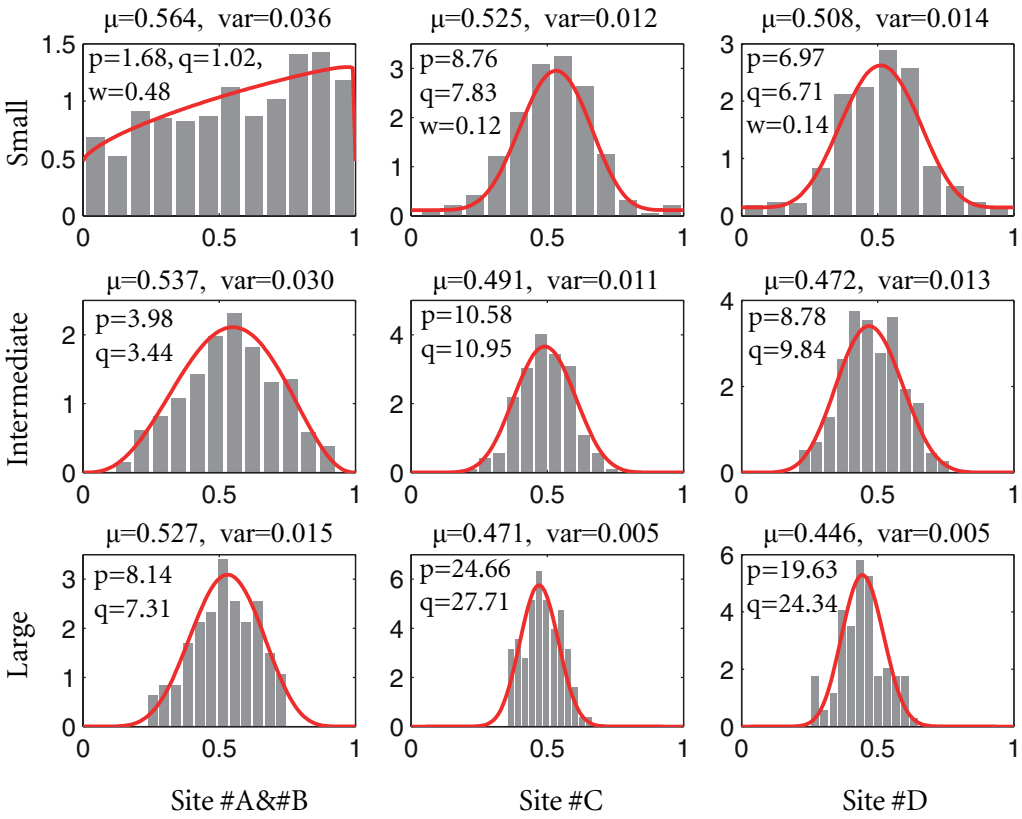

Figure 3.1 Distribution functions for phase difference in Thrainsson's model (Thrainsson and Kiremidjian, 2003)

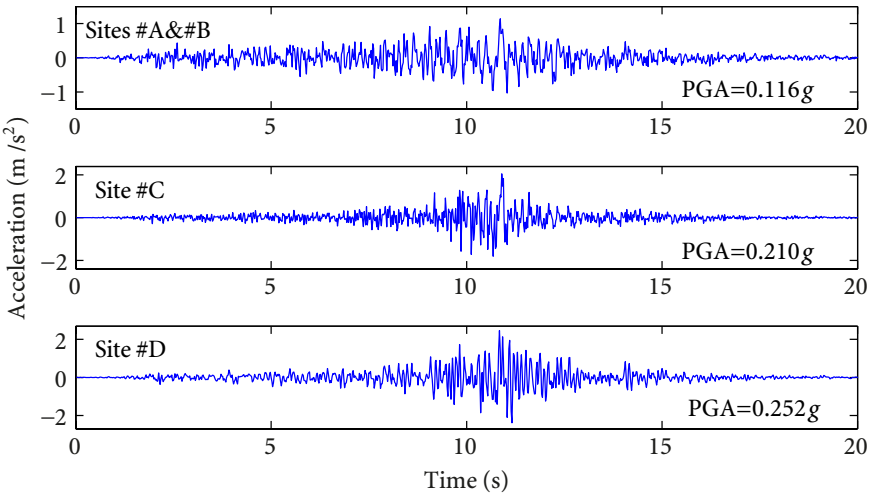

Figure 3.2 Synthetic spatial ground motions using phase difference of different site condition

the component response spectrum as (Park, 1995)

$$S_g(\omega)=\sum_{j=1}^{M} S(\omega_j)\Delta\omega_j\delta(\omega_j)=\sum_{j=1}^{m} p_j\delta(\omega_j),\ \ R_t^2(\omega_k,\xi)=\sum_{j=1}^{M} p_j R_{k,j}^2(\omega_k,\omega_j,\xi),$$

$$k=1,2,\ldots,N_{rs}, \quad (3.3.1)$$

where $R_{k,j}^2(\omega_k,\omega_j,\xi)$ represents the peak acceleration response of a single degree-of-freedom system with natural frequency ω_k and viscous damping ξ, excited by an extremely narrow band process with PSD function $\delta(\omega_j)$.

Using the peak factor approximation by Davenport (1964), $R_{k,j}^2(\omega_k,\omega_j,\xi)$ is given by

$$R_{k,j}^2(\omega_k,\omega_j,\xi)\approx\sqrt{\frac{1+4\xi^2(\omega_j/\omega_k)^2}{\left(1-(\omega_j/\omega_k)^2)^2+4\xi^2(\omega_j/\omega_k\right)^2}}\left[\sqrt{2\ln\left(\nu_j T_e\right)}+\frac{0.5772}{\sqrt{2\ln\left(\nu_j T_e\right)}}\right], \quad (3.3.2)$$

where $\nu_j=\omega_j/\pi$ and T_e is the effective time duration. The PSD components p_j can then be obtained by the following optimization problem

$$\text{Minimize}\ \sum_{k=1}^{N_{rs}}\left[R_t^2(\omega_k,\xi)-\sum_{j=1}^{M} p_j R_{k,j}^2(\omega_k,\omega_j,\xi)\right]^2,\ \text{subject to}\ p_j\geqslant 0,\ j=1,2,\ldots,M. \quad (3.3.3)$$

The equivalent PSD function is then obtained as $S_j=p_j/\Delta\omega_j, j=1,2,\ldots,M$.

For simplicity, the uniform hazard spectrum with probability of exceedence $\bar{P}=2.7\times10^{-3}$, derived from the seismic source configuration in Zhang *et al.* (2012b), is adopted as the design response spectrum at the bedrock. The target spectrum, along with the optimally estimated response spectrum, is shown in Figure 3.3(a), and its equivalent PSD function $S_{\text{bedrock}}(\omega)$ is presented in Figure 3.3(b). It is seen that the optimally estimated response spectrum agrees with the target at almost every point and the corresponding PSD function can be accurately and effectively obtained.

Using the equivalent PSD function $S_{\text{bedrock}}(\omega)$ converted from the response spectrum at bedrock, the PSD functions at the ground surface $S_{\text{surface}}^i(\omega)$, $i=1,2,\cdots,N_s$, can be obtained through $S_{\text{surface}}^i(\omega)=\left|H(\mathrm{i}\omega)\right|^2 S_{\text{bedrock}}(\omega)$, where $H(\mathrm{i}\omega)$ is the FTF of a given site,

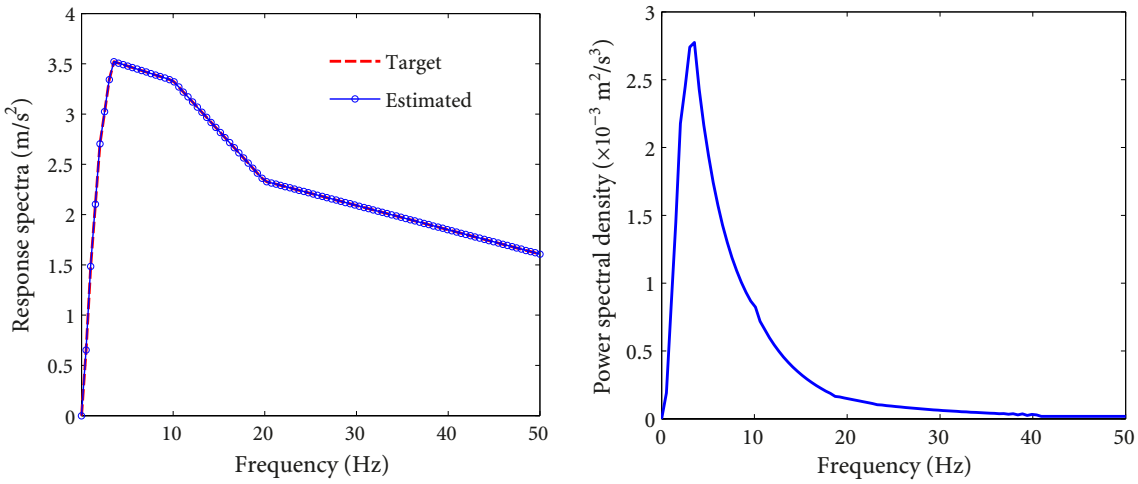

(a) Reponse spectrum (b) Power spectral density

Figure 3.3 Conversion from response spectrum to PSD

which can be obtained through the site response analysis in Section 2.4.1. Finally, the response spectrum at the ground surface can be determined.

3.3.2 Nonstationarity and Spectra-compatibility of Spatial Motions

As discussed in Section 2.2, $\varphi_{m'l}$ in equation (2.2.8) is the random phase angle that is often assumed to be uniformly distributed over $[0, 2\pi]$, leading to stochastic process $u_j(t)$ being stationary. The nonstationary ground motions may be obtained by using the time-domain amplitude modulating function (Deodatis, 1996; Hao *et al.*, 1989; Bi and Hao, 2010). However, the time-domain amplitude modulating function is often criticized to be inaccurate and arbitrary to well model nonstationarity of ground motions. The PDS introduced in Section 3.2, which can well reveal and model nonstationarity of time series, is used for phase angles $\varphi_{m'l}$ to produce the nonstationary and spatially correlated ground motions.

Besides nonstationarity, synthetic spatial ground motions should also be compatible with target response spectrum at ground surface points i', j', and k' in Figure 2.1 (ASCE, 1998; CEN, 2005b; NCC, 2010; NBCC, 2010). The generated time histories are usually used to test

if they can match well with the multiple target response spectra at different sites. If response spectra of generated time histories $R^i(\omega)$, $i=1,2,\ldots,N_s$, do not match satisfactorily with target spectra $R_t^i(\omega)$, iterations are required by multiplying the PSD function $S_i(\omega)$ with the ratio $\left[R_t^i(\omega)/R^i(\omega)\right]^2$. This process can be repeated until satisfactory compatibility is achieved. Usually good match can be obtained after a few iterations (Ohsaki, 1979).

3.4 Numerical Examples

The schemes presented in this chapter demonstrated using a bridge structure across a canyon site, with different site conditions at each pier, as shown in Figure 3.4. Bridge piers i', j', and k', located on site categories #C, #B, and #D specified in NEHRP provisions (FEMA, 2010), respectively, are spaced at 100 m, and the corresponding spatial points i, j, and k are on the base rock with site category #A. Site properties and classifications are listed in the figure.

Using the site amplification approach presented in Section 2.4.1, site amplification spectra for both in-plane and out-of-plane wave motions are shown in Figures 3.5 and 3.6. Figure 3.5 presents the modulus of FTF of sites #A, #B, #C, and #D for both the out-of-plane horizontal (V) and in-plane vertical (W) motions under the assumption that the amplitude of the vertical motion is 2/3 of that of the horizontal component for the incoming waves consisting of SH wave and combined P and SV waves. Site amplification results for in-plane horizontal (U) motions, not shown in the figure, are similar to those in the V direction. It is seen that the fundamental frequencies increase, in numerical ordering, by 5 Hz, 10 Hz and 30 Hz (in V direction) for sites #D, #C, and #B, respectively, but the site amplification values decrease from sites #D, #C, to #B. Similar results can also be obtained for ground motions in W direction. These results agree with the fact that the harder the site, the larger the fundamental frequency of the site, and the smaller the site amplification factor. It is anticipated that site amplification results in horizontal V direction are smaller than those in the vertical W direction because P-wave contrast is greater than S-wave contrast (or P-wave damping is smaller than S-wave damping). More importantly, fundamental frequencies in the W direction are larger than those in the V direction for each site, e.g., the fundamental

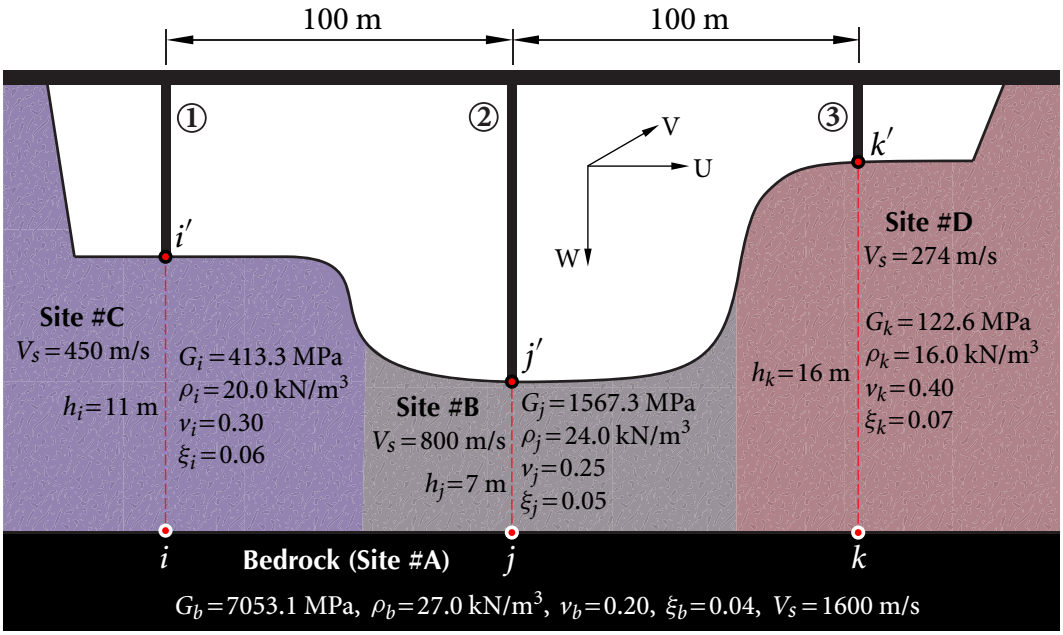

Site classification in NEHRP provisions (FEMA P-749, Dec. 2010)

Site class	General description	Shear wave velocity, V_s (m/s)	Shear strength (Pa)
#A	Hard rock	>1524	—
#B	Rock	762–1524	—
#C	Very dense soil and soft rock	366–762	> 95800
#D	Stiff soil	183–366	47900–95800

Figure 3.4 Schematic view of a exemplified bridge structure across a canyon site

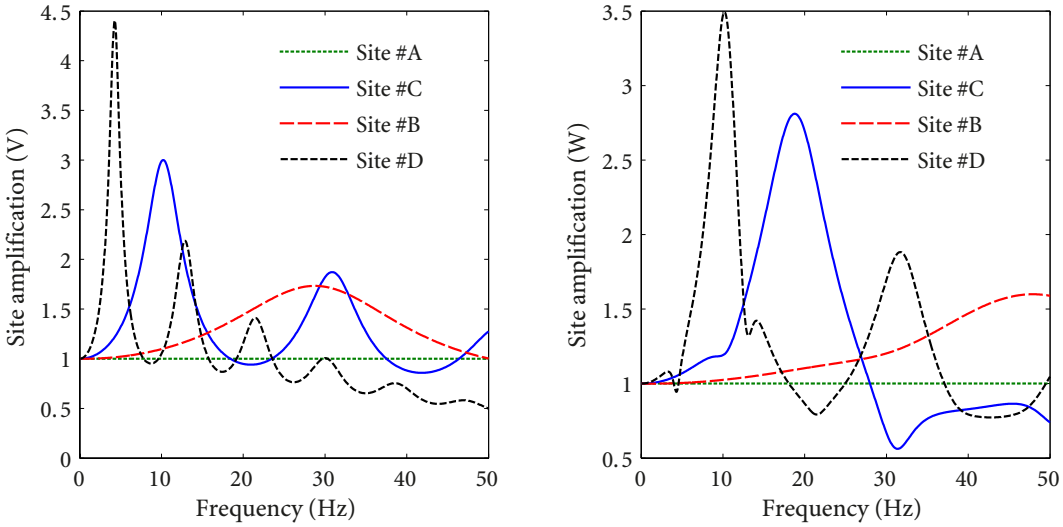

Figure 3.5 Site amplification spectra at different site condition

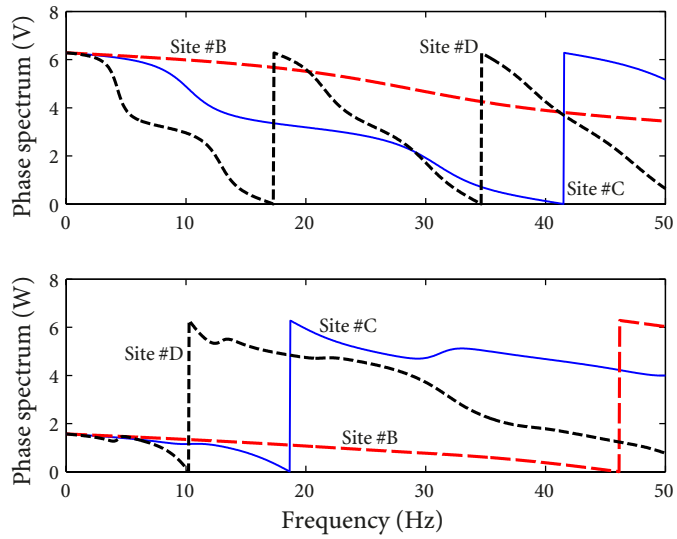

(a) Phase spectrum

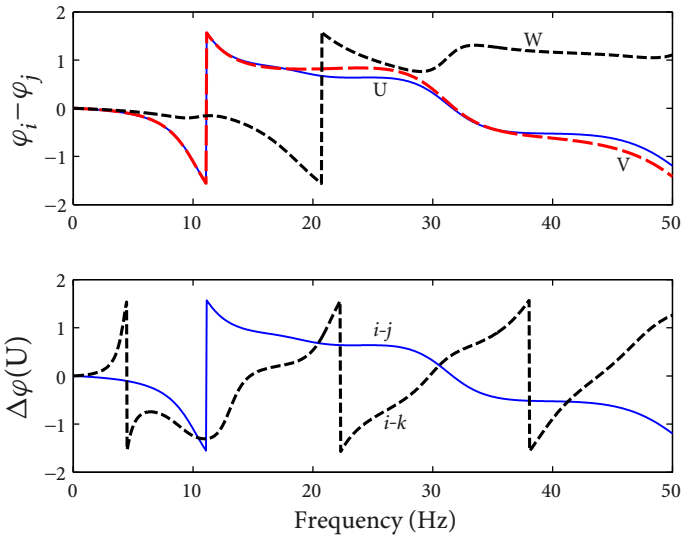

(b) Phase difference spectrum

Figure 3.6 Phase spectrum and phase difference at different site condition

frequencies for sites #D, #C, and #B increase from 5 Hz, 10 Hz, and 30 Hz to 10 Hz, 20 Hz, and 50 Hz. This is due to the fact that the vertical component of ground motion is primarily dominated by the compressive P wave with larger wave velocity, causing site in the vertical direction to be more stiff. However, in engineering practice, site amplification spectra in

the vertical direction are often directly obtained from those in the horizontal direction by only scaling the amplitude and ignoring the variation of fundamental frequency of local site (without using the frequency-dependent V/H ratios), which is inappropriate in providing a reasonable site amplification to be used in the simulation of vertical ground motions.

Soil conditions also affect the seismic wave propagation velocity and hence the phase difference between motions at spatial points. Figure 3.6(a) shows phase spectra of each site in V and W directions. The phase differences between motions at points *i*-*j* and *i*-*k* owing to wave propagation from base rock to ground surface are shown in Figure 3.6(b). It is shown that the softer is the soil, the more drastic variations are the phase spectrum and phase difference. The variations of phase or phase difference in the W direction are also more drastic than those in the U and V directions. This is because that wave velocity is slower at softer site and larger in the vertical direction.

After obtaining the site amplification results, spatially correlated, nonstationary, and design response spectra compatible ground motions with and without site effects are generated using the scheme presented in Section 3.4.1.

3.4.1 Synthesis of Spatially Correlated Ground Motions at Bedrock

The response spectrum presented in Figure 3.3(a) is selected as the target design spectrum at base rock; the equivalent PSD function is shown in Figure 3.3(b) (Zhang *et al.*, 2012b). Phase difference spectrum model for site class #A is used (Thrainsson and Kiremidjian, 2003).

The synthetic spatial accelerations at points *i*, *j*, and *k* are shown in Figure 3.7(a); it is seen that they have similar values of PGA and similar characteristics of time histories. This is because that these generated bedrock ground motions are from the same site condition (site #A) in modelling of phase difference and do not account for the varying local site effects. Compatibility of target response spectra and bedrock coherency function is presented in Figures 3.8 and 3.9. It is observed, in Figure 3.8, that the simulated ground motions at bedrock points *i*, *j*, and *k* are in good agreement with their targets. Good agreement is also

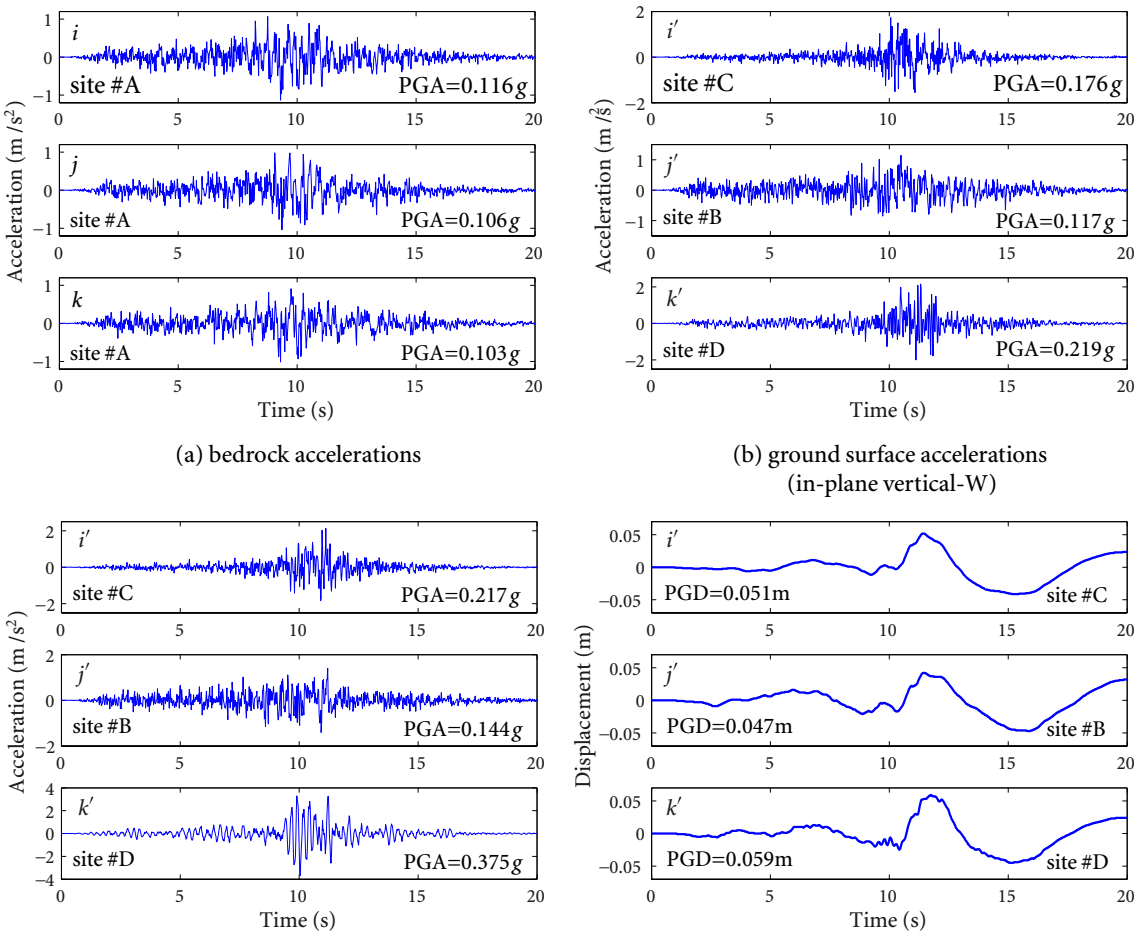

(a) bedrock accelerations

(b) ground surface accelerations (in-plane vertical-W)

(c) ground motions at surface (out-of-plane horizontal-V)

Figure 3.7 Generated spatially correlated ground motions at bedrock and ground surface

observed in Figure 3.9 for coherency values of wave motions (mean values of 25 simulations) for points *i*-*j*, *j*-*k*, and *i*-*k*.

3.4.2 Synthesis of Spatially Correlated Ground Motions at Ground Surface

In practice, supports of a structure occupying a large space have varying local site condition. Spatially correlated wave motions on ground surface points i', j', and k' with different site conditions in Figure 3.4 are presented in this section.

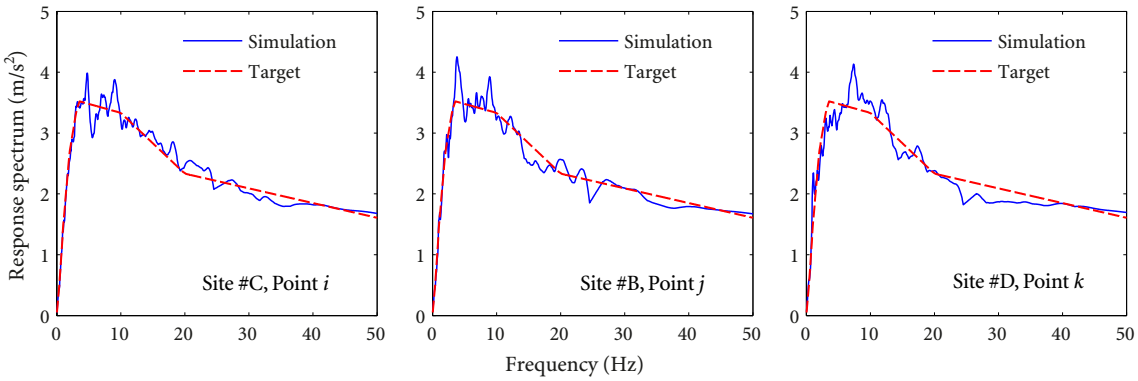

Figure 3.8 Compatibility of response spectrum for generated bedrock ground motions

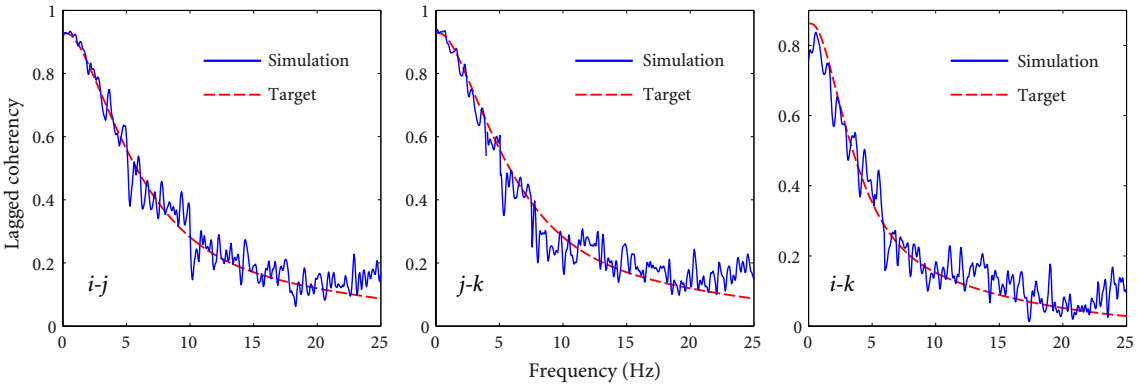

Figure 3.9 Compatibility of spatial coherency functions for generated bedrock ground motions

Using the approach introduced in Section 3.3, Figure 3.10 presents target response spectrum on ground surface at each site condition in the U, V, and W directions, where similar conclusions obtained from Figure 3.2 can also be reached. Using the phase difference model corresponding to each site condition in Figure 3.1, spatially correlated and nonstationary ground surface wave motions, compatible with target response spectrum on ground surface at points i', j', and k', are generated and shown in Figures 3.7(b) and 3.7(c) for the wave motions in V and W directions. It is observed that PGA at softer sites are larger than those at harder sites for ground motions in both V and W directions, e.g., PGA at sites #D, #C, and #B decrease by 0.219 g, 0.176 g, and 0.117 g in the W direction and they are larger than PGA of bedrock ground motions (site #A) in Figure 3.7(a). Furthermore, PGA in the V direction are larger than those in the vertical W direction as compared between Figure 3.7(b) and Figure 3.7(c), where similar results can also be observed for peak ground displacement in

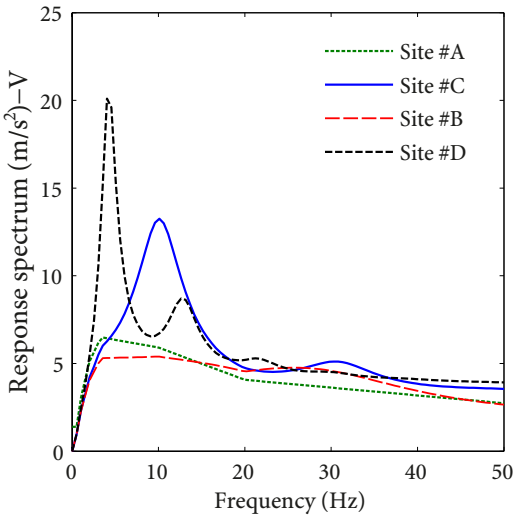

(a) Surface response spectrum (V-direction)

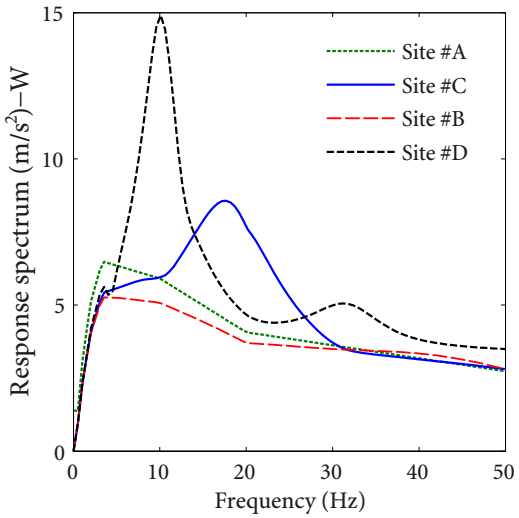

(b) Surface response spectrum (W-direction)

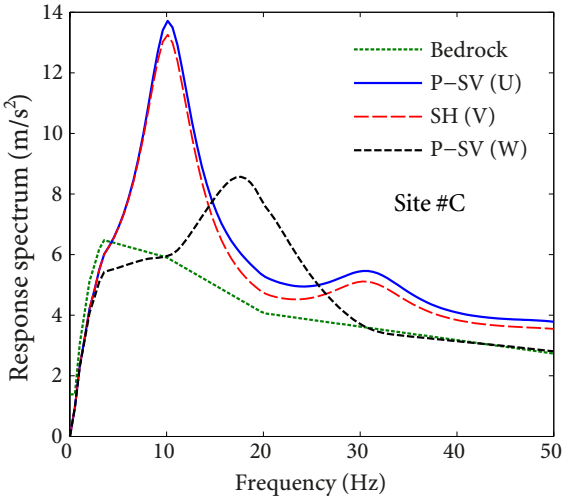

(c) Surface response spectrum (U, V, W-directions)

Figure 3.10 Response spectra at ground surface

the V direction. These observations agree with the conclusions that a softer site amplifies bedrock motions more than a harder site, and ground motions in the horizontal V direction are amplified more than those in the vertical W direction.

Similar to the results obtained in Section 3.2, synthetic ground motions at sites #C and #D experience shorter duration in the stronger parts, while time histories at sites #A and #B spread in a longer duration for both the horizontal and vertical ground motions. These results are in agreement with observations of real wave motions recorded at hard and soft

sites (Thrainsson and Kiremidjian, 2003; Kramer, 1996). Moreover, it seems that simulated wave motions in the V direction are filtered much more by the sites than ground motions in the W direction, especially for ground motion at site #D. This is because that more frequency contents are filtered in the V direction as illustrated in the FTF of sites in Figure 3.5.

Compatibility of simulated surface wave motions with the target design spectra in Figure 3.10 is presented in Figure 3.11 for both horizontal and vertical ground motions, in which good agreement is observed.

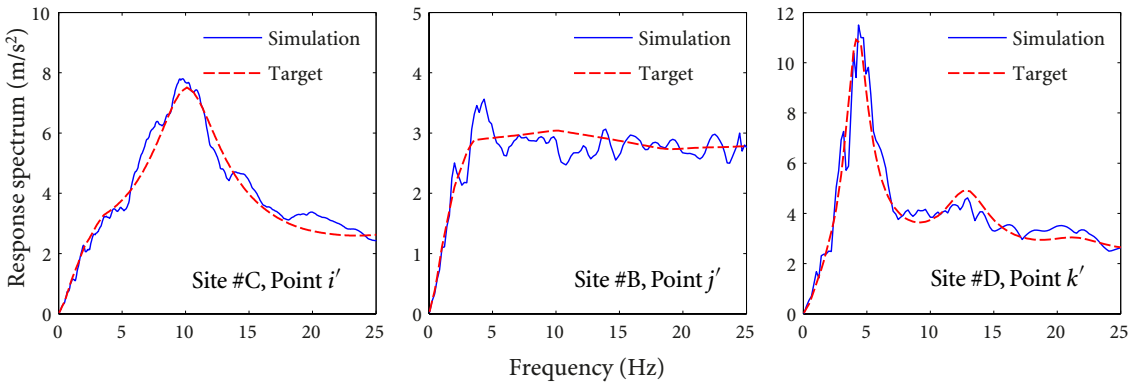

(a) Out-of-plane horizontal (V) ground motions at ground surface

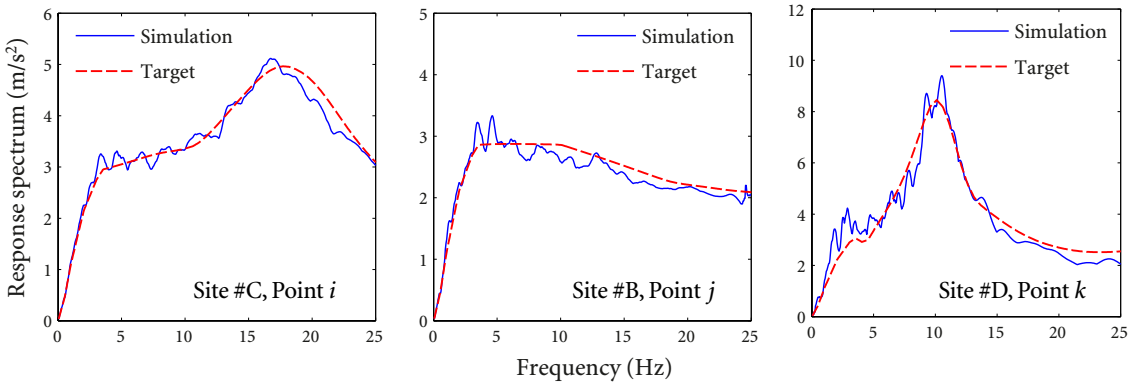

(b) In-plane vertical (W) ground motions at ground surface

Figure 3.11 Compatibility of response spectrum for generated ground motions at ground surface

3.5 Summary and Conclusions

In this chapter, an approach of synthesizing spatially correlated, site reflected, nonstationary, and response spectra compatible ground motions is presented, which includes

1. The phase difference method is developed and proved to be effective in conditional modelling of nonstationarity of spatial ground motions.
2. The scheme of transforming response spectra at bedrock to the ground surface in tridirections using the site amplification method is established. Modelling of SVGM nonstationarity and spectra-compatibility within the SRM scheme is introduced.
3. Numerical examples are presented to demonstrate the proposed method. It is seen that the generated nonstationary bedrock or ground surface wave motions are compatible with the bedrock response spectra or derived ground surface response spectra associated with the respective site conditions, and any two of these motions are compatible with a target coherency function.
4. The synthesized SVGM can be applied to the nonlinear RHA of multiply supported structures under multiple excitations or the experimental shake-table tests of structures under SVGM.

C H A P T E R 4

Stochastic Seismic Analysis of Bridges under SVGM: (I) Theoretical Methodology

Because seismic motions are random (stochastic) in nature (Housner, 1947), spatial effects of long span bridges can be analyzed using stochastic vibration analysis (SVA). In this chapter, a comprehensive, systematic, and efficient SVA methodology is developed for bridge structures under spatially varying ground motions (SVGM).

4.1 Introduction

SVA is a theoretically advanced, efficient, and effective tool providing stable and physically compliant structural response results; it has been adopted by bridge seismic design standards (CEN, 2005b; MCPRC, 2008) in dealing with effect of ground motion spatial variations. In SVA of bridges under SVGM, spatial variations (commonly known as the incoherence, wave-passage, and local site effects), nonstationarity, and tridirectionality of SVGM should be accounted for.

Earthquake motions are in essence nonstationary and they are usually treated as uniformly modulated random processes in most of the response history analysis (RHA) or SVA of large structures under SVGM (Zhang *et al.*, 2012a). In SVA, it is better to model earthquake motions as nonuniformly modulated seismic excitations, because substantial

high frequency components of ground acceleration, which emerge in the early stages of an earthquake, decay much faster than the low frequency components that the ground acceleration involves only low frequency components eventually. This nonstationary pattern of frequency components of an earthquake cannot be characterized by the uniformly modulated evolutionary random process. Numerical analysis of structural responses to such nonuniformly modulated evolutionary random seismic excitations is very rare in the literature, let alone being included in stochastic seismic analysis of spatially extended structures under tridirectional SVGM.

However, nonstationary SVA is too complicated and difficult to be widely used in general engineering computations in spite of its recognized importance. In particular, for structures having many degrees-of-freedom (DoF) and dozens of spatial supports, or the input nonuniformly modulated nonstationary ground motions being spatially correlated and tridirectional, their stochastic response formulas are rather complex and involve a great deal of multiple integration and summation operations, requiring considerable computational effort.

To reduce the large computational effort involved in the conventional nonstationary SVA, Lin *et al.* (1997a) proposed an accurate and efficient method, known as pseudo-excitation method (PEM), to transform both stationary and nonstationary stochastic analyses to deterministic dynamic response problems. PEM has excluded any computation associated with multiple integration and/or summation operations, making structural stochastic analysis very simple yet accurate and making PEM particularly attractive for engineering purposes. To be more specific, PEM is accurate because the cross-correlation terms between the participant structural modes and between the excitations are included in the results. PEM is computationally efficient and simple to be adopted, because stationary random analyses are transformed accurately into harmonic analyses, and nonstationary random analyses (for both uniformly modulated and nonuniformly modulated ground motions) are transformed exactly into deterministic transient analyses, which can be solved very easily using direct dynamic integration methods, such as the Duhamel integration, Newmark method, or Wilson-θ method (Lin *et al.*, 1997a). Hence, the PEM is adopted in this chapter for nonstationary stochastic seismic analysis of bridges under tridirectional SVGM.

Since PEM is very effective and accurate in SVA of complex structures with a large number of DoF, it is natural to integrate (implement) on general finite element analysis (FEA) platforms, which have powerful modelling and analysis tools for seismic analysis of complex structures, so that engineers can readily access PEM. In addition, the implementation can improve and resolve drawbacks of some self-developed PEM programs without good computational efficiencies and powerful modelling and analysis techniques. As discussed in Section 1.1.3, the conventional indirect approach for solving equations of motion of structures under SVGM can result in massive computations on static influence matrix and inverse of structure stiffness matrix. Furthermore, it is also prevented from possible extension to the nonlinear SVA used for performance-based earthquake engineering (PBEE) because of the linear superposition treatment.

Therefore, an absolute-response-oriented scheme of PEM in nonstationary SVA of bridge structures under tridirectional SVGM has been derived in Section 4.2. In Section 4.3, the mathematical scheme for modelling tridirectional SVGM, accounting for the incoherence effect, wave-passage effect, and local site effect, is proposed for stochastic analysis of structures extended in large areas, where the site amplification approach of Section 2.4.1 is incorporated in the nonstationary SVA scheme systematically to provide tridirectional site responses. The input pseudo-forces, used in the absolute-response-oriented scheme of PEM, are determined in Section 4.4 through decomposition of cross-power spectral density (PSD) matrix. The proposed SVA scheme is implemented and verified in the general FEA platform ANSYS in Section 4.5. Some conclusions are drawn in Section 4.6.

4.2 PEM in Seismic Analysis of Structures under Tridirectional Nonstationary Spatial Motions

Considering a long span bridge structure (with m supports and n nodes) under tridirectional (three translational components) multiple ground motions, the discrete equations of motion can be written in the global coordinate system as

$$\begin{bmatrix} \mathbf{M}_{ss} & \mathbf{M}_{sb} \\ \mathbf{M}_{sb}^{T} & \mathbf{M}_{bb} \end{bmatrix} \begin{Bmatrix} \ddot{\mathbf{X}}_{s} \\ \ddot{\mathbf{X}}_{b} \end{Bmatrix} + \begin{bmatrix} \mathbf{C}_{ss} & \mathbf{C}_{sb} \\ \mathbf{C}_{sb}^{T} & \mathbf{C}_{bb} \end{bmatrix} \begin{Bmatrix} \dot{\mathbf{X}}_{s} \\ \dot{\mathbf{X}}_{b} \end{Bmatrix} +$$

$$\begin{bmatrix} \mathbf{K}_{ss} & \mathbf{K}_{sb} \\ \mathbf{K}_{sb}^T & \mathbf{K}_{bb} \end{bmatrix} \begin{Bmatrix} \mathbf{X}_s \\ \mathbf{X}_b \end{Bmatrix} = \begin{Bmatrix} \mathbf{0} \\ \mathbf{P}_b \end{Bmatrix}, \quad (4.2.1)$$

in which the subscript b represents the master DoF, i.e., the support DoF, while the subscript s represents the slave DoF. $\{\mathbf{X}_b\}_{3\times m}$ denotes the vector of enforced displacements at m supports, $\{\mathbf{X}_s\}_{3\times n}$ is the vector of absolute displacements of the slave DoF, and $\{\mathbf{P}_b\}_{3\times m}$ is the vector of enforced forces applied on all supports. Matrices **M**, **C**, and **K** are the mass matrix, damping matrix, and stiffness matrix, respectively. $\ddot{\mathbf{X}}$ and $\dot{\mathbf{X}}$ are vectors of the absolute acceleration and velocity responses, respectively. The lumped mass model is assumed, i.e., $\mathbf{M}_{sb}$ is null, and soil-structure interaction (SSI) effect is not included for simplicity.

4.2.1 Conventional Indirect Approach in Solving Equations of Motion under Pseudo-excitations

For the sake of solving equation (4.2.1) conveniently, the absolute displacement vector $\mathbf{X}_s$ is decomposed into the quasi-static displacement vector $\mathbf{Y}_s$ and the relative dynamic displacement vector $\mathbf{Y}_r$ as

$$\begin{Bmatrix} \mathbf{X}_s \\ \mathbf{X}_b \end{Bmatrix} = \begin{Bmatrix} \mathbf{Y}_s \\ \mathbf{X}_b \end{Bmatrix} + \begin{Bmatrix} \mathbf{Y}_r \\ 0 \end{Bmatrix}, \quad (4.2.2)$$

in which the quasi-static displacement vector $\mathbf{Y}_s$ satisfies

$$\begin{bmatrix} \mathbf{K}_{ss} & \mathbf{K}_{sb} \\ \mathbf{K}_{sb}^T & \mathbf{K}_{bb} \end{bmatrix} \begin{Bmatrix} \mathbf{Y}_s \\ \mathbf{X}_b \end{Bmatrix} = \begin{Bmatrix} \mathbf{0} \\ \mathbf{P}_b^s \end{Bmatrix}. \quad (4.2.3)$$

in which $\mathbf{P}_b^s$ is the support reaction vector due to $\mathbf{X}_b$ being imposed statically at the supports. Hence, one obtains

$$\mathbf{Y}_s = -\mathbf{K}_{ss}^{-1}\mathbf{K}_{sb}\mathbf{X}_b = \mathbf{F}\mathbf{X}_b, \quad (4.2.4)$$

where **F** is the static influence matrix that can be expressed as

$$\mathbf{F} = -\mathbf{K}_{ss}^{-1}\mathbf{K}_{sb}. \quad (4.2.5)$$

Substituting equations (4.2.2) and (4.2.4) into equation (4.2.1) gives

$$\mathbf{M}_{ss}\ddot{\mathbf{Y}}_r + \mathbf{C}_{ss}\dot{\mathbf{Y}}_r + \mathbf{K}_{ss}\mathbf{Y}_r = \mathbf{M}_{ss}\mathbf{K}_{ss}^{-1}\mathbf{K}_{sb}\ddot{\mathbf{X}}_b + \left(\mathbf{C}_{ss}\mathbf{K}_{ss}^{-1}\mathbf{K}_{sb} - \mathbf{C}_{sb}\right)\dot{\mathbf{X}}_b. \quad (4.2.6)$$

For the assumed stiffness proportional damping, the velocity part $\left(\mathbf{C}_{ss}\mathbf{K}_{ss}^{-1}\mathbf{K}_{sb}-\mathbf{C}_{sb}\right)\dot{\mathbf{X}}_b$ is proved to be zero. For other types of damping, the velocity part $\left(\mathbf{C}_{ss}\mathbf{K}_{ss}^{-1}\mathbf{K}_{sb}-\mathbf{C}_{sb}\right)\dot{\mathbf{X}}_b$ is very small that it can be ignored, in comparison with the response contribution from the inertia term $\mathbf{M}_{ss}\mathbf{K}_{ss}^{-1}\mathbf{K}_{sb}\ddot{\mathbf{X}}_b$. Thus, equation (4.2.6) can be simplified as

$$\mathbf{M}_{ss}\ddot{\mathbf{Y}}_r+\mathbf{C}_{ss}\dot{\mathbf{Y}}_r+\mathbf{K}_{ss}\mathbf{Y}_r=\mathbf{M}_{ss}\mathbf{K}_{ss}^{-1}\mathbf{K}_{sb}\ddot{\mathbf{X}}_b=\mathbf{M}_{ss}\mathbf{F}\ddot{\mathbf{X}}_b, \tag{4.2.7}$$

where the quasi-static displacement vector $\mathbf{Y}_s$ and the relative dynamic displacement vector $\mathbf{Y}_r$ can be solved from equations (4.2.4) and (4.2.7), respectively, and the absolute displacement vector $\mathbf{X}_s$ can be obtained from equation (4.2.2).

As seen from equation (4.2.2), dynamic responses of structures under spatially varying support excitations can be expressed as the superposition of two components: a pseudo-static component and a dynamic component. The dynamic component is attributed to the dynamic inertia forces induced by the support motions, while the pseudo-static component arises from the static response of the bridge (at each time instant) to the differential support displacements prescribed by the SVGM (without inertia and damping forces, in equation (4.2.3)). It is noteworthy that the pseudo-static component is zero in the case of uniform support excitations.

In the PEM, pseudo-excitations at structural supports can be assumed to be (Lin *et al.*, 2004a)

$$\ddot{\tilde{\mathbf{X}}}_b=\mathbf{P}e^{i\omega t},\quad \dot{\tilde{\mathbf{X}}}_b=\frac{\mathbf{P}e^{i\omega t}}{i\omega},\quad \tilde{\mathbf{X}}_b=-\frac{\mathbf{P}e^{i\omega t}}{\omega^2}, \tag{4.2.8}$$

in which $\mathbf{P}$ is obtained through the decomposition of PSD matrix $\left[\mathbf{S}_0(i\omega,t)\right]_{3m\times 3m}$ of input ground motions by

$$\mathbf{S}_0(i\omega,t)=\mathbf{P}^*\mathbf{P}^T. \tag{4.2.9}$$

By substituting equation (4.2.8) into equation (4.2.7), one obtains

$$\mathbf{M}_{ss}\ddot{\tilde{\mathbf{Y}}}_r+\mathbf{C}_{ss}\dot{\tilde{\mathbf{Y}}}_r+\mathbf{K}_{ss}\tilde{\mathbf{Y}}_r=\mathbf{M}_{ss}\mathbf{K}_{ss}^{-1}\mathbf{K}_{sb}\ddot{\tilde{\mathbf{X}}}_b=\mathbf{M}_{ss}\mathbf{F}\cdot\mathbf{P}e^{i\omega t}, \tag{4.2.10}$$

where $\tilde{\mathbf{Y}}_r$ is the vector of relative dynamic displacement of the slave DoF under pseudo-excitations. Similarly, substituting equation (4.2.8) into equation (4.2.4) gives

$$\tilde{\mathbf{Y}}_s=\mathbf{F}\tilde{\mathbf{X}}_b=-\mathbf{F}\cdot\frac{\mathbf{P}e^{i\omega t}}{\omega^2}, \tag{4.2.11}$$

where $\tilde{\mathbf{Y}}_s$ is the vector of the quasi-static displacement of the slave DoF under pseudo-excitations.

The pseudo-response of absolute displacement $\tilde{\mathbf{X}}_s$ can be obtained by solving $\tilde{\mathbf{Y}}_r$ in equation (4.2.10) and $\tilde{\mathbf{Y}}_s$ in equation (4.2.11) as

$$\tilde{\mathbf{X}}_s = \tilde{\mathbf{Y}}_s + \tilde{\mathbf{Y}}_r. \tag{4.2.12}$$

Then, nonstationary PSD of the absolute displacement $\tilde{\mathbf{X}}_s$ is

$$\mathbf{S}_{X_S X_S}(\omega, t) = \left[\tilde{\mathbf{Y}}_s(\mathrm{i}\omega, t) + \tilde{\mathbf{Y}}_r(\mathrm{i}\omega, t)\right]^* \left[\tilde{\mathbf{Y}}_s(\mathrm{i}\omega, t) + \tilde{\mathbf{Y}}_r(\mathrm{i}\omega, t)\right]^T. \tag{4.2.13}$$

Equations (4.2.2) to (4.2.13) are the conventional indirect approach in solving equations of motion of structures under tridirectional nonstationary spatial seismic motions using PEM. Some other statistical response parameters, such as the root mean square values, spectral moments, and mean peak responses, can be derived based on the PSD of absolute displacements $\tilde{\mathbf{X}}_s$ in equation (4.2.13).

4.2.2 Absolute-response-oriented Direct Approach in Solving Equations of Motion under Pseudo-excitations

In comparison with the indirect approach in Section 4.2.1, the direct approach, which is an absolute-response-oriented scheme, is presented to solve the absolute response displacement directly using the large mass method (Zhang *et al.*, 2012a; Jia *et al.*, 2013).

By matrix manipulation of the second block row of equation (4.2.1), one obtains

$$\mathbf{M}_{sb}^T \ddot{\mathbf{X}}_s + \mathbf{M}_{bb} \ddot{\mathbf{X}}_b + \mathbf{C}_{sb}^T \dot{\mathbf{X}}_s + \mathbf{C}_{bb} \dot{\mathbf{X}}_b + \mathbf{K}_{sb}^T \mathbf{X}_s + \mathbf{K}_{bb} \mathbf{X}_b = \mathbf{P}_b, \tag{4.2.14}$$

where the vector of seismic forces $\mathbf{P}_b$ can be expressed in terms of mass of supports $\mathbf{M}_{bb}$ and the ground acceleration $\ddot{\mathbf{u}}_b$ as

$$\mathbf{P}_b = \mathbf{M}_{bb} \ddot{\mathbf{u}}_b. \tag{4.2.15}$$

Then equation (4.2.14) can be expressed as

$$\mathbf{M}_{sb}^T \ddot{\mathbf{X}}_s + \mathbf{M}_{bb} \ddot{\mathbf{X}}_b + \mathbf{C}_{sb}^T \dot{\mathbf{X}}_s + \mathbf{C}_{bb} \dot{\mathbf{X}}_b + \mathbf{K}_{sb}^T \mathbf{X}_s + \mathbf{K}_{bb} \mathbf{X}_b = \mathbf{M}_{bb} \ddot{\mathbf{u}}_b. \tag{4.2.16}$$

By multiplying $\mathbf{M}_{bb}^{-1}$ in equation (4.2.16), one obtains

$$\mathbf{M}_{bb}^{-1} \left[\mathbf{M}_{bs} \ddot{\mathbf{X}}_s + \mathbf{M}_{bb} \ddot{\mathbf{X}}_b + \mathbf{C}_{bs} \dot{\mathbf{X}}_s + \mathbf{C}_{bb} \dot{\mathbf{X}}_b + \mathbf{K}_{bs} \mathbf{X}_s + \mathbf{K}_{bb} \mathbf{X}_b\right] = \ddot{\mathbf{u}}_b. \tag{4.2.17}$$

A very large value can be assigned to $\mathbf{M}_{\mathrm{bb}}$, i.e.,

$$\mathbf{M}_{\mathrm{bb}}^{-1}=0,\ \mathbf{M}_{\mathrm{bb}}^{-1}\mathbf{M}_{\mathrm{bs}}=0,\ \mathbf{M}_{\mathrm{bb}}^{-1}\mathbf{C}_{\mathrm{bs}}=0,\ \mathbf{M}_{\mathrm{bb}}^{-1}\mathbf{C}_{\mathrm{bb}}=0,\ \mathbf{M}_{\mathrm{bb}}^{-1}\mathbf{K}_{\mathrm{bs}}=0,\ \mathbf{M}_{\mathrm{bb}}^{-1}\mathbf{K}_{\mathrm{bb}}=0. \quad (4.2.18)$$

Hence one obtains

$$\ddot{\mathbf{X}}_{\mathrm{b}}=\ddot{\mathbf{u}}_{\mathrm{b}}, \quad (4.2.19)$$

which indicates that the acceleration responses at structural supports approximately equal the input ground accelerations. This is called the large mass method that has been widely used in seismic analysis of structures under multiple earthquake excitations. Values of the large mass $\mathbf{M}_{\mathrm{bb}}$ are usually selected between 10^5 and 10^8 times of structural total weights for an acceptable approximation of structural seismic responses (Zhang *et al.*, 2012a). It is noteworthy that the primary advantage of large mass method in the structural response analysis to SVGM is that it allows using spatial ground accelerations, instead of spatial ground displacements, as input of earthquake excitations. Ground displacement is difficult to be reliably defined because the true acceleration baseline is difficult to know (Jia *et al.*, 2013).

Substituting equation (4.2.19) into equation (4.2.1) and expanding components in the first block row of equation (4.2.1) yield

$$\mathbf{M}_{\mathrm{ss}}\ddot{\mathbf{X}}_{\mathrm{s}}+\mathbf{C}_{\mathrm{ss}}\dot{\mathbf{X}}_{\mathrm{s}}+\mathbf{K}_{\mathrm{ss}}\mathbf{X}_{\mathrm{s}}=-\left(\mathbf{M}_{\mathrm{sb}}\ddot{\mathbf{u}}_{\mathrm{b}}+\mathbf{C}_{\mathrm{sb}}\dot{\mathbf{u}}_{\mathrm{b}}+\mathbf{K}_{\mathrm{sb}}\mathbf{u}_{\mathrm{b}}\right). \quad (4.2.20)$$

In the PEM, pseudo-excitations at structural supports are (Lin *et al.*, 2004a)

$$\ddot{\tilde{\mathbf{u}}}_{\mathrm{b}}=\mathbf{P}\mathrm{e}^{\mathrm{i}\omega t},\quad \dot{\tilde{\mathbf{u}}}_{\mathrm{b}}=\frac{\mathbf{P}\mathrm{e}^{\mathrm{i}\omega t}}{\mathrm{i}\omega},\quad \tilde{\mathbf{u}}_{\mathrm{b}}=-\frac{\mathbf{P}\mathrm{e}^{\mathrm{i}\omega t}}{\omega^2}, \quad (4.2.21)$$

in which $\mathbf{P}$ is obtained through the decomposition of PSD matrix $\left[\mathbf{S}_0(\omega)\right]_{3m\times 3m}$ of input ground motions by equation (4.2.9).

By substituting equation (4.2.21) into equation (4.2.20), one obtains

$$\mathbf{M}_{\mathrm{ss}}\ddot{\tilde{\mathbf{X}}}_{\mathrm{s}}+\mathbf{C}_{\mathrm{ss}}\dot{\tilde{\mathbf{X}}}_{\mathrm{s}}+\mathbf{K}_{\mathrm{ss}}\tilde{\mathbf{X}}_{\mathrm{s}}=-\left(\mathbf{M}_{\mathrm{sb}}+\frac{\mathbf{C}_{\mathrm{sb}}}{\mathrm{i}\omega}-\frac{\mathbf{K}_{\mathrm{sb}}}{\omega^2}\right)\mathbf{P}\mathrm{e}^{\mathrm{i}\omega t}, \quad (4.2.22)$$

where $\tilde{\mathbf{X}}_{\mathrm{s}}$ is the vector of absolute displacements of the slave DoF under pseudo-excitations given in equation (4.2.21). This is the dynamic equation in the PEM with equivalent forces on the right hand of equation(4.2.22).

After the absolute displacement $\tilde{\mathbf{X}}_s$ is obtained from equation (4.2.22), its nonstationary PSD can be obtained as

$$\mathbf{S}_{\mathbf{X}_s\mathbf{X}_s}(\omega, t) = \tilde{\mathbf{X}}_s^*(\mathrm{i}\omega, t)\, \tilde{\mathbf{X}}_s^T(\mathrm{i}\omega, t). \tag{4.2.23}$$

Equations (4.2.14) to (4.2.23) are direct approach in solving equations of motion of structures under tridirectional nonstationary SVGM using PEM.

4.2.3 Discussions on the Indirect and Direct Approaches in Solving Equations of Motion

As seen in Section 4.2.1, the conventional indirect approach solves equations of motion (4.2.1) under pseudo-excitations by decomposing the absolute displacement into the quasi-static and the relative dynamic terms. In this procedure, the static influence matrix $\mathbf{F}$ and the inverse of matrix $\mathbf{K}_{ss}$ have to be computed in equations (4.2.7) and (4.2.4) to obtain the absolute response, which can significantly increase time of computation in structural seismic analysis. Moreover, most self-developed programs of PEM that are based on the indirect approach usually cannot be readily used in stochastic seismic analysis of practical complex structures due to the high computational requirement and shortage of more versatile and powerful modelling and analysis tools.

However, in the direct approach, the absolute displacement can be directly and easily obtained in equation (4.2.22) by using the large mass method, where massive computations are avoided. Moreover, unlike the conventional indirect approach, the direct scheme in conjunction with PEM can be readily implemented on a general FEA platform. In Section 4.5, the absolute-response-oriented direct approach is integrated with the ANSYS platform for stochastic analysis of complex structures.

As noted from equations (4.2.10) and (4.2.22), obtaining the pseudo-forces, i.e., matrix $\mathbf{P}$, is a crucial step in performing the stochastic analysis using PEM. A procedure on obtaining the pseudo-forces through modelling of tridirectional nonstationary spatially correlated ground motions is presented in Sections 4.3 and 4.4

4.3 Modelling of Tridirectional Nonstationary Spatial Motions at Varying Sites

The SVGM, exhibiting variabilities in space, should be modelled by considering the coherence effect, wave-passage effect, and local site effect. The modelling of tridirectional spatial earthquake motions by accounting for the varying site conditions beneath every support of the structures is presented in this section. Properties of these SVGM with different site conditions should be reflected in the input pseudo-forces of the PEM. The spectral representation method (SRM) given in Section 2.2 is used in modelling spatial ground motions and determining the pseudo-forces.

Consider the spatial points i-i', j-j', and k-k' with different site properties at a canyon site in Figure 2.1, the cross-PSD matrix of tridirectional nonstationary ground motions at m ground surface locations can be expressed by

$$\mathbf{S}^3_{\text{surface}}(\mathrm{i}\omega,t)=\left[\mathbf{S}_{i'j'}(\mathrm{i}\omega,t)\right]_{3m\times 3m},\quad \text{where}\quad \mathbf{S}_{i'j'}(\mathrm{i}\omega,t)=\left[S_{i'j',pq}(\mathrm{i}\omega,t)\right]_{3\times 3}, \tag{4.3.1}$$

in which $p,q\in\{x,y,z\}$ and each sub-matrix element of $\mathbf{S}^3_{\text{surface}}(\mathrm{i}\omega,t)$, i.e., $\mathbf{S}_{i'j'}(\mathrm{i}\omega,t)$, is a 3×3 matrix corresponding to two horizontal (x,y) and one vertical (z) components of tridirectional ground motions, given by

$$\mathbf{S}_{i'j'}(\mathrm{i}\omega,t)=\begin{bmatrix} S_{i'j',xx}(\mathrm{i}\omega,t) & S_{i'j',xy}(\mathrm{i}\omega,t) & S_{i'j',xz}(\mathrm{i}\omega,t)\\ S_{i'j',yx}(\mathrm{i}\omega,t) & S_{i'j',yy}(\mathrm{i}\omega,t) & S_{i'j',yz}(\mathrm{i}\omega,t)\\ S_{i'j',zx}(\mathrm{i}\omega,t) & S_{i'j',zy}(\mathrm{i}\omega,t) & S_{i'j',zz}(\mathrm{i}\omega,t)\end{bmatrix}. \tag{4.3.2}$$

Using the evolutionary spectra for nonstationary processes by Priestley (1965) and assuming the correlation coefficients between the horizontal components and vertical component to be 0.6 (Smeby and Kiureghian, 1985), the off-diagonal elements of $\mathbf{S}_{i'j'}(\mathrm{i}\omega,t)$ are given by

$$\begin{aligned} S_{i'j',xy}(\mathrm{i}\omega,t)&=S_{i'j',yx}(\mathrm{i}\omega,t)=\sqrt{S_{i'j',xx}(\mathrm{i}\omega,t)S_{i'j',yy}(\mathrm{i}\omega,t)}\,,\\ S_{i'j',xz}(\mathrm{i}\omega,t)&=S_{i'j',zx}(\mathrm{i}\omega,t)=0.6\sqrt{S_{i'j',xx}(\mathrm{i}\omega,t)S_{i'j',zz}(\mathrm{i}\omega,t)}\,,\\ S_{i'j',yz}(\mathrm{i}\omega,t)&=S_{i'j',zy}(\mathrm{i}\omega,t)=0.6\sqrt{S_{i'j',yy}(\mathrm{i}\omega,t)S_{i'j',zz}(\mathrm{i}\omega,t)}\,, \end{aligned} \tag{4.3.3}$$

where $S_{i'j',xx}(\mathrm{i}\omega,t)$, $S_{i'j',yy}(\mathrm{i}\omega,t)$, and $S_{i'j',zz}(\mathrm{i}\omega,t)$ can be related to $S_{ij,xx}(\mathrm{i}\omega,t)$, $S_{ij,yy}(\mathrm{i}\omega,t)$, and $S_{ij,zz}(\mathrm{i}\omega,t)$ (cross-PSD functions of tridirectional nonstationary bedrock motions) through the tridirectional site response transfer functions by

$$\begin{aligned} S_{i'j',xx}(\mathrm{i}\omega,t) &= H_{\mathrm{U},i}(\mathrm{i}\omega)\, H^{*}_{\mathrm{U},j}(\mathrm{i}\omega)\, S_{ij,xx}(\mathrm{i}\omega,t)\,, \\ S_{i'j',yy}(\mathrm{i}\omega,t) &= H_{\mathrm{V},i}(\mathrm{i}\omega)\, H^{*}_{\mathrm{V},j}(\mathrm{i}\omega)\, S_{ij,yy}(\mathrm{i}\omega,t)\,, \\ S_{i'j',zz}(\mathrm{i}\omega,t) &= H_{\mathrm{W},i}(\mathrm{i}\omega)\, H^{*}_{\mathrm{W},j}(\mathrm{i}\omega)\, S_{ij,zz}(\mathrm{i}\omega,t)\,, \end{aligned} \tag{4.3.4}$$

in which $H_{\mathrm{U},i}(\mathrm{i}\omega)$, $H_{\mathrm{W},i}(\mathrm{i}\omega)$, $H_{\mathrm{V},i}(\mathrm{i}\omega)$, and $H_{\mathrm{U},j}(\mathrm{i}\omega)$, $H_{\mathrm{W},j}(\mathrm{i}\omega)$, $H_{\mathrm{V},j}(\mathrm{i}\omega)$ are site frequency transfer functions (FTF) between spatial points i-i' and j-j' for the P-SV wave motions in the horizontal and vertical directions and SH wave motions in the horizontal direction, respectively. $S_{ij,xx}(\mathrm{i}\omega,t)$, $S_{ij,yy}(\mathrm{i}\omega,t)$, and $S_{ij,zz}(\mathrm{i}\omega,t)$ can be obtained based on the theory of evolutionary power spectrum for nonstationary stochastic processes by Priestley (1965) (for x-component)

$$S_{ij,xx}(\mathrm{i}\omega,t) = G_{i,x}(\omega,t)G_{j,x}(\omega,t)\sqrt{S_{ii,xx}(\mathrm{i}\omega)S_{jj,xx}(\mathrm{i}\omega)}\cdot\gamma_{ij}(\mathrm{i}\omega), \tag{4.3.5}$$

where $S_{ii,xx}(\mathrm{i}\omega)$ is the auto-PSD function of x-component of tridirectional stationary bedrock ground motions at the ith spatial support. $\gamma_{ij}(\mathrm{i}\omega)$ is the coherence function of bedrock ground motions between the ith and jth spatial supports, which consists of the lagged coherence part $\left|\gamma_{ij}(\mathrm{i}\omega)\right|$ and the wave-passage effect $\exp[-\mathrm{i}\,\omega d_{ij}/v_{\mathrm{app}}(\omega)]$ of SVGM given by $\gamma_{ij}(\mathrm{i}\omega) = \left|\gamma_{ij}(\mathrm{i}\omega)\right|\exp[-\mathrm{i}\,\omega d_{ij}/v_{\mathrm{app}}(\omega)]$, where d_{ij} is the spatial distance from point i to point j, and $v_{\mathrm{app}}(\omega)$ is apparent wave velocity (Zerva, 2009). $G_{i,x}(\omega,t)$ is the modulating function (in time and frequency domain) of x-component of tridirectional ground motions at the ith spatial support. Based on the formulation of $G_{i,x}(\omega,t)$, three types of ground motion process can be obtained, which are

- stationary: $G_{i,x}(\omega,t) = 1$,
- uniformly modulated nonstationary: $G_{i,x}(\omega,t) = g(t)$,
- nonuniformly modulated nonstationary: $G_{i,x}(\omega,t) = G(\omega,t)$.

To obtain site FTF in equation (4.3.4), the one-dimensional wave propagation theory in equation (2.4.4) is used. The base rock motions for a site with horizontally extended

multiple soil layers are assumed to consist of out-of-plane SH wave or in-plane combined P-SV waves propagating into a site with assumed incident angles, and the site FTF $H_{U,i}(\mathrm{i}\omega)$, $H_{V,i}(\mathrm{i}\omega)$, and $H_{W,i}(\mathrm{i}\omega)$ can be obtained for each of the varying sites in tridirections by solving equations of wave motion in equation (2.4.4) in the frequency domain for the SH wave and P-SV wave.

Hence, based on equations (4.3.1) to (4.3.5), the cross-PSD matrix of tridirectional nonstationary ground motions at ground surface in equation (4.3.1) can be obtained uniquely. For the modelling approach of tridirectional nonstationary spatial motions in this section,

1. Stationary, uniformly modulated nonstationary, and nonuniformly modulated nonstationary tridirectional spatial motions can be modelled.
2. More rational tridirectional site response approach, which can reflect varying site conditions, are incorporated systematically in the modelling of out-of-plane SH wave and in-plane ground motions.

$\mathbf{S}^3_{\text{surface}}(\mathrm{i}\omega, t)$ will be used in Section 4.4 to obtain the input pseudo-forces in stochastic seismic analysis of structures using PEM.

4.4 Determination of Pseudo-forces through Decomposition of Cross-PSD Matrix

To obtain the pseudo forces in equations (4.2.10) and (4.2.22), the cross-PSD matrix of tridirectional nonstationary SVGM on ground surface $\mathbf{S}^3_{\text{surface}}(\mathrm{i}\omega, t)$ can be decomposed as (Lin *et al.*, 2001)

$$\begin{aligned}\mathbf{S}^3_{\text{surface}}(\mathrm{i}\omega, t) &= \mathbf{P}^*(\mathrm{i}\omega, t)\mathbf{P}^T(\mathrm{i}\omega, t) \\ &= \mathbf{G}(\omega, t)\,\mathbf{W}^*(\mathrm{i}\omega)\,\sqrt{\mathbf{S}_g(\mathrm{i}\omega)}\,\mathbf{Q}\,\mathbf{Q}^T\sqrt{\mathbf{S}_g(\mathrm{i}\omega)}\,\mathbf{W}^T(\mathrm{i}\omega)\,\mathbf{G}^T(\omega, t),\end{aligned} \tag{4.4.1}$$

where the dimension of matrix $\mathbf{P}$ is $3m \times r$, and r is the rank of matrix $\mathbf{S}^3_{\text{surface}}(\mathrm{i}\omega, t)$.

Matrix $\mathbf{W}(\mathrm{i}\omega)$ in equation (4.4.1) has dimension $3m \times 3m$ and denotes the wave-passage effect and the phase part of the local site effect

$$\mathbf{W}(\mathrm{i}\omega) = \mathrm{diag}\Big[\,\cdots, \mathrm{e}^{-\mathrm{i}(\omega T_{i,x}+\theta_{i,x})}, \mathrm{e}^{-\mathrm{i}(\omega T_{i,y}+\theta_{i,y})}, \mathrm{e}^{-\mathrm{i}(\omega T_{i,z}+\theta_{i,z})}, \cdots\Big]_{3m\times 3m}, \tag{4.4.2}$$

where $T_{i,x}$, $i=1,2,\cdots,m$, represents the time at which x-component of tridirectional ground motions propagate to the ith support. $\theta_{i,x}$, $\theta_{i,y}$, and $\theta_{i,z}$ represent phases in the x, y, and z directions of the local site at support i, respectively, and they can be determined by the relationship of PSD functions between the bedrock and ground surface as

$$S_{i'j',xx}(\mathrm{i}\omega,t)=\underbrace{\left|H_{\mathrm{U},i}(\mathrm{i}\omega)\,H^{*}_{\mathrm{U},j}(\mathrm{i}\omega)\right|}_{\text{amplitude}}\underbrace{\exp\left[\mathrm{i}(\theta_{i,x}-\theta_{j,x})\right]}_{\text{phase}}S_{ij,xx}(\mathrm{i}\omega,t),$$

$$\theta_{ij,xx}=\theta_{i,x}-\theta_{j,x}=\tan^{-1}\left[\frac{\Im\left(H_{\mathrm{U},i}(\omega)H_{\mathrm{U},j}(-\omega)\right)}{\Re\left(H_{\mathrm{U},i}(\omega)H_{\mathrm{U},j}(-\omega)\right)}\right],\quad\text{in } x \text{ direction,}\tag{4.4.3}$$

in which $\theta_{ij,xx}$ is the phase difference in x direction between spatial points i-i' and j-j'.

Matrix $\mathbf{S}_g(\mathrm{i}\omega)$ in equation (4.4.1) represents the PSD functions of bedrock ground motions and amplification effects of the local site conditions, which is expressed as

$$\sqrt{\mathbf{S}_g(\mathrm{i}\omega)}=\mathrm{diag}\Big[\cdots,|H_{U,i}|\sqrt{S_{gi,x}},\ |H_{V,i}|\sqrt{S_{gi,y}},\ |H_{W,i}|\sqrt{S_{gi,z}},\cdots\Big]_{3m\times 3m},\tag{4.4.4}$$

where $S_{gi,x}$, $i=1,2,\cdots,m$, denotes the PSD function of x-component of tridirectional bedrock ground motions in the ith spatial support, and the ratio of PSD amplitudes of horizontal bedrock motions ($S_{gi,x}$ or $S_{gi,y}$) and vertical bedrock motions ($S_{gi,z}$) is assumed to be 3/2.

Matrix $\mathbf{G}(\omega,t)$ in equation (4.4.1) represents the nonuniformly modulated functions of tridirectional nonstationary ground motions

$$\mathbf{G}(\omega,t)=\mathrm{diag}\Big[\cdots,G_{i,x}(\omega,t),G_{i,y}(\omega,t),G_{i,z}(\omega,t),\cdots\Big]_{3m\times 3m},\tag{4.4.5}$$

which can be obtained by assuming $G_{i,x}(\omega,t)=G_{i,y}(\omega,t)=G_{i,z}(\omega,t)=G(\omega,t), i=1,2,\cdots,m$, for simplicity.

Matrix $\mathbf{R}$ in equation (4.4.1) denotes the coherence matrix of the tridirectional ground motions, which is either positive definite or positive semi-definite symmetric and can be decomposed through the LDLT-decomposition as

$$\mathbf{R}=\mathbf{Q}_{3m\times r}\left[\mathbf{Q}^{T}\right]_{r\times 3m}=\Big[|\gamma_{ij}|\Big]_{3m\times 3m},\ \Big(|\gamma_{ij}|=1,\ \text{when } i=j;\ \ 0\leqslant|\gamma_{ij}|<1,\ \text{when } i\neq j\Big),\tag{4.4.6}$$

which can be decomposed as the summation of non-zero eigenvalues α_j with the corresponding normalized eigenvectors $\boldsymbol{\varphi}_j$ with dimension $3m\times 1$ ($j=1,2,\cdots,r,\ r\leqslant 3m$) given by

$$\mathbf{R}=\sum_{j=1}^{r}\alpha_j\boldsymbol{\varphi}_j^*\boldsymbol{\varphi}_j^T,\ \text{ where } \mathbf{R}\boldsymbol{\varphi}_j=\alpha_j\boldsymbol{\varphi}_j \text{ and } \boldsymbol{\varphi}_i^T\boldsymbol{\varphi}_j^*=\delta_{ij}\ (j=1,2,\cdots,r). \tag{4.4.7}$$

Pseudo-excitation corresponding to the jth eigen-mode can then be obtained for *partially coherent* (diagonal elements of matrix $\mathbf{R}$ are 1) SVGM

$$\mathbf{P}_j e^{i\omega t}=\mathbf{G}(\omega,t)\mathbf{W}\sqrt{\alpha_j}\boldsymbol{\varphi}_j\sqrt{\mathbf{S}_g(i\omega)}\,e^{i\omega t}, \tag{4.4.8}$$

where the coherence effect, wave-passage effect, local site effect, and ground motion non-stationarity are reflected in the input pseudo forces of the PEM through $\sqrt{\alpha_j}\boldsymbol{\varphi}_j$ (matrix $\mathbf{Q}$), $\mathbf{W}$, $\mathbf{S}_g(i\omega)$, and $\mathbf{G}(\omega,t)$, respectively.

It is noteworthy that pseudo-excitations for the *fully coherent* (rank of $\mathbf{R}$ is 1, i.e., $r=1$, and all of its elements are 1; $\alpha_1=1$, $\{\boldsymbol{\varphi}_1\}_{3m\times 1}$ is a vector of all ones) and *completely incoherent* ($\mathbf{R}$ has full rank and its off-diagonal elements are 0 and diagonal elements are 1; $\alpha_j=1$, $\{\boldsymbol{\varphi}_j\}_{3m\times 1}$ is the jth natural basis of the Euclidean space $\mathbf{e}_j, j=1,2,\cdots,r$) can be simplified through pseudo-excitation of *partially coherent* SVGM in equation (4.4.8), which are

Fully coherent:

$$\mathbf{P}_j e^{i\omega t}=\mathbf{G}(\omega,t)\mathbf{W}\mathbf{Q}\sqrt{\mathbf{S}_g(i\omega)}\,e^{i\omega t}, \tag{4.4.9}$$

Completely incoherent:

$$\mathbf{P}_j e^{i\omega t}=\mathbf{G}(\omega,t)\mathbf{W}\sqrt{\mathbf{S}_g(i\omega)}\,e^{i\omega t}. \tag{4.4.10}$$

After obtaining the pseudo-excitations corresponding to different coherence level of spatial seismic motions, the pseudo-responses can be derived in both the conventional indirect and direct approaches, which are presented in Sections 4.4.1 and 4.4.2.

4.4.1 Conventional Indirect Approach

Substituting equation (4.4.8) into equations (4.2.8) and (4.2.10), the pseudo-response of relative dynamic displacement under partially coherent spatial ground motions can be

obtained as

$$\tilde{\mathbf{Y}}_{\mathrm{r}}(\mathrm{i}\omega,t)=\sum_{j=1}^{r}\tilde{\mathbf{y}}_{\mathrm{rj}}=\sum_{j=1}^{r}\mathbf{F}\sqrt{\alpha_j\mathbf{S}_{\mathrm{g}}(\mathrm{i}\omega)}\,\mathbf{I}_j(t), \tag{4.4.11}$$

where

$$\mathbf{I}_j(t)=\int_0^t\mathbf{h}(t-\tau)\mathbf{G}(\tau)\mathbf{W}\boldsymbol{\varphi}_j\,\mathrm{e}^{\mathrm{i}\omega\tau}\,\mathrm{d}\tau. \tag{4.4.12}$$

Similarly, substituting equation (4.4.8) into equations (4.2.4) and (4.2.8), the pseudo-response of quasi-static displacement under partially coherent spatial ground motions is

$$\tilde{\mathbf{Y}}_{\mathrm{s}}(\mathrm{i}\omega,t)=\sum_{j=1}^{r}\tilde{\mathbf{y}}_{\mathrm{sj}}=\sum_{j=1}^{r}-\mathbf{F}\sqrt{\alpha_j\mathbf{S}_{\mathrm{g}}(\mathrm{i}\omega)}\omega^{-2}\mathbf{G}(\tau)\mathbf{W}\boldsymbol{\varphi}_j. \tag{4.4.13}$$

Hence, PSD of the pseudo-response of absolute displacement under *partially coherent* spatial ground motions can be resulted by substituting equations (4.4.11) and (4.4.13) into equation (4.2.13), which is

$$\mathbf{S}_{X_SX_S}(\mathrm{i}\omega,t)=\left[\sum_{j=1}^{r}-\mathbf{F}\sqrt{\alpha_j\mathbf{S}_{\mathrm{g}}(\mathrm{i}\omega)}\,\omega^{-2}\mathbf{G}(\tau)\mathbf{W}\boldsymbol{\varphi}_j+\sum_{j=1}^{r}\mathbf{F}\sqrt{\alpha_j\mathbf{S}_{\mathrm{g}}(\mathrm{i}\omega)}\,\mathbf{I}_j(t)\right]^{*}\cdot$$

$$\left[\sum_{j=1}^{r}-\mathbf{F}\sqrt{\alpha_j\mathbf{S}_{\mathrm{g}}(\mathrm{i}\omega)}\,\omega^{-2}\mathbf{G}(\tau)\mathbf{W}\boldsymbol{\varphi}_j+\sum_{j=1}^{r}\mathbf{F}\sqrt{\alpha_j\mathbf{S}_{\mathrm{g}}(\mathrm{i}\omega)}\,\mathbf{I}_j(t)\right]^{T}. \tag{4.4.14}$$

Similarly, PSD of pseudo-response of absolute displacement under *fully coherent* and *completely incoherent* spatial seismic motions are

Fully coherent:

$$\mathbf{S}_{X_SX_S}(\mathrm{i}\omega,t)=\left[-\mathbf{F}\sqrt{\mathbf{S}_{\mathrm{g}}(\mathrm{i}\omega)}\omega^{-2}\mathbf{G}(\mathrm{t})\mathbf{W}\mathbf{Q}+\mathbf{F}\sqrt{\mathbf{S}_{\mathrm{g}}(\mathrm{i}\omega)}\mathbf{I}_0(t)\right]^{*}\cdot$$

$$\left[-\mathbf{F}\sqrt{\mathbf{S}_{\mathrm{g}}(\mathrm{i}\omega)}\omega^{-2}\mathbf{G}(\mathrm{t})\mathbf{W}\mathbf{Q}+\mathbf{F}\sqrt{\mathbf{S}_{\mathrm{g}}(\mathrm{i}\omega)}\mathbf{I}_0(t)\right]^{T}, \tag{4.4.15}$$

where

$$\mathbf{I}_0(t)=\int_0^t\mathbf{h}(t-\tau)\mathbf{G}(\tau)\mathbf{W}\mathbf{Q}\mathrm{e}^{\mathrm{i}\omega\tau}\,\mathrm{d}\tau. \tag{4.4.16}$$

Completely incoherent:

$$\mathbf{S}_{X_SX_S}(\mathrm{i}\omega,t)=\left[-\mathbf{F}\sqrt{\mathbf{S}_{\mathrm{g}}(\mathrm{i}\omega)}\omega^{-2}\mathbf{G}(\mathrm{t})\mathbf{W}+\mathbf{F}\sqrt{\mathbf{S}_{\mathrm{g}}(\mathrm{i}\omega)}\mathbf{I}(t)\right]^{*}\cdot$$

$$\left[-\mathbf{F}\sqrt{\mathbf{S}_{\mathrm{g}}(\mathrm{i}\omega)}\omega^{-2}\mathbf{G}(\mathrm{t})\mathbf{W}+\mathbf{F}\sqrt{\mathbf{S}_{\mathrm{g}}(\mathrm{i}\omega)}\mathbf{I}(t)\right]^{T}, \tag{4.4.17}$$

where

$$\mathbf{I}(t)=\int_0^t \mathbf{h}(t-\tau)\mathbf{G}(\tau)\mathbf{W}\mathrm{e}^{\mathrm{i}\omega\tau}\,\mathrm{d}\tau. \tag{4.4.18}$$

4.4.2 Absolute-response-oriented Direct Approach

In the direct approach, the pseudo-response of absolute displacement $\tilde{\mathbf{y}}_{aj}$ with respect to the jth eigenvalue can be obtained by substituting equation (4.4.8) into equation (4.2.22)

$$\tilde{\mathbf{y}}_{aj}=\sqrt{\alpha_j\mathbf{S}_{\mathrm{g}}(\mathrm{i}\omega)}\mathbf{I}_j(t), \tag{4.4.19}$$

where $\mathbf{I}_j(t)$ is given in equation (4.4.12).

Then, the PSD of pseudo-response of absolute displacement under *partially coherent* tridirectional nonstationary ground motions can be expressed by substituting equation (4.4.19) into equation (4.2.23)

$$\mathbf{S}_{X_SX_S}(\mathrm{i}\omega,t)=\sum_{j=1}^{r}\tilde{\mathbf{y}}_{\mathrm{aj}}^{*}\tilde{\mathbf{y}}_{\mathrm{aj}}^{T}=\sum_{j=1}^{r}\mathbf{I}_j^{*}\mathbf{I}_j^{T}\alpha_j\mathbf{S}_g(\mathrm{i}\omega). \tag{4.4.20}$$

Similarly, PSD of the pseudo-response of absolute displacement $\tilde{\mathbf{y}}_{\mathrm{a}}$ under *fully coherent* and *completely incoherent* spatial ground motions are

Fully coherent:

$$\mathbf{S}_{X_SX_S}(\mathrm{i}\omega,t)=\tilde{\mathbf{y}}_{\mathrm{a}}^{*}\tilde{\mathbf{y}}_{\mathrm{a}}^{T}=\mathbf{I}_0^{*}\mathbf{I}_0^{T}\mathbf{S}_g(\mathrm{i}\omega), \tag{4.4.21}$$

in which $\mathbf{I}_0$ is given in equation (4.4.16).

Completely incoherent:

$$\mathbf{S}_{X_SX_S}(\mathrm{i}\omega,t)=\tilde{\mathbf{y}}_{\mathrm{a}}^{*}\tilde{\mathbf{y}}_{\mathrm{a}}^{T}=\mathbf{I}^{*}\mathbf{I}^{T}\mathbf{S}_g(\mathrm{i}\omega), \tag{4.4.22}$$

where $\mathbf{I}$ is given in equation (4.4.18).

As discussed in Section 4.2.3, the formulations are more complicated for the indirect method (equations (4.4.14), (4.4.15), and (4.4.17)) in obtaining the pseudo-response of absolute displacement than the direct method (equations (4.4.20), (4.4.21), and (4.4.22)). Moreover, in the indirect method, the static influence matrix [$\mathbf{F}$] and the inverse of matrix [$\mathbf{K}_{\mathrm{ss}}$] have to be calculated at every eigenmode, increasing the time of computation of PEM

in structural seismic analysis. On the other hand, the direct approach provides an explicit and simple formulation that can be readily implemented in a general FEA platform without increasing the computation time. A brief description of the implementation and verification on the ANSYS platform is presented in Section 4.5.

4.5 Implementation and Verification of Stochastic Analysis Scheme in General FEA Platform

The direct approach presented in Sections 4.2.2 and 4.4.2 is implemented in the general FEA platform ANSYS to make PEM readily applicable for stochastic seismic analysis of complex long span structures under tridirectional nonstationary SVGM (Kohnke, 2010). The procedure for the implementation is presented in detail in the flow chart of Figure 4.1.

To validate the implementation, a single DoF oscillator under nonstationary excitations is studied for comparison. The mathematical statement is (Caughey and Stumpf, 1961)

$$\ddot{y}+2\zeta\omega_0\dot{y}+\omega_0^2 y=g(t)x(t), \tag{4.5.1}$$

$$y(0)=\dot{y}(0)=0, \quad g(t)=\begin{cases}1.0, & t>0,\\ 0, & t\leqslant 0.\end{cases} \tag{4.5.2}$$

The analytical solutions of the time-dependent PSD of the single DoF oscillator are

$$S_{yy}(\omega,t)=|H|^2 S_{xx}(\omega)\cdot\left\{\left[\exp(-\varepsilon t)\left(\frac{\varepsilon}{\omega_\varepsilon}\sin\omega_\varepsilon t+\cos\omega_\varepsilon t\right)-\cos\omega t\right]^2+\left[\exp(-\varepsilon t)\left(\frac{\omega}{\omega_\varepsilon}\sin\omega_\varepsilon t\right)-\sin\omega t\right]^2\right\}, \tag{4.5.3}$$

where $H=\left(\omega_0^2-\omega^2+2\mathrm{i}\zeta\omega_0\omega\right)^{-1}$, $\varepsilon=\zeta\omega_0$, $\omega_\varepsilon=\omega_0\sqrt{1-\zeta^2}$, $\omega_0=\sqrt{k/m}$, the oscillator mass $m=1.0$, stiffness $k=1.0$, and damping ratio $\zeta=0.05$.

Figures 4.2, 4.3, and 4.4 present the theoretical solutions and ANSYS solutions (based on the implementation) for the time-dependent PSD at $\omega=0.5, 1.5,$ and 15 (rad/s), respectively, where it is observed that the ANSYS solutions agree with the theoretical solutions very well, meaning that the implementation of PEM in ANSYS is accurate in obtaining structural seismic results. Based on the implementation, the nonstationary stochastic analysis approach is

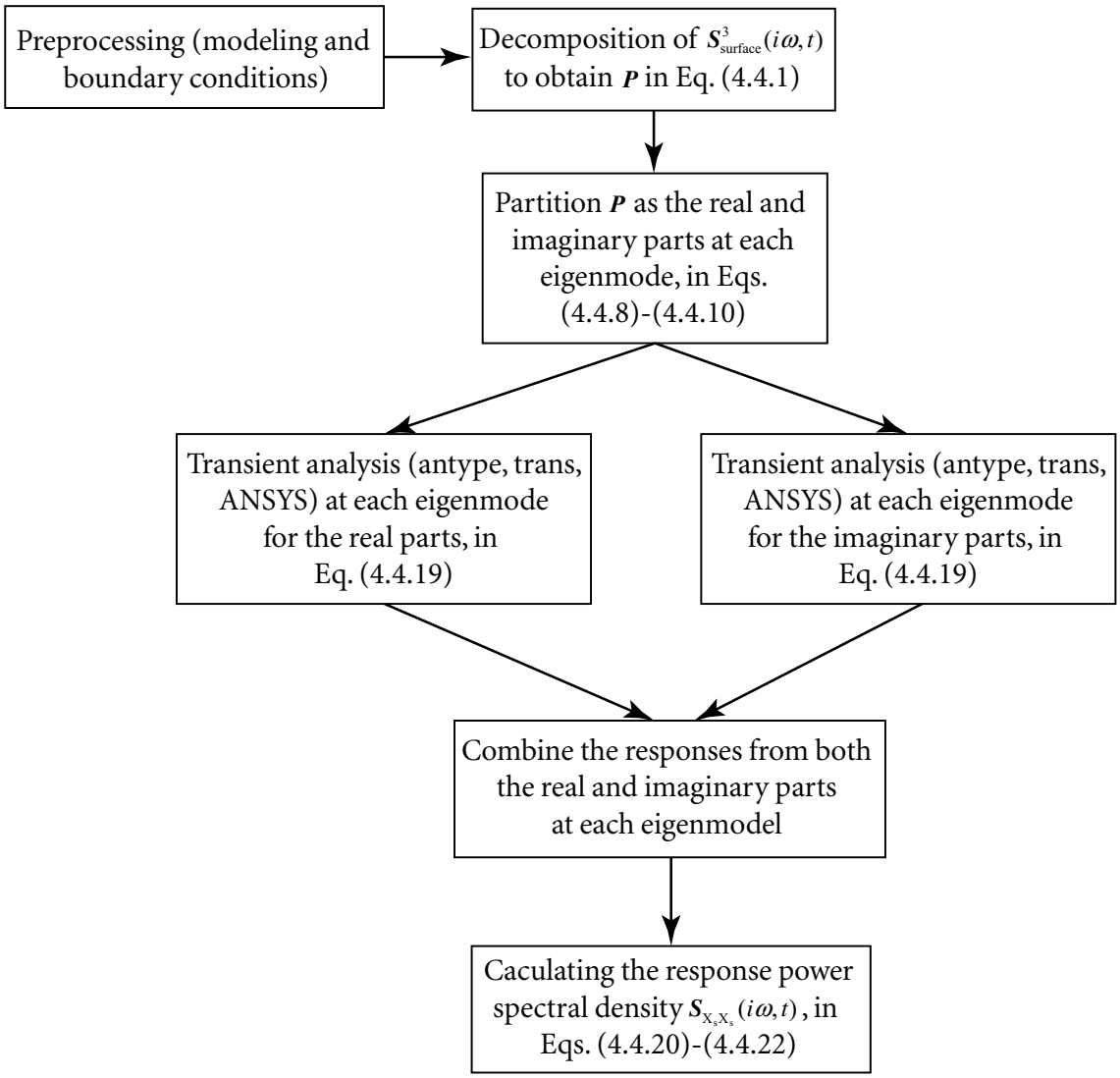

Figure 4.1 Flow chart of implementation of the direct approach of PEM in ANSYS

applied to a high-pier railway bridge under tridirectional nonstationary SVGM in Chapter 5.

4.6 Summary and Conclusions

In this chapter, a comprehensive, systematic, and efficient stochastic seismic analysis approach is derived for long span structures under tridirectional nonstationary spatial mo-

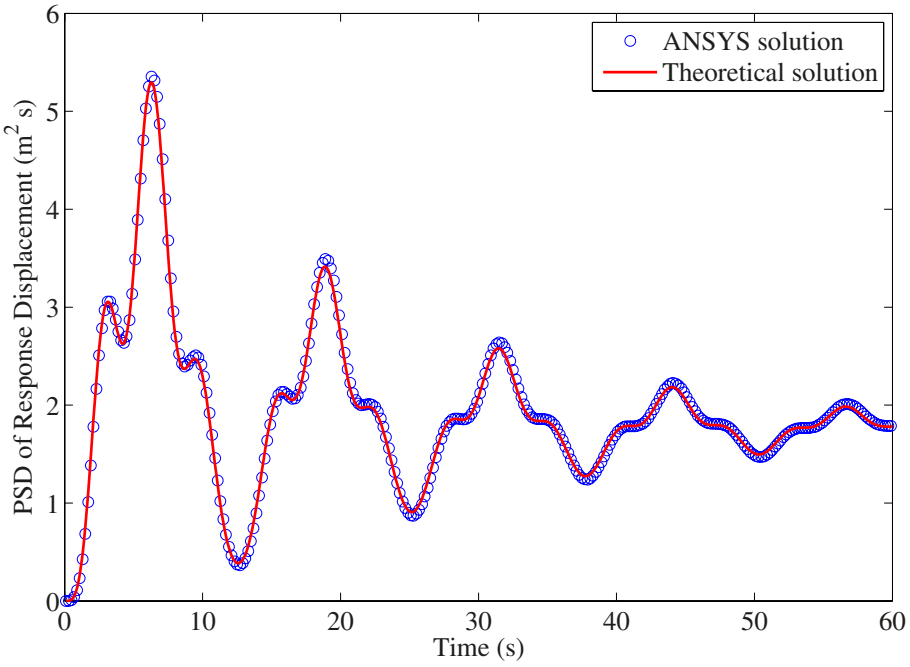

Figure 4.2 PSD of displacements ($\omega = 0.5$ rad/s)

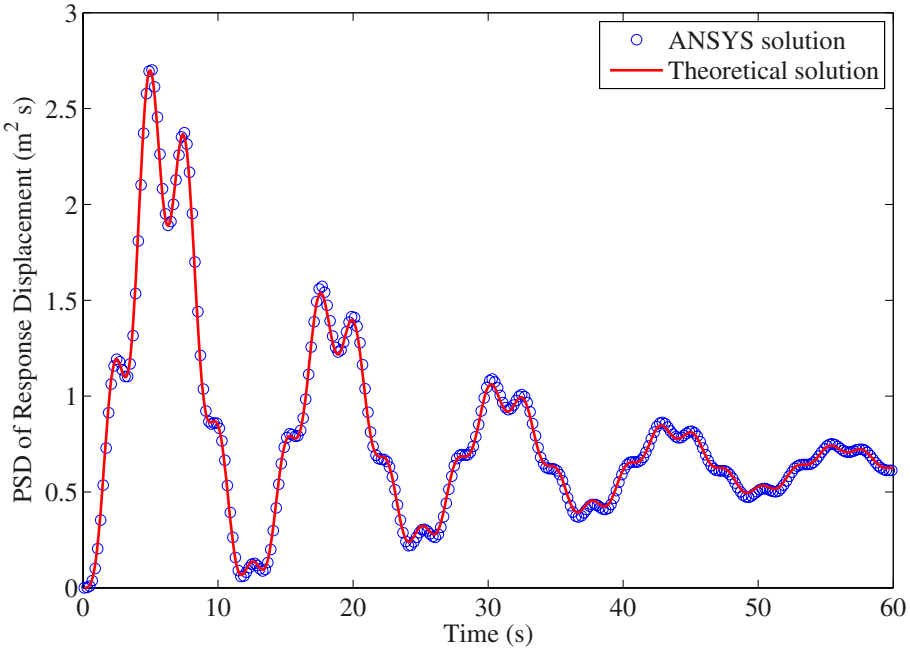

Figure 4.3 PSD of displacements ($\omega = 1.5$ rad/s)

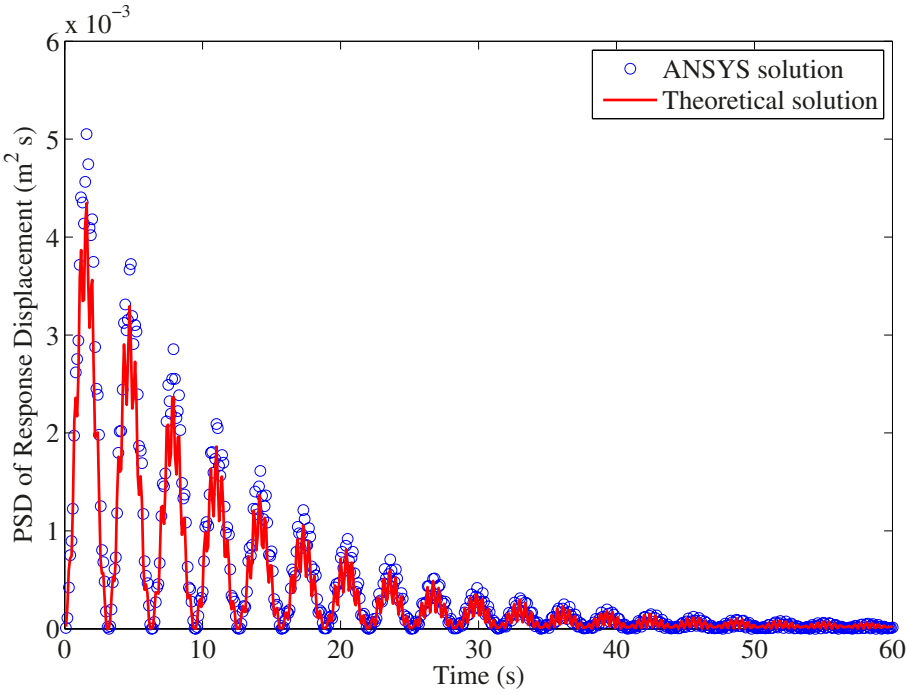

Figure 4.4 PSD of displacements ($\omega =$ 15 rad/s)

tions, considering ground motion incoherence effect, wave-passage effect, tridirectional local site effect (uniform and non-uniform site conditions), nonstationarity, and tridirectionality, which includes

1. An absolute-response-oriented scheme of PEM (in time domain) is developed to reduce the enormous computational effort of the conventional indirect nonstationary SVA (in frequency domain) in solving equations of motion of structures under nonstationarity tridirectional SVGM.
2. A scheme in accounting for tridirectional varying site-response effect is incorporated in the nonstationary SVA scheme systematically.
3. The proposed SVA approach is implemented and verified in the general FEA platform to make it readily applicable in stochastic seismic analysis of complex structures.
4. This analytical SVA approach is more attractive for nonstationary stochastic seismic analysis of practical long span structures under tridirectional SVGM.

CHAPTER 5

Stochastic Seismic Analysis of Bridges under SVGM: (II) Practical Applications

Based on the theoretical stochastic vibration analysis (SVA) methodology in Chapter 4, two practical bridges, a concrete-filled steel tubular (CFST) arch bridge and a high-pier railway bridge, are analyzed in details in this chapter.

5.1 Introduction

During the past two decades, responses of bridges to spatially varying ground motions (SVGM) have been studied extensively on various types of long span bridge structures, such as suspension bridges (Harichandran *et al.*, 1996; Wang, 1999), cable-stayed bridges (Nazmy and Abdel-Ghaffar, 1992; Dumanoglu and Soyluk, 2003; Soyluk, 2004a), and arch bridges (Hao, 1993; Zanardo *et al.*, 2004), and bridge pounding and isolation (Ates *et al.*, 2005) under SVGM. In these works, SVA has been widely used (Zerva, 1990; Hao, 1993; Harichandran *et al.*, 1996; Dumanoglu and Soyluk, 2003; Soyluk, 2004a; Ates *et al.*, 2006; Zhang *et al.*, 2009).

The Long Span Arch Bridge

The long span CFST arch bridges have been widely accepted and rapidly constructed because of its advantageous structural style, which impels indepth studies of CFST arch bridge for its design and analysis. Most of the previous studies are devoted to the static behavior, thermal and creep effects of concrete and steel, forms of structural members, or the construction technology; few researches have been carried out on the analysis of seismic behaviors of the CFST arch bridge, especially on its seismic performance under SVGM.

Hao (1993, 1994) investigated an in-plane circular incompressible arch under multiple earthquake motions by considering the incoherence effect of spatial seismic motions, and concluded that seismic responses could be overestimated or underestimated if spatial variabilities of ground motions were not taken into account. Several similar studies, Harichandran *et al.* (1996), Kawashima and Mizoguti (2000), Zanardo *et al.* (2004), Soyluk (2004a), and Su *et al.* (2007), have been conducted for the arch bridges. However, these studies only partially and simplistically provide a systematic approach in the seismic analysis of arch bridges under SVGM.

The Long Span High-pier Railway Bridge

Constructions of railways are under enormous development in China in recent years; many of them have been built or are being built in the southwestern regions of China. Among these railways, high-pier railway bridges are usually constructed due to mountainous site topographies of southwest China, around 40% of which have piers higher than 40m, e.g., the Beipanjiang railway bridge located on the Yunnan-Guizhou Plateau has the highest pier of 100m (Wang and Gan, 2011). These mountainous railway bridges usually have continuous and rigid frame girders in the superstructure and thin-walled hollow piers with varying heights in the substructure, besides the large slenderness ratio of piers.

As known, the southwestern regions of China, where these railway bridges are located, are seismic zones with high incidence of earthquakes, e.g., the 2008 Sichuan Earthquake (occurred on May 12, 2008 in the Sichuan province with moment magnitude $M_w = 7.9$ and caused a wide range of damages on different types of railway bridges). Thus, seismic analysis and design of these high-pier railway bridges are essential and significant and have

been regulated in the seismic design code of railway engineering in China (MRC, 2006). However, the dimensions of many newly built railway bridges, such as the span lengths and pier heights, are beyond the bridge dimensions to which specifications of MRC (2006) are applicable, e.g., the China railway seismic design code applies only to railway bridges with span shorter than 120m and pier lower than 30m. Hence, special seismic analysis becomes necessary for those railway bridges with large dimensions.

Moreover, seismic performance of high-pier railway bridges may differ significantly from highway or pedestrian bridges due to their special structural configurations and varying complex gully site conditions, e.g., piers of railway bridges in the substructure are usually high yet flexible, while the girders in the superstructure are often required to be more rigid to avoid derailment of high-speed train and excessive vertical deflection caused by rail loads. However, the seismic performance of these high-pier railway bridges has been studied in only a few works (Caglayan *et al.*, 2011), besides some studies on dynamic interaction of bridge-train system under SVGM (Xia *et al.*, 2006).

Based on the analytical SVA methodology in Chapter 4, a systematic and detailed seismic analysis for a long span arch bridge and a high-pier railway bridge is presented in Sections 5.2 and 5.3, respectively. Some conclusions drawn from these two examples are presented in Section 5.4.

5.2 Example I: A Long Span CFST Arch Bridge

5.2.1 Structural Systems

The three-span CFST arch bridge considered, with layout of 51m+158m+51m, is a swallows-type half-through bridge structure having single arch rib and has been in operation for around 2 years. The main arch rib has the triangular cross-section composed of three steel tubes connected by pulling slabs on the sides and bottom, and the stable arch rib has the single tube cross-section. The angle between the plane of the stable arch rib and the vertical plane is 21.8°. The main arch rib is connected with the left and right stable arch ribs using the diagonal bracing with box cross section, while the left and right stable arch ribs are connected by the lateral bracing with tube cross section.

The main girders of the side spans are constructed using prestressed concrete materials, and they are fixed together with the V-shape legs and the foot parts of the main arch rib. The main girders of the side spans extend across the foot parts of the main arch rib to connect with the box-girder of the main span using two corbels, and the box-girders of the main span are simply supported in the corbels by using the vertical bearings and the transverse restrict-sliding bearings. The forward inclined legs act as part of the main arch rib and are fixed with main girders of the side spans, while the axial lines of the backward inclined legs are designed to have the parabola forms and are fixed with main girders of the side spans. The forward and backward inclined legs are constructed using prestressed concrete structures with single-box dual-chamber cross section. The CFST bridge has a total of 16 suspenders and 6 horizontal flexible ties (Li *et al.*, 2013).

Figure 5.1(a) shows the 3-D schematic view of the bridge structure, and the integral layout of the actual bridge is shown in Figure 5.1(b). Material properties of the concrete, steel, suspenders, and tie bars, i.e., the elastic modulus, density, and the design compressive and tensile stresses, are given in Table 5.1 (Li *et al.*, 2013).

5.2.2 The Finite Element Analysis Model

The 3-D linear elastic finite element analysis (FEA) model of the CFST arch bridge is built using ANSYS (Kohnke, 2010). The beam189 element (Timoshenko beam element including shear deformation effect) is used to model the main arch rib, with section properties determined from the composite section given in Figure 5.2. The stable arch rib, diagonal bracing, lateral bracing, box-type concrete girder, steel main girder, forward and backward inclined legs, and the upright columns are modeled by the beam44 element (3-D tapered unsymmetric beam). The link10 element is used to model the suspenders and tie bars, and connections between the concrete girders and steel girders are simulated using combin14 element (linear spring-damper element) by coupling their translational degrees-of-freedom (DoF) and releasing the rotational DoF. Other detailing about the FEA model is shown in Figure 5.2, such as connections of the FEA model at detail-A and detail-B. The FEA model has a total of 445 nodes, 484 beam elements, 34 link elements, 6 spring elements, and 2650 DoF, shown in Figure 5.2 (Li *et al.*, 2013).

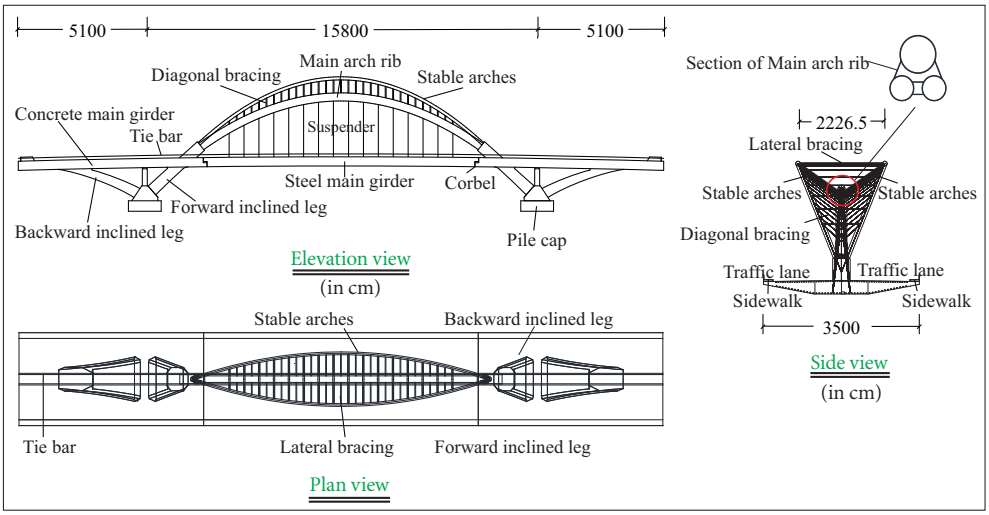

(a) 3-D schematic view of the CFST arch bridge

(b) The integral layout of the actual bridge

Figure 5.1 Schematic view of the CFST arch bridge (Li *et al.*, 2013)

Table 5.1: Material properties of the CFST arch bridge

Property	Concrete		Steel	Cable	
	C30	C50	Q345	suspender PES(FD)7-199	tie bar PES(FD)7-61
elastic modulus E (MPa)	3.00×10^4	3.45×10^4	2.06×10^5	2.05×10^5	2.05×10^5
design compressive stress f_{sd} (MPa)	20.1	32.4	345	-	-
design tensile stress f_{td} (MPa)	2.01	2.65	345	1140	1140
poisson ratio ν	0.2	0.2	0.3	0.3	0.3
mass density ρ (kg/m^3)	2.55×10^3	2.55×10^3	7.70×10^3	7.85×10^3	7.85×10^3

Using the FEA model, the modal analysis is conducted by using the block-Lanzos method. The first two natural frequencies are 0.6280 Hz and 1.6236 Hz and have the transverse symmetric and antisymmetric mode shapes, respectively. The third and fourth mode shapes have the vertically antisymmetric and symmetric deformation with natural frequencies 2.1738 Hz and 2.4576 Hz, respectively. The fifth mode shape maintains a symmetric transverse deflection with frequency 3.1617 Hz. These mode shapes are shown schematically in Figure 5.3 for the 3-D plot.

5.2.3 Stationary Stochastic Seismic Response Analysis

Based on the formulations presented in Chapter 4, stochastic seismic analysis of the CFST arch bridge under SVGM, considering effects of the incoherence, wave-passage, local site condition, and ground motion dimensionality, is performed in the following subsections.

5.2.3.1 Effect of Spatial Variability of Ground Motions

As discussed in Section 1.1.1, the inconsistency of earthquake excitations is due to incoherency effect, wave-passage effect, and site-response effect. These effects can be accounted for separately in the wave coherence function model as $\gamma_{ij}(\omega) = \gamma_{ij}(\omega)^{\mathrm{i}}\gamma_{ij}(\mathrm{i}\,\omega)^{\mathrm{w}}\gamma_{ij}(\mathrm{i}\,\omega)^{\mathrm{s}}$, respectively (Der Kiureghian, 1996).

Based on the site response analysis approach in Section 2.4.1, the influence of apparent wave velocity is only related to the base rock properties and the incident angle of wave motion on the base rock, meaning that the apparent wave velocity is fixed for a specific site. However, the variations of apparent wave velocity in cases #4, #6, #7, and #8 are to study the wave-passage effect on structural responses, and to investigate which incoherence effect and wave-passage effect plays a more significant role on structural responses. Thus, no site conditions are assumed or considered in these cases and details of the site-response effect are presented in Section 5.2.3.2.

To investigate effects of spatial variability of ground motions on structural responses, 8 cases are considered, as listed in Table 5.2. Specifically, case #1 is the uniform ground motion (no time delay and no loss of coherency between support excitations, $\gamma_{ij}(\omega)^{\mathrm{i}}\gamma_{ij}(\mathrm{i}\,\omega)^{\mathrm{w}} = 1$); case #2 is for the wave-passage effect (no loss of coherency between the support excitations,

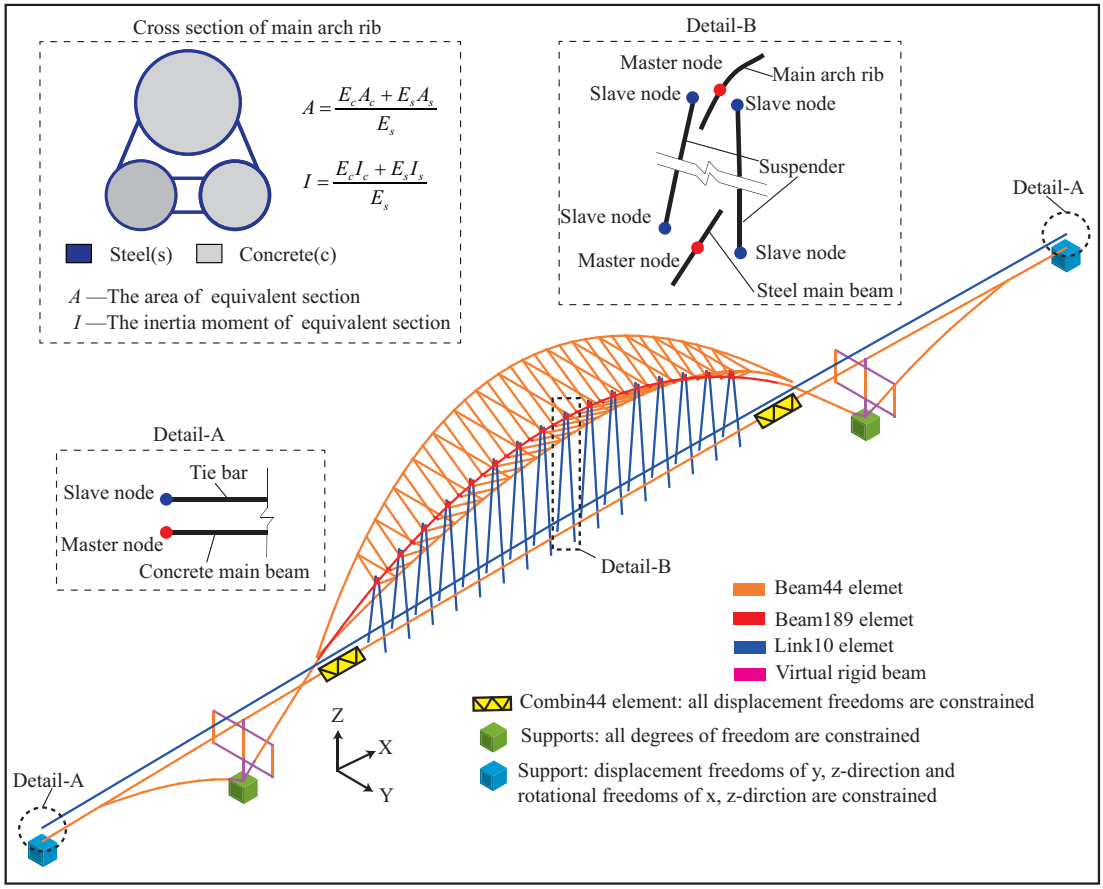

Figure 5.2 FEA model of the CFST arch bridge (Li *et al.*, 2013)

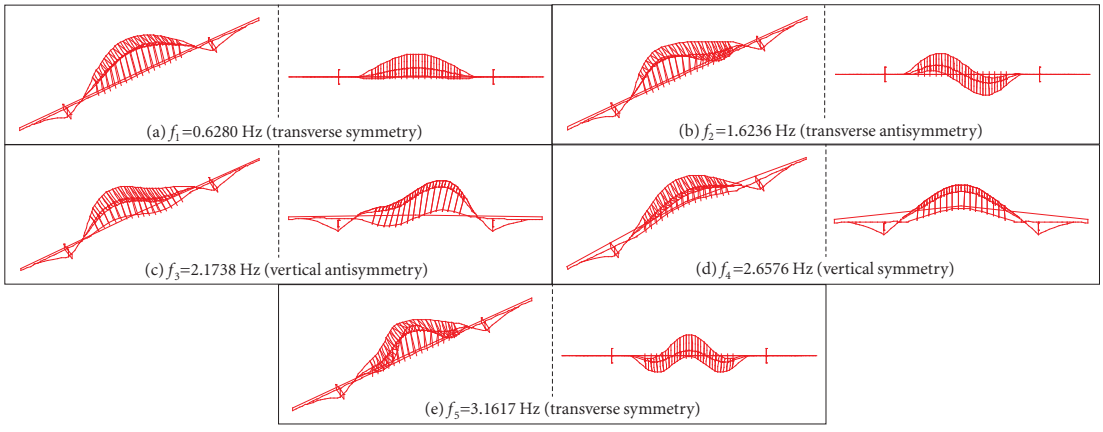

Figure 5.3 Natural frequencies and mode shapes from FEA model

$\gamma_{ij}(\omega)^{\mathrm{i}}=1$); case #8 is for the incoherence effect (no time delay between support excitations, $\gamma_{ij}(\mathrm{i}\,\omega)^{\mathrm{w}}=1$); #3 to #7 are general excitation cases with different degrees of coherency losses and wave-passage effect.

Table 5.2: Effect of spatial variability of ground motions

Number	Incoherence effect	Wave-passage effect
#1	$\gamma_{ij}(\omega)^{\mathrm{i}}=1$	$\gamma_{ij}(\mathrm{i}\,\omega)^{\mathrm{w}}=1$
#2	$\gamma_{ij}(\omega)^{\mathrm{i}}=1$	intermediate
#3†	high ($\beta=1.109\times10^{-4}, a=3.583\times10^{-3}$)	intermediate
#4	intermediate ($\beta=3.697\times10^{-4}, a=1.194\times10^{-2}$)	intermediate ($V_{\mathrm{app}}=400$)
#5	weak ($\beta=1.109\times10^{-3}, a=3.583\times10^{-2}$)	intermediate
#6	intermediate	small ($V_{\mathrm{app}}=50$)
#7	intermediate	large ($V_{\mathrm{app}}=2000$)
#8	intermediate	$\gamma_{ij}(\mathrm{i}\,\omega)^{\mathrm{w}}=1$ ($V_{\mathrm{app}}=\inf$)

† Parameters are obtained based on spatial earthquake array of SMART1-Event45.

The ground motion coherence model by Oliveira *et al.* (1991) is used

$$|\gamma(d_{ij},f)|=\exp(-\beta d_{ij})\exp\left(-\alpha(f)d_{ij}^{1/2}f^{2}\right), \tag{5.2.1}$$

where β is a constant, d_{ij} is the spatial distance between supports i and j in the wave propagation, α is a function of f as $\alpha(f\leqslant10)=a/f+bf+c, \alpha(f>10)=\alpha(f=10)$, and f is the frequency in Hz. For SMART1-Event45, the parameters are $\beta=1.109\times10^{-4}$, $a=3.853\times10^{-3}$, $b=-1.811\times10^{-5}$, and $c=1.177\times10^{-4}$, corresponding to case #3 in Table 5.2.

For the half-through CFST arch bridge with single arch rib, the transverse direction is more vulnerable to the stability failure due to the smaller transverse stiffness, while the arch bridge exhibits larger stiffness in the longitudinal and vertical directions because the arch rib is supposed to resist the compression forces. In this section, analyses of the CFST arch bridge under transverse, vertical, and longitudinal ground motions are conducted, and the

resulting peak responses for cases in Table 5.2 are presented in Figure 5.4 (based on the stationary peak factor formulas in Appendix A.3).

Comparing the responses of case #1 (uniform excitations) and the other 7 cases (multiple excitations) in Figure 5.4, spatial variabilities of ground motions can introduce a significant effect on structural responses of the arch rib under transverse, vertical, and longitudinal excitations (e.g., displacements U_Y and bending moments M_Z in Figure 5.4(a) and (b) under transverse excitations, axial forces F_X and bending moments M_Y in Figure 5.4(c) and (d) under vertical excitations, and axial forces F_X and bending moments M_Y in Figure 5.4(e) and (f) under longitudinal excitations). It is concluded from these observations that

1. the conventionally used uniform input assumption by neglecting both the phase shifts and the coherency losses might greatly underestimate or overestimate the responses,
2. neglecting ground motion spatial variations in analysis may lead to incorrect predictions of structural responses,
3. it is necessary and important to include spatial variabilities of ground motions in seismic analysis and design of CFST arch bridges with large span.

For the wave-passage effect, transverse displacements of the arch rib and bending moments in the middle of the arch rib increase as the apparent wave velocity V_{app} increases from 50 m/s (in case #6) to infinite (neglecting the wave-passage effect, in case #8), and the rate of increase decreases as the apparent wave velocity decreases. Specifically, large discrepancies of displacements and bending moments (in the middle of the arch rib) can be observed in Figure 5.4(a) and (b), respectively, between cases #6 and #8 as $U_Y^{\#8}/U_Y^{\#6} = 1.20$ and $M_Z^{\#8}/M_Z^{\#6} = 1.42$. Similar observations can also be obtained for the axial forces F_X of the arch rib under vertical ground motions in Figure 5.4(c), but the opposite observations that the responses decrease as the apparent wave velocity increases are made for the axial forces F_X and bending moments M_Y of the arch rib under longitudinal ground motions in Figure 5.4(e) and (f).

These observations show that, at the same apparent wave velocity level, the wave-passage effect becomes more significant for structures with larger spans. On the other hand, it is also demonstrated that the wave-passage effect is more significant than the effect of coherence

loss on structural responses, which can be seen from variations of the structural responses (U_Y and M_Z in Figure 5.4(a) and (b), F_X and M_Y in Figure 5.4(c) and (d), and F_X and M_Y in Figure 5.4(e) and (f)) for cases #3 (high coherence loss), #4 (intermediate coherence loss), and #5 (weak coherence loss) under the transverse, vertical, and longitudinal multiple ground motions, respectively. These observations are in good agreement with results obtained by Hao (1994) and Su *et al.* (2007).

More importantly, as seen from comparisons of responses between case #1 (uniform excitations) and the other 7 cases (multiple excitations) under the transverse motions in Figure 5.4(a) and (b), the vertical motions in Figure 5.4(c) and (d), and the longitudinal motions in Figure 5.4(e) and (f), it is concluded that

1. ignoring spatially variable transverse ground motions would overestimate the response displacements and bending moments of the arch rib,
2. ignoring variabilities of vertical ground motions can also overestimate responses of the arch rib,
3. ignoring spatially correlated longitudinal excitations can underestimate the axial forces F_X and bending moments M_Y of the arch rib.

Similar conclusions to observations 2 and 3 are made by Su *et al.* (2007) for a 2-D steel truss arch system by the response history analysis (RHA). Hence, the conventional assumptions that vertical and transverse free-field ground motions are spatially uniform can be used to assure the degree of seismic safety of the half-through CFST arch bridge with single arch rib. Multiple longitudinal excitations are recommended in the actual seismic design of CFST arch bridge structures from the safety perspective.

These phenomena are attributed to the following reasons. For structural responses under transverse excitations, the uniform (symmetric) excitations would excite the 1st mode (symmetric shape in the transverse direction) as the dominant mode, while spatially variable ground motions can induce both the 1st mode and 2nd mode (antisymmetric in the transverse direction) to be the dominant modes, where the antisymmetric transverse mode shape can reduce (''average'') the transverse displacements or internal forces of the arch rib, as shown in Figure 5.4(a) and (b). Similarly, for structural responses under vertical

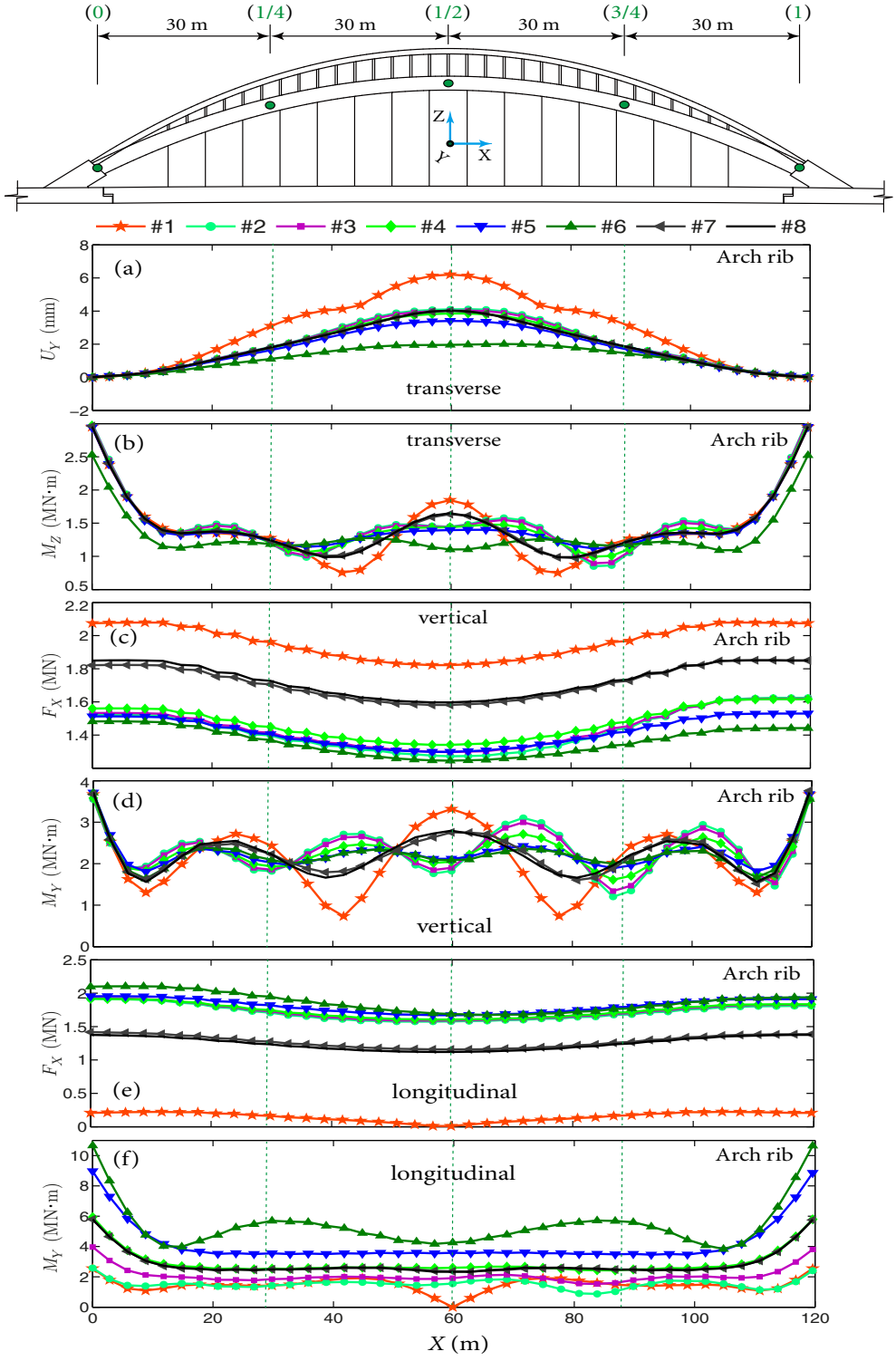

Figure 5.4 Effect of spatially varying transverse, vertical, and longitudinal ground motions

excitations, the uniform ground motions would mainly induce the vertically symmetric 4th mode, while spatial motions can excite both the 3rd (vertically antisymmetric) and 4th modes, reducing F_X and M_Y of the arch rib of the CFST arch bridge. For structural responses under longitudinal excitations, spatially varying wave motions would excite the 3rd coupled mode (coupling between the longitudinal and vertical deformations), because of which large vertical deformations can be induced by the longitudinal multiple excitations, causing large axial forces and bending moments in the arch rib as seen in Figure 5.4(e) and (f).

Additionally, the vertical and longitudinal excitations contribute to the axial forces of the arch rib much more than the transverse excitations do; the transverse motions maintain a negligible effect on the axial forces of the arch rib. Hence, unlike the conventional seismic analysis of arch structures under longitudinal and transverse excitations, the vertical excitations are recommended to be included in the seismic design of the arch bridge structures. Moreover, the transverse, vertical, and longitudinal excitations can all lead to significant bending moments of the arch rib. The longitudinal excitations can result in the largest bending moments at the springing joint of the arch rib, suggesting that special attentions should be paid to the design of springing joint of the arch rib to avoid possible plastic hinges occurring under longitudinal motions at multiple supports.

Besides the displacements U_Y in Figure 5.4(a), the axial forces F_X in Figure 5.4(c) and (e), and the bending moments M_Y in Figure 5.4(f), it is also observed that the bending moments M_Z under the transverse multiple excitations (in Figure 5.4(b)) and M_Y under the vertical multiple motions (in Figure 5.4(d)) are larger than those under the uniform transverse or vertical excitations. These observations agree with results obtained by other researchers that spatial variabilities of ground motions can sometimes increase or decrease structural responses as compared with those under the uniform excitations; the levels of increase or decrease depend on the response quantities and their positions along the arch (Hao, 1994). However, comparing with structural responses obtained from the uniform excitations, all of the responses at key sections (0, $L/4$, $L/2$, $3L/4$, L, the controlling parts in design of the arch structures) are smaller under the spatial transverse and vertical spatial motions. Hence, the aforementioned three observations still hold, i.e., the conventional seismic evaluations

of arch structures under uniform transverse and vertical excitations are conservative, which are recommended in the actual seismic design and analysis of the half-through CFST arch bridge with single arch rib.

5.2.3.2 Effect of Local Site Conditions

Effects of the local site conditions, varying site conditions, site irregularities, and different incident angles of bedrock ground motions are considered in this section. Categories of site conditions specified in National Earthquake Hazard Reduction Program (NEHRP) are used and presented in Table 5.3, with the corresponding soil properties (G is the shear modulus, ρ the mass density, ν_0 the Poisson's ratio, ξ the damping coefficient, V_s the shear wave velocity, and h the depth of the soil layer) (FEMA, 2010).

Table 5.3: Soil properties of site categories specified in NEHRP (FEMA, 2010)

Site categories	**Property**	G (MPa)	ρ (kg/m^3)	ν_0	ξ	V_s (m/s)	h (m)
#A: hard rock	$V_s > 1524$	5285.5	2200	0.20	0.03	1550	--
#B: rock	$762 < V_s < 1524$	1344.0	2100	0.25	0.05	800	46.5
#C: soft rock	$366 < V_s < 762$	326.5	2041	0.30	0.06	400	46.5
#D: stiff soil	$183 < V_s < 366$	65.3	1633	0.35	0.07	200	46.5
#E: soft soil	$V_s < 183$	15.0	1500	0.45	0.09	100	46.5

For effects of the local site conditions and varying site conditions, a total of 5 (#1-#5) and 6 (#6-#11) cases are considered, respectively. Depths of the soil profiles are chosen to be $h = 46.5$ m as inferred from the actual depths of piles of the CFST arch bridge. To study the effects of site irregularities and different incident angles of bedrock ground motions, a total of 7 cases (#12-#18) are considered ($h_1 = 23$ m, $h_2 = 69$ m). The incident angles of bedrock motions propagating towards the sites are varied by 10°, 60°, and 90°. Details of these cases are given in Table 5.4.

The site response analysis in Section 2.4.1 is performed for different site categories in Table 5.4. Amplification results of sites #B and #D for both in-plane (U, W) and out-of-plane (V) wave motions are shown in Figure 5.5(a), which indicate that the fundamental

Table 5.4: Analysis cases in study of effect of local site conditions

Local site conditions[†1]	**Varying site conditions**	**Site irregularities and incident angles**[†2]
#1: A-A-A-A	#6: C-B-B-C	#12: C(h_1)-C(h_2)-C(h_2)-C(h_1)
#2: B-B-B-B	#7: D-C-C-D	#13: C(h_1)-C(h_1)-C(h_2)-C(h_2)
#3: C-C-C-C	#8: E-D-D-E	#14: E(h_1)-E(h_2)-E(h_2)-E(h_1)
#4: D-D-D-D	#9: D-C-B-E	#15: E(h_1)-E(h_1)-E(h_2)-E(h_2)
#5: E-E-E-E	#10: B-C-D-E	#16: D(10°)-D(10°)-D(10°)-D(10°)
--	#11: B-D-E-C	#17: D(60°)-D(60°)-D(60°)-D(60°)
--	--	#18: D(90°)-D(90°)-D(90°)-D(90°)

[†1] A-B-C-D denotes that site conditions beneath the 1st to the 4th supports are categories of #A, #B, #C, and #D, respectively.

[†2] C(h_1) denotes the site category #C with depth of soil layer h_1, and D(10°) denotes the site category #D with incident angle of bedrock motions as 10°.

frequencies increase by around 1.0 Hz to 4.8 Hz in the U and V directions for sites #B and #D, respectively. Similar results can also be obtained for ground motions in the W direction. These results indicate that the harder the site, the higher the fundamental frequency of the site, and the smaller the site amplification factor. More importantly, fundamental frequencies in the W direction are higher than those in the V direction for each site, which is due to the fact that the vertical component of ground motion is dominated by the compressive P wave with larger wave velocity, causing site to be more stiff in the vertical direction. However, in practice, site amplification spectra in the vertical direction are directly obtained from those in the horizontal direction by scaling only the amplitude and ignoring the variation of fundamental frequency of local site, which is inappropriate in providing a reasonable site amplification in the vertical direction.

Figure 5.5(b) presents the site amplification results in the V direction of site #D for different incident angles of the bedrock wave motions. It is seen that larger site amplification results can be induced by larger incident angles. Specifically, the site amplification results for 90° incident angle are around 3 times larger than those for 10° incident angle. This

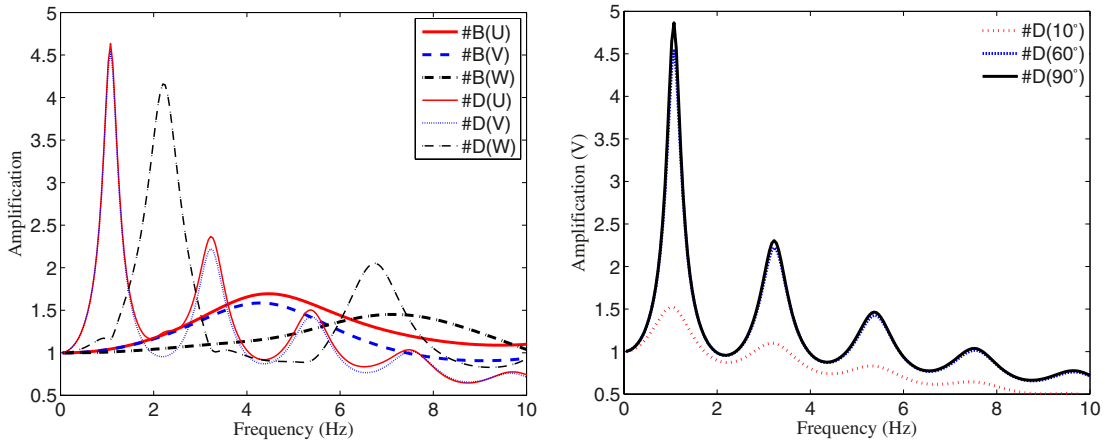

(a) Amplification of different site conditions

(b) Amplification of different incident angles

Figure 5.5 Site amplification results at different site conditions and different incident angles

is the reason why incident angles of bedrock motions are usually assumed to be 90° in the conventional site response analysis from the conservative perspective (Kramer, 1996). In addition, the differences between the site amplifications for different incident angles decrease as the incident angles increase. These observations show that site amplifications are largely dependent on incident angles of bedrock wave motions. In practice, however, it is difficult to know or even measure these incident angles; hence site response results for 90° incident angle are usually adopted in site response analysis. Alternatively, the incident angle can be assumed to be a random variable and the effect of the incident angle in site response analysis can be accounted for by using the Monte-Carlo simulation (Zhang *et al.*, 2012b). However, for brevity and because of the minor differences of site amplifications for 60° and 90° incident angles, the incident angles can be reasonably assumed to be 60° in other cases (besides cases #16 and #18) in Table 5.4.

Figure 5.6 presents the displacements, axial forces, and bending moments of the arch rib under the transverse, vertical, and longitudinal spatial motions at site categories #B, #C, #D, and #E. The response amplification factors $R_{\text{amp}} = R_s/R_0$ at key-sections of the arch rib are listed in each sub-figure (R_s and R_0 are the structural responses with and without considering the site effect, respectively). It can be seen that the site conditions can have a significant effect on the resulting structural responses under the transverse, vertical, and

longitudinal spatial motions, e.g., site #5 amplifies the transverse displacement in the middle of the arch rib by around 10 times as shown in Figure 5.6(a).

In addition, the softer the site conditions, the larger the response amplification factors. These observations can be obtained from the transverse displacements U_Y, axial forces F_X, and bending moments M_Y and M_Z of the arch rib in Figure 5.6(a), (c), (b), and (d), respectively. Because softer sites have lower fundamental frequencies (at which peaks of site amplification factors occur) and these dominant frequencies are close to the natural frequencies of the predominant mode of the CFST bridge, structural responses are amplified much more under the softer site conditions due to the resonant effect. Moreover, structural responses amplified under the vertical multiple excitations are less than those under the transverse and longitudinal motions, because the site amplification factors in the vertical direction (W) are less than those in the horizontal directions (U and V) as shown in Figure 5.5(a).

However, it is noted that softer sites do not always induce larger response amplifications, and this can be seen from Figure 5.6(e) and (f) for axial forces and bending moments of the arch rib under longitudinal multiple excitations. As discussed above, structural response amplifications are dependent on site amplification factors and structural modal properties. For example, the fundamental frequency of site #C in the U direction is around 2.2 Hz, which is close to the 3rd and 4th predominant coupling frequencies of the CFST arch bridge, resulting in the largest structural response at site #C in Figure 5.6(e) and (f). These results indicate that more advanced yet easily applicable methods in modelling of local site effect are desired, because fundamental frequencies of the site can significantly affect the structural response amplifications. The site amplification approach in Section 2.4.1 can provide amplification results under both in-plane and out-of-plane wave motions for multi-layer soil profiles with varying site conditions, and is therefore recommended for seismic analysis of structures accounting for the local site effect. Moreover, the conventional vertical site amplification, which is obtained directly from those in the horizontal directions by scaling only the amplitude and ignoring the variation of fundamental frequencies of local site, can lead to inappropriate response amplifications of structures under vertical excitations.

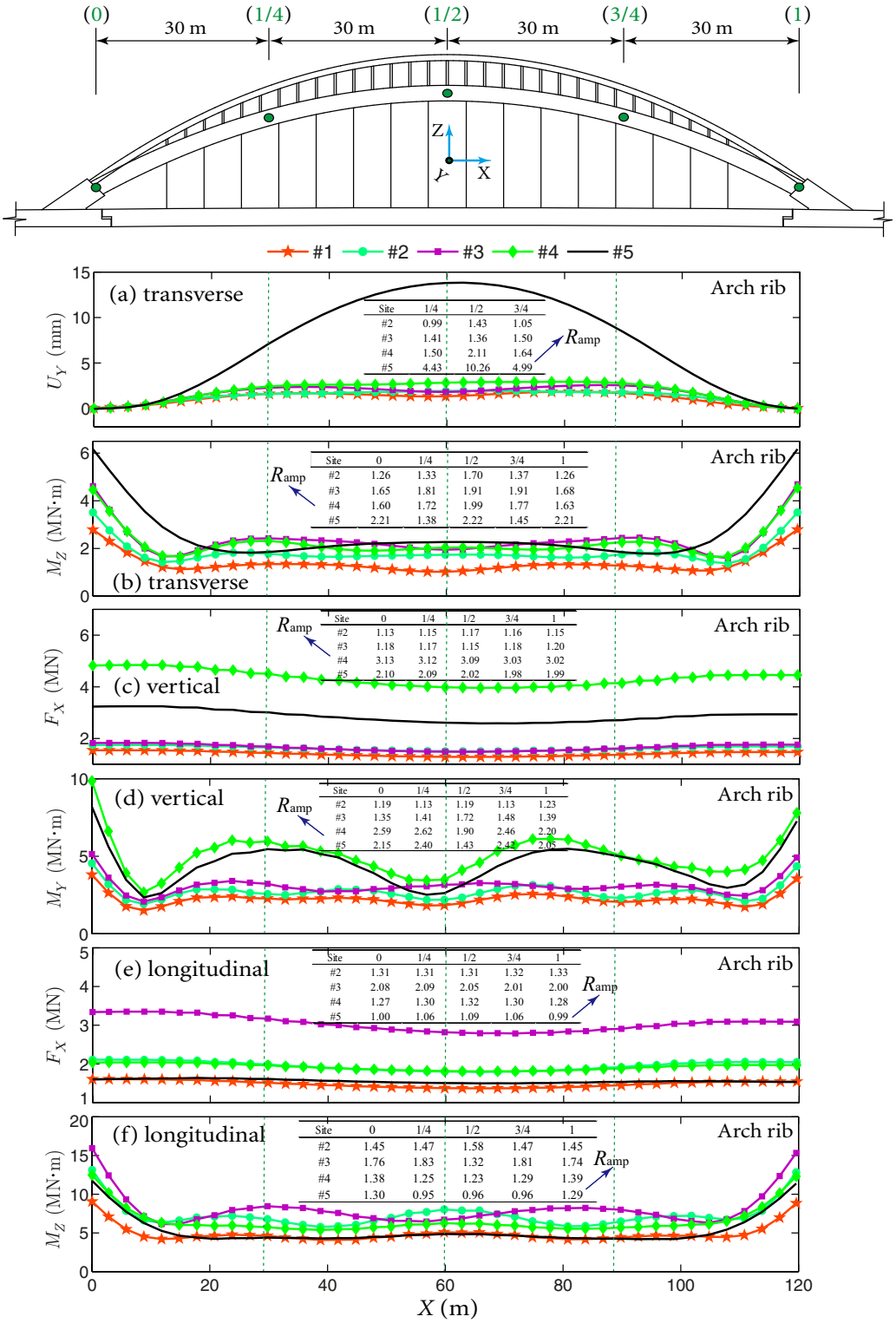

Figure 5.6 Effect of local site conditions

To study the effect of varying site conditions, 6 cases (from #6 to #11 in Table 5.4) are considered with varying site conditions beneath each support. The axial forces of the suspenders and bending moments of the arch rib under transverse multiple excitations are presented in Figure 5.7(a) and (b), respectively. It is observed that the varying site conditions can induce significant variations of structural responses, suggesting that different site conditions beneath each support should be accounted for in the seismic analysis and design of structures extended in large space. Responses of case #11 are significantly different from those of other cases, because the softest site #E is assumed for the 3rd structural support (excitations at the 2nd and 3rd supports have dominant contributions in responses).

Similarly, as seen from Figure 5.7(c) and (d), significant variations of structural responses induced by site irregularities can be observed for cases #12 to #15 in Table 5.4. The irregular site conditions of cases #12 and #13 can introduce the most significant variations of transverse displacements (at middle of the arch rib) and bending moments (at around 1/4 and 3/4 span of the arch rib). This demonstrates that site conditions beneath supports of critical structures with large spans should be characterized in details, to avoid incorrect predictions of structural responses.

Axial forces and bending moments of cases #16, #17, and #18 are shown in Figure 5.7(e) and (f) to illustrate the effect of incident angles of bedrock motions. It is seen that the responses with 10° incident angle exhibit larger variations than those with 60° and 90° incident angles, due to the site amplification factors shown in Figure 5.5(b). Response forces and bending moments of the arch rib with 60° and 90° incident angles are approximately the same, showing that the assumption of the 60° incident angle of bedrock motions is conservative and reasonable.

5.2.3.3 Effect of Dimensionality of Multiple Seismic Motions

A total of 10 cases, cases #1 to #5 without the site effect and cases #6 to #10 with site category #D as listed in Table 5.5, are considered to study the effect of dimensionality of multiple seismic motions on structural responses. Assuming that amplitudes of the power spectral density (PSD) inputs in the vertical (V) direction are 2/3 of those in the

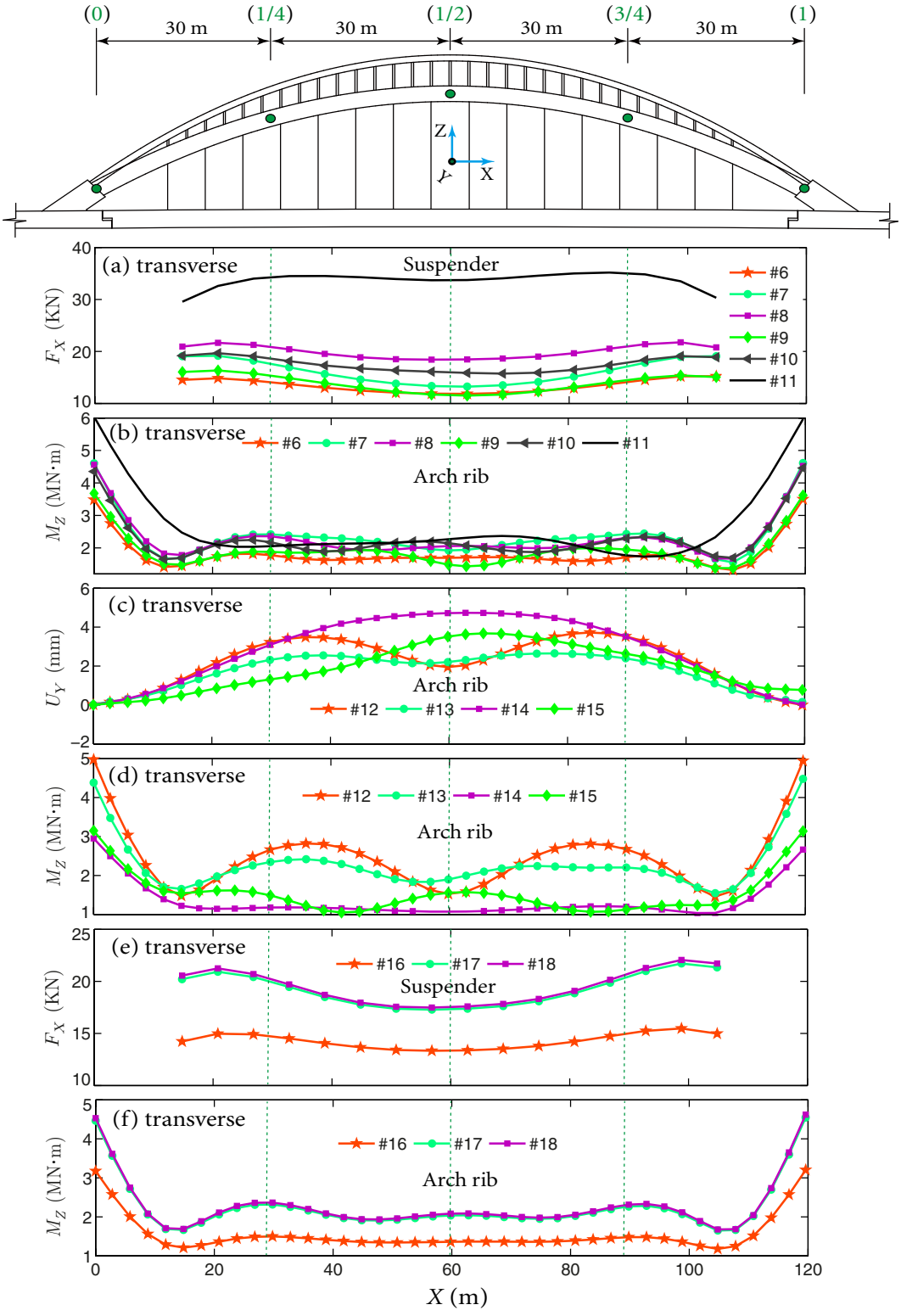

Figure 5.7 Effect of varying site conditions and site irregularities

horizontal directions H_1 (longitudinal) and H_2 (transverse), the displacements, axial forces, and bending moments of the arch rib are presented in Figure 5.8.

Table 5.5: Effect of dimensionality of multiple earthquake motions

Case number	Without the site effect	Case number	With the site effect
#1	H_1 (A-A-A-A)	#6	H_1 (D-D-D-D)
#2	H_2 (A-A-A-A)	#7	H_2 (D-D-D-D)
#3	V (A-A-A-A)	#8	V (D-D-D-D)
#4	H_1+H_2 (A-A-A-A)	#9	H_1+H_2 (D-D-D-D)
#5	H_1+H_2+V(A-A-A-A)[†1]	#10	H_1+H_2+V (D-D-D-D)

[†1] H_1, H_2, and V denote the longitudinal, transverse, and vertical directions, respectively.

It is seen from Figure 5.8 that large variabilities of responses exist between cases #5 and #10 (under tridirectional excitations) and cases #1 to #4, #6 to #9 (under unidirectional or bidirectional excitations), showing that neglecting the tridirectional excitations would lead to significantly inaccurate predictions of structural responses. Specifically, as shown in Figure 5.8(b), (c), (e), and (f), the tridirectional motions (cases #5 and #10) can induce the largest axial forces and bending moments of the arch rib with and without the site effect. This suggests that structural responses can be underestimated if the tridirectional motions are not considered, causing the resulting responses unconservative in the seismic evaluations and design.

More importantly, by comparing the responses in cases #4 and #9 (H_1+H_2) and cases #5 and #10 (H_1+H_2+V) in Figure 5.8, it is observed that results between these two cases exhibit significant differences, suggesting that the vertical ground motions should be included in cases #4 and #9 to avoid the erroneous response predictions. Conventionally, only the longitudinal and transverse directions are concerned in the seismic analysis of arch bridge under multidimensional earthquake loadings; however, as observed in Figure 5.8, the vertical components of seismic motions should be included in the seismic evaluations and design of arch bridges under multidimensional excitations.

It should be noted that the longitudinal excitations can result in larger responses than the transverse motions can, while the transverse excitations have a negligible effect on F_X

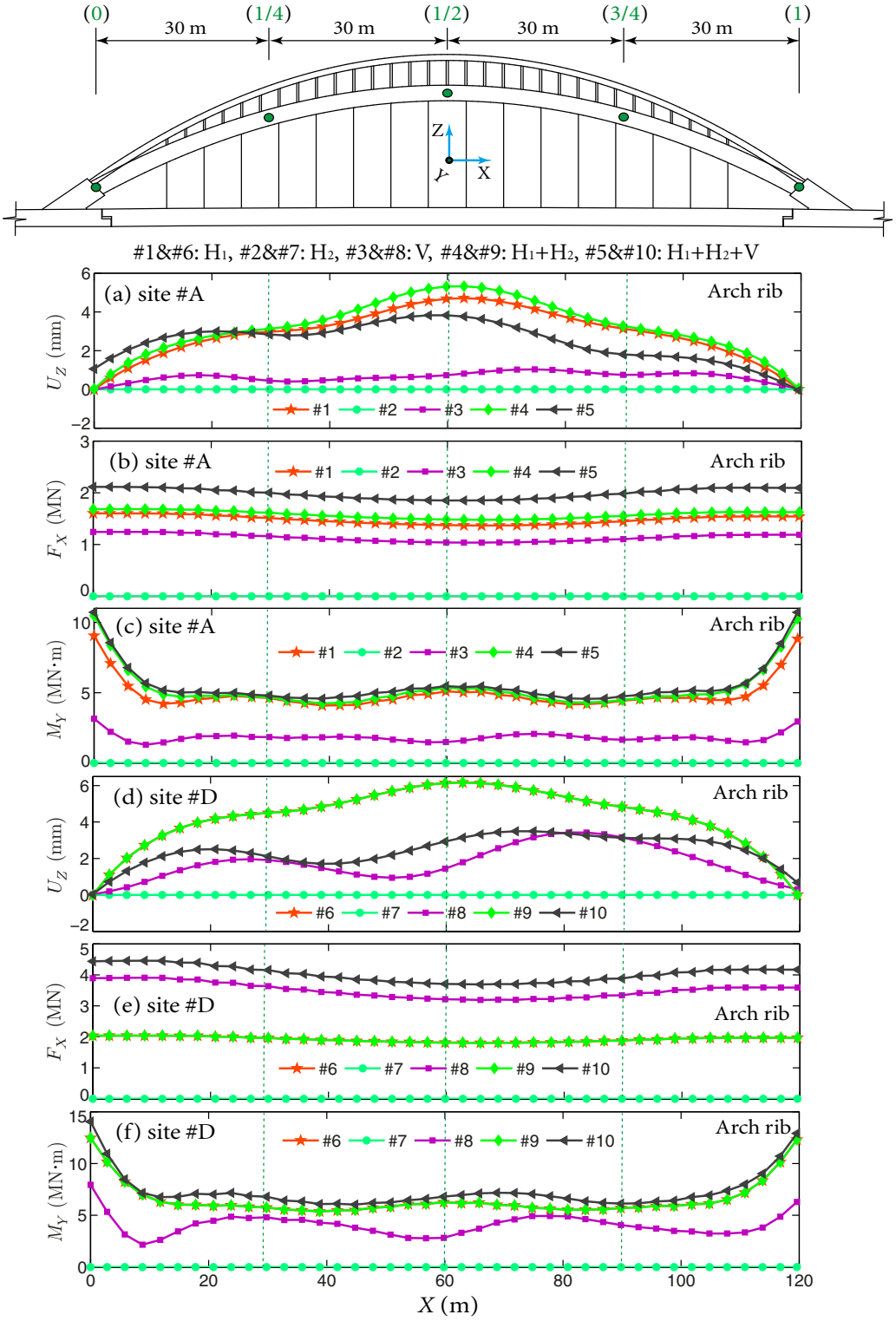

Figure 5.8 Effect of dimensionality of multiple earthquake motions

and M_Y; this is because the spatially varying longitudinal wave motions can excite the 3rd coupled mode (coupling between the longitudinal and vertical deformations).

5.3 Example II: A Long Span High-pier Railway Bridge

5.3.1 Structural Systems

To study local site effects on high-pier railway bridges under tridirectional nonstationary spatial motions, a large-span high-pier continuous rigid frame bridge, which is under construction in the western Guizhou province of China, is considered. The railway bridge consists of the left bridge system (LBS) and the right bridge system (RBS) and has a total span of 466 m. The left bridge segment is a prestressed-concrete continuous rigid frame system with layout of 88 m+168 m+88 m , while the right segment is a prestressed-concrete continuous beam system with layout of 33 m+56 m+33 m. This bridge is situated on a V-shape gully zone with the river-bed length around 15∼25 m and the water depth less than 1.0 m.

Piers of the railway bridge are numbered from Piers #1 to #5. The highest pier, i.e., Pier #2, has height of 103 m. Pier #1 and Pier #2 have the variable hollow rectangular cross-sections, while the other three piers have variable hollow oval cross-sections. These configurations are presented in details in Figure 5.9.

A 3-D FEA model of the high-pier railway bridge is built using a general FEA platform ANSYS (Kohnke, 2010). The beam189 element is used to model main girders and piers. The mass21 element is adopted to simulate the large masses that are attached to structural supports in the large mass method. The fixed boundary conditions apply to the bottom of Piers #1 to #5. The vertical DoF (Z), transverse DoF (Y), and the rotational DoF with respect to Z (Rotz) and X (Rotx) directions are fixed in both the north and south abutments of the railway bridge. All DoF of Pier #1, Pier #2, and Pier #4 (the DoF in the connection point of the piers and main girders) are coupled with the corresponding DoF of the main girders, while the longitudinal DoF (X) in the connection points of Pier #3, Pier #5, and the main girders are released. The 3-D FEA model of the high-pier railway bridge in ANSYS is shown in Figure 5.10(a).

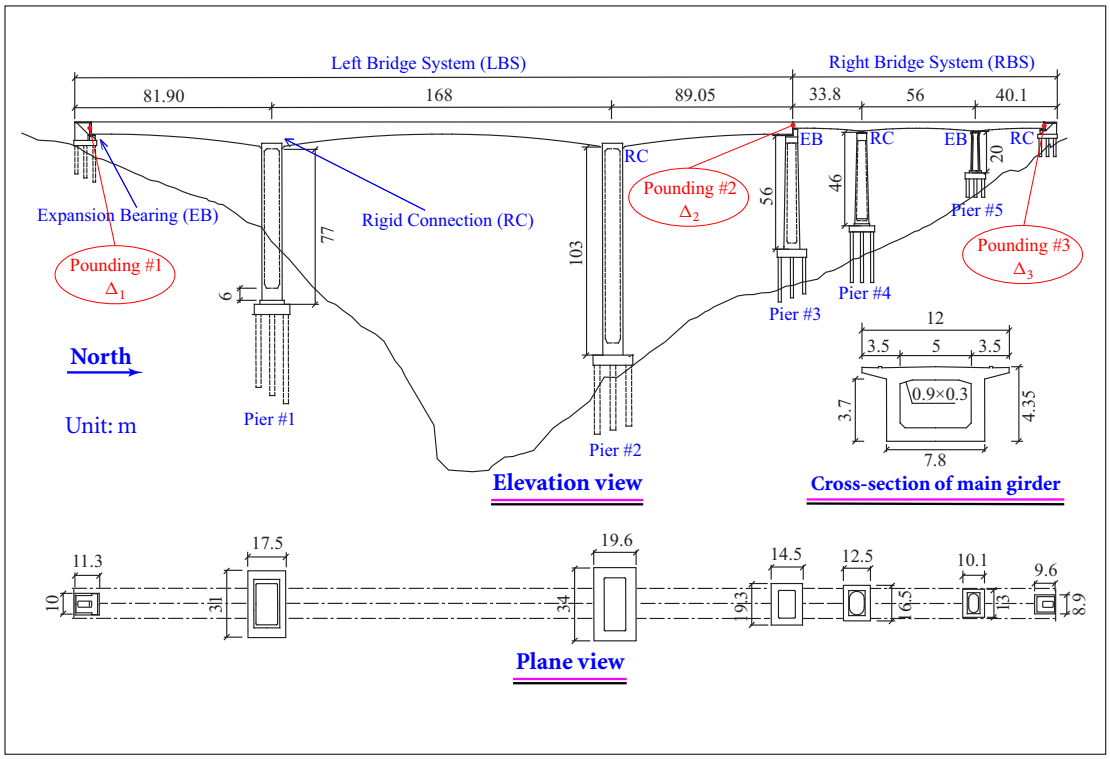

Figure 5.9 Schematic view of the high-pier railway bridge (Jia *et al.*, 2013)

Using the FEA model, modal analysis is conducted using the block-Lanczos method (Kohnke, 2010). The first nine natural frequencies and their respective mode shapes are presented in Figure 5.10(b), where it is seen that most of these modes have dominant transverse deflections because of the smaller stiffness in the transverse direction.

5.3.2 Ground Motion Input

The Clough-Penzien spectrum is used as the auto-PSD functions, which is given by

$$S_g(\omega) = \frac{1+4\zeta_g^2(\omega/\omega_g)^2}{\left[1-(\omega/\omega_g)^2\right]^2+4\zeta_g^2(\omega/\omega_g)^2}\frac{(\omega/\omega_f)^4}{\left[1-(\omega/\omega_f)^2\right]^2+4\zeta_f^2(\omega/\omega_f)^2}S^*, \tag{5.3.1}$$

where S^* is the constant spectral density of the white-noise input, ω_g and ζ_g are the filter parameters of the well-known Kanai-Tajimi model representing, respectively, the natural frequency and damping of the soil layer, and ω_f and ζ_f are the parameters of a second filter

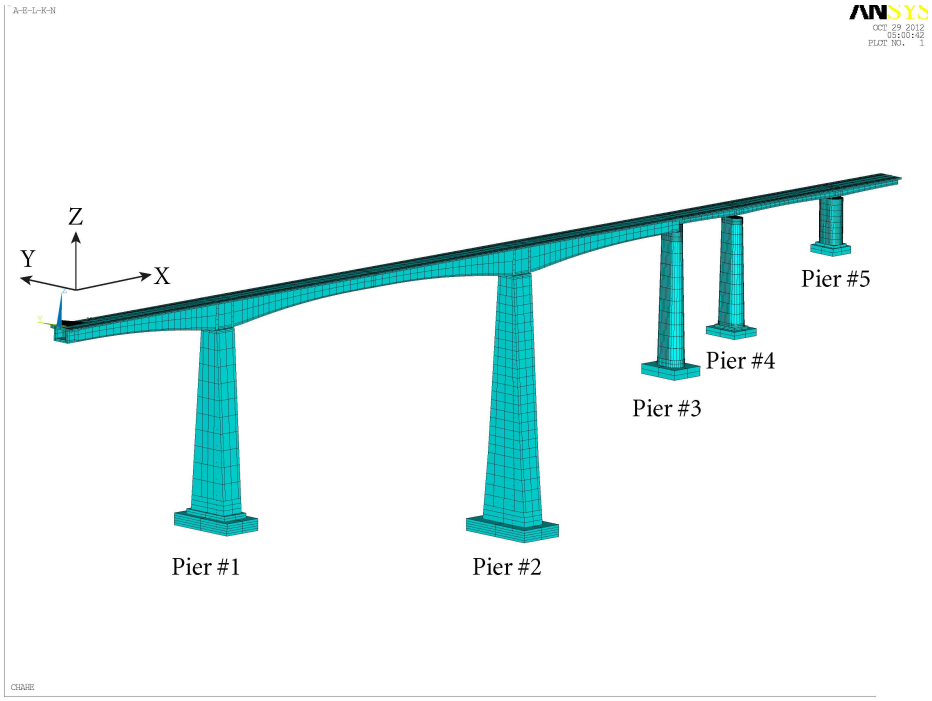

(a) FEA model of the high-pier railway bridge in ANSYS

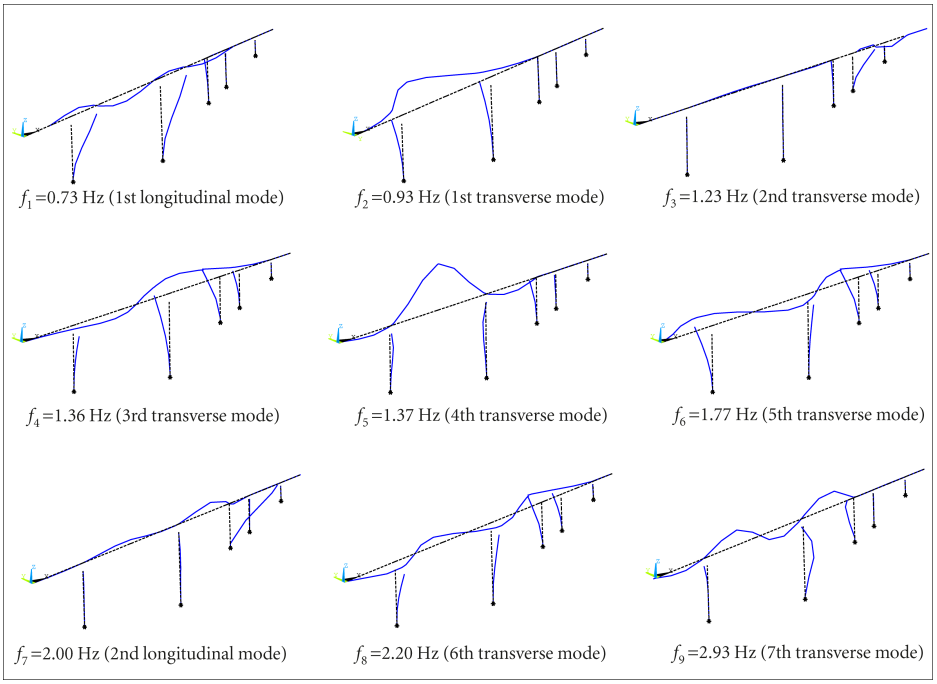

(b) Modal frequencies and mode shapes

Figure 5.10 FEA model and mode parameters of the high-pier railway bridge

that is introduced to assure a finite power for the ground displacement. The proportion of PSD amplitudes of the tridirectional ground motions in x, y, and z directions is assumed to be 1:0.72:0.42 (MCPRC, 2008; NCC, 2010). The local site effect is considered in the input ground PSD model for the firm (F), medium (M), and soft (S) site conditions using the physical parameters given in Table 5.6.

Table 5.6: Parameters of PSD functions of different soil types (Der Kiureghian and Neuenhofer, 1992; Dumanoglu and Soyluk, 2003)

Soil types	ω_g (rad/s)	ζ_g	ω_f (rad/s)	ζ_f	S^* (m^2/s^3)
Firm (F)	15.0	0.6	1.5	0.6	0.00177
Medium (M)	10.0	0.4	1.0	0.6	0.00263
Soft (S)	5.0	0.2	0.5	0.6	0.00369

The ground motion coherence model by Lin *et al.* (2004b), $\left|\gamma(d_{ij},f)\right| = \exp\left[-a(\omega)d_{ij}^{b(\omega)}\right]$ is used, in which $a(\omega)=a_1\omega^2+a_2, b(\omega)=b_1\omega^2+b_2, a_1=0.00001678, a_2=0.001219, b_1=-0.0055$, and $b_2=0.7674$.

Earthquake ground motions are nonstationary, because they initially grow from zero, then have a steady phase, and eventually decay to zero. Therefore, nonstationarity of earthquake ground motions should be considered. The uniformly modulated function $G(t)$ is widely used and is adopted to model the nonstationarity of ground motions (Jennings *et al.*, 1968)

$$G(t)=\begin{cases}\left(t/t_1\right)^2, & 0\leqslant t\leqslant t_1,\\ 1, & t_1\leqslant t\leqslant t_2,\\ \mathrm{e}^{-c(t-t_2)}, & t\geqslant t_2,\end{cases} \tag{5.3.2}$$

where t_1, t_2, and c are shape-control parameters of the time modulating function, which are given as $t_1=7.1$ sec, $t_2=19.5$ sec, and $c=0.16$. The duration of ground motions is assumed to be 25 sec. For simplicity, the modulating functions at x, y, and z directions are assumed to be the same.

Table 5.7: Analysis cases under different sites (F-firm site, M-medium site, S-soft site)

Group	Case	P #1	P #2	P #3	P #4	P #5
	#1	F	F	F	F	F
	#5	F	M	F	F	F
#A	#6	F	S	F	F	F
	#8	F	F	F	F	M
	#9	F	F	F	F	S
	#2	M	M	M	M	M
	#4	M	F	M	M	M
#B	#7	M	M	M	M	F
	#10	M	M	M	M	S
	#15	M	S	M	M	M
	#3	S	S	S	S	S
	#11	S	S	S	S	F
#C	#12	S	S	S	S	M
	#13	S	F	S	S	S
	#14	S	M	S	S	S

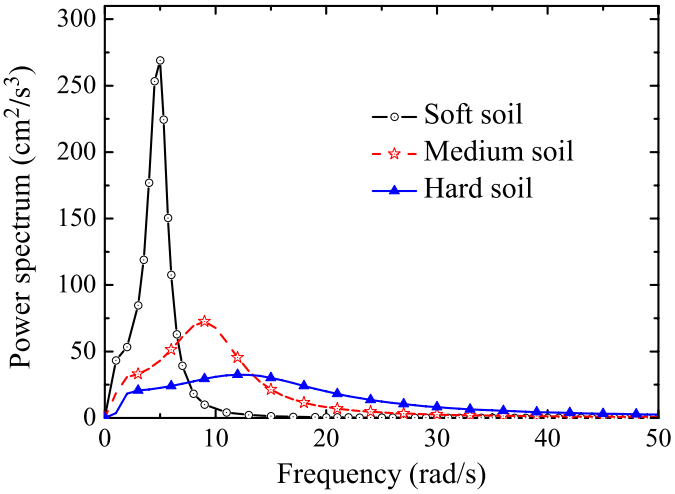

Figure 5.11 PSD of different site conditions

5.3.3 Analysis Cases under Different Site Conditions

As seen in Figure 5.9, dimensions of piers of the high-pier railway bridge vary significantly, e.g., the height difference between the highest pier (Pier #2) and the shortest pier (Pier #5) is around 50m. In addition, since the highest pier plays a significant role on seismic responses of the railway bridge, local site conditions beneath Piers #2 and #5 are varied and are studied primarily for the local site effects on structural seismic response.

The analysis cases are presented in Table 5.7 for various combinations of site categories (including firm (F), medium (M), and soft (S) sites) under Pier #1 to Pier #5. As discussed in Section 5.3.2, local site effect is reflected in the input PSD functions; the PSD functions corresponding to the three site conditions are shown in Figure 5.11 using site parameters given in Table 5.6. It is noteworthy that the shape parameters ω_g, ζ_g, ω_f, ζ_f used in Table 5.6 for each site condition are developed by Der Kiureghian and Neuenhofer (1992), while the corresponding amplitude parameters S^* used in Table 5.6 are determined by Dumanoglu and Soyluk (2003) by equating the variance of the input Clough-Penzien spectrum to the variance of the East-West components of Erzincan earthquake accelerations in 1992.

Cases #1, #2, and #3 are uniform site conditions for all five piers under site categories F, M, and S, respectively, based on which a total of 15 cases are considered and categorized into

three groups, i.e., Groups #A, #B, and #C. Group #A (cases #1, #5, #6, #8, and #9) is to study the local site effect induced by varying site conditions under the highest Pier #2 and the shortest Pier #5 when the other three piers are in the F site conditions. Similarly, Group #B (cases #2, #4, #7, #10, and #15) and Group #C (cases #3, #11, #12, #13, and #14) are to study the effect of varying site conditions under Pier #2 and Pier #5 when Piers #1, #3, and #4 are in M and S site conditions, respectively. If the specific site condition beneath every pier is known in practice, the local site effects can be directly accounted in the seismic analysis, otherwise the worst response scenario of site conditions in Table 5.7 can be considered as the local site conditions of the high-pier railway bridge in the seismic analysis and design.

In seismic response analysis of the high-pier railway bridge under SVGM, the local site effect is primarily investigated and the wave-passage effect is ignored, because there are extensive previous investigations for the wave-passage effect on structural seismic response but very few works for the local site effect. Similarly, only completely incoherent spatial motions are considered as the input SVGM, since they can cause the worst structural response among the fully coherent, partially coherent, and completely incoherent spatial seismic motions.

5.3.4 Nonstationary Stochastic Seismic Response Analysis: Results and Discussions

The nonstationary stochastic seismic analysis is conducted for the high-pier railway bridge under tridirectional SVGM considering the local site effect. In the analysis, the circular frequency is bounded as $\omega \in [0.1, 50]$ rad/s with the frequency resolution as $\Delta\omega = 0.05$ rad/s. The damping ratios of all the modes of interest are assumed to be 0.05.

5.3.4.1 Effect of Uniform Local Site Conditions

For local site effects on structural response, the uniform site conditions, i.e., the soft site S, medium site M, and firm site F, are considered under all piers of the railway bridge in case #3, #2, and #1 of Table 5.7, respectively. For brevity, structural responses, such as shear forces F_X and F_Y and bending moments M_X and M_Y, at the bottom of Pier #2 only are reported because of the dominant role of Pier #2 in the bridge seismic responses. The 3-D

response PSD functions under site F, M, and S are presented in Figures 5.12, 5.13, and 5.14, respectively.

As expected, PSD functions of structural responses exhibit time and frequency non-stationary characteristics. Moreover, as seen in Figure 5.12(a) and (c), the predominant response frequencies of F_X and M_X are bounded between 0.60 to 0.80 Hz, meaning that the first mode (0.73 Hz, shown in Figure 5.10(b)) has been excited to be the dominant mode on the responses of F_X and M_X. Similarly, responses of F_Y and M_Y, with predominant frequencies of 0.60∼0.80 and 1.35 Hz, are dominated by the first, third, and fourth modes of the railway bridge (0.73 Hz, 1.23Hz, and 1.36Hz, shown in Figure 5.10(b)).

As observed in Figures 5.12(b), 5.13(b), and 5.14(b) for structural response M_Y, the response PSD function at S site is different from those at M and F sites with more predominant frequencies and larger site amplification results, because of the narrow frequency band of the soft site and the resonance between the soft site and the railway bridge. Similar conclusions can also be drawn for PSD of response F_Y in Figures 5.12(d), 5.13(d), and 5.14(d).

A more important observation is that the softer the uniform site conditions the larger the structural response results. Specifically, the ratios between the peaks of PSD at S, M, and F site conditions are 1.00:0.74:0.62 for M_X, 1.00:0.50:0.45 for M_Y, 1.00:0.53:0.49 for F_X, and 1.00:0.72:0.61 for F_Y, respectively.

5.3.4.2 Effect of Non-uniform Local Site Conditions

Besides the effect of uniform local site conditions on structural seismic responses, the effect of the non-uniform (varying) site conditions is studied. The time-dependent response mean square deviation $\sigma(t)$ is derived based on the obtained nonstationary PSD function of response $S(\omega, t)$ by

$$\sigma(t) = \sqrt{2\int_0^\infty S(\omega, t)\mathrm{d}\omega}. \tag{5.3.3}$$

Responses of Group #A (#1, #5, #6, #8, #9) are presented in Figure 5.15. They include the longitudinal (X) displacement of main girder in the left bridge system D_X, shear forces F_X and F_Y at the bottom of Pier #2, axial force F_N at the bottom of Pier #2, bending moments

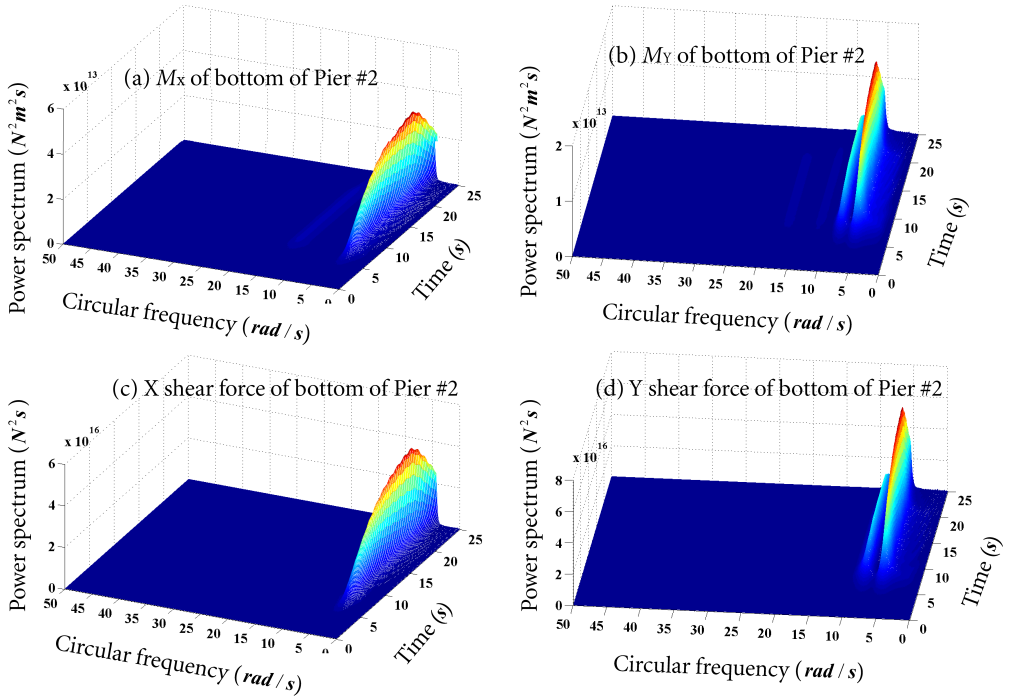

Figure 5.12 PSD functions of nonstationary structural responses under site #1: F-F-F-F-F

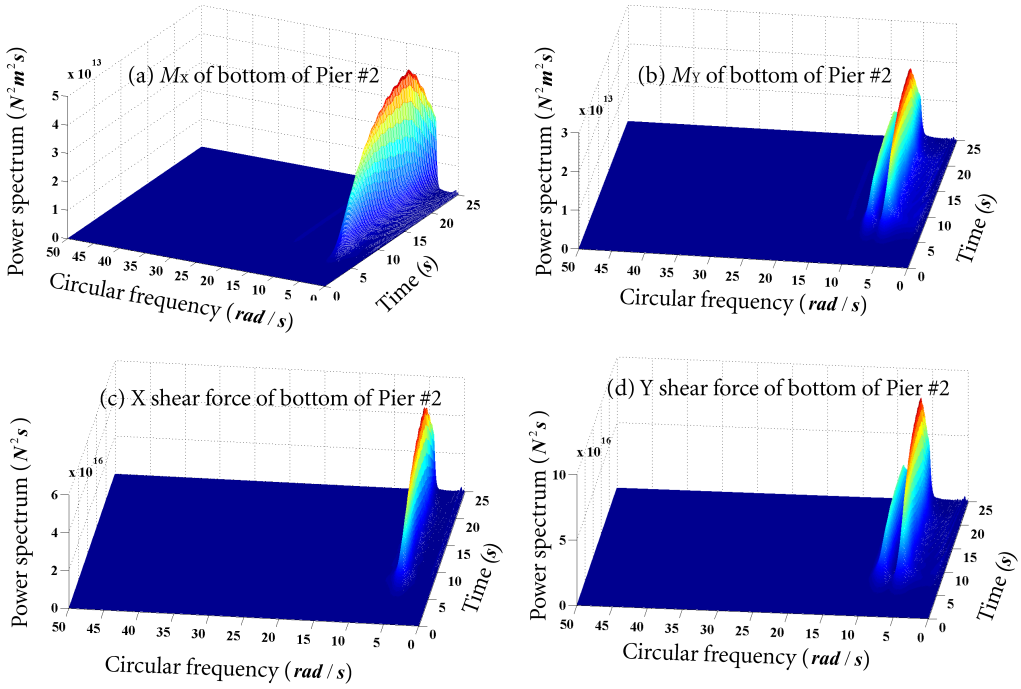

Figure 5.13 PSD functions of nonstationary structural responses under site #2: M-M-M-M-M

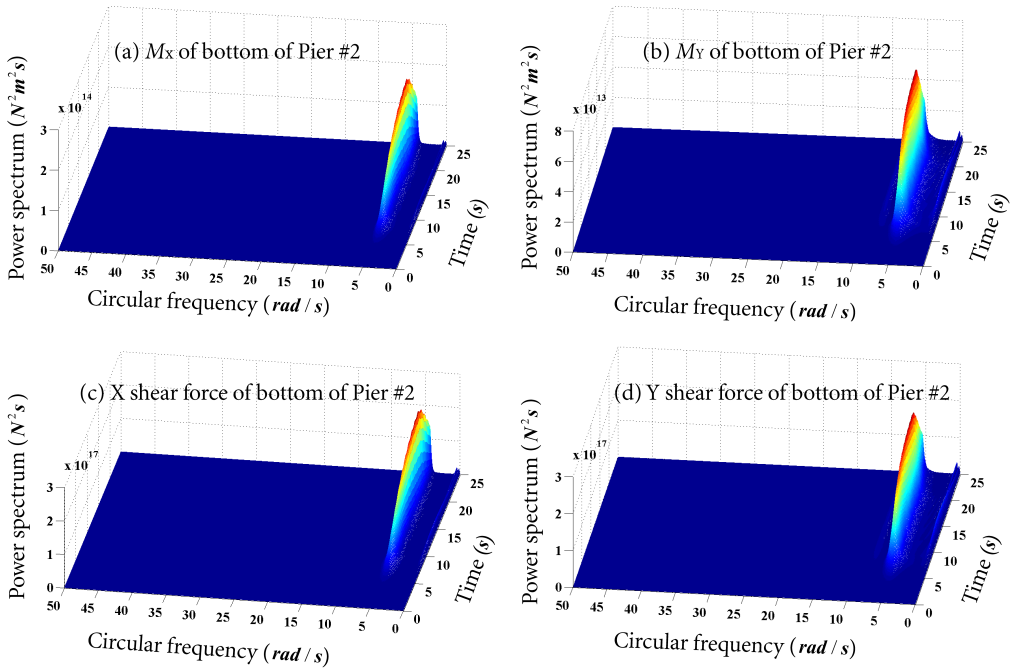

Figure 5.14 PSD functions of nonstationary structural responses under site #3: S-S-S-S-S

M_X and M_Y at the bottom of Pier #2, and bending moments $M_{L,Y}$ and $M_{R,Y}$ on the left and right side of the main girder supported by Pier #2. It is seen in Figure 5.15 that effects of the varying site conditions are very significant in the time-dependent nonstationary structural seismic responses.

Specifically, case #6 (F-S-F-F-F) can result in the largest structural response and case #5 (F-M-F-F-F) can lead to the second largest structural response among all the cases in Group #A. This indicates that the larger site difference between Pier #2 and the other piers the larger the structural seismic responses obtained, which confirms the fact that the highest Pier #2 plays a dominant role on the seismic response of the railway bridge. In addition, site variations under Pier #5 play a negligible effect on structural responses, i.e., all seismic responses of case #1 (F-F-F-F-F), case #8 (F-F-F-F-M), and case #9 (F-F-F-F-S) are overlapped over the entire duration of ground motion, because the longitudinal (X) constraint between Pier #5 and the main girder of the right bridge system has been released to avoid shear failure of Pier #5.

The ratios between peak responses of case #6 and peaks of the other three overlapped cases #1, #8, and #9 are 5.57, 3.50, 1.76, 3.60, 2.12, 4.96, 3.00, and 15.38, respectively, for D_X, F_X, F_Y, F_N, M_X, M_Y, $M_{L,Y}$, and $M_{R,Y}$ in Figure 5.15, which indicate that the varying site conditions can significantly affect structural seismic response in comparison with the uniform site conditions. It is also concluded that structural seismic response may be largely underestimated if effect of varying site conditions is not considered, especially the variation of local site conditions beneath the highest pier. Therefore, it is of primary importance to account for the varying site effect in seismic evaluations of high-pier railway bridge under tridirectional nonstationary spatial ground motions.

Similar to Group #A, Figure 5.16 presents D_X, F_X, F_Y, F_N, M_X, M_Y, $M_{L,Y}$, and $M_{R,Y}$, for Group #B (#2, #4, #7, #10, #15). The largest responses are resulted in case #15 (M-S-M-M-M) due to the largest site difference between Pier #2 and the other piers. The ratios between peak responses of case #15 and peaks of the other three overlapped cases #2, #7, and #10 are 4.44, 3.64, 1.58, 2.47, 1.50, 4.04, 2.01, and 14.16 for D_X, F_X, F_Y, F_N, M_X, M_Y, $M_{L,Y}$, and $M_{R,Y}$ in Figure 5.16, respectively. It again reveals that the varying site conditions can significantly affect structural seismic response in comparison with the uniform site conditions, and it is essential to account for the varying site effect in structural seismic analysis. Similar conclusions can also be drawn for response mean square deviation functions presented in Figure 5.17 for Group #C (#3, #11, #12, #13, #14), where the ratios between peak responses of case #13 and peaks of the other three overlapped cases #3, #11, and #12 are 2.16, 1.69, 1.21, 3.42, 1.40, 1.90, 1.76, and 10.00 for D_X, F_X, F_Y, F_N, M_X, M_Y, $M_{L,Y}$, and $M_{R,Y}$ in Figure 5.17, respectively.

More importantly, ratios between the peaks (between case #6 and the three overlapped cases #1, #8, and #9 in Group #A, between case #15 and the three overlapped cases #2, #7, and #10 in Group #B, and between case #13 and the three overlapped cases #3, #11, and #12 in Group #C) of a specific structural response, e.g., D_X, decrease from site Group #A to Group #C. Specifically, the ratios for each structural response are listed as

1. from 5.57, 4.44, to 2.16 for D_X shown in Figures 5.15(a), 5.16(a), and 5.17(a);
2. from 3.50, 3.64, to 1.69 for F_X shown in Figures 5.15(b), 5.16(b), and 5.17(b);
3. from 1.76, 1.58, to 1.21 for F_Y shown in Figures 5.15(c), 5.16(c), and 5.17(c);

4. from 3.60, 2.47, to 3.42 for F_N shown in Figures 5.15(d), 5.16(d), and 5.17(d);
5. from 2.12, 1.50, to 1.40 for M_X shown in Figures 5.15(e), 5.16(e), and 5.17(e);
6. from 4.96, 4.04, to 1.90 for M_Y shown in Figures 5.15(f), 5.16(f), and 5.17(f);
7. from 3.00, 2.01, to 1.76 for $M_{L,Y}$ shown in Figures 5.15(g), 5.16(g), and 5.17(g);
8. from 15.38, 14.16, 10.00 for $M_{R,Y}$ shown in Figures 5.15(h), 5.16(h), and 5.17(h).

These observations again indicate the fact that the softer the local site conditions beneath the highest pier the larger the structural response results. Hence, two important and effective measures can be taken at the design stage to prevent or mitigate structural failures of high-pier railway bridges induced by site amplification:

- to avoid soft site beneath the highest pier,
- to avoid large difference of site conditions between the highest pier and the other piers.

Comparing cases #6 (F-S-F-F-F), #15 (M-S-M-M-M), and #13 (S-F-S-S-S) that induce the largest structural responses in Groups #A, #B, and #C, case #6 results in the largest structural responses among these three cases, although site differences between Pier #2 and other piers are the same in cases #6 and #13. It is because the resonance between local site condition of Pier #2 and the railway bridge is more significant in case #6 than in case #13; it again indicates that avoiding soft site conditions under the highest pier and large site differences between the highest pier and other piers are effective to prevent or mitigate seismic failures of high-pier railway bridges caused by local site amplification.

5.3.4.3 Effect of Ground Motion Nonstationarity

It is well known that recorded ground motions exhibit intrinsic nonstationary characteristics in both time and frequency domains, and inclusion of ground motion nonstationarity in SVA of structures is appropriate. It is seen from Figures 5.12 to 5.14 that PSD functions of structural responses exhibit nonstationary time and frequency dependent characteristics in the 3-D time frequency plot. In addition, similar to the piecewise modulating function, the response mean square deviation functions also show nonstationary characteristics that can be divided into three segments, i.e., the rising part, the plateau, and the decaying part, as shown in Figures 5.15 to 5.17.

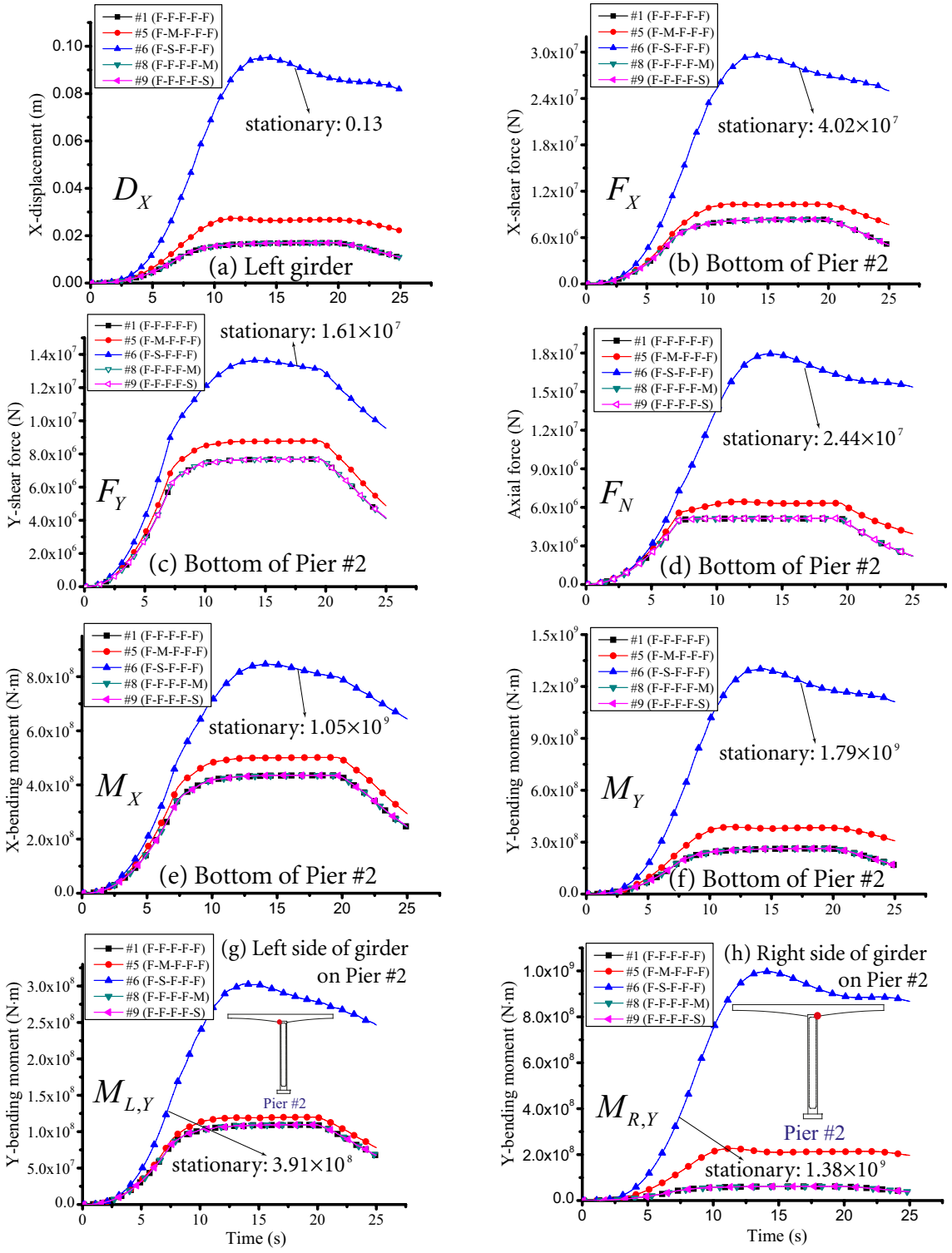

Figure 5.15 Nonstationary seismic responses at key positions of the bridge under site group #A

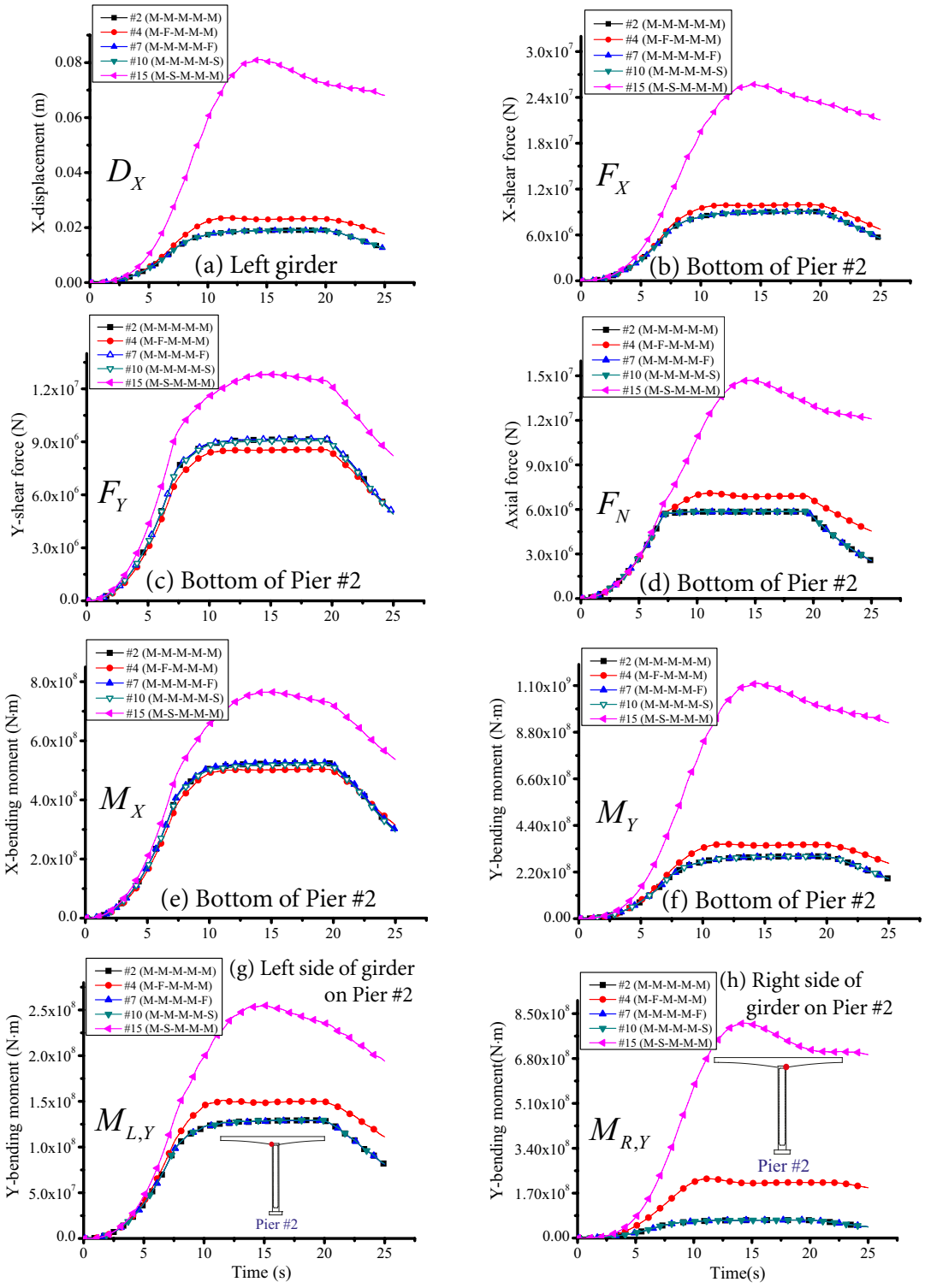

Figure 5.16 Nonstationary seismic responses at key positions of the bridge under site group #B

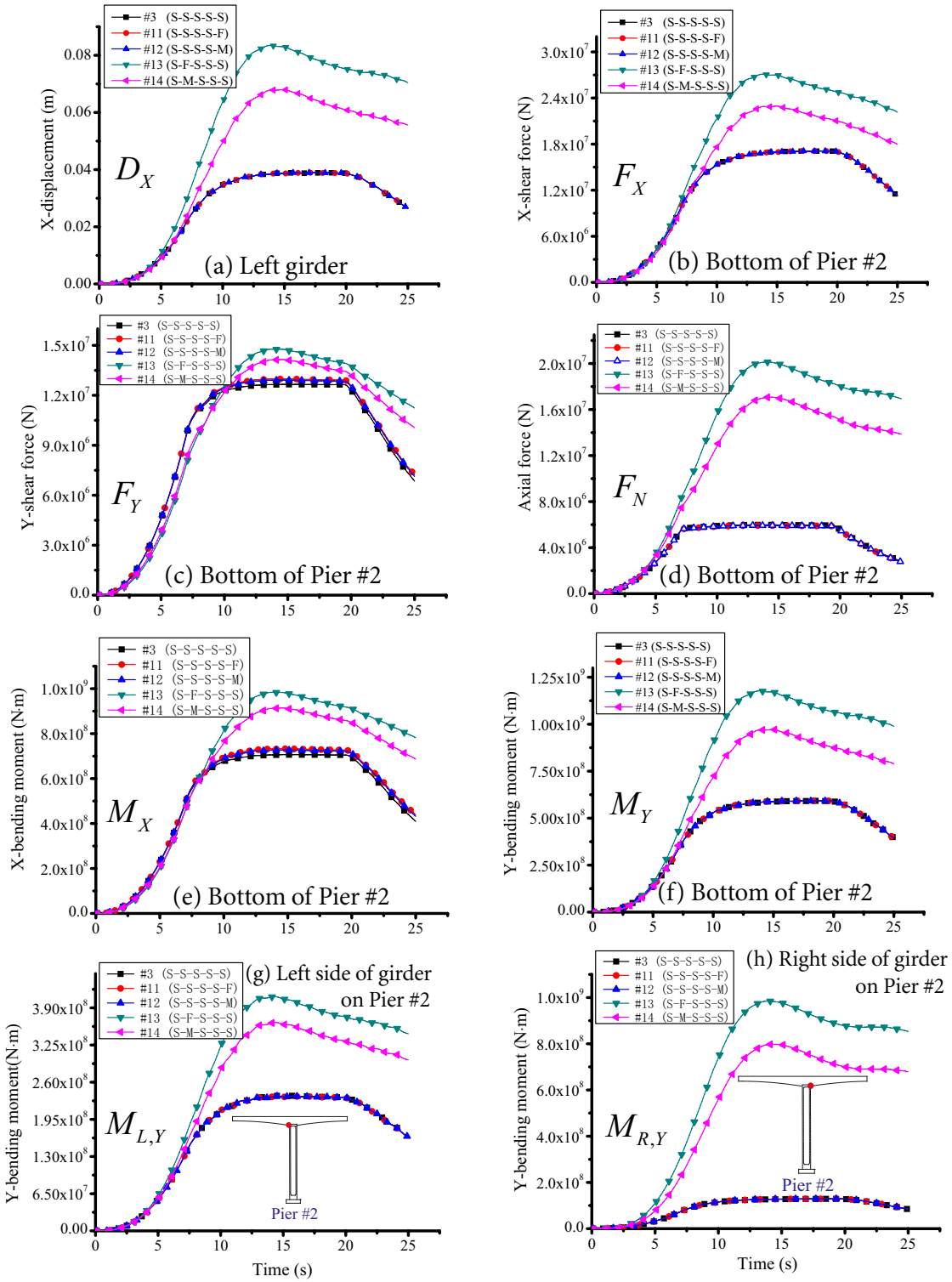

Figure 5.17 Nonstationary seismic responses at key positions of the bridge under site group #B

To explore the effect of ground motion nonstationarity on structural seismic response, stationary SVA is conducted in case #6 (F-S-F-F-F) of Group #A for comparison with nonstationary response results, shown in Figure 5.15. The ratios between the stationary responses and peaks of nonstationary responses for D_X, F_X, F_Y, F_N, M_X, M_Y, $M_{L,Y}$, and $M_{R,Y}$ are 1.32, 1.34, 1.17, 1.36, 1.28, 1.32, 1.30, and 1.36, shown in Figure 5.15, respectively (stationary response results are $D_X = 0.13$ m, $F_X = 4.02 \times 10^7$ N, $F_Y = 1.61 \times 10^7$ N, $F_N = 2.44 \times 10^7$ N, $M_X = 1.05 \times 10^9$ N·m, $M_Y = 1.79 \times 10^9$ N·m, $M_{L,Y} = 3.91 \times 10^8$ N·m, and $M_{R,Y} = 1.38 \times 10^9$ N·m).

As seen, structural seismic responses can be overestimated by 20% to 30% if ground motion nonstationarity is not taken into account. Hence, ground motion nonstationarity should be considered in structural SVA to represent more accurate and appropriate seismic design loads, although conventional stationary stochastic seismic analysis can lead to conservative design results.

It is noteworthy that this chapter is devoted to study effects of ground motion spatial variations on structural responses, and comparison of the seismically induced loads to structure members capacities (from structure design point) is ignored in this study.

5.4 Summary and Conclusions

From the parametric studies of the CFST arch bridge and the high-pier railway bridge under SVGM, conclusions are drawn below.

The Long Span Arch Bridge

1. The conventionally used uniform input motions by neglecting both the phase shifts and the coherency losses might greatly underestimate or overestimate the responses. The wave-passage effect is more significant than the effect of coherence loss on structural responses, and the wave-passage effect becomes more significant for structures with larger spans.
2. Variabilities of transverse and vertical ground motions can decrease responses of the half-through CFST arch bridge, while spatially correlated longitudinal excitations can increase structural responses. Hence, the uniform vertical and transverse input ground

motions and multiple longitudinal excitations are recommended in the actual seismic design of half-through CFST arch bridge to ensure structural seismic safety.

3. The site effect must be included in seismic analysis of structures under multiple excitations because it significantly affects structural responses under the transverse, vertical, and longitudinal spatial motions. Softer site conditions can cause larger structural responses. Furthermore, the varying and irregular site conditions can induce significant variations of structural responses, and they should be accounted for in seismic design to avoid erroneous response predictions.

4. The tridirectional motions must be used in seismic evaluations and design, because structural responses can be underestimated if the tridirectional motions are not considered. Moreover, the vertical ground motions should be included in the conventional seismic evaluations and design of arch bridges under multidimensional excitations.

The Long Span High-pier Railway Bridge

1. Ground motion nonstationarity should be considered in stochastic seismic analysis of structures to represent more accurate and appropriate seismic design loads, although conventional stationary analysis can lead to conservative design results. Structural seismic responses can be overestimated by 20% to 30% if ground motion nonstationarity is not taken into account.

2. Under uniform site conditions, softer site can induce larger structural responses. Spatially non-uniform sites can induce more significant structural responses than the uniform sites.

3. The spatially varying site conditions, especially site variations under the highest pier, should be considered in seismic analysis and design of high-pier railway bridge structures; otherwise, structural seismic responses could be significantly underestimated.

4. Site conditions beneath the highest pier and site difference between the highest pier and other piers play a dominant role in the seismic responses of high-pier railway bridges. The larger the site difference between the highest pier and other piers, the larger the structural seismic response results.

5. Two important and effective ways can be adopted at the design stage to prevent or mitigate seismic failures of the high-pier railway bridge caused by site amplification:

   - to avoid soft sites beneath the highest pier,
   - to avoid large site difference between the highest pier and other piers.

6. Detailed inspections of geological conditions and appropriate design of site conditions beneath the high-piers are recommended to effectively reduce the site induced earthquake damages to the high-pier railway bridges.

C H A P T E R 6

Stochastic Seismic Analysis of Bridges under SVGM: (III) A Highly Efficient and Accurate Scheme

The pseudo-excitation method (PEM) scheme developed in Chapter 4 can transform the nonstationary stochastic vibration analysis (SVA) in the frequency domain to deterministic dynamic response problems in time domain, where the direct dynamic integration methods are required to solve the transient analyses. However, these direct dynamic integration methods usually require rather small integration time steps that are dependent on the natural periods of structures to ensure sufficient computational precision and stable response results, thereby increasing the computational effort. To resolve this problem, the high precision direct integration method (HPDIM) is studied in this chapter to improve the computation efficiency.

6.1 Introduction

The HPDIM, which can use larger time step and is not subjected to any limitation from the natural periods of structures, was proposed by Zhong and Williams (1994) in station-

ary/nonstationary random response analysis, reducing the computation time considerably (Lin *et al.*, 1997a).

Because of good computational efficiency of PEM and HPDIM, these two methods can be combined to make nonstationary SVA, whether for uniformly or nonuniformly modulated evolutionary random excitations, much easier and much more efficient. However, the combined scheme is generally still very time consuming and costly, because the time step of HPDIM still has to be small enough to simulate recursively varying pseudo loadings properly, especially for nonuniformly modulated nonstationary pseudo loadings (the limitation of assumption of loading form between two adjacent time steps, e.g., linear loading form, sinusoidal loading form). This becomes the bottle-neck problem in the application of HPDIM in nonstationary random response analysis (Lin *et al.*, 1997a). To resolve the bottle-neck problem, the HPDIM parallel algorithm, in conjunction with PEM, was used to solve the independent structural equations of motion subjected to deterministic pseudo loadings at each frequency step (Lin *et al.*, 1997b). However, the parallel algorithm improves the efficiency of computation utilizing the parallel capability of computer hardware, rather than improving on the algorithms of HPDIM.

To resolve the bottle-neck problem in the application of HPDIM in solving structure equations of motion, an improved high precision direct integration method (I-HPDIM), in conjunction with the absolute-response-oriented scheme of PEM in Section 4.2.2, is proposed in Section 6.2. It reduces significantly the number of transient analyses, without requiring small time step to maintain accurate approximation of forms of pseudo loadings between two adjacent time steps. The proposed I-HPDIM, combined with the absolute-response-oriented scheme of PEM, can greatly improve the computational efficiencies of both PEM and conventional HPDIM, and it becomes more attractive for engineering purposes, particularly in the SVA of some large yet complex structures under tridirectional nonstationary spatially varying ground motions (SVGM).

To demonstrate the proposed SVA scheme, a seismic pounding analysis of a high-pier railway bridge under tridirectional nonuniformly modulated SVGM is conducted in Section 6.2 using the proposed absolute-response-oriented scheme of PEM combined with the I-

HPDIM. Seismic pounding frequently caused serious damage on the superstructures of bridges and even the collapse of bridges during past earthquakes (Bi *et al.*, 2011).

6.2 Theoretical Basis: Scheme of I-HPDIM

In the absolute-response-oriented direct approach presented in Section 4.4.2, structural absolute responses can be derived in equations (4.4.20), (4.4.21), and (4.4.22) for *partially coherent*, *fully coherent*, and *completely incoherent* tridirectional nonstationary SVGM, respectively, based on the obtained pseudo-response of absolute displacement given in equation (4.4.19).

In obtaining structural absolute responses in Section 4.4.2, the conventional method (CM) is used (Jia *et al.*, 2013). Besides, this section presents three other methods in obtaining structural absolute responses, including improved conventional method (I-CM) in Section 6.2.2, HPDIM in Section 6.2.3, I-HPDIM in Section 6.2.4, discussions on these four methods in Section 6.2.5, and implementation and verification of the proposed SVA methodology in general finite element analysis (FEA) platform ANSYS in Section 6.2.6.

6.2.1 Conventional Method (CM)

In the direct scheme of equations of motion presented in Section 4.4.2, power spectral density (PSD) of absolute displacement $\mathbf{X}_s$ under *partially coherent* tridirectional nonstationary ground motions is derived in equation (4.4.20), where the conventional method (CM) is used in obtaining structural stochastic response (Jia *et al.*, 2013)

As seen from equation (4.4.20), a total of $2r$ transient analyses are required to be conducted for both the real and imaginary parts of the input pseudo-excitation $\mathbf{P}_j e^{i\omega t}$, by means of direct dynamic integration methods, such as the Duhamel integration, Newmark method, or Wilson-θ method, to derive response PSD function at each discrete frequency step by superposition of response results from all r modes, i.e., the total number of transient analyses n_{total} is $2n_\omega r$ (n_ω is total number of discrete frequency step). However, transient analysis is a time-consuming procedure, especially for large n_{total}. Moreover, for some large and complex structures having dense modal frequencies and significant contributions from

higher modes, the computation demand may be greatly increased by requiring a large n_ω to accurately represent the response dynamic characteristics of these structures. Furthermore, the rank r of matrix $\mathbf{R}$ may be large for long span structures having many spatial supports (denoted as n_s) and being subjected to tridirectional (denoted as $n_{dof}=3$) spatial seismic motions, i.e., $r=n_s\times n_{dof}=3n_s$. As a result, huge computation requirements are needed in CM (Zhang *et al.*, 2013a).

The computation demands of obtaining response PSD functions in the absolute-response-oriented scheme of PEM are attributed to three sources:

- the total number of discrete frequency step n_ω,
- the discrete number of time domain n_t in transient analysis for every frequency step,
- matrix rank r owning to spatially correlated ground motions.

Hence, the computation efficiency can be further improved on these three aspects. The improved conventional method (I-CM) is proposed on the aspect of parameter r (presented in Section 6.2.2). The adopted HPDIM (Zhong and Williams, 1994) and the proposed improved HPDIM, i.e., I-HPDIM, are presented in Sections 6.2.3 and 6.2.4, respectively, on the aspect of parameter n_t. It is noteworthy that improvements of computational efficiency on the aspect of parameter n_ω are not under investigations because parameter n_ω is determined by the modal information of structures. Some possible ways, such as the parallel computing, can be applied in solving equations of motion at each frequency step independently (Lin *et al.*, 1997b), which are out of the scope of this study.

6.2.2 Improved Conventional Method (I-CM)

The computational efficiency is achieved by the proposed improved algorithm of the CM to reduce r transient analyses into one transient analysis at every frequency step.

The I-CM is based on the principle that a total of r pseudo-excitations $\mathbf{P}_j e^{i\omega t}$, $j=1,2,\ldots,r$, can be first superposed owning to the linear elastic stochastic seismic vibration analysis. Hence, one pseudo-excitation input $\mathbf{P}e^{i\omega t}$ for the *partially coherent* spatial ground motions can be obtained

$$\mathbf{P}\,e^{i\omega t}=\mathbf{G}(\omega,t)\mathbf{W}\mathbf{U}\sqrt{\mathbf{S}_g(i\omega)}\,e^{i\omega t}, \tag{6.2.1}$$

where $\mathbf{U}=\sum_{j=1}^{r}\boldsymbol{\varphi}_j\sqrt{\alpha_j}$, and the corresponding response PSD function is

$$\mathbf{S}_{\mathbf{X}_s\mathbf{X}_s}(\mathrm{i}\omega,t)=\mathbf{I}_\gamma^{*}\,\mathbf{I}_\gamma^{T}\mathbf{S}_g(\mathrm{i}\omega),\quad \text{where } \mathbf{I}_\gamma(\omega,t)=\int_0^t \mathbf{h}(t-\tau)\mathbf{G}(\omega,\tau)\mathbf{W}\mathbf{U}\,\mathrm{e}^{\mathrm{i}\omega\tau}\mathrm{d}\tau, \tag{6.2.2}$$

based on which a total of $2n_\omega$ transient analyses are required in the I-CM compared to $2n_\omega r$ transient analyses in the CM.

As discussed above, deterministic transient analyses $\mathbf{I}_j$ and $\mathbf{I}_\gamma$ can be solved by means of direct integration methods, such as Newmark or Wilson-θ methods, which usually require rather small time step to ensure sufficient computational precision and stable response results, thus increasing the computational effort on the aspect of n_t (Lin *et al.*, 1997a). Hence, HPDIM is proposed and used in place of these direct integration methods in nonstationary random response analysis (Zhong and Williams, 1994), which can use larger time step to reduce computation time considerably and the time step size is not dependent on natural periods of structures (Lin *et al.*, 1997a).

6.2.3 High Precision Direct Integration Method (HPDIM)

Let $\tilde{\mathbf{Y}}(\omega,t)=\left(\mathbf{M}_{\mathrm{sb}}+\mathbf{C}_{\mathrm{sb}}/\mathrm{i}\omega-\mathbf{K}_{\mathrm{sb}}/\omega^2\right)\mathbf{P}\mathrm{e}^{\mathrm{i}\omega t}$, system state equation of equation (4.2.22) and its general solution can be derived as (Lin *et al.*, 1997a, 1995)

$$\dot{\mathbf{V}}=\mathbf{H}\,\mathbf{V}+\mathbf{F}(\omega,t),\quad \mathbf{V}(t)=\mathrm{e}^{\mathbf{H}t}\mathbf{V}(0)+\int_0^t \mathrm{e}^{\mathbf{H}(t-\tau)}\mathbf{F}(\omega,\tau)\mathrm{d}\tau, \tag{6.2.3}$$

in which $\mathrm{e}^{\mathbf{H}t}$ is termed as the exponential matrix, $\mathbf{Y}(\omega,t)$ is the nonstationary input pseudo-excitation at circular frequency ω, and

$$\mathbf{V}=\begin{Bmatrix}\tilde{\mathbf{X}}_\mathrm{s}\\ \dot{\tilde{\mathbf{X}}}_\mathrm{s}\end{Bmatrix},\ \mathbf{F}=-\mathbf{W}\tilde{\mathbf{Y}},\ \mathbf{H}=\begin{bmatrix}\mathbf{0} & \mathbf{I}\\ -\mathbf{M}_{\mathrm{ss}}^{-1}\mathbf{K}_{\mathrm{ss}} & -\mathbf{M}_{\mathrm{ss}}^{-1}\mathbf{C}_{\mathrm{ss}}\end{bmatrix},\ \mathbf{W}=\begin{Bmatrix}\mathbf{0}\\ \mathbf{M}_{\mathrm{ss}}^{-1}\end{Bmatrix}. \tag{6.2.4}$$

The general solution of equation (6.2.3) can be calculated recursively using the time domain discrete integration method with time step Δt, namely, responses $\mathbf{V}(t_i)=\mathbf{V}_i$ at time t_i can be expressed by responses $\mathbf{V}(t_{i-1})=\mathbf{V}_{i-1}$ at time t_{i-1} as

$$\mathbf{V}_i=\mathbf{T}\cdot\mathbf{V}_{i-1}+\int_{t_{i-1}}^{t_i}\mathrm{e}^{\mathbf{H}(t_i-\tau)}\mathbf{F}(\omega,\tau)\mathrm{d}\tau, \tag{6.2.5}$$

where $\mathbf{T}=e^{\mathbf{H}\Delta t}$ is the exponential matrix that can be expressed as $\mathbf{T}=e^{\mathbf{H}\Delta t}=\left[e^{\mathbf{H}\Delta t/m}\right]^m$ (Zhong and Williams, 1994). Let $\tau_0=\Delta t/m$ and $m=2^N$; τ_0 becomes very small as m is very large ($N=20$). $\mathbf{T}$ can then be approximated by the Taylor series expansion as

$$\mathbf{T}(\tau_0)=\left[e^{\mathbf{H}\tau_0}\right]^m\approx\left[\mathbf{I}+\mathbf{H}\tau_0+(\mathbf{H}\tau_0)^2/2!+\cdots+(\mathbf{H}\tau_0)^L/L!\right]^m\equiv[\mathbf{I}+\mathbf{T}_{a,0}]^m, \tag{6.2.6}$$

where L is the truncation order of the Taylor expansion of the exponential matrix $\mathbf{T}$.

In equation (6.2.6), the approximation is caused by the truncation of the Taylor expansion of the exponential matrix $\mathbf{T}(\tau_0)$. It is generally negligibly small when $L=4$ and $N=20$, the first term ignored by the truncation is of the order $O(\Delta\tau_0{}^5)=10^{-30}O(\Delta t^5)$, which is of the order of the round-off errors of ordinary computers.

It is further noted that

$$\left(\mathbf{I}+\mathbf{T}_{a,i-1}\right)^2=\mathbf{I}+2\mathbf{T}_{a,i-1}+\mathbf{T}_{a,i-1}\mathbf{T}_{a,i-1}\equiv\mathbf{I}+\mathbf{T}_{a,i},\quad i=1,2,\cdots N. \tag{6.2.7}$$

Hence, we have

$$\mathbf{I}+\mathbf{T}_{a,N}\equiv\left(\mathbf{I}+\mathbf{T}_{a,N-1}\right)^2=\left(\mathbf{I}+\mathbf{T}_{a,N-2}\right)^4=\cdots=\left(\mathbf{I}+\mathbf{T}_{a,0}\right)^m=\mathbf{T}(\tau_0). \tag{6.2.8}$$

Equations (6.2.6) and (6.2.8) suggest that, in order to avoid the loss of significant digits in matrix $\mathbf{T}(\tau_0)$, it is desirable to compute $\mathbf{T}_{a,1}$ directly from $\mathbf{T}_{a,0}$, $\mathbf{T}_{a,2}$ from $\mathbf{T}_{a,1}$, and so on, i.e.,

$$\mathbf{T}_{a,i}=2\mathbf{T}_{a,i-1}+\mathbf{T}_{a,i-1}\mathbf{T}_{a,i-1},\quad i=1,2,\cdots N. \tag{6.2.9}$$

Then $\mathbf{T}(\tau_0)$ is computed from $\mathbf{T}(\tau_0)=\mathbf{I}+\mathbf{T}_{a,N}$.

Assuming that the input nonstationary pseudo-excitations $\mathbf{F}(\omega,t)$ are piecewise linear functions within the ith time interval $\left[t_{i-1},t_i\right]$, $\mathbf{F}(\omega,t)$ can be discretized as a sequence of excitations $\mathbf{F}_0$, $\mathbf{F}_1$, $\mathbf{F}_2$, $\cdots$, $\mathbf{F}_k$ at time steps t_0, t_1, t_2, $\cdots$, t_k that is expressed for a given frequency step ω as

$$\mathbf{F}(\omega,t)=\mathbf{r}_0+\mathbf{r}_1(t-t_{i-1}),\quad t\in\left[t_{i-1},t_i\right], \tag{6.2.10}$$

where $\mathbf{r}_0$ and $\mathbf{r}_1$ are the time-invariant vectors.

By substituting equation (6.2.10) into equation (6.2.5), the recurrence formula can be obtained (Zhong and Williams, 1994)

$$\mathbf{V}_i=\mathbf{T}\mathbf{V}_{i-1}-\mathbf{H}^{-1}\left[\mathbf{H}^{-1}\left(\mathbf{F}_i-\mathbf{F}_{i-1}\right)/\Delta t+\mathbf{F}_i\right]+\mathbf{T}\mathbf{H}^{-1}\left[\mathbf{H}^{-1}\left(\mathbf{F}_i-\mathbf{F}_{i-1}\right)/\Delta t+\mathbf{F}_{i-1}\right], \tag{6.2.11}$$

where $\mathbf{H}^{-1}$ can be obtained as $\mathbf{H}^{-1}=\mathbf{H}^{*}/|\mathbf{H}|$.

As discussed in Section 6.1, HPDIM can use large time step to obtain structural response recursively by equation (6.2.11) (Zhong and Williams, 1994); however, the accuracy of approximation of pseudo loadings in equation (6.2.10) cannot be ensured if a large time step is adopted. This becomes the bottle-neck problem when the HPDIM method is used in nonstationary random response analysis (Lin *et al.*, 1997a); the I-HPDIM is proposed to resolve the bottle-neck problem of HPDIM.

6.2.4 Improved High Precision Direct Integration Method (I-HPDIM)

Equation (6.2.11) can be further written as

$$\mathbf{V}_i=\mathbf{T}\mathbf{V}_{i-1}+\left[(\mathbf{I}-\mathbf{T})\left(\mathbf{H}^{-2}/\Delta t\right)+\mathbf{T}\mathbf{H}^{-1}\right]\mathbf{F}_{i-1}+\left[(\mathbf{T}-\mathbf{I})\left(\mathbf{H}^{-2}/\Delta t\right)-\mathbf{H}^{-1}\right]\mathbf{F}_i, \tag{6.2.12}$$

which can be simplified as

$$\mathbf{V}_i=\mathbf{T}\mathbf{V}_{i-1}+\mathbf{S}_1\mathbf{F}_{i-1}+\mathbf{S}_2\mathbf{F}_i,\quad i=1,2,\cdots,k, \tag{6.2.13}$$

in which

$$\mathbf{S}_1=(\mathbf{I}-\mathbf{T})\left(\mathbf{H}^{-2}/\Delta t\right)+\mathbf{T}\mathbf{H}^{-1},\ \mathbf{S}_2=(\mathbf{T}-\mathbf{I})\left(\mathbf{H}^{-2}/\Delta t\right)-\mathbf{H}^{-1},\ \mathbf{H}^{-2}=\mathbf{H}^{-1}\mathbf{H}^{-1}. \tag{6.2.14}$$

Hence, for every given circular frequency ω having initial condition $\mathbf{V}_0=\mathbf{0}$, one can obtain the following equations based on equation (6.2.13)

$$\begin{cases}\mathbf{V}_1=\mathbf{S}_1\mathbf{F}_0+\mathbf{S}_2\mathbf{F}_1,\quad i=1,\\ \mathbf{V}_i=\mathbf{T}^{i-1}\mathbf{S}_1\mathbf{F}_0+\mathbf{T}^{i-2}\mathbf{S}_3\mathbf{F}_1+\cdots+\mathbf{T}^{0}\mathbf{S}_3\mathbf{F}_{i-1}+\mathbf{S}_2\mathbf{F}_i,\quad 2\leqslant i\leqslant k,\end{cases} \tag{6.2.15}$$

where $\mathbf{S}_3=\mathbf{T}\mathbf{S}_2+\mathbf{S}_1$.

Alternatively, letting matrices $\mathbf{A}_{i,0}$, $\mathbf{A}_{i,1}$, $\mathbf{A}_{i,2}$, $\cdots$, $\mathbf{A}_{i,i-1}$, and $\mathbf{A}_{i,i}$ denote the coefficient matrices of $\mathbf{F}_0,\mathbf{F}_1,\mathbf{F}_2,\cdots,\mathbf{F}_{i-1}$, and $\mathbf{F}_i$, respectively, equation (6.2.15) can be written as

$$\mathbf{V}_i=\mathbf{A}_{i,0}\mathbf{F}_0+\mathbf{A}_{i,1}\mathbf{F}_1+\mathbf{A}_{i,2}\mathbf{F}_2+\cdots\mathbf{A}_{i,i-1}\mathbf{F}_{i-1}+\mathbf{A}_{i,i}\mathbf{F}_i,\quad 2\leqslant i\leqslant k, \tag{6.2.16}$$

where $\mathbf{A}_{i,0}, \mathbf{A}_{i,1}, \mathbf{A}_{i,2}, \cdots, \mathbf{A}_{i,i-1}$, and $\mathbf{A}_{i,i}$ are completely determined by structural properties that represent structural response characteristics under excitations $\mathbf{F}_0, \mathbf{F}_1, \mathbf{F}_2, \cdots, \mathbf{F}_{i-1}$, and $\mathbf{F}_i$. $\mathbf{A}_{i,0}, \mathbf{A}_{i,1}, \mathbf{A}_{i,2}, \cdots, \mathbf{A}_{i,i-1}$, and $\mathbf{A}_{i,i}$ can be obtained recursively by

$$\begin{cases} \mathbf{A}_{1,0} = \mathbf{S}_1, \\ \mathbf{A}_{1,1} = \mathbf{S}_2, \end{cases} \quad \begin{cases} \mathbf{A}_{2,0} = \mathbf{T}\mathbf{A}_{1,0}, \\ \mathbf{A}_{2,1} = \mathbf{S}_3, \\ \mathbf{A}_{2,2} = \mathbf{A}_{1,1}, \end{cases} \quad \begin{cases} \mathbf{A}_{i,0} = \mathbf{T}\mathbf{A}_{i-1,0}, \\ \mathbf{A}_{i,1} = \mathbf{T}\mathbf{A}_{i-1,1}, \\ \mathbf{A}_{i,j} = \mathbf{T}\mathbf{A}_{i-1,j-1}, \end{cases} \quad 3 \leqslant i \leqslant k, 2 \leqslant j \leqslant i, \tag{6.2.17}$$

By substituting equation (6.2.17) into equation (6.2.15), the matrix form of equation (6.2.15) can be obtained as $\mathbf{AF} = \mathbf{V}$ at the given circular frequency point ω, given by

$$\begin{bmatrix} \mathbf{0} & \times & \times & \times & \times & \times \\ \mathbf{A}_{1,0} & \mathbf{A}_{1,1} & \times & \times & \times & \times \\ \mathbf{A}_{2,0} & \mathbf{A}_{2,1} & \mathbf{A}_{1,1} & \times & \times & \times \\ \vdots & \vdots & \vdots & \ddots & \times & \times \\ \mathbf{A}_{k-1,0} & \mathbf{A}_{k-1,1} & \mathbf{A}_{k-2,1} & \cdots & \mathbf{A}_{1,1} & \times \\ \mathbf{A}_{k,0} & \mathbf{A}_{k,1} & \mathbf{A}_{k-1,1} & \cdots & \mathbf{A}_{2,1} & \mathbf{A}_{1,1} \end{bmatrix} \begin{Bmatrix} \mathbf{F}_0 \\ \mathbf{F}_1 \\ \mathbf{F}_2 \\ \vdots \\ \mathbf{F}_{k-1} \\ \mathbf{F}_k \end{Bmatrix} = \begin{Bmatrix} \mathbf{V}_0 \\ \mathbf{V}_1 \\ \mathbf{V}_2 \\ \vdots \\ \mathbf{V}_{k-1} \\ \mathbf{V}_k \end{Bmatrix}, \tag{6.2.18}$$

where it is seen that all block-elements of $\mathbf{A}$ can be determined if the block-elements in the first two block-columns of $\mathbf{A}$ are known. As observed, the block-elements in the first block-columns of $\mathbf{A}$, i.e., $\{\mathbf{0}, \mathbf{A}_{1,0}, \mathbf{A}_{2,0}, \mathbf{A}_{3,0}, \cdots, \mathbf{A}_{k-2,0}, \mathbf{A}_{k-1,0}, \mathbf{A}_{k,0}\}$, can be obtained in a transient analysis by letting $\mathbf{F}_0$ be a vector of ones and all other elements of $\mathbf{F}$ are zeros. Similarly, block-elements in the second block-columns of $\mathbf{A}$ can be obtained in a transient analysis by letting $\mathbf{F}_1$ be a vector with ones and all other elements of $\mathbf{F}$ are zeros. For response X_i or X_j at a specific degree-of-freedom (DoF), e.g., vertical displacement in the midspan, the input excitations $\mathbf{F}$ in obtaining block-elements in the first two block-columns of $\mathbf{A}$ correspond to the triangular unit impulse excitations at instants t_0 and t_1, respectively, which are given in Figure 6.1(b).

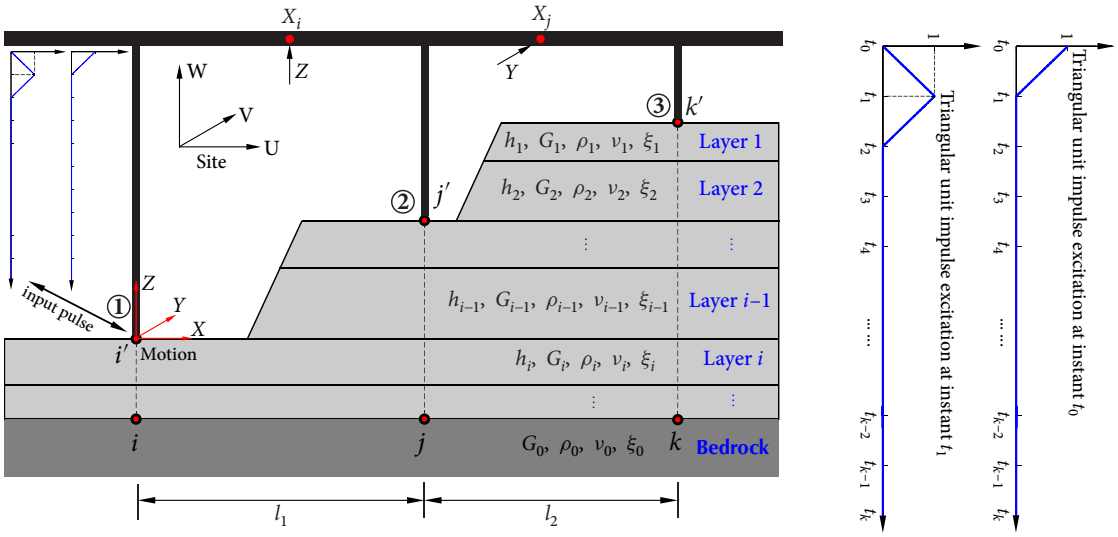

(a) Spatially distributed supports at varying sites for tridirectional spatial motions (b) Unit excitation in I-HPDIM

Figure 6.1 Scheme of I-HPDIM for nonstationary stochastic analysis of bridges under tridirectional spatial motions

Once matrix **A** is obtained, responses **V** of the structure under nonstationary pseudo-excitations **F** can be determined directly from $\mathbf{AF}=\mathbf{V}$, without transient analysis, for all discrete frequency steps in the frequency domain. More specifically, the triangular unit impulse excitations at instants t_0 and t_1 should be exerted in each direction at every spatial pier support to construct the respective matrix **A** for responses X_i or X_j at a given DoF, respectively, as shown in Figure 6.1(a). Then, tridirectional structural response **V** of X_i or X_j can be obtained by $\mathbf{V}(\omega_i) = \mathbf{AF}(\omega_i)$ at the ith circular frequency ω_i. Finally, structural pseudo-response $\mathbf{V}(\omega)$ at all the frequency steps can be determined, and their PSD functions can then be obtained by equation (4.2.23).

As observed, the proposed I-HPDIM scheme has not only overcome the time-consuming drawbacks of CM and I-CM that require r and 1 transient analyses at every single frequency step, respectively, but also resolved the bottle-neck problem of HPDIM that requires rather small time step to simulate recursively varying pseudo loadings properly, as discussed in Section 6.1. It is very attractive for engineering applications, particularly in stochastic seismic analysis of complex structures extended in space under tridirectional nonstationary

spatial seismic motions. Moreover, I-HPDIM can also enhance computational efficiency by choosing only the output responses of interest, rather than the entire structural responses required to be calculated in the scheme of I-HPDIM and the absolute-response-oriented scheme of PEM. Because structural responses at certain locations of structures are of interest as response output, these outputs of interest, e.g., X_i and X_j in Figure 6.1(a), can be selected in I-HPDIM, thereby reducing time of computation (Zhang *et al.*, 2013a).

Because the proposed I-HPDIM can achieve significant computational efficiencies and good accuracy, it is implemented in a general FEA platform (with powerful and versatile modelling and analysis capabilities) for stochastic seismic analysis of structures. Details on the improved computational efficiency of I-HPDIM are given in Section 6.2.5, and details of its FE implementation are presented in Section 6.2.6.

6.2.5 Discussions on CM, I-CM, HPDIM, and I-HPDIM

Because transient analysis is a time-consuming procedure, the total number of transient analyses has been adopted as a measure of computational efficiency for comparison of schemes of CM, I-CM, HPDIM, and I-HPDIM. The respective total numbers of transient analyses of these four methods are $n_{\text{CM}} = 2n_\omega r$, $n_{\text{I-CM}} = 2n_\omega$, $n_{\text{HPDIM}} = 2n_\omega r$, and $n_{\text{I-HPDIM}} = 2n_{\text{s}}n_{\text{dof}} = 2r$.

As seen, CM and HPDIM have the same total number of transient analyses, but larger time step can be adopted in HPDIM, i.e., smaller discrete number of time domain n_{t} can be adopted to increase computational efficiency in every single transient analysis. However, sometimes time step of HPDIM is required to be rather small to simulate recursively varying pseudo loadings properly, and this becomes the bottle-neck problem for application of HPDIM method, as discussed in Section 6.1. I-HPDIM, proposed in this study, has overcome the bottle-neck problem of HPDIM and is more computationally efficient than all the other three methods.

Specifically, one can obtain the following formula for comparison of computational efficiencies between the four approaches

$$n_{\text{I-HPDIM}} = \frac{1}{n_\omega} n_{\text{HPDIM}} = \frac{r}{n_\omega} n_{\text{I-CM}} = \frac{1}{n_\omega} n_{\text{CM}}. \tag{6.2.19}$$

Assuming that $n_\omega = 2000$ for a complex structure with dense modal frequencies, $r = n_{\text{dof}} \times n_{\text{s}} = 3 \times 6 = 18$, then equation (6.2.19) becomes

$$n_{\text{I-HPDIM}} = \frac{1}{2000} n_{\text{HPDIM}} = \frac{1}{110} n_{\text{I-CM}} = \frac{1}{2000} n_{\text{CM}}, \tag{6.2.20}$$

from which it is seen that the proposed I-HPDIM and I-CM have higher computational efficiencies than conventional CM and HPDIM schemes; in particular the I-HPDIM scheme can achieve the highest efficiency of computation and has improved the computational efficiencies of the conventional methods significantly.

6.2.6 Implementation and Verification of the Proposed SVA Scheme in General FEA Platform

Since the proposed I-HPDIM, in conjunction with the absolute-response-oriented scheme of PEM, is very effective and accurate in stochastic response analysis of complex structures with a large number of DoF, it can be integrated (implemented) with general FEA platforms that have powerful modelling and analysis tools for seismic analysis of complex structures. Furthermore, the implementation can improve and resolve the drawbacks of some self-developed programs lacking computational efficiencies and powerful modelling and analysis techniques.

The proposed I-HPDIM combined with the absolute-response-oriented scheme of PEM in nonstationary stochastic seismic analysis of structures under tridirectional spatial motions is implemented in the general FEA platform ANSYS (Kohnke, 2010). Procedure of the implementation is presented in the flow chart of Figure 6.2.

To validate the implementation, the theoretical stochastic response solution of a single DoF oscillator under nonuniformly modulated nonstationary excitations is derived for comparison. The equation of motion is

$$\ddot{\tilde{y}} + 2\xi\omega_0\dot{\tilde{y}} + \omega_0^2\tilde{y} = F(\omega, t) = \sqrt{S_g(\omega)}\beta(\omega, t)g(t), \quad \tilde{y}(0) = \dot{\tilde{y}}(0) = 0, \tag{6.2.21}$$

in which $F(\omega, t)$ is any nonuniformly modulated evolutionary pseudo excitation, $g(t)$ is the time-domain amplitude modulation function given by $g(t) = 1.0$ when $t \geqslant 0$ and $g(t) = 0$ when $t < 0$, $\beta(\omega, t)$ is the frequency modulation function given by $\beta(\omega, t) = \mathrm{e}^{-\eta\omega t/\omega_a t_a}$, η is the frequency modulation factor and is adjustable to adapt to engineering circumstances

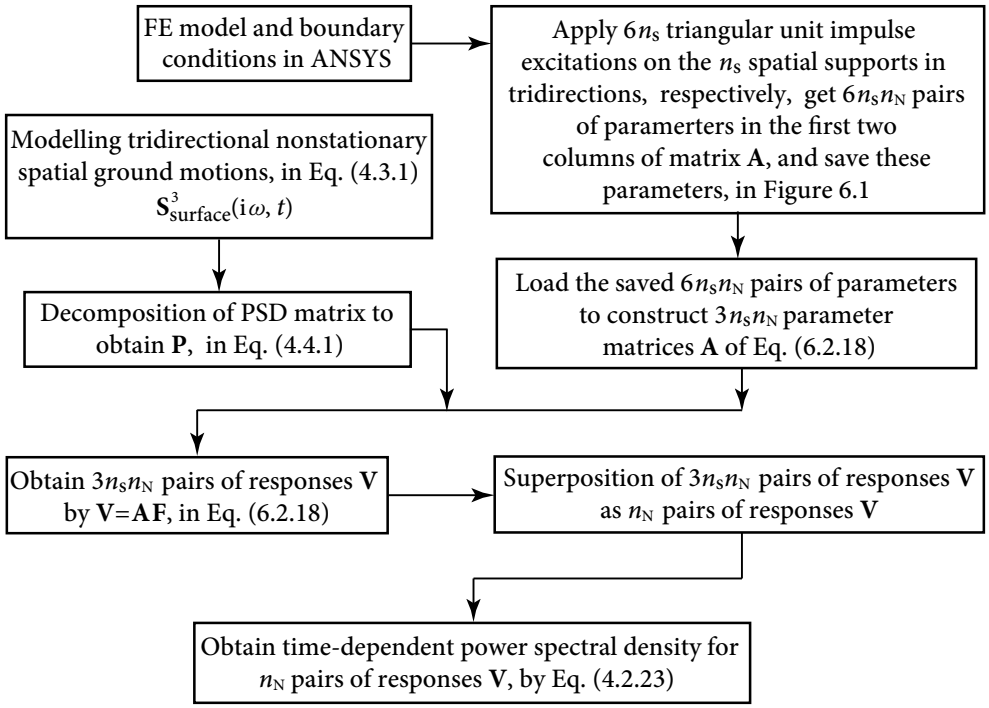

Figure 6.2 Flow chart of implementation of the proposed I-HPDIM scheme combined with the absolute-response-oriented scheme of PEM in ANSYS

and experimental data, and ω_a and t_a are arbitrarily assigned parameters used to make ω and t dimensionless. When ω_a and t_a are fixed, η can be adjusted to make different frequency components decay at different rates. $S_g(\omega)$ is the Clough-Penzien acceleration power spectrum model in equation (5.3.1) with the constant spectral density of the white-noise input $S^* = 1.0\,\text{m}^2/\text{s}^3$ and ground motion filter parameters $\omega_g = 15.0$ rad/s, $\xi_g = 0.6$, $\omega_f = 1.5$ rad/s, and $\xi_f = 0.6$ (Jia *et al.*, 2013).

After lengthy derivations, the pseudo-response $\tilde{y}$ in equation (6.2.21) is given by

$$\tilde{y} = \left\{ e^{-\xi\omega_0 t}\left[-\frac{1}{\lambda^2 + 2\xi\omega_0\lambda + \omega_0^2}\cos(\omega_d t) - \frac{\lambda + \xi\omega_0}{\omega_d(\lambda^2 + 2\xi\omega_0\lambda + \omega_0^2)}\sin(\omega_d t)\right] + \right.$$

$$\left. \frac{e^{\lambda t}}{\lambda^2 + 2\xi\omega_0\lambda + \omega_0^2} \right\} \sqrt{S_g(\omega)}, \tag{6.2.22}$$

and the response PSD function of displacement y can be obtained as

$$S(\omega,t)=\tilde{y}^{*}\tilde{y}^{T}=\left\{e^{\lambda t}-e^{-\xi\omega_0 t}\left[\cos(\omega_d t)+\frac{\lambda+\xi\omega_0}{\omega_d}\sin(\omega_d t)\right]\right\}^{2}\cdot\frac{S_g(\omega)}{(\lambda^2+2\xi\omega_0\lambda+\omega_0^2)^2},\tag{6.2.23}$$

where damping ratio $\xi=0.05$, natural frequency $\omega_0=\sqrt{k/m}=1.0$ rad/s ($m=1.0$ kg, $k=1.0$ N/m), $\omega_d=\omega_0\sqrt{1-\xi^2}$, and $\lambda=-\eta\omega/\omega_a t_a+\mathrm{i}\omega$. The time-dependent response standard deviation (SD) function $\sigma(t)$ is derived based on the obtained nonstationary PSD function of response $S(\omega,t)$ as $\sigma(t)=\sqrt{2\int_0^\infty S(\omega,t)\mathrm{d}\omega}$.

Figure 6.3 presents the theoretical solutions and ANSYS solutions (based on the implementation) for the contour plot of the time-dependent PSD and the response SD functions for $\eta=0$, 5, and 10, where it is observed that ANSYS solutions agree with the theoretical results very well, implying that the implementation of the proposed I-HPDIM scheme, in conjunction with the absolute-response-oriented scheme of PEM, in ANSYS is accurate in obtaining structural seismic responses.

Based on the implementation, the proposed nonstationary stochastic analysis approach is applied in seismic pounding analysis of a high-pier railway bridge under tridirectional nonuniformly modulated SVGM in Section 6.3.

6.3 Practical Application: Seismic Pounding Analysis of Bridges

To demonstrate the ANSYS implementation of the proposed I-HPDIM combined with the absolute-response-oriented scheme of PEM, seismic pounding analysis of a high-pier railway bridge under tridirectional nonuniformly modulated nonstationary SVGM is conducted.

6.3.1 Bridge Seismic Pounding

Seismic pounding of bridge is attributed to the large out-of-phase movement between adjacent segments owning to different dynamic characteristics, spatial variabilities of ground motions, and soil-structure interaction (SSI). To preclude pounding effect, the most straightforward approach is to provide sufficient separation distances between adjacent

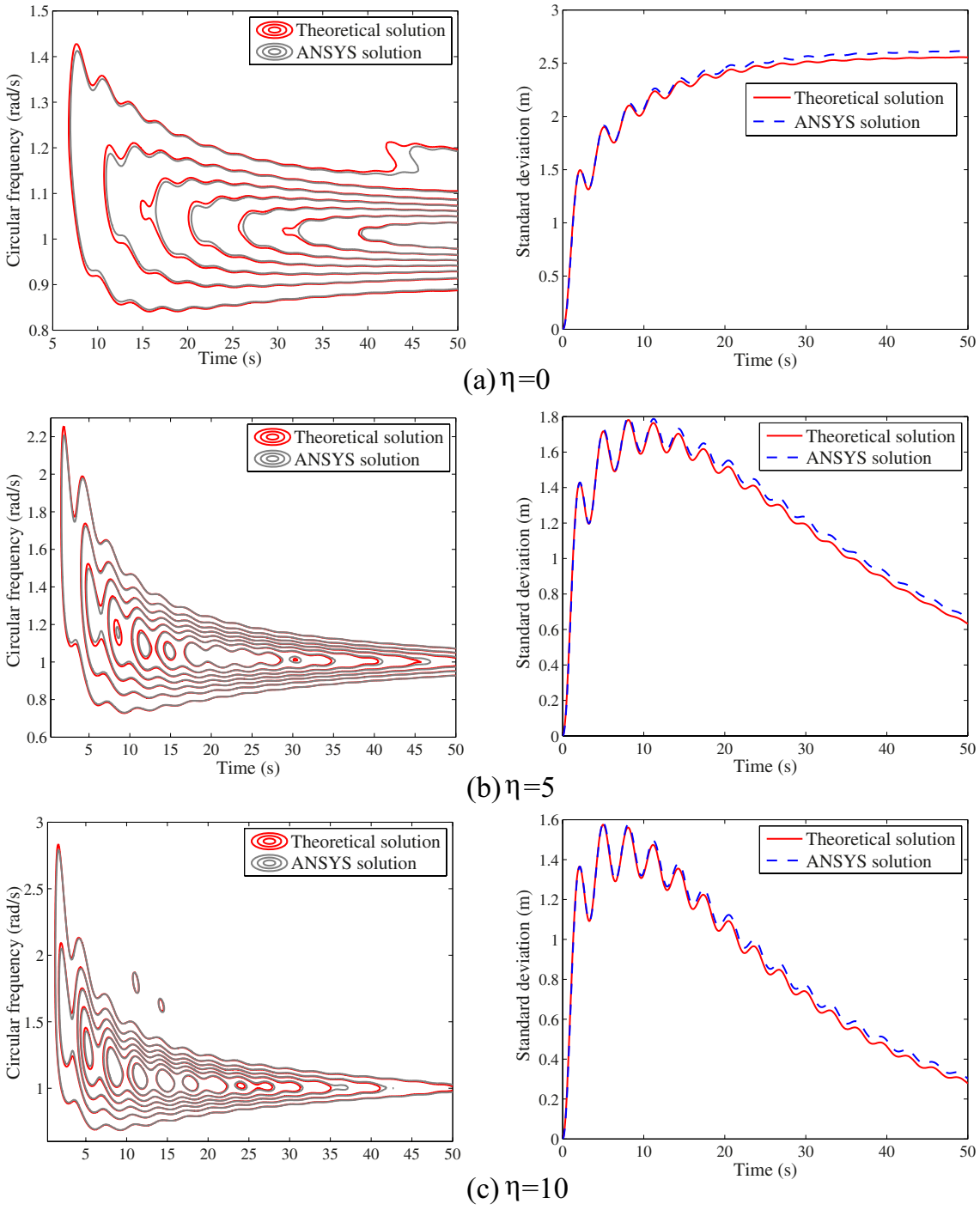

Figure 6.3 Contour plot of the time-dependent PSD of displacements and their response SD functions

structures; however, the seating gap between adjacent bridge segment cannot be arbitrarily large in practice in order to maintain smoothness of traffic. Hence, these required separation distances (RSD) should be specified for bridges to avoid the pull-off-and-drop collapse of their decks owning to the large differential movements of the adjacent segments compared to the seating lengths provided.

Studies on the RSD, i.e., the maximum relative displacement of adjacent bridge segments, for bridge structures under SVGM have been carried out by many researchers using SVA techniques (Bi *et al.*, 2011; Hao, 1998). However, in these works, very simple 2-D bridge models (excluding the rotational DoFs), which cannot model 3-D eccentric pounding between adjacent segments, i.e., surface-to-surface pounding, are adopted in the SVA. Moreover, only point-to-point pounding in the longitudinal direction is considered, failing to study transverse pounding of adjacent segments induced by tridirectional ground motions (particularly the transverse ground motions) due to analysis complexity. Furthermore, only stationary vibration analysis, rather than the more appropriate and accurate nonstationary stochastic vibration analysis, is conducted to obtain the RSD, because of analysis complexity and large computational effort. These shortcomings (Bi *et al.*, 2011; Hao, 1998) can be resolved by the proposed scheme of I-HPDIM, combined with the absolute-response-oriented scheme of PEM, that has been implemented in a general FEA platform.

For brevity, this section focuses on only the local site effects of SVGM on the longitudinal RSD between adjacent bridge segments to avoid multi-sided pounding. Some other rarely studied effects on the RSD, e.g., ground motion dimensionality, 3-D surface-to-surface pounding modelling, the RSD in the transverse direction, SSI, will be studied in the future. It is noted that tridirectional SVGM are included when considering the local site effect, while the effect of the frequency ratio of adjacent bridge segments is ignored for brevity.

6.3.2 Bridge Model and Analysis Cases

The large-span high-pier continuous rigid frame railway bridge in Figure 5.9 is adopted for stochastic seismic pounding analysis. There are three potential locations for multi-sided pounding, including the connection area of the main girder with the left and right bridge

abutments and the connection part between LBS and RBS, with RSD, i.e., maximum relative longitudinal displacements, $\triangle_1$, $\triangle_3$, and $\triangle_2$, respectively.

The 3-D FE model of the high-pier railway bridge is built using ANSYS (Kohnke, 2010). The fixed boundary conditions are applied to the bottom of Piers #1 to #5. Based on the actual structural configurations, the vertical DoF (Z), transverse DoF (Y), and the rotational DoF with respect to Z (Rotz) and X (Rotx) directions are fixed in both the north and south abutments of the railway bridge. All DoF of Pier #1, Pier #2, and Pier #4 (the DoF in the connection point of the piers and main girders) are coupled with the corresponding DoF of the main girders, while the longitudinal DoF (X) in the connection points of Pier #3, Pier #5, and the main girders are released.

Effects of uniform local site conditions, varying site conditions, and site irregularities are studied on the RSD of adjacent bridge segments to avoid seismic pounding. Categories of site conditions specified in National Earthquake Hazard Reduction Program (NEHRP) are used and presented in Table 5.3, with the corresponding soil properties (FEMA, 2010).

Table 6.1: Analysis cases in study of effect of local site conditions

Uniform site condition[†1]	**Varying site condition**[†1]	**Site irregularity**[†2]
#1: B-B-B-B-B	#4: B-C-B-B-B	#10: C(40)-C(40)-C(40)-C(60)-C(60)
#2: C-C-C-C-C	#5: B-E-B-B-B	#11: C(40)-C(40)-C(40)-C(20)-C(20)
#3: E-E-E-E-E	#6: C-B-C-C-C	#12: C(60)-C(60)-C(60)-C(40)-C(40)
--	#7: C-E-C-C-C	#13: C(20)-C(20)-C(20)-C(40)-C(40)
--	#8: E-B-E-E-E	#14: C(60)-C(40)-C(50)-C(50)-C(60)
--	#9: E-C-E-E-E	--

[†1] A-B-C-D-E denotes that site conditions (with depth of soil layer $h = 40$ m) beneath the 1st to the 5th pier supports are categories of #A, #B, #C, #D, and #E, respectively. [†2] C(h_1) denotes site category #C with depth of soil layer h_1.

A total of 3 (#1 to #3) and 6 (#4 to #9) cases are considered for effects of the uniform site conditions and varying site conditions, respectively, where depths of the soil profiles are chosen to be $h = 40$ m. To study the effects of site irregularities, a total of 5 cases (#10 to #14) are considered with varying depths of the soil profiles. Details of these cases are given

in Table 6.1. The site response analysis approach in Section 2.4.1 is performed for the site cases in Table 6.1, and the site response results are incorporated in the proposed stochastic seismic analysis scheme by equation (4.3.4).

In the stochastic analysis, the lagged coherency model of SVGM proposed by Menke (1990) is used, which is $|\gamma_{ij}(\mathrm{i}\omega)| = \mathrm{e}^{-\kappa(\omega/2\pi)d_{ij}}$, where $\kappa = 0.7\,\mathrm{km}^{-1}\mathrm{Hz}^{-1}$. The incident angle of bedrock motions propagating to the layered sites is assumed to be 60°. Based on bedrock property and the incident angle of bedrock motion, the apparent wave velocity of base rock is 3100 m/s.

The Jennings's time-domain amplitude modulation function in equation (5.3.2) is used, where $t_1 = 7.1$ s, $t_2 = 19.5$ s, and $c = 0.16$ (Jennings *et al.*, 1968). The frequency modulation function $\beta(\omega, t) = \mathrm{e}^{-\eta\omega t/\omega_a t_a}$ is used with $\eta = 3$, $\omega_a = 15.6$ rad/s, and $t_a = (t_1 + t_2)/2$. The Clough-Penzien power spectrum in equation (5.3.1) is used, with the constant spectral density of the white-noise input $S^* = 0.00177\,\mathrm{m}^2/\mathrm{s}^3$ and ground motion filter parameters $\omega_g = 15.0$ rad/s, $\xi_g = 0.6$, $\omega_f = 1.5$ rad/s, and $\xi_f = 0.6$ (Jia *et al.*, 2013).

The circular frequency ω is bounded within interval [0, 25] rad/s with circular frequency resolution $\Delta\omega = 0.0244$ rad/s, and the time t is bounded within interval [0, 25] s with time step $\Delta t = 0.05$ s. The damping ratios of all the modes of interest are assumed to be 0.05.

6.3.3 Effect of Uniform and Non-uniform Local Site Conditions on RSD

For the uniform local site effect on RSD Δ_1, Δ_2, and Δ_3, three cases, i.e., #1, #2, and #3, are considered. The response SD functions of the 3-D nonstationary response PSD functions of Δ_1, Δ_2, and Δ_3 are presented in Figure 6.4, from which it is observed that the softer uniform site conditions can cause larger RSD Δ_1, Δ_2, and Δ_3. Specifically, the ratios between the peaks of response SD functions at E (#3), C (#2), and B (#1) site conditions are 4.55:4.09:3.70 for Δ_1, 8.62:6.66:6.12 for Δ_2, and 7.52:6.60:5.91 for Δ_3, respectively.

The response SD functions of Δ_1, Δ_2, and Δ_3 under varying spatial site conditions in Group #A (#1, #4, #5), Group #B (#2, #6, #7, #10, #11, #12, #13, #14), and Group #C (#3, #8, #9) are presented in Figure 6.5(a), (b), and (c), respectively. It is seen in Figure

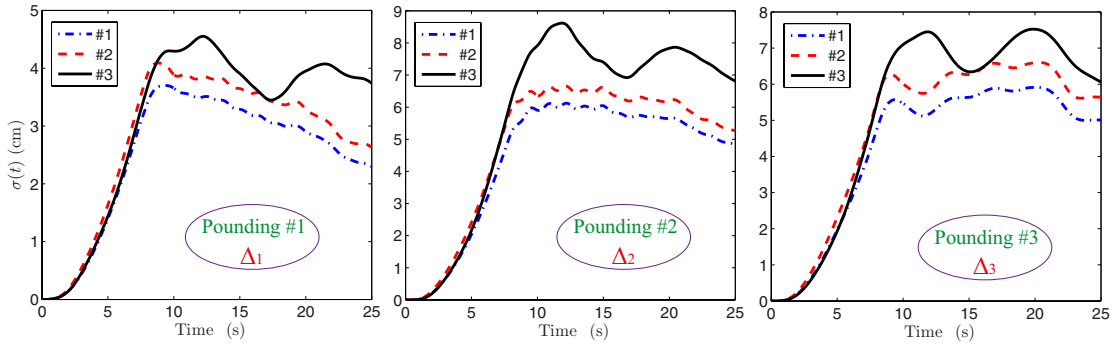

Figure 6.4 Effect of uniform site conditions on the RSD

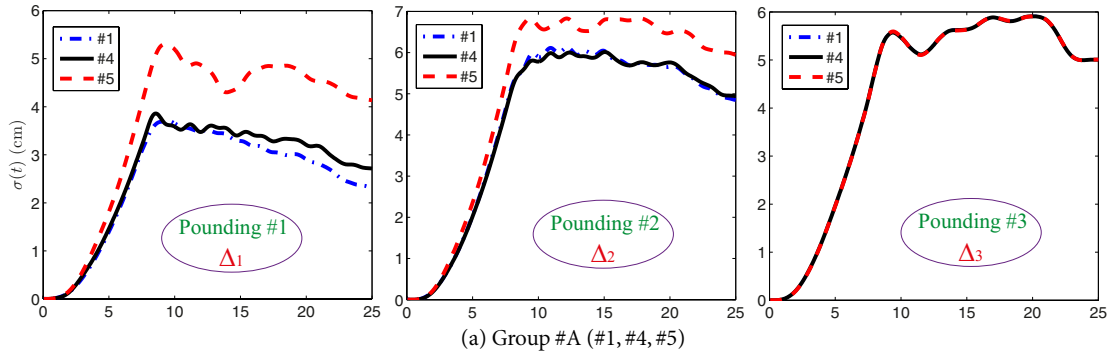

(a) Group #A (#1, #4, #5)

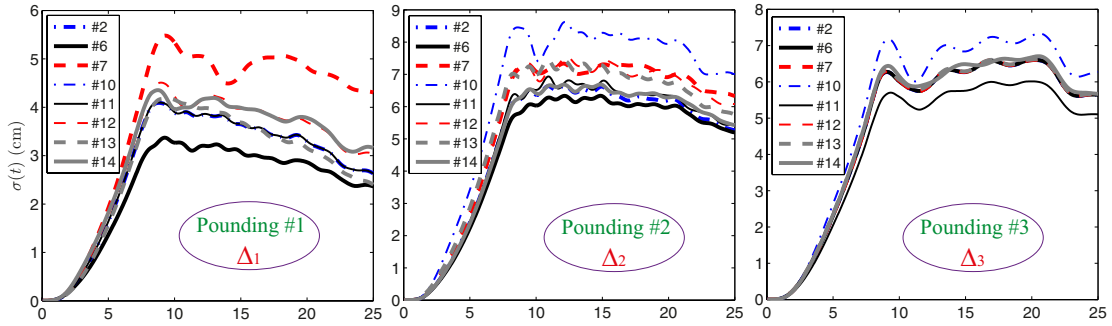

(b) Group #B (#2, #6, #7, #10, #11, #12, #13, #14)

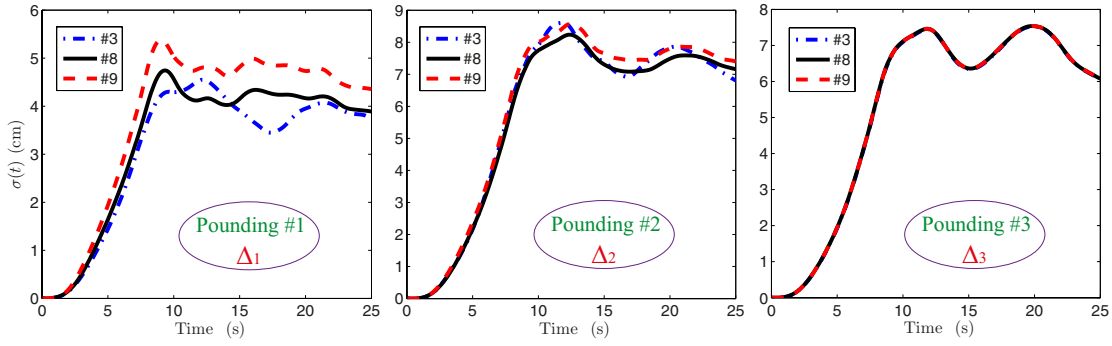

(c) Group #C (#3, #8, #9)

Figure 6.5 Effect of varying site conditions on the RSD

6.5 that effects of the varying site conditions are very significant in the time-dependent nonstationary structural seismic pounding responses.

For Group #A in Figure 6.5(a), case #5 (B-E-B-B-B) can result in the largest required pounding distance among all the cases in Group #A, which indicates that the larger site difference between Pier #2 and the other piers the larger structural pounding responses obtained, confirming the fact that the highest Pier #2 plays a dominant role on the seismic response of the railway bridge. In addition, it is noteworthy that site variations under Pier #2 play a negligible effect on Δ_3, i.e., all seismic pounding responses of Δ_3 in case #1 (B-B-B-B-B), case #4 (B-C-B-B-B), and case #5 (B-E-B-B-B) are overlapped in the entire duration of ground motion, because the site conditions of piers of the right bridge system remain the same among cases #1, #4, and #5. Similar observations can be obtained for cases #2, #6, and #7 in Group #B and cases #3, #8, and #9 in Group #C in Figure 6.5(b) and 6.5(c), respectively.

The ratios between peaks of response SDs between cases #5, #4, and #1 in Group #A are 5.30:3.86:3.7 for Δ_1 and 6.83:6.01:6.12 for Δ_2, 5.48:4.09:3.37 for Δ_1 and 7.33:6.66:6.34 for Δ_2 between cases #7, #2 and #6 in Group #B, 5.38:4.74:4.55 for Δ_1 and 8.58:8.24:8.62 for Δ_2 between cases #9, #8 and #3 in Group #C. It is indicated that the varying site conditions can significantly affect structural pounding response in comparison with the uniform site conditions. Additionally, it is concluded that structural pounding response may be largely underestimated if effect of varying site conditions are not considered, especially the variation of local site conditions beneath the highest pier. Therefore, it is of prime importance to account for the varying site effect in seismic pounding evaluations of high-pier railway bridge under tridirectional nonstationary spatial ground motions. Two important and effective measures can be taken to prevent or mitigate the seismic pounding failure of the high-pier railway bridge induced by the site:

- to avoid the soft site beneath the highest pier,
- to avoid large difference of site conditions between the highest pier and the other piers.

The pounding response results of Δ_1, Δ_2, and Δ_3 in cases #2, #10 to #14 are presented in Figure 6.5(b) for effect of site irregularities. The ratios between peaks of response SDs for cases #2, #10 to #14 are 4.09:4.09:4.1:4.51:4.19:4.35, 6.66:8.62:6.93:7.54:7.45:6.69, and

6.60:7.33:6.01:6.59:6.62:6.71 for $\Delta_1, \Delta_2,$ and $\Delta_3,$ respectively. It is seen that site irregularities can sometimes significantly affect the seismic pounding responses between adjacent bridge segments. Hence, detailed inspections of geological conditions and appropriate design of site conditions beneath the high-piers are recommended to effectively reduce site induced seismic pounding damages to the high-pier railway bridges.

6.4 Summary and Conclusions

From the theoretical background and numerical examples presented in this chapter, the following conclusion can be drawn.

1. The I-HPDIM, in conjunction with absolute-response-oriented scheme of PEM, has been derived for nonstationary SVA of structures extended in space under tridirectional nonuniformly modulated SVGM. The proposed I-HPDIM has resolved the bottle-neck problem of conventional HPDIM that it can significantly improve computational efficiency of HPDIM in nonstationary SVA.
2. This highly efficient and accurate SVA approach is more attractive in engineering practices for nonstationary SVA of structures with large geometrical dimensions.
3. The proposed nonstationary SVA scheme has been implemented and verified in a general FEA platform for SVA of some large and complex structures under tridirectional nonstationary SVGM.
4. Effects of local site conditions on RSD of adjacent segments of a high-pier railway bridge have been studied to avoid bridge seismic pounding. It is concluded that

    - the varying site conditions can significantly affect and underestimate structural pounding response in comparison with the uniform site conditions, especially the variation of local site conditions beneath the highest pier,
    - the site irregularities can also significantly affect the seismic pounding responses between adjacent bridge segments.

CHAPTER 7

Random Field Representation of Spatial Soil Profiles: A Meshfree-Galerkin Approach

Besides wave-passage, incoherence, and site-response effects, spatial variations of ground motions can be further modified by soil-structure interaction (SSI) effect. In SSI analysis, the inherent spatial variability and uncertainty of soil should be accounted for, since soil exhibits great spatial variation and uncertainty that may exert a dominant influence in SSI (Lumb, 1966). The study of representing spatial soil profiles using random fields (RF) approach is conducted in this chapter.

7.1 Introduction

Unlike some artificial materials, such as concrete or steel, soil exhibits great spatial variation and uncertainty due to the variations in deposition conditions and stress histories (Phoon and Kulhawy, 1999b). Because of the significant effect of variability and uncertainty of soil properties, it is necessary to account for the spatially variable and uncertain soil profiles in practical analysis, e.g., SSI analysis of bridges under spatially varying ground motions (SVGM). The representation of spatial variability and uncertainty characterizing the soil-structure system parameters (input) is a fundamental issue in SSI analysis.

A convenient way for describing these uncertain soil quantities in space is using RF, where the probability distributions and correlation structures of these soil properties are required (Vanmarcke, 1977). However, due to the lack of relevant experimental data, assumptions have to be made regarding these probabilistic characteristics. For example, RF are usually assumed to have finite second order statistics, and they are usually categorized into Gaussian and non-Gaussian fields.

There are several methods in simulating Gaussian and non-Gaussian, homogeneous and nonhomogeneous RF. The spectral representation method (SRM) is widely used in conjunction with the transformed field to simulate non-Gaussian RF. However, it usually requires an iterative procedure between the underlying Gaussian field and the target non-Gaussian field, where the existence of the underlying Gaussian field cannot be ensured. Furthermore, the spectral representation method fails to represent the nonhomogeneity of RF satisfactorily (Li *et al.*, 2007). However, modelling the nonhomogeneity of soil properties is necessary because most of soil properties exhibit strong nonhomogeneity in reality (Lumb, 1966). The Karhunen-Loève (K-L) expansion offers a unified framework for the simulation of homogeneous and nonhomogeneous RF, which can be seen as a special case of orthogonal series expansions and can effectively represent the covariance kernel of a homogeneous or nonhomogeneous random field (Ghanem and Spanos, 1991; Phoon *et al.*, 2002b).

However, the implementation of K-L expansion is often hindered by the difficulty encountered in solving the Fredholm integral equation. Closed-form solutions are only available when the covariance kernel has simple functional forms, such as exponential or linear functions, and numerical treatments are required in realistic problems involving complex covariance functions (Ghanem and Spanos, 1991). The numerical Galerkin method is often used to solve the integral equations, where the trigonometric, polynomial, and wavelet basis functions are usually adopted (Phoon *et al.*, 2002b).

However, these basis-function-based methods may not be effective or applicable if the domain of a multi-dimensional random field is irregular (i.e., an arbitrary shape of domain associated with a general covariance function) (Rahman and Xu, 2005). Irregular domains, in which the system properties are considered to be spatially variable, are usually required in

engineering problems, such as dynamic SSI analysis of nuclear power plant structures. For example, in accounting for the transmitting boundary for wave propagation in unbounded domains in SSI analysis, these domains usually have arbitrary geometry, over which the simulation of spatially variable soil properties is required (Bazyar and Song, 2008). Another example would be the SSI analysis by considering different layers of soil profiles, where each soil layer may have variable and arbitrary domain due to different historical accumulations (Simos and Costantinoa, 2004). Moreover, it is important to note that the accuracy in computing the eigen-pairs of the covariance kernel strongly influences the efficiency of K-L series. Hence, more general methods are required to solve the eigenvalue problem.

Alternatively, the meshfree shape functions can be employed as a set of complete basis functions within the Galerkin scheme for solving the eigenvalue problems of Fredholm integral equation of K-L expansion. The meshfree method, which is applicable to domains with arbitrary shape, is applied to avoid meshing problems in the finite element analysis (FEA) of fracture, crack, or dislocation problems (Belytschko *et al.*, 1994; Rahman and Xu, 2005; Arun *et al.*, 2010). The meshfree method is more general than the methods using other basis functions and can solve problems involving a multi-dimensional random field with an arbitrary covariance function and an arbitrary domain (Rahman and Xu, 2005). It is preferred in modelling spatial soil properties with arbitrary covariance functions and arbitrary domains.

In this chapter, a Galerkin scheme using meshfree shape functions for the calculation of eigen-pairs of integral equation is introduced and applied in modelling and synthesizing spatially variable soil properties. The proposed scheme is applied to the modelling and synthesis of 1-D spatial soil properties with various covariance models. Studies on other related topics, such as the probability distribution of a random field, and the modelling and synthesis of spatial soil property field with higher dimensions and arbitrary domains, are reccomended in Section 8.4.4.

The K-L expansion approach for representation of the random field, with an optimization scheme in treating the compatibility of target covariance model, is presented in Section 7.2. The meshfree-Galerkin scheme is introduced for eigenvalue problems of integral equation in Section 7.3. The meshfree-Galerkin scheme for eigen-solutions and representations

of RF with diverse covariance models is assessed in Section 7.4. The proposed scheme in modelling and synthesizing spatially variable soil properties is applied in Section 7.5. Conclusions are drawn in Section 7.6.

7.2 Random Field Representation by Karhunen-Loève Expansion

For the mathematical preliminaries, define a complete probability space $(\Omega, \mathcal{F}, \mathcal{P})$ with sample space Ω, which corresponds to the outcomes of some experiments, $\mathcal{F}$ the σ-algebra of subsets in Ω (events), and $\mathcal{P}$: $\mathcal{F} \rightarrow [0, 1]$ the probability measure. Let $\mathcal{L}_2(\mathcal{D})$ be the space of those measurable functions on $\mathcal{D}$ for which the integral of the square of the function is finite.

A random field $\beta(\mathbf{x}, \omega)$, indexed by a spatial coordinate $\mathbf{x} \in \mathcal{D} \in \mathbb{R}^n$ ($\mathcal{D}$ is bounded), is a measurable function $\beta : \mathcal{D} \times \Omega \rightarrow \mathbb{R}$. For a fixed $\omega \in \Omega$, $\beta(\mathbf{x}, \omega)$ is a realization of the random field, i.e., a function $\mathcal{D} \rightarrow \mathbb{R}$; for a fixed $\mathbf{x} \in \mathcal{D}$, $\beta(\mathbf{x}, \omega)$ is a random variable with respect to the probability space $(\Omega, \mathcal{F}, \mathcal{P})$.

7.2.1 Finite Dimensional Noise Assumption

Any second-order random field $\beta(\mathbf{x}, \omega)$ can be represented as a sequence of random variables at each spatial location $\{\beta(\mathbf{x}_1, \omega), \beta(\mathbf{x}_2, \omega), ..., \beta(\mathbf{x}_n, \omega)\}$ as

$$\beta(\mathbf{x}, \omega) \approx \left\{\beta(\mathbf{x}_1, \omega), \beta(\mathbf{x}_2, \omega), ..., \beta(\mathbf{x}_n, \omega)\right\}. \tag{7.2.1}$$

An infinite number of random variables are required to completely characterize a random field, which poses a numerical challenge in modelling uncertainty in physical quantities that have spatial variations, hence necessitating the need for a reduced-order representation (i.e. reducing the infinite-dimensional probability space to finite-dimension). Such a procedure, commonly known as a finite dimensional noise assumption, can be achieved through any truncated spectral expansion of the random field in the probability space. One such choice is K-L expansion (Ma, 2010).

7.2.2 Karhunen-Loève Expansion

The K-L expansion of a random field $\beta(\mathbf{x},\omega)$ is based on the spectral expansion of its covariance function $K_{\beta\beta}(\mathbf{x},\mathbf{y})$, where $\mathbf{x}$ and $\mathbf{y}$ denote spatial coordinates, and ω denotes the random nature of the corresponding quantity. The K-L theorem is a projection of the random field $\beta(\mathbf{x},\omega)$ onto a particular Hilbert basis. It is analogous to a Fourier series representation of a function, but the distinction is that the "Fourier" coefficients are uncorrelated random variables. The K-L theorem can be stated as follows (Ghanem and Spanos, 1991)

Karhunen-Loève Theorem: Consider a random field $\beta(\mathbf{x},\omega)$ ($\mathbf{x}\in\mathcal{D}$) with the continuous covariance function $K_{\beta\beta}(\mathbf{x},\mathbf{y})$ on $\mathcal{D}^2$, there exist a summable sequence of non-negative numbers λ_i, orthonormal basis $\phi_i(\mathbf{x})(i\in\mathbb{N}_0)$ in $\mathcal{L}_2(\mathcal{D})$, and a sequence of zero-mean variance-one random variables $\xi_i(\omega)$ such that

$$\beta(\mathbf{x},\omega) = \bar{\beta}(\mathbf{x}) + \sum_{i=1}^{\infty} \sqrt{\lambda_i}\,\xi_i(\omega)\,\phi_i(\mathbf{x}), \tag{7.2.2}$$

and the convergence is in the mean square value and is uniform in $\mathbf{x}$. Furthermore, $\{\phi_i(\mathbf{x})\}$ are the eigenfunctions and $\{\lambda_i\}$ are the eigenvalues of the covariance kernel, and can be evaluated as the solution of the following Fredholm integral equation of the second kind as

$$\int_{\mathcal{D}} K_{\beta\beta}(\mathbf{x},\mathbf{y})\phi_i(\mathbf{y})\mathrm{d}\mathbf{y} = \lambda_i\phi_i(\mathbf{x}), \tag{7.2.3}$$

where $\bar{\beta}(\mathbf{x})$ denotes the mean of the random field, and $\mathcal{D}$ denotes the spatial domain over which the random field $\beta(\mathbf{x},\omega)$ is defined.

The covariance function $K_{\beta\beta}(\mathbf{x},\mathbf{y})$, being symmetric and positive definite by definition, has all its eigenfunctions mutually orthogonal and they form a complete set spanning the function space to which $\beta(\mathbf{x},\omega)$ belongs (Ghanem and Spanos, 1991). It is shown that the deterministic set $\left\{\sqrt{\lambda_i}\phi_i(\mathbf{x})\right\}$, which are orthogonal, are used to represent the field $\beta(\mathbf{x},\omega)$, and the random coefficients $\{\xi_i(\omega)\}$ used in the expansion are also orthogonal. This is the reason why K-L expansion is called "bi-orthogonal" expansion.

The most important aspect of K-L expansion is that the spatial random fluctuations have been decomposed into a set of deterministic functions in the spatial variables multiplying random coefficients that are independent of these variables. If the random field $\beta(\mathbf{x},\omega)$ is

Gaussian, then the random coefficients $\{\xi_i(\omega)\}$ form an orthogonal Gaussian vector. The K-L expansion is mean square convergent irrespective of the probabilistic structure of the field or process being expanded, provided it has a finite variance (Ghanem and Spanos, 1991). K-L expansion, given by equation (7.2.2), is quite useful in stochastic mechanics, because it provides a parametric representation of an arbitrary random field with bounded covariance functions. This representation does not require any spatial discretization of the domain.

In practice, the truncated K-L expansion is often used by truncating the order larger than M as

$$\beta(\mathbf{x},\omega) = \bar{\beta}(\mathbf{x}) + \sum_{i=1}^{M} \sqrt{\lambda_i}\,\xi_i(\omega)\,\phi_i(\mathbf{x}). \tag{7.2.4}$$

The second order statistics of the random field can be reproduced by the target covariance model as

$$\begin{aligned}\hat{K}_{\beta\beta}(\mathbf{x},\mathbf{y}) &= \mathrm{E}\left[\beta(\mathbf{x},\omega) - \bar{\beta}(\mathbf{x})\right]\mathrm{E}\left[\beta(\mathbf{y},\omega) - \bar{\beta}(\mathbf{y})\right] \\ &= \sum_{i=1}^{M}\sum_{j=1}^{M} \sqrt{\lambda_i\lambda_j}\phi_i(\mathbf{x})\phi_i(\mathbf{y})\mathrm{E}\left[\xi_i(\omega)\xi_j(\omega)\right] \\ &= \sum_{i=1}^{M} \lambda_i\phi_i(\mathbf{x})\phi_i(\mathbf{y}).\end{aligned} \tag{7.2.5}$$

7.2.3 An Optimization Scheme for Compatibility of the Target and Analytical Covariance Models

In general, solving the associated eigenvalue problem in equation (7.2.3) is not an easy task. Closed-form solutions are only available when the covariance kernel has simple functional forms, such as exponential and linear functions. When the covariance function is more complex, numerical methods are needed to solve the eigenvalue problem.

Moreover, the compatibility of the target covariance model $\hat{K}_{\beta\beta}(\mathbf{x},\mathbf{y})$, given by equation (7.2.2), with the analytical, $K_{\beta\beta}(\mathbf{x},\mathbf{y})$, is often required in the simulation of random field with an analytical covariance model. The compatibility is also employed as a way to validate the accuracy of calculated eigen-pairs in integral equation (7.2.3). Thus, an optimization scheme is employed in the following to accommodate the compatibility between the target

and the analytical covariance models, where parameter α_i is introduced to each calculated eigenvector $\phi_i(\mathbf{x})$, given by (Zhang *et al.*, 2013d)

$$\begin{aligned} &\text{Minimize } \left\|K_{\beta\beta}(\mathbf{x},\mathbf{y}) - \hat{K}_{\beta\beta}(\mathbf{x},\mathbf{y})\right\| = \left\|K_{\beta\beta}(\mathbf{x},\mathbf{y}) - \sum_{i=1}^{M} \lambda_i \cdot \alpha_i\phi_i(\mathbf{x}) \cdot \alpha_i\phi_i(\mathbf{y})\right\|, \\ &\text{subject to } \alpha_i \geqslant 0, \ \ i = 1, 2, \ldots, M, \end{aligned} \tag{7.2.6}$$

in which $\|\cdot\|$ denotes the $\mathcal{L}_2$ norm.

From equation (7.2.6), parameter α_i can be interpreted as a scaling factor of the eigenvector, whose amplitude is modulated without loss of the orthogonality, and this modification can be viewed as a postprocess scheme of the calculated eigenvectors. In spite of its simplicity, this scheme is very effective in modifying the target covariance model to be compatible with the analytical covariance. Incompatibility may result if the amplitude scaling parameter is not taken into consideration, such as the eigenvectors obtained in Arun *et al.* (2010). These observations will be shown through examples in Section 7.4.

To obtain the eigen-pairs of the analytical covariance model, a meshfree-Galerkin scheme in the solution of the associated eigenvalue problem (7.2.3) is illustrated in Section 7.3.

7.3 Meshfree-Galerkin Scheme in Eigenvalue Problems of Integral Equation

As discussed in Section 7.1, the meshfree-Galerkin scheme, employing meshfree shape functions as a complete set of basis functions, is more general and effective in solving the integral equation (Rahman and Xu, 2005). The meshfree shape functions, meshfree-Galerkin scheme, the assessment of meshfree-Galerkin scheme in solving the eigen-pairs of integral equation, and the representation of various covariance models are introduced in the following.

7.3.1 Meshfree Shape Function

Meshfree approximations for a scalar function $u(\mathbf{x}, t)$ in terms of the Lagrangian coordinates can be expressed as

$$u(\mathbf{x}, t) = \sum_{I \in \mathcal{S}} \Phi_I(\mathbf{x}) u_I(t) = \mathbf{\Phi}^T \mathbf{u}, \tag{7.3.1}$$

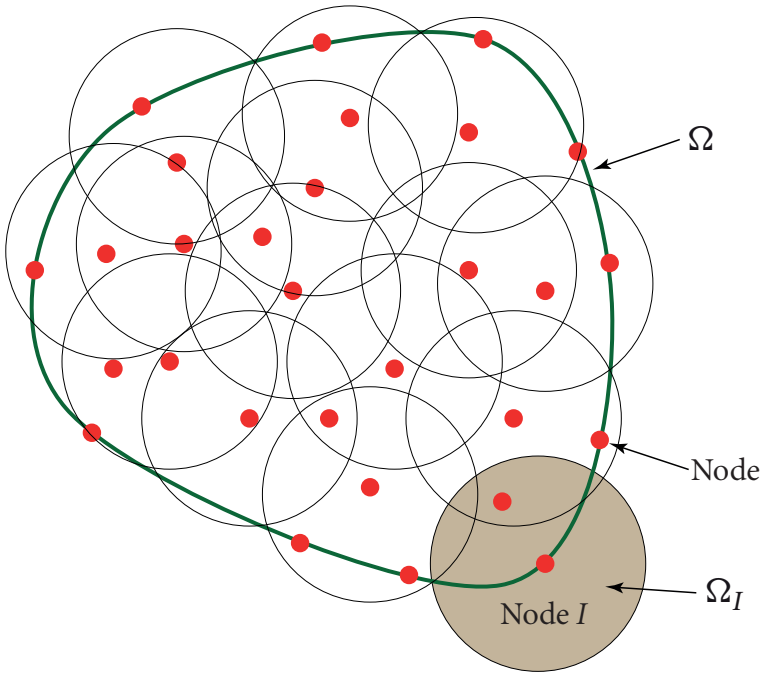

Figure 7.1 Discretization of meshfree method (nodes, domains of influence)

where $\Phi_I : \Omega \to \mathbb{R}$ are the shape functions, u_I are the nodal values at particles I located at position $\mathbf{x}_I$, and $\mathcal{S}$ is the set of nodes I for which $\Phi_I(\mathbf{x}) \neq 0$. Equation (7.3.1) is identical to a FEA approximation; however, it differs from FEA in that the shape function $\Phi_I(\mathbf{x})$ in equation (7.3.1) are only approximations and not interpolants, since $u_I \neq u(\mathbf{x}_I)$.

The shape functions Φ_I are obtained from the kernel (weight) functions, which are often called window or weighting functions, and they are denoted as $\omega_I : \Omega \to \mathbb{R}$. The kernel functions have compact support and the support size is defined by the dilatation parameters, which play the role of element size in the finite element method as shown in Figure 7.1. The weight function should be continuous and positive in its support, and the continuity of the shape function is determined solely by the continuity of the kernel function (Nguyen *et al.*, 2008).

For node I, the quartic spline kernel function used in this study has the following form

$$\Upsilon_I(r) = \begin{cases} 1 - 6r^2 + 8r^3 - 3r^4, & r \leqslant 1, \\ 0, & r \geqslant 1, \end{cases} \quad \text{with } r = \frac{\|\mathbf{x}_I - \mathbf{x}\|}{d_I}, \text{ for all node } I, \tag{7.3.2}$$

where d_I is the support size of node I. In the two-dimensional cases, circular and rectangular supports are usually used. It is noted from equation (7.3.2) that the weight function is expressed as a functional form with the scale parameters d_I and the dilation parameter $\|\mathbf{x}_I - \mathbf{x}\|$, causing the meshfree shape functions to be a set of function with different scale and dilation parameters. This observation is like the wavelet basis functions and it will be illustrated in the following paragraph.

The moving least squares (MLS) approximation method was first introduced by Shepard for constructing smooth approximations to fit a specified cloud of points (Shepard, 1968). It was then applied within the element-free Galerkin method by Belytschko *et al.* (1994). The approximation $u^h : \Omega \to \mathbb{R}$ of function $u : \Omega \to \mathbb{R}$ can be expressed as a polynomial of degree m with nonconstant coefficients. The local approximation around a point $\bar{x} \in \Omega$, evaluated at a point $x \in \Omega$, is given by

$$u_L^h(x, \bar{x}) = \mathbf{p}^T \mathbf{a}(\bar{x}), \tag{7.3.3}$$

where

$$\mathbf{p}^T(x) = \left\{1, x, x^2, ..., x^m\right\}, \tag{7.3.4}$$

and $\mathbf{a}(\bar{x})$ contains nonconstant coefficients that depend on $\mathbf{x}$ (hence the name moving)

$$\mathbf{a}^T(x) = \left\{a_0(x), a_1(x), a_2(x), ..., a_m(x)\right\}. \tag{7.3.5}$$

The unknown parameters $a_j(x)$ are determined at any points x by minimizing the functional $\mathcal{J}(x)$ as

$$\mathcal{J}(x) = \sum_{I=1}^{n} \omega(x - x_I)\Big[u_L^h(x_I, x) - u_I\Big]^2 = \sum_{I=1}^{n} \omega(x - x_I)\left[\mathbf{p}^T(x_I)\mathbf{a}(x) - u_I\right]^2, \tag{7.3.6}$$

where n is the number of nodes in the neighborhood of x with the weight function $\Upsilon_I(x - x_I) \neq 0$.

An extremum of $\mathcal{J}(x)$ with respect to the coefficients $\mathbf{a}(x)$ can be obtained as

$$\sum_{I=1}^{n} \omega(x - x_I) p_1(x_I)\left[\mathbf{p}^T(x_I)\mathbf{a}(x) - u_I\right] = 0,$$

$$\sum_{I=1}^{n} \omega(x - x_I) p_2(x_I)\left[\mathbf{p}^T(x_I)\mathbf{a}(x) - u_I\right] = 0,$$

$$\vdots$$

$$\sum_{I=1}^{n} \omega(x - x_I) p_m(x_I) \left[\mathbf{p}^T(x_I)\mathbf{a}(x) - u_I \right] = 0. \tag{7.3.7}$$

Equations (7.3.7) can be written, by rearrangement, as

$$\sum_{I=1}^{n} \omega(x - x_I)\mathbf{p}(x_I)\mathbf{p}^T(x_I)\mathbf{a}(x) = \sum_{I=1}^{n} \omega(x - x_I)\mathbf{p}(x_I)u_I, \tag{7.3.8}$$

or

$$\mathbf{A}(x)\mathbf{a}(x) = \mathbf{B}(x)\mathbf{u}, \tag{7.3.9}$$

where

$$\mathbf{A}_{m\times m}(x) = \sum_{I=1}^{n} \omega(x - x_I)\mathbf{p}(x_I)\mathbf{p}^T(x_I), \tag{7.3.10}$$

$$\mathbf{B}_{m\times n}(x) = [\omega(x - x_I)\mathbf{p}(x_1), \omega(x - x_2)\mathbf{p}(x_2), ..., \omega(x - x_n)\mathbf{p}(x_n)]. \tag{7.3.11}$$

The solved $\mathbf{a}(x)$ in equation (7.3.9) can be substituted into equation (7.3.3) to yield

$$u_L^h(x, \bar{x}) = \mathbf{p}^T\mathbf{A}^{-1}(x)\mathbf{B}(x)\mathbf{u}. \tag{7.3.12}$$

Based on the approximation given in equation (7.3.1), the shape function from MLS approximation can be given by

$$\mathbf{\Phi}^T(x) = \mathbf{p}^T\mathbf{A}^{-1}(x)\mathbf{B}(x), \tag{7.3.13}$$

or the shape function $\Phi_I(x)$ associated with node I at a point x

$$\Phi_I(x) = \mathbf{p}^T\mathbf{A}^{-1}(x)\omega(x - x_I)\mathbf{p}(x_I). \tag{7.3.14}$$

The computation of the MLS shape functions involves the inverse of the moment matrix $\mathbf{A}$, which becomes burdensome in two and three dimensions. In order to avoid the direct computation of the inverse of the moment matrix, the MLS shape function is usually written in the form

$$\Phi_I(\mathbf{x}) = \mathbf{c}^T(\mathbf{x})\omega_I(\mathbf{x})\mathbf{p}(\mathbf{x}_I), \quad \text{where } \mathbf{A}(\mathbf{x})\mathbf{c}(\mathbf{x}) = \mathbf{p}(\mathbf{x}), \tag{7.3.15}$$

with

$$\mathbf{A}(\mathbf{x}) = \sum_{I=1}^{n} \omega_I(\mathbf{x})\mathbf{p}(\mathbf{x}_I)\mathbf{p}^T(\mathbf{x}_I). \tag{7.3.16}$$

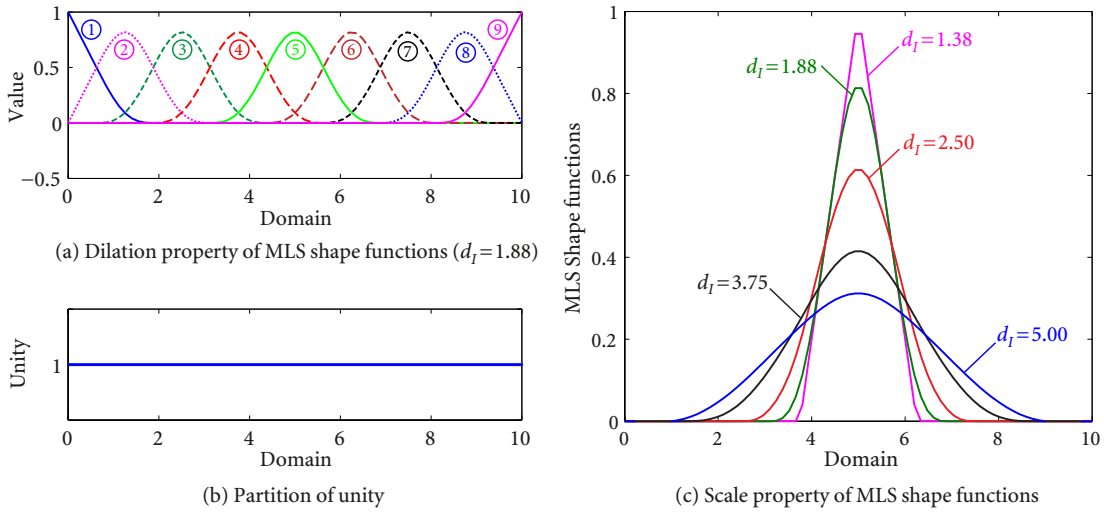

(a) Dilation property of MLS shape functions (d_I=1.88)

(b) Partition of unity

(c) Scale property of MLS shape functions

Figure 7.2 Dilation and scale properties of 1-D MLS shape functions

To compute $\mathbf{c}(\mathbf{x})$ efficiently in equation (7.3.15), the LU factorization of $\mathbf{A}$ is performed together with backward substitution as

$$\mathbf{LUc}(\mathbf{x}) = \mathbf{p}(\mathbf{x}), \quad \mathbf{Uc}(\mathbf{x}) = \mathbf{L}^{-1}\mathbf{p}(\mathbf{x}), \quad \mathbf{c}(\mathbf{x}) = \mathbf{U}^{-1}\mathbf{L}^{-1}\mathbf{p}(\mathbf{x}). \tag{7.3.17}$$

It is noted that the MLS shape functions obtained from equation (7.3.15) satisfy the rule of partition of unity, which is a paradigm where a domain is divided into overlapping subdomains Ω_I (in Figure 7.1), each of which is associated with a function $\Phi_I(\mathbf{x})$ that is nonzero only in Ω_I, and (Nguyen *et al.*, 2008)

$$\sum_{I=1}^{N} \Phi_I(\mathbf{x}) = 1, \quad \text{in } \Omega. \tag{7.3.18}$$

This characteristics of MLS shape functions can be observed from the following examples.

Consider a 1-D domain $0 \leqslant x \leqslant 10$, divided into 9 equal sub-domains, with the quartic spline weight function and size of sub-domains of influence 2.5, Figure 7.2(a) shows the dilation property of the MLS shape functions, a set of "moving" functions over the domain, and the property of partition of unit for these shape functions is presented in Figure 7.2(b). The scaling property of MLS shape functions at node 5 is shown in Figure 7.2(c), from which it is seen that the shape functions can exhibit different scale for different sizes of domain of influence. In addition, Figure 7.3(a) presents a typical 2-D MLS shape function (on

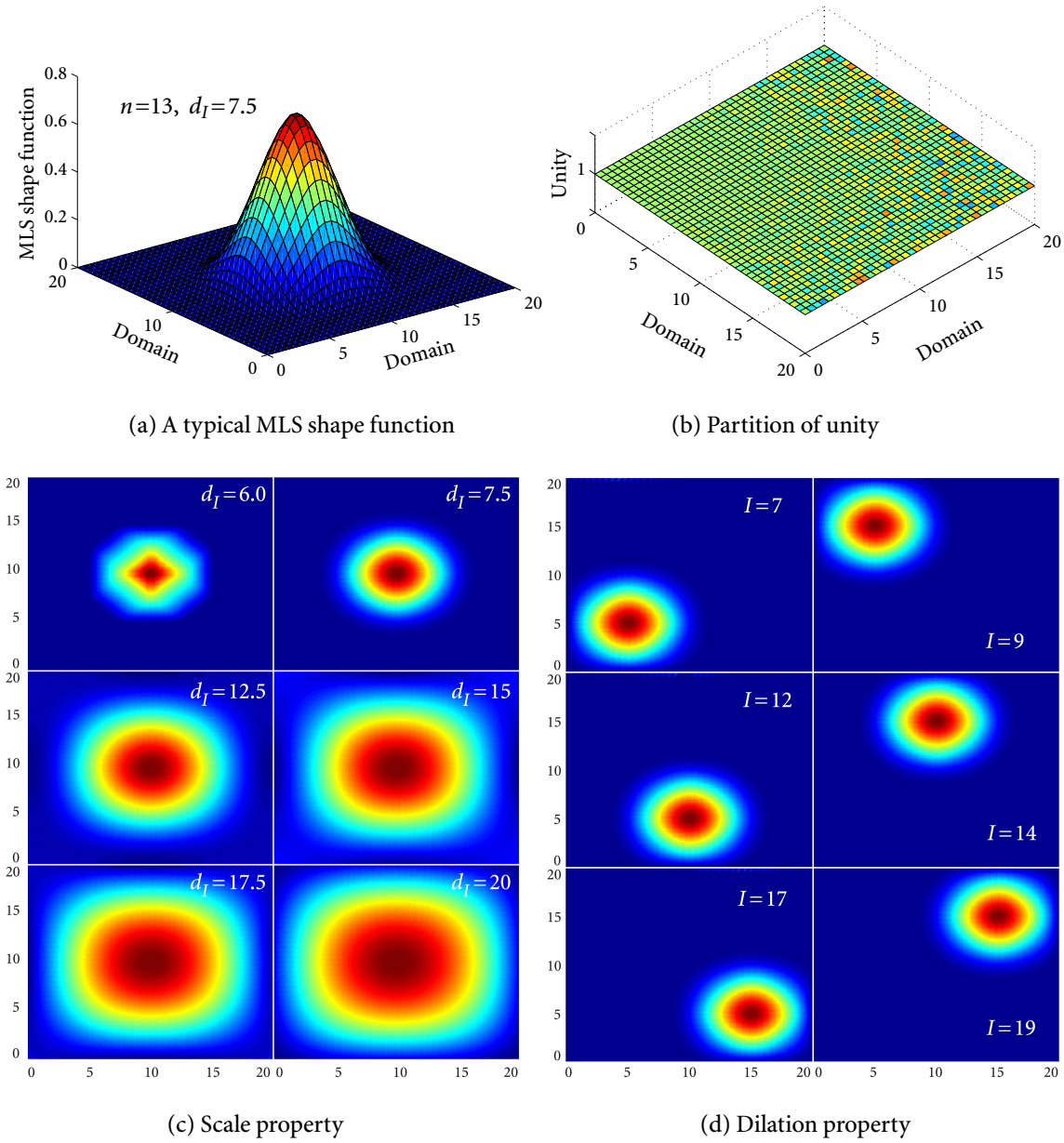

(a) A typical MLS shape function

(b) Partition of unity

(c) Scale property

(d) Dilation property

Figure 7.3 Dilation and scale properties of 2-D MLS shape functions

node 13 with $d_I = 7.5$), over domain $[x, y] = [0, 20] \times [0, 20]$, and the property of partition of unit for shape functions over this domain is shown in Figure 7.3(b). The scaling (with different domain of influence) and dilation (at different nodes) properties of the 2-D shape functions are given in Figure 7.3(c) and Figure 7.3(d). These observations from both 1-D

and 2-D examples show that the MLS shape functions, with partition of unity property and un-orthogonality, are similar to a set of wavelet basis functions, but are more advantageous than the wavelet basis functions that they can be applied in the following meshfree-Galerkin scheme in solving eigenvalue problems of integral equation.

7.3.2 Meshfree-Galerkin Scheme

The MLS shape functions $\Phi_k(\mathbf{x})$, obtained from equation (7.3.15), can be used as a set of basis functions in the Hilbert space $\mathbb{H}$ of the Galerkin scheme, and each eigenfunction of kernel $K_{\beta\beta}(\mathbf{x},\mathbf{y})$ may be represented approximately as

$$\phi_i(\mathbf{x}) = \sum_{k=1}^{N} d_{ik}\Phi_k(\mathbf{x}), \quad i=1,2,\ldots,N, \tag{7.3.19}$$

with an error ε_N^i resulting from truncating the summation after the Nth term given by

$$\varepsilon_N^i = \phi_i(\mathbf{x}) - \sum_{k=1}^{N} d_{ik}\Phi_k(\mathbf{x}). \tag{7.3.20}$$

Substituting equation (7.3.19) into equation (7.2.3) yields the following expression of error

$$\varepsilon_N^i = \sum_{k=1}^{N} d_{ik}\left[\int_{\mathcal{D}} K_{\beta\beta}(\mathbf{x},\mathbf{y})\Phi_k(\mathbf{y})\mathrm{d}\mathbf{y} - \lambda_i\Phi_k(\mathbf{x})\right]. \tag{7.3.21}$$

By setting the error in equation (7.3.21) to be orthogonal to each basis function $\Phi_j(\mathbf{x})$

$$\left(\varepsilon_N^i,\ \Phi_j(\mathbf{x})\right) = 0, \quad j=1,2,\ldots,N, \tag{7.3.22}$$

the following equation can be obtained

$$\sum_{k=1}^{N} d_{ik}\left[\int_{\mathcal{D}}\int_{\mathcal{D}} K_{\beta\beta}(\mathbf{x},\mathbf{y})\Phi_k(\mathbf{y})\Phi_j(\mathbf{x})\mathrm{d}\mathbf{x}\mathrm{d}\mathbf{y}\right] - \lambda_i\sum_{k=1}^{N} d_{ik}\left[\int_{\mathcal{D}}\Phi_k(\mathbf{x})\Phi_j(\mathbf{x})\mathrm{d}\mathbf{x}\right] = 0, \tag{7.3.23}$$

or

$$\mathbf{AD} = \mathbf{\Lambda BD}, \tag{7.3.24}$$

in which the components in all the $N\times N$ matrices are

$$A_{kj} = \int_{\mathcal{D}}\int_{\mathcal{D}} K_{\beta\beta}(\mathbf{x},\mathbf{y})\Phi_k(\mathbf{y})\Phi_j(\mathbf{x})\mathrm{d}\mathbf{x}\mathrm{d}\mathbf{y},\ D_{ik} = d_{ik},\ \Lambda_{ij} = \delta_{ij}\lambda_j,\ B_{kj} = \int_{\mathcal{D}}\Phi_k(\mathbf{x})\Phi_j(\mathbf{x})\mathrm{d}\mathbf{x}, \tag{7.3.25}$$

in which the dimensions of integral of A_{kj} for 1-D, 2-D, and 3-D fields are 2, 4, and 6, respectively, and these multiple integration in equation (7.3.25) can be integrated numerically by Gaussian quadrature method.

The generalized algebraic eigenvalue problem, in equation (7.3.24), can be solved to obtain the eigenvalue λ_i and coefficient d_{ik}, then the corresponding eigenfunction can be obtained from equation (7.3.19). The Galerkin scheme described above is known to produce lower bound solutions for the eigenvalues and is more accurate for eigenvalues than for eigenvectors (Ghanem and Spanos, 1991). The validity and accuracy of this meshfree-Galerkin scheme is assessed in Section 7.4.

7.4 Assessment of the Meshfree-Galerkin Scheme

To assess the validity and merits of the meshfree-Galerkin method introduced in Section 7.3, assessment of the resulting eigen-solutions of integral equation and the representation of various RF is conducted in the following.

7.4.1 Assessment of Solutions for Eigenvalue Problems of Integral Equation

Three commonly used covariance functions for both homogeneous and nonhomogeneous RF are employed to assess the validity and accuracy of meshfree-Galerkin scheme in obtaining the eigen-solutions of integral equation. Numerical solutions of these covariance models, with Galerkin scheme, using the Legendre polynomial and trigonometric basis functions are also presented for comparisons. Information regarding the Legendre polynomial and trigonometric basis functions is given in Appendix A.4.

Example 1. *Homogeneous field with rational spectra.* An example in this class is the first-order Markov random field that has the exponential covariance function

$$K_{\beta\beta}(x,y)=\sigma^2\exp\big(-|x-y|/l\big),\quad x,y\in[0,a], \tag{7.4.1}$$

where σ is the standard deviation of field $\beta(x)$, and l is the correlation parameter (Phoon *et al.*, 2002a). In this example, $\sigma=1$, $a=2$, $l=1, 0.5, 0.2$.

Example 2. *Stochastic field with squared exponential covariance.* Consider the random field with squared exponential covariance function

$$K_{\beta\beta}(x,y)=\sigma^2\exp\big(-(x-y)^2/l^2\big),\quad x,y\in[0,a], \tag{7.4.2}$$

where σ is the standard deviation of field $\beta(x)$, and l is the correlation parameter. In this example, $\sigma=1, a=2, l=1, 0.5, 0.2$. The squared exponential covariance function is differentiable everywhere, while the exponential covariance function in Example 1 is non-differentiable at the origin and this feature poses considerable difficulties for K-L expansion (Phoon *et al.*, 2002a).

Example 3. *Special class of nonhomogeneous field.* Consider the Wiener-Levy field with covariance function

$$K_{\beta\beta}(x,y)=\sigma^2\min(x,y),\quad x,y\in[0,a]. \tag{7.4.3}$$

In this example, $\sigma=a=1$. This example is provided to demonstrate that K-L expansion can provide an efficient and unified simulation tool for both homogeneous and nonhomogeneous fields if the proposed meshfree-Galerkin scheme is applied.

Figure 7.4 presents the eigen-results from the meshfree-Galerkin method and Galerkin schemes using the Legendre polynomial and trigonometric basis functions ($N_p=10$). It is seen that the meshfree-Galerkin scheme achieves good accuracy in obtaining the eigenvalues and eigenvectors (normalized with unit length) for both the homogeneous (exponential and squared exponential) and nonhomogeneous (Wiener–Levy) fields. Good agreement is also seen in the eigen-results for the exponential and squared exponential covariance models with different correlation lengths, i.e., $l/a=0.5, 0.25, 0.1$.

Moreover, it is observed that Galerkin scheme using meshfree shape functions can achieve more accurate and robust eigen-results than those based on the Legendre polynomial and trigonometric basis functions, as demonstrated in the resulting eigenvectors in Figure 7.4(b). All three methods can obtain eigenvalues accurately; the Galerkin scheme is more accurate in obtaining the eigenvalues than the eigenvectors (Ghanem and Spanos, 1991). Specifically, the meshfree-Galerkin method results in accurate and robust eigenvectors for the exponential, squared exponential, and Wiener–Levy covariance functions, while Galerkin scheme using the Legendre polynomial and trigonometric basis functions fail to

provide satisfactory results for the 6th eigenvector of the exponential and squared exponential covariance functions, and the covariance function of nonhomogeneous Wiener–Levy field, respectively.

An additional fact, shown in Figure 7.4(a), that should be noted is that the rate at which the magnitude of the eigenvalue decreases strongly depends on the correlation length parameter l (for the exponential and squared exponential covariance models). The smaller the value of l, the more contribution is expected from the terms associated with smaller eigenvalues (Ghanem and Spanos, 1991).

As demonstrated in Section 7.3.1, the meshfree shape functions are a set of basis functions, having scaling and dilation properties, and it plays an effective role in obtaining the eigen-results for covariance functions of various RF. It is therefore necessary to study the effects of the scaling property (number of discrete nodes over the domain) and dilation property (d_I/a) on the obtained eigen-results. Figure 7.5(a) shows the calculated eigenvalues and eigenvectors for the exponential and Wiener–Levy covariance models with different number of discrete nodes over the domain ($N_s = 5, 20, 50, 100$), where it is seen that the resulting eigen-pairs converge to the targets as the number of discrete node points increases, and the case of $N_s = 20$ can be reasonably selected due to its good accuracy of results and efficiency in computation time. As shown in Figure 7.5(b), the obtained eigenvalues of the squared exponential covariance model remain unchanged with the variation of scaling parameter of meshfree shape functions ($d_I/a = 0.0579, 0.1053, 0.1579, 0.2632$), which indicates that the scaling parameter of meshfree shape functions has minor influence on the obtained eigen-results. Similar results are also obtained for eigenvectors of the other two covariance functions, but are not reported here for the sake of brevity.

However, it should be noted that these conclusions are limited to most of commonly used covariance models that have regular eigenvectors, i.e., those selected in this study, but the resulting eigen-pairs may vary with d_I/a, and meshfree shape functions with smaller d_I/a may be required to capture local irregular variation of eigenvectors of certain covariance models that are not usually used.

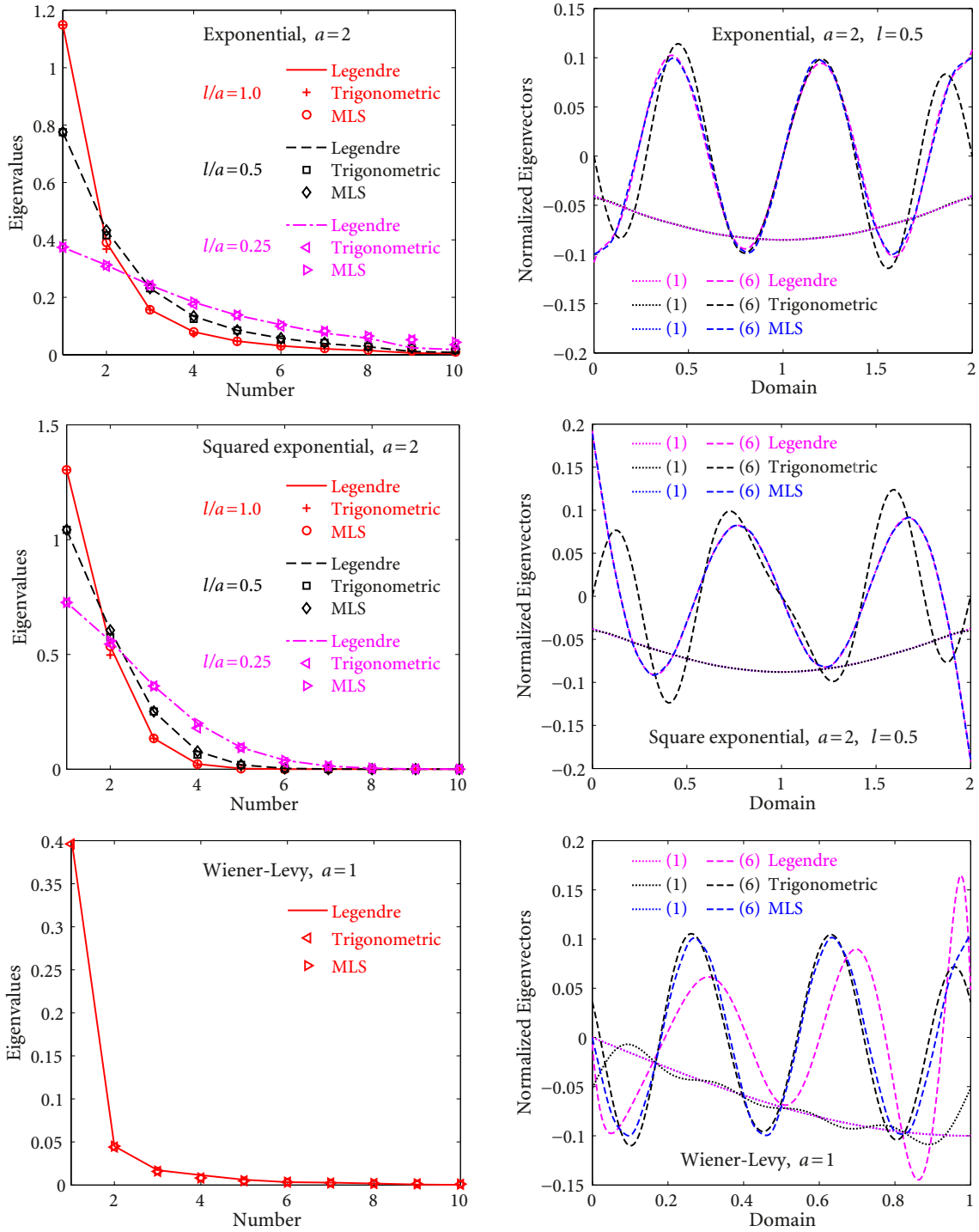

(a) Eigenvalues (b) Eigenvectors

Figure 7.4 Eigenvalues and eigenvectors

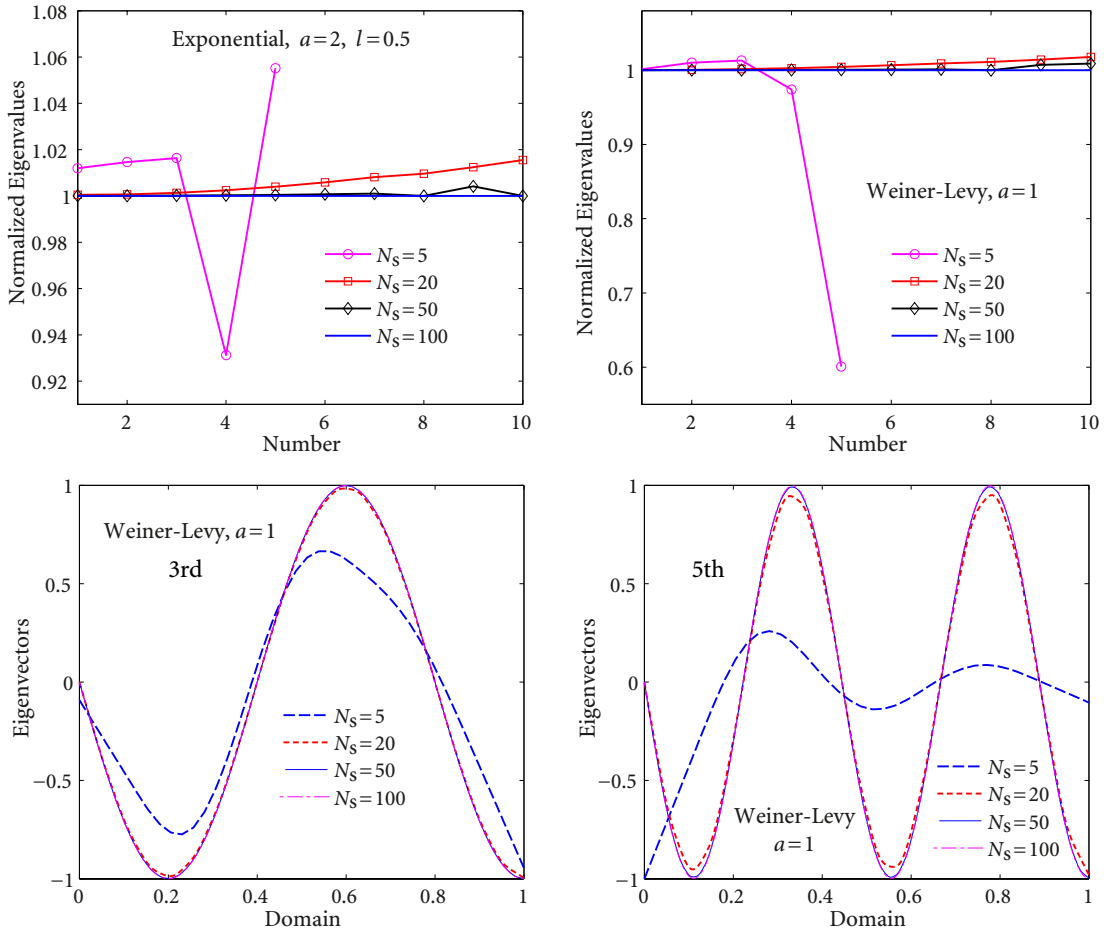

(a) Effect of dilation parameter (number of discrete points of domain)

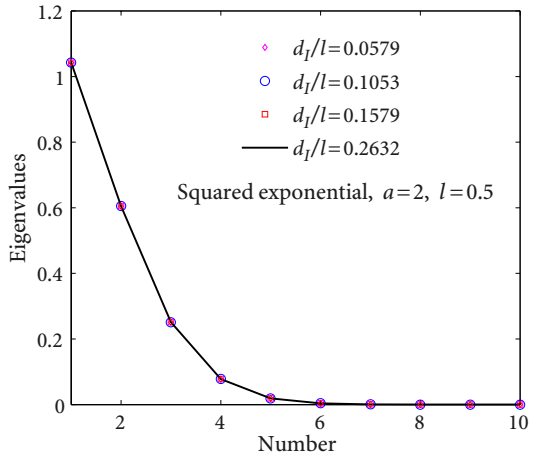

(b) Effect of scaling parameter

Figure 7.5 Convergence of meshfree-Galerkin scheme

7.4.2 Assessment on the Representation of Various Random Fields

The eigen-results, obtained through meshfree-Galerkin scheme in Section 7.4.1, are used to represent various RF with a wide range of covariance functions. A total of eight commonly used models are selected in Table 7.1 to assess the target covariance models, constructed from equation (7.2.5), and to compare between the target and analytical covariance functions.

The selected models in Table 7.1 include the first-order Markov field with exponential covariance function (#1), the second-order Markov field with linear-exponential (modified) covariance function (#2), the random field with squared exponential covariance function (#3), band-limited (truncated) white noise field with sine covariance function (#4), the binary noise field with triangular covariance (#5), and the nonhomogeneous fields #6, #7, and #8. The parameters of each model are listed in Table 7.1 and details of these models are provided in Ghanem and Spanos (1991).

Table 7.1: Selected covariance models (the homogeneous and nonhomogeneous, $\sigma = 1$)

No	Name	Covariance functions	[a, b]	Parameter
1	Exponential	$\sigma^2 \exp\left(-\frac{\lvert x_1 - x_2\rvert}{l}\right)$	$[0,2]$	$l = 0.5$
2	M-exponential[(1)]	$\sigma^2 \exp\left(-2.276\lvert x_1 - x_2\rvert\right)\left(1 + 2.276\lvert x_1 - x_2\rvert\right)$	$[0,2]$	-
3	S-exponential[(2)]	$\sigma^2 \exp\left(-\left[\frac{\lvert x_1 - x_2\rvert}{l}\right]^2\right)$	$[0,2]$	$l = 0.5$
4	T-white-noise[(3)]	$\sigma^2 \frac{\sin(x_1 - x_2)}{\pi(x_1 - x_2)}$	$[0,2]$	-
5	Triangular	$\sigma^2\left(1 - l\lvert x_1 - x_2\rvert\right)$	$[0,2]$	$l = 0.5$
6	Wiener-Levy	$\sigma^2 \min(x_1, x_2)$	$[0,1]$	-
7	Brownian-Bridge	$\sigma^2\left(\min(x_1, x_2) - \frac{x_1 x_2}{l}\right)$	$[0,1]$	$l = 1.0$
8	U-modulated[(4)]	$\sigma^2 \exp[-(x_1 + x_2)] \exp\left(\frac{\lvert x_1 - x_2\rvert}{l}\right)$	$[0,2]$	$l = 0.5$

(1) the modified exponential model. (2) the squared exponential model. (3) the truncated white noise model. (4) the uniformly modulated model (nonhomogeneous).

Figure 7.6(a) shows the first five eigenvectors for the modified exponential covariance model using meshfree-Galerkin method, which are in good agreement with the analytical

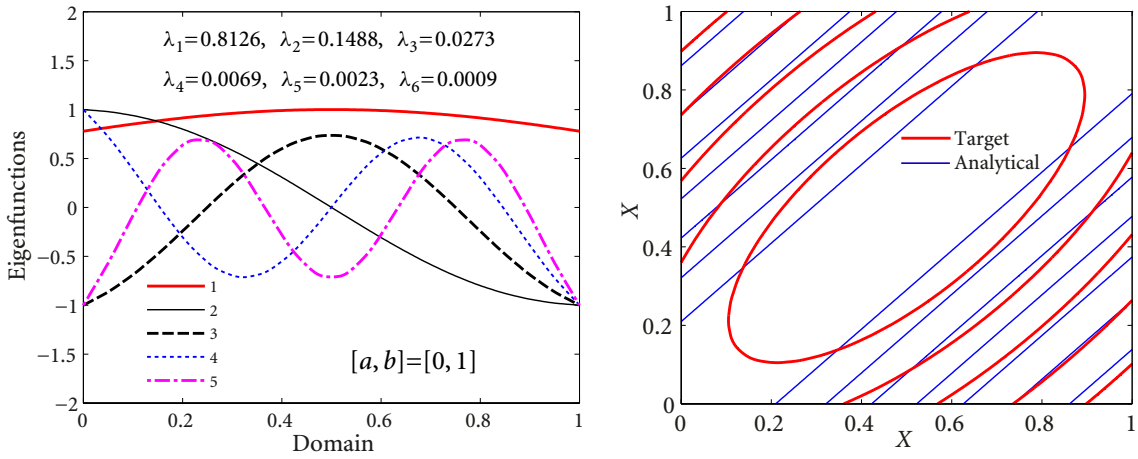

(a) Eigenvalues and eigenvectors

(b) Analytical and target covariance models

Figure 7.6 Eigen-pairs and contour plot of modified exponential covariance model

solutions (Spanos *et al.*, 2007; Arun *et al.*, 2010). Using these eigenvectors, the target covariance model is constructed by equation (7.2.5) ($M = 20$), without the optimization scheme proposed in equation (7.2.6), and is given in Figure 7.6(b) together with the analytical model. It is observed that the target covariance model, with sufficient truncated number $M = 20$, does not exhibit good agrement with the analytical modified covariance function. Similar observations and conclusions can also be obtained for other covariance models, but are not presented for brevity. However, this problem can be effectively resolved by using the optimization scheme in equation (7.2.6), which is shown in Figure 7.7.

The target and analytical covariance functions and their comparisons, for selected RF in Table 7.1, are shown in Figure 7.7. It is demonstrated that the meshfree-Galerkin scheme, in conjunction with K-L expansion and optimization scheme in Section 7.2.3, can accurately and effectively represent various homogeneous and nonhomogeneous RF with different covariance models. This is an additional validation on the accuracy, validity, and merits of the proposed scheme, which can be readily applied in the simulation of spatially varying soil properties in Section 7.5.

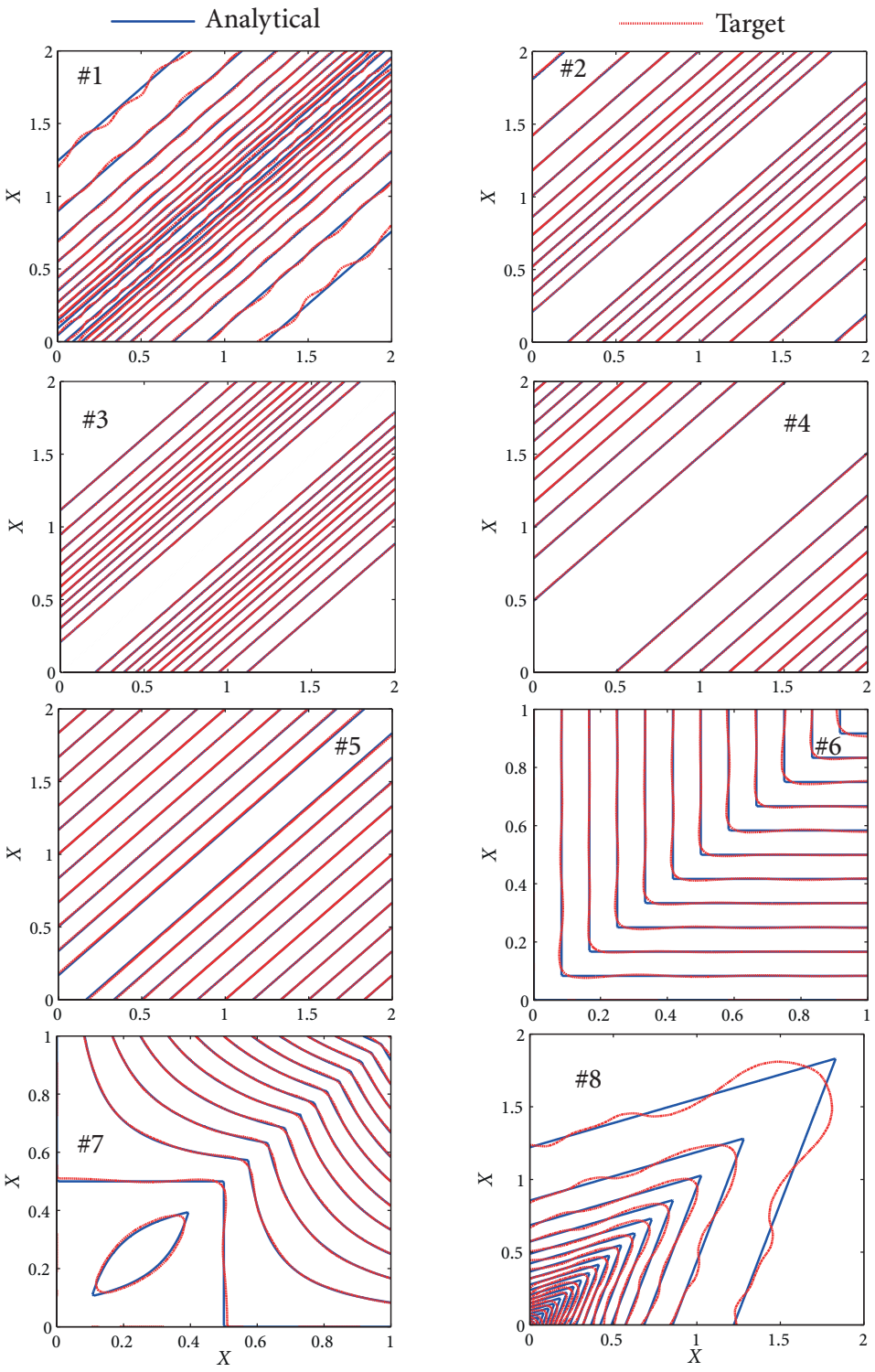

Figure 7.7 The various target and analytical covariance functions

7.5 Modelling and Synthesis of Spatially Varying Soil Properties

As discussed in Section 7.1, the site-specific soil properties are always random and variable in space, and these uncertainties and variabilities are demonstrated and qualified using the field measurements. In this section, the spatial variability modelling of soil properties is first qualified and calibrated using field measurements, based on which the meshfree-Galerkin scheme is applied to simulate these spatially varying soil properties.

7.5.1 Soil Variability Models Inferred from the Field Measurements

In practice, the physical properties of soil (e.g., shear modulus, cohesion, friction angle, elastic modulus, Poisson's ratio) and the associated uncertainties and variabilities can be inferred from the cone penetration test (CPT), vanes shear test (VST), or laboratory test during the soil investigation (Phoon and Kulhawy, 1999b; Popescu, 1995). The soil property $\beta(\mathbf{x})$ at space point $\mathbf{x}$ can be represented by

$$\beta(\mathbf{x}) = \bar{\beta}(\mathbf{x}) + \varepsilon_{\beta}(\mathbf{x}), \tag{7.5.1}$$

in which $\bar{\beta}(\mathbf{x})$ is the deterministic (trend) function giving the mean soil property, and $\varepsilon_{\beta}(\mathbf{x})$ is the residual at point $\mathbf{x}$, representing the uncertainty and spatial variability of soil property, which can be defined as a random field (Vanmarcke, 1977, 2010). $\varepsilon_{\beta}(\mathbf{x})$ is often attributed to include the inherent variability, the measurement errors, and the transformation uncertainty (Phoon and Kulhawy, 1999a), but only the inherent variability is considered in this study.

As seen from equation (7.5.1), the probabilistic characteristics of inherent spatial variability of soil can be represented by the trend function $\bar{\beta}(\mathbf{x})$, the marginal probability distribution function $\mathcal{P}_{\beta}$, and the covariance function $K_{\beta\beta}(\mathbf{x}, \mathbf{y})$ between spatial points $\mathbf{x}$ and $\mathbf{y}$ (the second-order random field). By varying $\mathcal{P}_{\beta}$, different types of RF, e.g., the Gaussian field, Gamma field and Beta field, can be obtained using generalized polynomial chaos expansion (gPCE) method. However, as discussed in Section 7.1, this topic is recommended for future research in Section 8.4.4.

The covariance function of random field $\beta(\mathbf{x})$ can be written as

$$K_{\beta\beta}(\mathbf{x},\mathbf{y}) = \mathrm{E}\left(\left[\beta(\mathbf{x}) - \bar{\beta}(\mathbf{x})\right]\left[\beta(\mathbf{y}) - \bar{\beta}(\mathbf{y})\right]\right) = \mathrm{E}[\varepsilon_\beta(\mathbf{x})\varepsilon_\beta(\mathbf{y})] = \sigma^2\rho_{\beta\beta}(\mathbf{x},\mathbf{y}), \quad (7.5.2)$$

where σ is the variance parameter, and $\rho_{\beta\beta}(\mathbf{x},\mathbf{y})$ is the correlation structure between spatial points $\mathbf{x}$ and $\mathbf{y}$. As seen from equations (7.5.1) and (7.5.2), the mean value $\bar{\beta}(\mathbf{x})$ varies with spatial location, which is a characteristic of nonhomogeneous field (generalized homogeneous field). In contrast, it can be reasonably assumed that the variance σ in equation (7.5.2) remains constant over the space, because σ may not exhibit large variation over the space, and it is very difficult to obtain the specific expressions of σ as a function of spatial location in practice. To the best knowledge of the authors, most of the soil variability models, determined from the field measurements, provide one scalar value of σ over the entire spatial domain for various types of soil (Phoon and Kulhawy, 1999a; Nobahar, 2003; Popescu, 1995).

After extensive research conducted in the evaluation and calibration of the probabilistic characteristics of soil property by geotechnical measurements (Phoon and Kulhawy, 1999b; Popescu, 1995; Cressie, 1993), the ranges of uncertainties in geotechnical properties have been suggested. The coefficient of variation, $C_v = \sigma/\bar{\beta}(\mathbf{x})$, was evaluated to account for uncertainty of soil property for various types of soil profiles due to the inherent variability. For the undrained shear strength of stiff clay soil deposits, a typical C_v ranges between 10% and 40%, and the variability may reach a possible upper limit of $C_v = 80\%$ for highly variable soft soil, both resulting solely from the inherent spatial variability of soil strength. In determining the spatial correlation structures of soil properties, various covariance models, such as those in Table 7.1, are calibrated from the field data, where it is demonstrated that most of the practical variations of soil properties in space follow these models (Vanmarcke, 2010; Popescu, 1995; Christakos, 1992).

However, to the best knowledge of the author, almost all of the field data, used for calibration of these models of soil physical properties, is limited to the 1-D random field. This may be due to the inconvenience of obtaining higher-dimensional measurements of soil mechanical properties in practice. Przewlocki (2000) presented the laboratory test of 2-D uniform layer of clay by simultaneously calibrating the probabilistic parameters of this

2-D random field for shear strength. Since the scope of this study is for the simulation of 1-D random field, the 1-D fields parametrized from the field measurements are selected in Table 7.2 (Przewlocki, 2000; Srivastava and Babu, 2009), which will be employed for simulation of spatially varying soil properties in Section 7.5.2.

Table 7.2: Selected 1-D random fields inferred from field measurements

$\beta(x)$	$\rho_{\beta\beta}(x,y)$	**Parameters**	**[a, b]**
c_u [(1)]	$\left(1+l\lvert x_1-x_2\rvert\right)\exp\left(-l\lvert x_1-x_2\rvert\right)$	$\bar{\beta}(x)=49.97, \sigma=14.99, l=3.588$ m	$(0, 4.5)$ m
E_s [(2)]	$\exp\left(-\left[\frac{\lvert x_1-x_2\rvert}{l}\right]^2\right)$	$\bar{\beta}(x)=5.5+1.189x, \sigma=2.87, l=4$ m	$(0, 8)$ m

[(1)] shear strength (KPa) (Przewlocki, 2000); [(2)] elastic modulus (MPa) (Srivastava and Babu, 2009).

7.5.2 Simulation of Spatially Varying Soil Properties

The RF, inferred from field measurements, in Table 7.2, can be simulated by using equation (7.2.4). The eigenvalues obtained from the meshfree-Galerkin method and the optimized eigenvectors by equation (7.2.6) are used for the field representation. As mentioned before, the components of random vector, $\xi_i(\omega)$, $i=1, 2, ..., M$, are uncorrelated but not independent. However, the independence between components of $\xi_i(\omega)$ is assumed in this study for simplicity, although Rosenblatt transformation can be used to resolve the problem to a set of independent random variables (Das *et al.*, 2009). Moreover, it has been numerically verified that this assumption can also give accurate results (Ma and Zabaras, 2011; Stefanou *et al.*, 2009).

Following the above simulation procedure, RF in Table 7.2 are represented. Figure 7.8(a) gives the simulated results of the shear strength c_u with variance $\sigma = 13.65$ KPa. It is seen that the variance of simulated shear strength is close to the target 14.99 KPa (Przewlocki, 2000), where good representation of uncertainties of the shear strength in the simulated results is observed. Besides the uncertainty, the spatial variability of simulated results can be seen from Figure 7.8(c), by using the optimized eigenvectors given in Figure 7.8(b). As observed, the simulated covariance model is in good agreement with the analytical model, which

shows the validity of the meshfree-Galerkin scheme in simulating the spatially varying soil properties.

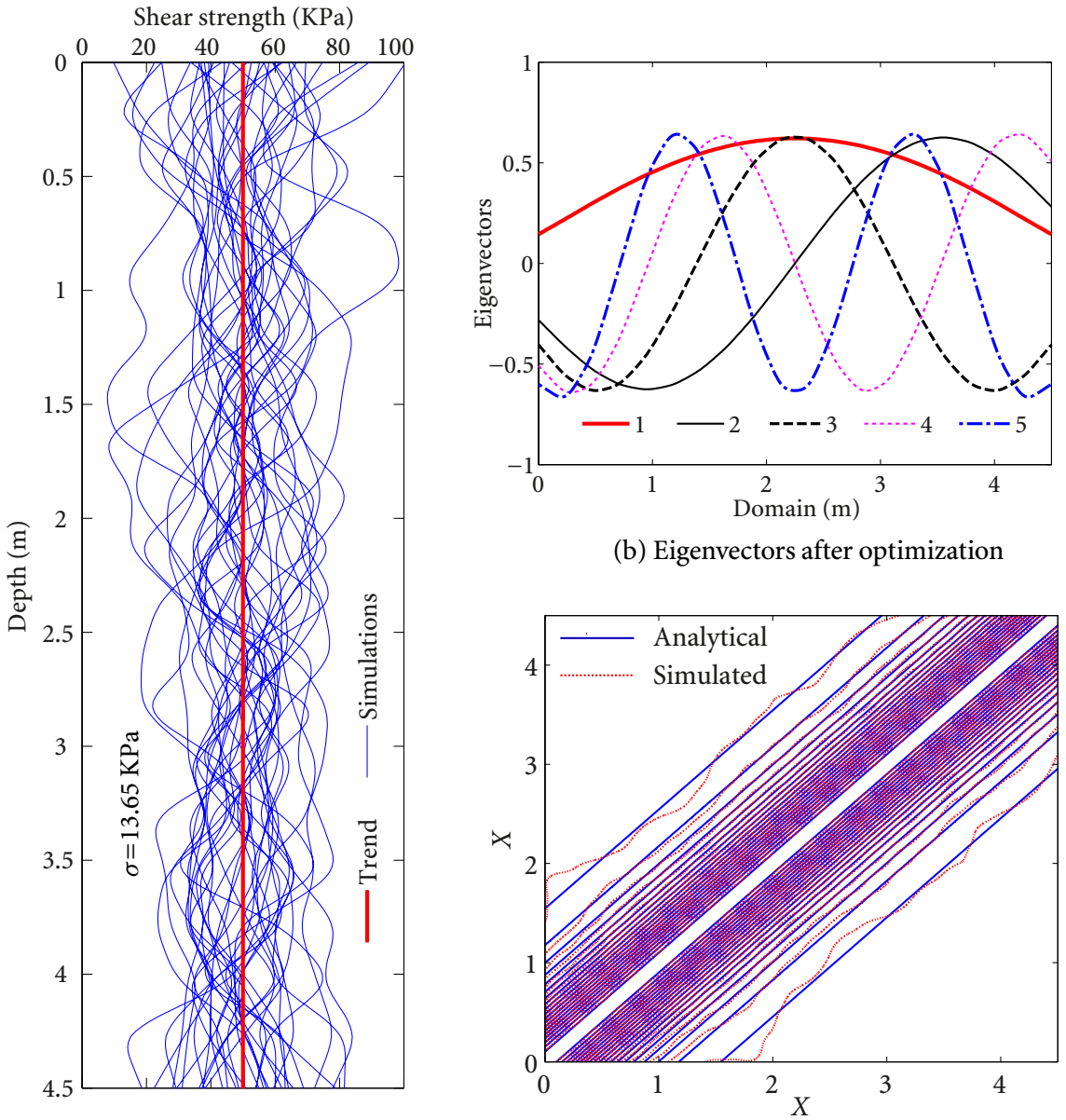

(a) Simulated results

(b) Eigenvectors after optimization

(c) Analytical and simulated convariance models

Figure 7.8 The simulated results for shear strength c_u

Similar observations can be made from Figure 7.9 for the simulation of elastic modulus E_s, the second random field in Table 7.2, based on the comparison of the simulated

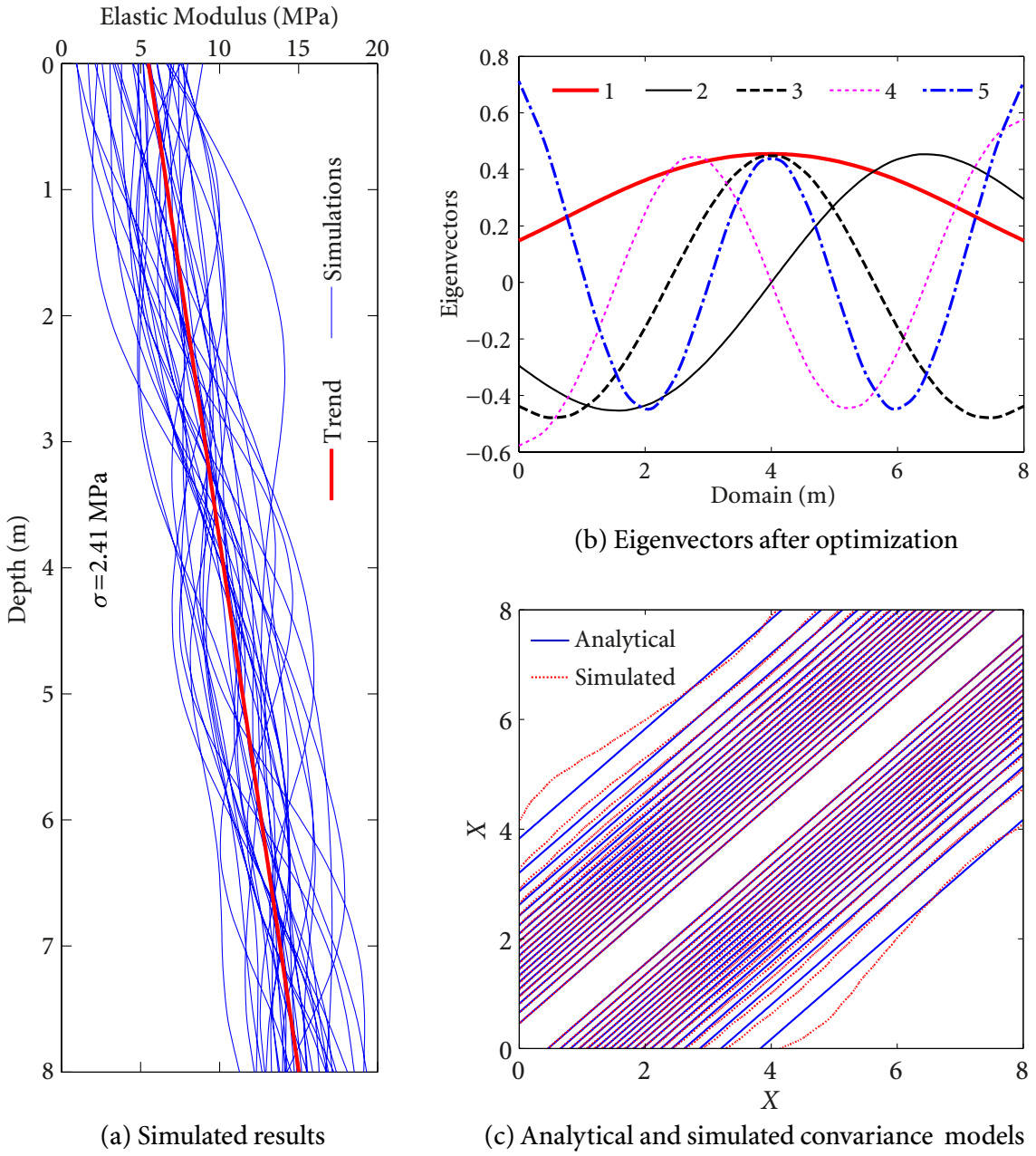

(a) Simulated results

(b) Eigenvectors after optimization

(c) Analytical and simulated convariance models

Figure 7.9 The simulated results for elastic modulus E_s

variance and covariance function with their target and analytical models. These results again demonstrate the validity of the meshfree-Galerkin scheme in simulating the spatially varying soil properties.

7.6 Summary and Conclusions

In this chapter, a meshfree-Galerkin approach is introduced within K-L expansion scheme for representation of spatial soil properties modelled as RF, which includes

1. The meshfree shape functions are introduced and employed as a set of basis functions in the Galerkin scheme to obtain the eigen-solutions of integral equation of K-L expansion. An optimization scheme is proposed for the resulting eigenvectors in treating the compatibility between the target and analytical covariance models.
2. The meshfree-Galerkin scheme is assessed by considering the resulting eigen-solutions and the representation of covariance models for various homogeneous and nonhomogeneous RF.
3. The accuracy and validity of the meshfree-Galerkin approach are demonstrated through the modelling and synthesis of the spatial field models, inferred from the field measurements, of soil properties.
4. Further studies should be conducted on the modelling and synthesis of RF of the spatial soil properties with higher dimensions and arbitrary domains, and the modelling of the probability distributions of the spatial soil field.

CHAPTER 8

Conclusions and Future Research

Recorded seismic ground motions exhibit spatial variations in their amplitude and phases, and spatial variations of ground motions have an important effect on the response of long structures, e.g., long span bridges. However, there is gap between the code-specified provisions and the realistic representation of spatially varying ground motions (SVGM) and the corresponding stochastic vibration analysis (SVA) approaches. This study is devoted to bridge this gap. The main contributions and findings are summarized below.

8.1 Modelling of SVGM

In Chapters 2 and 3, a complete and realistic SVGM representation approach is developed by accounting for the incoherence effect, wave-passage effect, site-response effect, ground motion nonstationarity, tridirectionality, and spectrum-compatibility. It includes

1. The physically compliant seismological spectra are employed to synthesize SVGM and their earthquake scenarios are determined by vector-valued seismic hazard deaggregation (VSHD), based on which a simulation framework is proposed to resolve the problem that a number of simulations need to be carried out for the uniform hazard spectra (UHS)-based ground motion generation.

2. A comprehensive method of accounting for varying site effects in synthesizing SVGM is proposed, including consideration of spatial-random-variable soil profiles, effect of

water saturation, effect of varying site conditions, and combining P-wave, SV-wave, and SH-wave motions to simulate tridirectional SVGM.

3. The phase difference method is developed and proved to be effective in conditional modelling of nonstationarity of SVGM.
4. Modelling of SVGM nonstationarity and spectrum-compatibility within the spectral representation method (SRM) scheme is established. A scheme of transforming response spectra at bedrock to the ground surface in tridirections using the site amplification method is developed.
5. Study of local site effects on the loss of motion coherency shows that the local site can significantly reduce the lagged coherency at certain frequencies, and they will not only cause the phase difference of coherency function but also affect the modulus of coherency function.
6. The synthesized SVGM can be applied to provide more refined solutions for quantitatively assessing the code-specified design provisions and developing new design provisions.

8.2 Development of SVA Approaches for Structures under SVGM

In Chapters 4, 5, and 6, a comprehensive, systematic, and efficient stochastic seismic analysis approach is derived for long span structures under tridirectional nonstationary spatial motions, considering ground motion incoherence effect, wave-passage effect, tridirectional local site effect (uniform and non-uniform site conditions), nonstationarity, and tridirectionality, which includes

1. An absolute-response-oriented scheme of pseudo-excitation method (PEM) (in time domain) is developed to reduce the enormous computational effort of the conventional indirect nonstationary SVA (in frequency domain) in solving equations of motion of structures under nonstationary tridirectional SVGM.
2. The improved high precision direct integration method (I-HPDIM), in conjunction with absolute-response-oriented scheme of PEM, has been derived for nonstationary

SVA of structures under tridirectional SVGM. The proposed I-HPDIM has resolved the bottle-neck problem of conventional HPDIM and, as a result, it can significantly improve computational efficiency of HPDIM in nonstationary SVA.

3. A scheme in accounting for tridirectional varying site-response effect is incorporated in the nonstationary SVA scheme systematically.
4. The proposed highly efficient and accurate SVA approach is implemented and verified in the general finite element analysis (FEA) platform to make it readily applicable in stochastic seismic analysis of complex structures.
5. This analytical SVA approach is more attractive in engineering practices for nonstationary stochastic seismic analysis of long span structures under tridirectional SVGM.
6. Based on the proposed SVA approach, parametric studies of a practical long span arch bridge and a long span high-pier railway bridge under SVGM are conducted.
7. The design values (considering structure ductility) can be further determined by dividing the elastic effects (obtained from the developed SVA approaches) by the appropriate behaviour factor q, which is recommended in D.3.2 of CEN (2005b).

8.3 Random Field Representation of Spatial Soil Profiles

To account for spatial randomness and variability of soil properties in soil-structure interaction (SSI) analysis of bridges under SVGM, a meshfree-Galerkin approach is proposed in Chapter 7 within the Karhunen-Loève (K-L) expansion scheme for representation of spatial soil properties modelled as random field (RF), which includes

1. The meshfree shape functions are introduced and employed as a set of basis functions in the Galerkin scheme to obtain the eigen-solutions of integral equation of K-L expansion. An optimization scheme is proposed for the resulting eigenvectors in treating the compatibility between the target and analytical covariance models.
2. The meshfree-Galerkin scheme is assessed by considering the resulting eigen-solutions and the representation of covariance models for various homogeneous and nonhomogeneous RF.

3. The accuracy and validity of the meshfree-Galerkin approach are demonstrated through the modelling and synthesis of the spatial field models, inferred from the field measurements, of soil properties.

8.4 Recommendations for Future Research

Following the conclusions drawn from Sections 8.1, 8.2, and 8.3, the following topics for future studies in the area of bridge responses under SVGM are recommended.

8.4.1 Development of Simplified Design Provisions for Bridges under SVGM

In Chapters 2 to 6, methodologies on modelling of SVGM and SVA approaches for long structures under SVGM are developed. These approaches can provide more refined solutions for quantitatively assessing the code-specified design provisions and developing new design provisions. It is found that CEN (2005b) is currently the only seismic code worldwide that gives a set of detailed guidelines to explicitly tackle spatial variabilities of ground motions in bridge design. Hence, development of these simplified design procedures in many other bridge seismic guidelines worldwide need to be conducted in the future.

8.4.2 Incorporation of SSI Effect in the SVA Methodology

The SVA approaches developed in Chapter 4 fail to include the SSI effect for simplicity; however, spatial variations of ground motions can be further modified by the SSI effect, and SSI is well-recognized to significantly affect structural responses but has not been adequately considered for structures under SVGM. Therefore, further investigations on inclusion of SSI effect in the SVA methodology are recommended.

8.4.3 Performance-based Seismic Pounding Analysis of Bridges

In Section 6.3.1, only the local site effects of SVGM on the longitudinal required separation distance (RSD) between adjacent bridge segments are studied. Some other rarely studied effects on the RSD, e.g., ground motion dimensionality, ground motion nonstationarity, 3-D surface-to-surface pounding modelling, the RSD in the transverse direction, SSI, need to be

studied in the future using the SVA approaches provided in Chapters 4 and 6. Furthermore, more rational approaches, e.g., the performance (reliability)-based methods for seismic pounding risk analysis, are also recommended in mitigating seismic pounding of bridge structures (Lin and Weng, 2001; Barbato and Tubaldi, 2012).

8.4.4 2-D and 3-D RF Representation of Spatial Soil using Generalized Polynomial Chaos Expansion

In modelling the spatial soil field in Chapter 7, only 1-D spatially varying soil properties are simulated based on the proposed meshfree-Galerkin scheme in conjunction with the K-L expansion. Further studies should be conducted on the modelling and synthesis of RF of the spatial soil properties with higher dimensions (2-D or 3-D) and arbitrary domains, and the modelling of the probability distributions of the spatial soil field (e.g., the Gaussian field, Gamma field, or Beta field) using the generalized polynomial chaos expansion (gPCE) method (Xiu, 2010).

Bibliography

AASHTO, 2002. *Standard Specifications for Highway Bridges (17th Edition)*. American Association of State Highway and Transportation Officials (AASHTO), Washington.

Abrahamson, N. and Silva, W., 1997. Empirical response spectral attenuation relations for shallow crustal earthquakes. *Seismological Research Letters*, **68**(1), 94–127.

Arun, C.O., Rao, B.N., and Srinivasan, S.M., 2010. Stochastic meshfree method for elasto-plastic damage analysis. *Computer Methods in Applied Mechanics and Engineering*, **199**(37), 2590–2606.

ASCE, 1998. *Seismic Analysis of Safety-related Nuclear Structures and Commentary, ASCE Standard **4-98***. American Society of Civil Engineers (ASCE).

ATC/MCEER, 2003. *Recommended LRFD Guidelines for the Seismic Design of Highway Bridges*, volume MCEER/ATC-49. Applied Technology Council (ATC) and Multidisciplinary Center for Earthquake Engineering Research (MCEER), California.

Ates, S., Bayraktar, A., and Dumanoglu, A.A., 2006. The effect of spatially varying earthquake ground motions on the stochastic response of bridges isolated with friction pendulum systems. *Soil Dynamics and Earthquake Engineering*, **26**(1), 31–44.

Ates, S., Dumanoglu, A.A., and Bayraktar, A., 2005. Stochastic response of seismically isolated highway bridges with friction pendulum systems to spatially varying earthquake ground motions. *Engineering Structures*, **27**(13), 1843–1858.

Atkinson, G., 2009. Earthquake time histories compatible with the 2005 National Building Code of Canada Uniform Hazard Spectrum. *Canadian Journal of Civil Engineering*, **36**(6), 991–1000.

Barbato, M. and Tubaldi, E., 2012. A probabilistic performance-based approach for mitigating the seismic pounding risk between adjacent buildings. *Earthquake Engineering and Structural Dynamics*.

Bazyar, M.H. and Song, C., 2008. A continued-fraction-based high-order transmitting boundary for wave propagation in unbounded domains of arbitrary geometry. *International Journal for Numerical Methods in Engineering*, **74**(2), 209–234.

Bazzurro, P. and Cornell, C.A., 1999. Disaggregation of seismic hazard. *Bulletin of the Seismological Society of America*, **89**(2), 501–520.

Bazzurro, P. and Park, J., 2011. Vector-valued probabilistic seismic hazard analysis of correlated ground motion parameters. In Faber, M., Koehler, J., and Nishijima, K., editors, *Applications of Statistics and Probability in Civil Engineering*, 1596–1603, Zürich, Switzerland. CRC Press.

Belytschko, T., Lu, Y.Y., and Gu, L., 1994. Element-free Galerkin methods. *Computer Methods in Applied Mechanics and Engineering*, **37**(2), 229–256.

Berrah, M. and Kausel, E., 1992. Response spectrum analysis of structures subjected to spatially varying motions. *Earthquake Engineering and Structural Dynamics*, **21**(6), 461–470.

Bi, K., Hao, H., and Chouw, N., 2011. Influence of ground motion spatial variation, site condition and SSI on the required separation distances of bridge structures to avoid seismic pounding. *Earthquake Engineering and Structural Dynamics*, **40**(9), 1027–1043.

Bi, K. and Hao, H., 2010. Influence of irregular topography and random soil properties on coherency loss of spatial seismic ground motions. *Earthquake Engineering and Structural Dynamics*, **40**(9), 1045–1061.

Bi, K. and Hao, H., 2011. Influence of irregular topography and random soil properties on coherency loss of spatial seismic ground motions. *Earthquake Engineering and Structural Dynamics*, **40**(9), 1045–1061.

Bi, K. and Hao, H., 2013. Numerical simulation of pounding damage to bridge structures under spatially varying ground motions. *Engineering Structures*, **46**, 62–76.

Bolt, B.A., Loh, C.H., Penzien, J., Tsai, Y.B., and Yeh, Y.T., 1982. *Preliminary Report on the SMART-1 Strong Motion Array in Taiwan*. Report No. UCB/EERC-82/13, Earthquake Engineering Research Center, University of California, Berkeley, California.

Boore, D., 1983. Stochastic simulation of high-frequency ground motions based on seismological model of the radiated spectra. *Bulletin of the Seismological Society of America*, **73**(6A), 1865–1894.

Boore, D., 2003A. Simulation of ground motion using stochastic method. *Pure and Applied Geophysics*, **160**, 635–676.

Boore, D., 2003B. Phase derivatives and simulation of strong ground motions. *Bulletin of the Seismological Society of America*, **93**(3), 1132–1143.

Brune, J.N., 1970. Tectonic stress and the spectra of seismic shear waves from earthquakes. *Journal of Geophysical Research*, **75**(26), 4997–5009.

Cacciola, P. and Deodatis, G., 2011. A method for generating fully nonstationary and spectrum-compatible ground motion vector processes. *Soil Dynamics and Earthquake Engineering*, **31**(3), 351–360.

Caglayan, O., Ozakgul, K., Tezer, O., and E, E. Uzgider, 2011. Evaluation of a steel railway bridge for dynamic and seismic loads. *Journal of Constructional Steel Research*, **67**(8), 1198–1211.

Campbell, K.W., 2003. Prediction of strong ground motion using the hybrid empirical method and its use in the development of ground-motion (attenuation) relations in Eastern North America. *Bulletin of the Seismological Society of America*, **93**(3), 1012–1033.

Caughey, T.K. and Stumpf, H.J., 1961. Transient response of a dynamic system under random vibration. *Journal of Applied Mechanics*, **28**, 563–566.

CEN, 2005B. *Eurocode 8: Design Provisions of Structures for Earthquake Resistance, Part 2: Bridges*, volume EN 1998-2. Comité Européen de Normalisation, Brussels.

Chouw, N. and Hao, H., 2008. Significance of SSI and nonuniform near-fault ground motions in bridge response I: Effect on response with conventional expansion joint. *Engineering Structures*, **30**(1), 141–153.

Christakos, G., 1992. *Random Field Models in Earth Sciences*. Academic Press, Inc., California.

Conte, J.P., Pister, K.S., and Mahin, S.A., 1992. Nonstationary ARMA modeling of seismic motions. *Soil Dynamics and Earthquake Engineering*, **11**(7), 411–426.

Cressie, N., 1993. *Statistics for Spatial Data*. John Wiley & Sons, Inc., New York.

CSA, 2006. *Commentary on CAN/CSA-S6-06, Canadian Highway Bridge Design Code*. Canadian Standards Association.

Das, S., Ghanem, R.G., and Finette, S., 2009. Polynomial chaos representation of spatio-temporal random fields from experimental measurements. *Journal of Computational Physics*, **228**(23), 8726–8751.

Datta, T.K., 2010. *Seismic Analysis of Structures*. John Wiley and Sons, Singapore.

Davenport, A.G., 1964. Note on the distribution of the largest value of a random function with application to gust loading. *Proceedings of the Institution of Civil Engineers*, **28**(2), 187–196.

Deodatis, G., 1996. Nonstationary stochastic vector processes: seismic ground motion applications. *Probabilistic Engineering Mechanics*, **11**(3), 149–167.

Der Kiureghian, A. and Fujimura, K., 2009. Nonlinear stochastic dynamic analysis for performance-based earthquake engineering. *Earthquake Engineering and Structural Dynamics*, **38**(5), 719–738.

Der Kiureghian, A. and Neuenhofer, A., 1992. Response spectrum method for multi-support seismic excitations. *Earthquake Engineering and Structural Dynamics*, **21**(8), 713–740.

Der Kiureghian, A., 1980. Structural response to stationary excitation. *Journal of the Engineering Mechanics Division*, **106**(6), 1195–1213.

Der Kiureghian, A., 1996. A coherency model for spatially varying ground motions. *Earthquake Engineering and Structural Dynamics*, **25**(1), 99–111.

Dumanoglu, A.A. and Soyluk, K., 2003. A stochastic analysis of long span structures subjected to spatially varying ground motions including the site-response effect. *Engineering Structures*, **25**(10), 1301–1310.

FEMA, 2010. *Earthquake-Resistant Design Concepts: An Introduction to the NEHRP Recommended Seismic Provisions for New Buildings and Other Structures*, volume FEMA P-749.

Federal Emergency Management Agency (FEMA).

Ghanem, R.G. and Spanos, P.D., 1991. *Stochastic Finite Element: A Spectral Approach*. Springer-Verlag, New York.

Hao, H., Oliveira, C.S., and Penzien, J., 1989. Multiple-station ground motion processing and simulation based on SMART-1 array data. *Nuclear Engineering and Design*, **111**(3), 193–310.

Hao, H., 1993. Arch responses to correlated multiple excitations. *Earthquake Engineering and Structural Dynamics*, **22**(5), 389–404.

Hao, H., 1994. Ground-motion spatial variation effects on circular arch responses. *Journal of Engineering Mechanics*, **120**(11), 2326–2341.

Hao, H., 1998. A parametric study of the required seating length for bridge decks during earthquake. *Earthquake Engineering and Structural Dynamics*, **27**(1), 91–103.

Harichandran, R.S., Hawwari, A., and Sweidan, B.N., 1996. Response of long span bridges to spatially varying ground motion. *Journal of Structural Engineering*, **122**(5), 476–484.

Harichandran, R.S. and Vanmarcke, E.H., 1986. Stochastic variation of earthquake ground motion in space and time. *Journal of Engineering Mechanics*, **112**(2), 154–174.

Harichandran, R.S., 1991. Estimating the spatial variation of earthquake ground motion from dense array recordings. *Structural Safety*, **10**(1), 219–233.

Heredia-Zavoni, E. and Santa-Cruz, S., 2000. Conditional simulation of a class of nonstationary space-time random fields. *Journal of Engineering Mechanics*, **126**(4), 398–404.

Heredia-Zavoni, E. and Vanmarcke, E.H., 1994. Seismic random-vibration analysis of multisupport-structural systems. *Journal of Engineering Mechanics*, **120**(5), 1107–1128.

Housner, G.W., 1947. Characteristics of strong-motion earthquakes. *Bulletin of the Seismological Society of America*, **37**(1), 19–31.

Housner, G. and Jennings, P., 1977. *Earthquake Design Criteria for Structures*. Report No. EERL-77-06, Earthquake Engineering Research Laboratory (EERL), California Institute of Technology, California.

Hu, L., Xu, Y.L., and Zheng, Y., 2012. Conditional simulation of spatially variable seismic ground motions based on evolutionary spectra. *Earthquake Engineering and Strcutral Dynamics*, **41**(15), 2125–2139.

Jayaram, N. and Baker, J.W., 2008. Statistical tests of the joint distribution of spectral acceleration values. *Bulletin of the Seismological Society of America*, **98**(5), 2231–2243.

Jennings, P.C., Housner, G.W., and Tsai, N.C., 1968. *Simulated Earthquake Motions*. Earthquake Engineering Research Laboratory, California Institute of Technology, California.

Jia, H-Y., Zhang, D-Y., Zheng, S-X., Xie, W-C., and Pandey, M.D., 2013. Local site effects on a high-pier railway bridge under tridirectional spatial excitations: nonstationary stochastic analysis. *Soil Dynamics and Earthquake Engineering*, **52**, 55–69.

JRA, 2002. *Design Specifications of Highway Bridges, Part V. Seismic Design*. Japan Road Association (JRA), Tokyo.

Kameda, H. and Morikawa, H., 1994. Conditioned stochastic processes for conditional random fields. *Journal of Engineering Mechanics*, **120**(4), 855–875.

Kawashima, K. and Mizoguti, A., 2000. Seismic response of a reinforced concrete arch bridge. In *12th World Conference on Earthquake Engineering*, Auckland, New Zealand.

Kim, S-H. and Feng, M.Q., 2003. Fragility analysis of bridges under ground motion with spatial variation. *International Journal of Non-Linear Mechanics*, **38**(5), 705–721.

Kohnke, P., 2010. *ANSYS Theory Reference-Release 13.0*. ANSYS Inc.

Konakli, K. and Der Kiureghian, A., 2011A. Extended MSRS rule for seismic analysis of bridges subjected to differential support motions. *Earthquake Engineering and Structural Dynamics*, **40**(12), 1315–1335.

Konakli, K. and Der Kiureghian, A., 2011B. Simulation of spatially varying ground motions including incoherence, wave-passage and differential site-response effects. *Earthquake Engineering and Structural Dynamics*, **41**(3), 495–513.

Konakli, K. and Der Kiureghian, A., 2012. Simulation of spatially varying ground motions including incoherence, wave-passage and differential site-response effects. *Earthquake Engineering and Structural Dynamics*, **41**(3), 495–513.

Kramer, S.L., 1996. *Geotechnical Earthquake Engineering*. Prentice-Hall, New Jersey.

Krishnamoorthy, A. and Menon, D., 2011. Matrix inversion using cholesky decomposition. *arXiv preprint arXiv:1111.4144*.

Liao, S. and Li, J., 2002. A stochastic approach to site-response component in seismic ground motion coherency model. *Soil Dynamics and Earthquake Engineering*, **22**(9), 813–820.

Liao, S. and Zerva, A., 2006. Physically compliant, conditionally simulated spatially variable seismic ground motions for performance-based design. *Earthquake Engineering and Structural Dynamics*, **35**(7), 891–919.

Lin, J.H., Shen, W.P., and Williams, F.W., 1995. A high precision direct integration scheme for structures subjected to transient dynamic loading. *Computer and Structures*, **56**(1), 113–120.

Lin, J.H., Shen, W.P., and Williams, F.W., 1997A. Accurate high-speed computation of nonstationary random structural response. *Engineering Structures*, **19**(7), 586–593.

Lin, J.H., Wang, X., and Williams, F.W., 1997B. Asynchronous parallel computing of structural nonstationary random seismic responses. *International Journal for Numerical Methods in Engineering*, **40**(12), 2133–2149.

Lin, J.H. and Weng, C.C., 2001. Probability analysis of seismic pounding of adjacent buildings. *Earthquake Engineering and Structural Dynamics*, **30**(10), 1539–1557.

Lin, J.H., Zhang, Y.H., Li, Q.S., and Williams, F.W., 2004A. Seismic spatial effects for long span bridges, using the pseudo excitation method. *Engineering Structures*, **26**(9), 1207–1216.

Lin, J.H., Zhang, Y., and Zhao, Y., 2004B. Seismic spatial effects on dynamic response of long span bridges in stationary inhomogeneous random fields. *Earthquake Engineering and Engineering Vibration*, **3**(2), 171–180.

Lin, J.H., Zhao, Y., and Zhang, Y., 2001. Accurate and highly efficient algorithms for structural stationary/nonstationary random responses. *Computer Methods in Applied Mechanics and Engineering*, **191**(1), 103–111.

Li, L.B., Phoon, K.K., and Quek, S.T., 2007. Comparison between Karhunen-Loève expansion and translation-based simulation of non-Gaussian processes. *Computers and Structures*, **85**(5), 264–276.

Li, W. and Assimaki, D., 2010. Site- and motion-dependent parametric uncertainty of site-response analyses in earthquake simulations. *Journal of Geotechnical and Geoenvironmental Engineering*, **100**(3), 954–968.

Li, X., Zhang, D-Y., Yan, W-M., Xie, W-C., and Pandey, M.D., 2013. Effects of model updating on the estimation of stochastic seismic response of a concrete-filled steel tubular (CFST) arch bridge. *Structure and Infrastructure Engineering*, (DOI:10.1080/15732479.2013.837079).

Loh, C.H. and Lin, S.G., 1990. Directionality and simulation in spatial variation of seismic waves. *Engineering Structures*, **12**(2), 134–143.

Lou, L. and Zerva, A., 2005. Effects of spatially variable ground motions on the seismic response of a skewed, multi-span, RC highway bridge. *Soil Dynamics and Earthquake Engineering*, **25**(7), 729–740.

Luco, J.E. and Wong, H.L., 1986. Response of a rigid foundation to a spatially random ground motion. *Earthquake Engineering and Structural Dynamics*, **14**(6), 891–908.

Lumb, P., 1966. The variability of natural soils. *Canadian Geotechnical Journal*, **3**(2), 74–97.

Lupoi, A., Franchin, P., Pinto, P.E., and Monti, G., 2005. Seismic design of bridges accounting for spatial variability of ground motion. *Earthquake Engineering and Structural Dynamics*, **34**(4), 327–348.

Ma, X. and Zabaras, N., 2011. Kernel principal component analysis for stochastic input model generation. *Journal of Computational Physics*, **130**(19), 7311–7331.

Ma, X., 2010. *An Efficient Computational Framework for Uncertainty Quantification in Multiscale Systems*. Ph. D. thesis, Cornell University.

MCPRC, 2008. *Guidelines for Seismic Design of Highway Bridges, JTG/T B02-01-2008*. China Communications Press, Beijing.

Menke, I., 1990. Polarization and coherence of 5 to 30 Hz seismic wave fields at a hard-rock site and their relevance to velocity heterogeneities in the crust. *Bulletin of the Seismological Society of America*, **80**(2), 430–449.

Moehle, J.P. and Eberhard, M.O., 2000. *Bridge Engineering Handbook: Earthquake Damage to Bridges*, volume CHAPTER 34. CRC Press, Boca Raton.

Montaldo, V., Kiremidjian, A.S., Thrainsson, H., and Zonno, G., 2003. Simulation of the fourier phase spectrum for the generation of synthetic accelerograms. *Journal of Earthquake Engineering*, **3**(7), 427–445.

MRC, 2006. *Code for Seismic Design of Railway Engineering*, volume GB 50111-2006. Ministry of Railways of China (MRC), Beijing.

Nazmy, A.S. and Abdel-Ghaffar, A.M., 1992. Effects of ground motion spatial variability on the response of cable-stayed bridges. *Earthquake Engineering and Structural Dynamics*, **21**(1), 1–20.

NBCC, 2010. *Natonal Building Code of Canada 2010*. National Research Council of Canada, Ottawa, Ontario.

NCC, 2010. *Code for Seismic Design of Buildings, GB 50011-2010*. National Code of China, Beijing.

Nguyen, V.P., Rabczuk, T., Bordas, S., and Duflot, M., 2008. Meshless methods: a review and computer implementation aspects. *Mathematics and Computers in Simulation*, **79**(3), 763–813.

Ni, S-H., Zhang, D-Y., , Xie, W-C., and Pandey, M.D., 2012. Vector-valued uniform hazard spectra. *Earthquake Spectra*, **28**(4), 1549–1568.

Nobahar, A., 2003. *Effects of Soil Spatial Variability on Soil-Structure Interaction*. Ph. D. thesis, University of Newfoundland.

Ohsaki, Y., 1979. On the significance of phase content in earthquake ground motions. *Earthquake Engineering and Structural Dynamics*, **61**(6), 427–439.

Oliveira, C.S., Hao, H., and Penzien, J., 1991. Ground motion modeling for multiple-input structural analysis. *Structural Safety*, **10**(1-3), 79–93.

Park, Y.J., 1992. Nonlinear 3-D piping analysis under stochastic dynamic loads: response spectrum approach. In *Proceedings of the ASME Pressure Vessels and Piping (PVP) Conference*, New York, N.Y., U.S.

Park, Y.J., 1995. New conversion method from response spectrum to PSD functions. *Journal of Engineering Merchanics*, **121**(12), 1391–1392.

Phoon, K.K., Huang, S.P., and Quek, S.T., 2002A. Implementation of Karhunen-Loève expansion for simulation using a wavelet-Galerkin scheme. *Probabilistic Engineering Mechanics*, **17**(3), 293–303.

Phoon, K.K., Huang, S.P., and Quek, S.T., 2002B. Simulation of second-order processes using Karhunen-Loève expansion. *Computers and Structures*, **80**(12), 1049–1060.

Phoon, K.K. and Kulhawy, F.H., 1999A. Characterization of geotechnical variability. *Canadian Geotechnical Journal*, **36**(4), 612–624.

Phoon, K.K. and Kulhawy, F.H., 1999B. Evaluation of geotechnical property variability. *Canadian Geotechnical Journal*, **36**(4), 625–639.

Popescu, R., 1995. *Stochastic Variability of Soil Properties: Data Analysis, Digital Simulation, Effects on System Behavior*. Ph. D. thesis, Princeton University.

Price, T.E. and Eberhard, M.O., 1998. Effects of spatially varying ground motions on short bridges. *Journal of Structural Engineering*, **124**(8), 948–955.

Priestley, M.B., 1965. Evolutionary spectra and nonstationary processes. *Journal of the Royal Statistical Society: Series B (Methodological)*, **27**(2), 204–237.

Przewlocki, J., 2000. Two-dimensional random field of mechanical soil properties. *Journal of Geotechnical and Geoenvironmental Engineering*, **126**(4), 373–377.

Rahman, S. and Xu, H., 2005. A meshless method for computational stochastic mechanics. *International Journal of Computational Methods in Engineering Science and Mechanics*, **6**(1), 41–48.

Rathje, E.M., Kottke, A.R., and Trent, W.L., 2010. Influence of input motion and site property variabilities on seismic site response analysis. *Journal of Geotechnical and Geoenvironmental Engineering*, **136**(4), 607–620.

Rosenblueth, E., 1981. Two-point estimates in probability. *Applied Mathematical Modelling*, **5**(5), 329–335.

Sato, T., Murono, Y., and Nishimura, A., 2002. Phase spectrum modeling to simulate design earthquake motion. *Journal of Natural Disaster Science*, **24**(2), 91–100.

Saxena, V., 2000. *Spatial variation of earthquake ground motion and development of bridge fragility curves*. PhD thesis, Princeton University, Princeton, NJ.

Sextos, A.G. and Kappos, A.J., 2009. Evaluation of seismic response of bridges under asynchronous excitation and comparisons with Eurocode 8-2 provisions. *Bulletin of Earthquake Engineering*, **7**(2), 519–545.

Shahi, S.K. and Baker, J.W., 2011. An empirically calibrated framework for including the effects of near-fault directivity in probabilistic seismic hazard analysis. *Bulletin of the Seismological Society of America*, **101**(2), 742–755.

Shepard, D., 1968. A two-dimensional function for irregularly spaced points. In *Proceedings of the 23rd ACM national conference*, New York, NY, USA.

Shinozuka, M. and Deodatis, G., 1988. Stochastic process models for earthquake ground motion. *Probabilistic Engineering Mechanics*, **3**(3), 114–123.

Simos, N. and Costantinoa, C.J., 2004. Soil spatial variability effect on soil structure interaction studies: enveloping uncertainties in structural response. In *Proceedings of the Third UJNR Workshop on Soil-Structure Interaction*, Menlo Park, California, USA.

Smeby, W. and Kiureghian, Der., 1985. Modal combination rules for multicomponent earthquake excitation. *Earthquake Engineering and Structural Dynamics*, **13**(1), 1–12.

Somerville, P.G., McLaren, J.P., Sen, M.K., and Helmberger, D.V., 1991. The influence of site conditions on the spatial incoherence of ground motions. *Structural Safety*, **10**(1), 1–13.

Soyluk, K., 2004a. Comparison of random vibration methods for multi-support seismic excitation analysis of long span bridges. *Engineering Structures*, **26**(11), 1573–1583.

Spanos, P.D., Beer, M., and Red-Horse, J., 2007. Karhunen-Loève expansion of stochastic process with a modified exponential covariance kernel. *Journal of Engineering Mechanics*, **133**(7), 773–779.

Spudich, P. and Cranswick, E., 1984. Direct observation of rupture propagation during the 1979 Imperial Valley earthquake using a short baseline accelerometer array. *Bulletin of the Seismological Society of America*, **74**(6), 2083–2114.

Srivastava, A. and Babu, G.L., 2009. Effect of soil variability on the bearing capacity of clay and in slope stability problems. *Engineering Geology*, **108**(1), 142–152.

Stefanou, G., Nouy, A., and Clement, A., 2009. Identification of random shapes from images through polynomial chaos expansion of random level set functions. *International Journal for Numerical Methods in Engineering*, **79**(2), 127–155.

Su, L., Dong, S., and Kato, S., 2007. Seismic design for steel trussed arch to multi-support excitations. *Journal of Constructional Steel Research*, **63**(6), 725–734.

Thrainsson, H. and Kiremidjian, A.S., 2003. Simulation of digital earthquake accelerograms using the inverse discrete Fourier transform. *Earthquake Engineering and Strcutral Dynamics*, **31**(12), 2023–2048.

Trifunac, M.D., 1971. A method for synthesizing realistic strong ground motion. *Bulletin of the Seismological Society of America*, **61**(6), 1739–1753.

Tsai, Y.B., 1987. The SMART I accelerograph array (1980-1987): a review. *Earthquake Spectra*, **3**(2), 263–287.

Vanmarcke, E.H., 1972. Properties of spectral moments with application to random vibration. *Journal of Engineering Merchanics Division*, **98**(EM2), 425–446.

Vanmarcke, E.H., 1977. Probabilistic modeling of soil profiles. *Journal of the Geotechnical Engineering Division*, **103**(11), 1227–1246.

Vanmarcke, E.H., 2010. *Random Fields: Analysis and Synthesis*. World Scientific Publishing Co. Pte. Ltd., NJ.

Vanmarcke, E., Zavoni, E., and Fenton, G., 1993. Conditional simulation of spatially correlated earthquake ground motion. *Journal of Engineering Merchanics*, **119**(11), 2333–2352.

Wang, M. and Gan, K., 2011. *The Railway of the 21st Century*. Tsinghua University Press, Beijing.

Wang, R., 1999. A simple orthonormalisation method for stable and efficient computation of Green's functions. *Bulletin of the Seismological Society of America*, **89**(3), 733–741.

Wang, S. and Hao, H., 2002. Effects of random variations of soil properties on site amplification of seismic ground motions. *Soil Dynamics and Earthquake Engineering*, **22**(7), 551–564.

Wen, Y.K. and Gu, P., 2004. Description and simulation of nonstationary processes based on Hilbert spectra. *Journal of Engineering Mechanics*, **130**(8), 942–951.

Wolf, J.P., 1985. *Dynamic Soil and Structure Interaction*. Prentice-Hall, Inc., NJ.

Xia, H., Han, Y., Zhang, N., and Guo, W., 2006. Dynamic analysis of train-bridge system subjected to non-uniform seismic excitations. *Earthquake Engineering and Structural Dynamics*, **35**(12), 1563–1579.

Xiu, D., 2010. *Numerical Methods for Stocahstic Computations: A Spectral Method Approach*. Princeton University Press, Princeton University, New Jersey.

Yang, J. and Sato, T., 2000. Interpretation of seismic vertical amplification observed at an array site. *Bulletin of the Seismological Society of America*, **90**(2), 275–285.

Zanardo, G., Hao, H., and Modena, C., 2002. Seismic response of multi-span simply supported bridges to a spatially varying earthquake ground motion. *Earthquake Engineering and Structural Dynamics*, **31**(6), 1325–1345.

Zanardo, G., Pellegrino, C., Bobisut, C., and Modena, C., 2004. Performance evaluation of short span reinforced concrete arch bridges. *Journal of Bridge Engineering*, **9**(5), 424–434.

Zeldin, B.A. and Spanos, P.D., 1996. Random field representation and synthesis using wavelet bases. *Journal of Applied Mechanics*, **63**(4), 946–953.

Zerva, A. and Stephenson, W., 2011. Stochastic characteristics of seismic excitations at a non-uniform (rock and soil) site. *Soil Dynamics and Earthquake Engineering*, **31**(9), 1261–1284.

Zerva, A., 1990. Response of multi-span beams to spatially incoherent seismic ground motions. *Earthquake Engineering and Structural Dynamics*, **19**(6), 819–832.

Zerva, A., 2009. *Spatial Variation of Seismic Ground Motions: Modeling and Engineering Applications*. CRC Press, Taylor and Francis Group, Boca Raton, FL.

Zhang, D-Y., Jia, H-Y., Zheng, S-X., and Xie, W-C., 2013A. A highly efficient and accurate stochastic seismic analysis approach for structures under tridirectional nonstationary multiple excitations. *Computers and Structures*, (ACCEPTED).

Zhang, D-Y., Liu, W., Xie, W-C., and Pandey, M.D., 2013B. Modeling of spatially correlated, site-reflected, and nonstationary ground motions compatible with response spectrum. *Soil Dynamics and Earthquake Engineering*, **55**, 21–32.

Zhang, D-Y., Li, X., Yan, W-M., Xie, W-C., and Pandey, M.D., 2012A. Stochastic seismic analysis of a concrete-filled steel tubular (CFST) arch bridge under tridirectional multiple excitations. *Engineering Structures*, **52**, 355–371.

Zhang, D-Y., Ni, S-H., Xie, W-C., and Pandey, M.D., 2013C. Multivariate distribution models for design spectral accelerations on uniform hazard spectra. *Structural Engineering and Mechanics*, (SUBMITTED).

Zhang, D-Y., Xie, W-C., and Pandey, M.D., 2012B. Synthesis of spatially correlated ground motions at varying sites based on Vector-valued Seismic Hazard Deaggregation. *Soil Dynamics and Earthquake Engineering*, **41**, 1–13.

Zhang, D-Y., Xie, W-C., and Pandey, M.D., 2013D. A meshfree-Galerkin method in modelling and synthesizing spatially varying soil properties. *Probabilistic Engineering Mechanics*, **31**, 52–64.

Zhang, Y.H., Lin, J.H., and Williams, F.W., 2009. Random vibration analysis of long span structures subjected to spatially varying ground motions. *Soil Dynamics and Earthquake Engineering*, **29**(4), 620–629.

Zhong, W.X. and Williams, F.W., 1994. A precise time step integration method. *Proceedings of the Institution of Mechanical Engineers, Part C: Journal of Mechanical Engineering Science*, **208**(6), 427–430.

APPENDIX A

A.1 Seismic Hazard Analysis

For seismic analysis and design of structures, ground motion shaking hazards are required. They are usually obtained through deterministic seismic hazard analysis (DSHA) and probabilistic seismic hazard analysis (PSHA). Figure A.1 shows the meanings and procedure for typical SHA, DSHA, and PSHA.

A.1.1 Scalar Probabilistic Seismic Hazard Analysis

In a typical hazard estimation for a site surrounded by N potential sources in PSHA, the total average exceedence rate λ_{s^*}, contributed by all seismic sources, is given by

$$\lambda_{s^*} = \sum_{i=1}^{N} \nu_i \left\{ \int_r \int_m \mathcal{P}\left\{S > s^* \,\middle|\, m, r\right\} f_M(m) f_R(r) \mathrm{d}m \,\mathrm{d}r \right\}_i, \tag{A.1.1}$$

in which S is a ground motion intensity parameter, such as the spectral acceleration, and s^* is the corresponding threshold value at a specified hazard exceedence level. ν_i is the mean rate of occurrence of the ith seismic source. $\mathcal{P}\left\{S > s^* \,\middle|\, m, r\right\}$ is the conditional probability of exceedence conditional on magnitude m and site-to-source distance r; it is usually assumed to be the complementary cumulative density function of lognormal distribution and can be derived through the ground motion predictive model that is presented in Appendix A.1.3. $f_M(m)$ and $f_R(r)$ are the probability density functions of earthquake magnitude and site-to-source distance, respectively. The distribution model of magnitude is usually

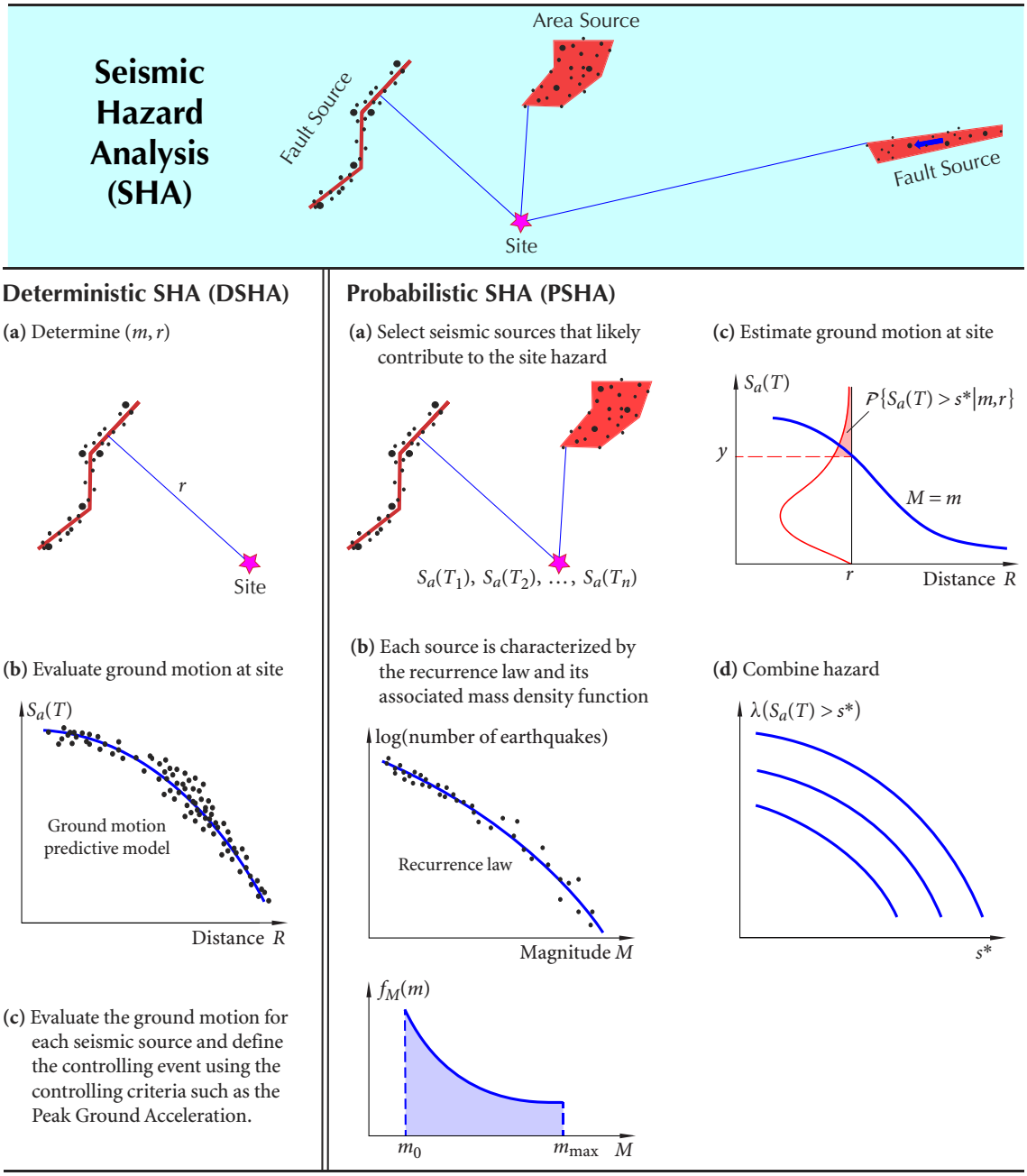

Figure A.1 DSHA and PSHA

obtained through the widely-used Gutenberg-Richter recurrence Law. The probability density function of site-to-source distance is usually derived based on the assumption that all potential seismic sources are composed of uniformly distributed point sources.

The uncertainty regarding the temporal occurrence of earthquakes is usually characterized by a Poisson distribution as

$$\bar{P}\left\{S_T > s^*\right\} = 1 - \mathrm{e}^{-\lambda_{s^*} T}, \tag{A.1.2}$$

where $\bar{P}\left\{S_T > s^*\right\}$ denotes the probability of S_T exceeding s^* in time period T, and it is often called the annual probability of exceeding s^* when $T = 1$ year.

Typical procedure for a PSHA at a site of interest, shown in Figure A.1, can be preformed in four steps (Kramer, 1996):

1. identification and characterization of the potential seismic sources;
2. characterization of the seismicity or temporal distribution of earthquake recurrence;
3. determination of the ground motion intensity parameters by earthquakes having any possible size occurring at any possible point in each source zone using the corresponding predictive model;
4. combining uncertainties from earthquake location, earthquake size, and ground motion parameter prediction to obtain the probability that the ground motion intensity parameter is exceeded during a specified time period.

A.1.2 Vector-valued Probabilistic Seismic Hazard Analysis

Vector-valued probabilistic seismic hazard analysis (VPSHA) can provide a multivariate statistical model when many ground motion parameters are of interests for structural analysis. Parameters contained in the vector of ground motion parameters may include spectral accelerations, earthquake intensities, or soil condition parameters. A detailed description of the methodology of VPSHA is given by Bazzurro and Cornell (1999).

For a ground motion vector $\left\{S_a(T_1), S_a(T_2), \ldots, S_a(T_n)\right\}$, the mean rate density (MRD) is given by

$$\begin{aligned}\mathrm{MRD}_{S_a(T_1),S_a(T_2),\ldots,S_a(T_n)}(s_1, s_2, \ldots, s_n) = \\ \sum_{i=1}^{N} \nu_i \left\{ \int_r \int_m f_{S_a(T_1),S_a(T_2),\ldots,S_a(T_n)}(s_1, s_2, \ldots, s_n \,|\, m, r) f_M(m)\, f_R(r)\, \mathrm{d}m\, \mathrm{d}r \right\}_i,\end{aligned} \tag{A.1.3}$$

where s_k, $k = 1, 2, \ldots, n$, is the threshold corresponding to $S_a(T_k)$, $f_M(m)$ and $f_R(r)$ are the probability density functions of magnitude M and source-site distance R, ν_i is the mean rate

of occurrence for source i, and N is the number of seismic sources. $f_{S_a(T_1),S_a(T_2),\ldots,S_a(T_n)}(s_1, s_2, \ldots, s_n \,|\, m, r)$ is the joint probability density function of vector $\{S_a(T_1), S_a(T_2), \ldots, S_a(T_n)\}$ conditional on m and r for source i, which is verified to be the multivariate lognormal probability density function (Jayaram and Baker, 2008).

A.1.3 Ground Motion Predictive Model

Proper design of earthquake-resistant structures and facilities requires estimation of the level of ground shaking to which they will be subjected. Ground motion parameters, such as intensity, peak ground acceleration (PGA), and spectral accelerations, have been frequently employed to describe the level of ground shaking. Models for estimating the ground motion parameters are thus required and are called ground motion predictive models.

A ground motion predictive model is expressed as the specified ground motion parameter, such as the spectral acceleration, PGA or other intensity parameters, in terms of the quantities having strongest affect on them, which is of great importance in the PSHA (Kramer, 1996). The spectral acceleration is considered in the following as a ground motion parameter to demonstrate a typical predictive model.

A widely-used predictive relation of spectral acceleration with intra-event and inter-event residuals is expressed as (Kramer, 1996; Jayaram and Baker, 2008)

$$\ln S_a(T_1) = \ln \hat{S}_a(m_i, r_j, \mathbf{p}_i, T_1) + \sigma(m_i, \mathbf{p}_{1i}, T_1)\varepsilon + \tau(m_i, \mathbf{p}_{2i}, T_1)\eta, \tag{A.1.4}$$

in which $S_a(T_1)$ is the spectral acceleration at vibration period T_1, $\ln \hat{S}_a(m_i, r_j, \mathbf{p}_i, T_1)$ denotes the logarithmic predicted median spectral acceleration that depends on magnitude m_i, distance r_j, period T_1, and other parameters $\mathbf{p}_i$, such as local-site conditions. ε and η denote the normalized intra-event and inter-event residuals, respectively, which are both univariate normal random variables with zero mean and unit standard deviation. $\sigma(m_i, \mathbf{p}_{1i}, T_1)$ and $\tau(m_i, \mathbf{p}_{2i}, T_1)$ are standard deviations, estimated as part of the ground-motion model, and are functions of period, earthquake magnitude, and other parameters $\mathbf{p}_{1i}$ and $\mathbf{p}_{2i}$.

For a specified earthquake event, e.g., earthquake with magnitude m_i, site-to-source distance r_j, spectral acceleration and intra-event residual ε and η in equation (A.1.4) at a

given vibration period T_1 are random variables usually assumed to be independent and individually follow standard normal distribution (Jayaram and Baker, 2008).

It is noted that ground motion predictive models are originally derived from the approximate physical model of earthquake rupture process. However, due to the complexity of earthquake rupture mechanism and more ground motion measurements are becoming available, these models are mostly derived or updated using regressed results based on actual earthquake records, such as models included in the Next Generation Attenuation (NGA) (Jayaram and Baker, 2008).

A.2 Dynamic Stiffness Matrix of Soil Layers

By using the trial function, solution of equation (2.4.3) can be obtained in the vertical plane (x-z) for the combination of P- and S-waves as (Wolf, 1985)

$$\begin{cases} u = l_x A_{\mathrm{P}} \exp\left[\mathrm{i}\,\omega\left(-\dfrac{l_x x}{c_p^*}-\dfrac{l_z z}{c_p^*}\right)\right] + m_z A_{\mathrm{SV}} \exp\left[\mathrm{i}\,\omega\left(-\dfrac{m_x x}{c_s^*}-\dfrac{m_z z}{c_s^*}\right)\right], \\ v = A_{\mathrm{SH}} \exp\left[\mathrm{i}\,\omega\left(-\dfrac{m_x x}{c_s^*}-\dfrac{m_z z}{c_s^*}\right)\right], \\ w = l_z A_{\mathrm{P}} \exp\left[\mathrm{i}\,\omega\left(-\dfrac{l_x x}{c_p^*}-\dfrac{l_z z}{c_p^*}\right)\right] + m_x A_{\mathrm{SV}} \exp\left[\mathrm{i}\,\omega\left(-\dfrac{m_x x}{c_s^*}-\dfrac{m_z z}{c_s^*}\right)\right], \end{cases} \tag{A.2.1}$$

in which

$$c_p^* = c_p\sqrt{1+2\zeta_p \mathrm{i}}, \quad c_s^* = c_s\sqrt{1+2\zeta_s \mathrm{i}}, \quad c_s = \sqrt{\frac{G}{\rho}}, \quad c_p = \sqrt{\frac{\lambda+2G}{\rho}},$$

l_x and l_z are the direction cosines of axis x and z for P-wave, m_x and m_z are the direction cosines of axis x and z for S-wave, c_p and c_s are the wave velocity for P-wave and S-wave, A_{P}, A_{SH} and A_{SV} are amplitudes for P-wave, SH-wave and SV-wave, λ is the lame constant, G and ρ are the shear modulus and mass density of the soil layer.

Based on equation (A.2.1), the dynamic equation for the out-of-plane motion (SH-wave) and in-plane motion (P- and SV-waves) can be obtained as

- Out-of-Plane Motion (SH-wave)

$$v(z,x) = \left[A_{\mathrm{SH}} \exp(\mathrm{i}ktz) + B_{\mathrm{SH}} \exp(-\mathrm{i}ktz)\right] \exp(-\mathrm{i}kx), \tag{A.2.2}$$

where

$$c=\frac{c_s^*}{m_x},\quad k=\frac{\omega}{c},\quad t=-\mathrm{i}\sqrt{1-\frac{1}{m_x^2}}.$$

- In-Plane Motion (P-SV-wave)

$$u(z,x)=u(z)\exp(-\mathrm{i}kx),\quad w(z,x)=w(z)\exp(-\mathrm{i}kx), \tag{A.2.3}$$

where

$$\begin{cases} u(z)=l_x\left[A_{\mathrm{P}}\exp(\mathrm{i}ksz)+B_{\mathrm{P}}\exp(-\mathrm{i}ksz)\right]-m_x t\left[A_{\mathrm{SV}}\exp(\mathrm{i}ktz)-B_{\mathrm{SV}}\exp(-\mathrm{i}ktz)\right], \\ w(z)=-l_x s\left[A_{\mathrm{P}}\exp(\mathrm{i}ksz)-B_{\mathrm{P}}\exp(-\mathrm{i}ksz)\right]-m_x\left[A_{\mathrm{SV}}\exp(\mathrm{i}ktz)+B_{\mathrm{SV}}\exp(-\mathrm{i}ktz)\right], \end{cases}$$

$$c=\frac{c_s^*}{m_x}=\frac{c_p^*}{l_x},\quad k=\frac{\omega}{c},\quad t=-\mathrm{i}\sqrt{1-\frac{1}{m_x^2}},\quad s=-\mathrm{i}\sqrt{1-\frac{1}{l_x^2}}.$$

Thus, the dynamic stiffness matrix for both out-of-plane and in-plane waves can be obtained.

- Out-of-Plane Motion (SH-wave)

$$K_{\mathrm{SH}}^{\mathrm{L}}(\omega)=\frac{kt^{\mathrm{L}}G^{*\mathrm{L}}}{\sin kt^{\mathrm{L}}d}\begin{bmatrix}\cos ktd & -1\\ -1 & \cos ktd\end{bmatrix}, \tag{A.2.4}$$

and the corresponding half-space rock stiffness matrix is

$$K_{\mathrm{SH}}^{\mathrm{R}}(\omega)=\mathrm{i}ktG^{*\mathrm{R}}. \tag{A.2.5}$$

- In-Plane Motion (P-SV-wave)

$$K_{\text{P-SV}}^{\mathrm{L}}(\omega)=\frac{(1+t^2)kG^{*\mathrm{L}}}{\mathrm{D}}\begin{bmatrix}K_{11} & K_{12} & K_{13} & K_{14}\\ . & K_{22} & K_{23} & K_{24}\\ . & . & K_{33} & K_{34}\\ . & . & . & K_{44}\end{bmatrix}, \tag{A.2.6}$$

where superscripts $*$, L, and R denote transpose and complex conjugate, soil layer, and bedrock, respectively, and D is given by

$$D=2(1-\cos ksd\cos ktd)+\left(st+\frac{1}{st}\right)\sin ksd\sin ktd. \tag{A.2.7}$$

The matrix elements in equation (A.2.6) are

$$K_{11}=\frac{1}{t}\cos ksd\sin ktd+s\sin ksd\cos ktd, \tag{A.2.8}$$

$$K_{12} = \frac{3-t^2}{1+t^2}(1-\cos ksd\cos ktd) + \frac{1+2s^2t^2-t^2}{st(1+t^2)}\sin ksd\sin ktd, \tag{A.2.9}$$

$$K_{13} = -s\sin ksd - \frac{1}{t}\sin ktd, \tag{A.2.10}$$

$$K_{14} = \cos ksd - \cos ktd, \tag{A.2.11}$$

$$K_{22} = \frac{1}{s}\sin ksd\cos ktd + t\cos ksd\sin ktd, \tag{A.2.12}$$

$$K_{23} = -\cos ksd + \cos ktd, \tag{A.2.13}$$

$$K_{24} = -\frac{1}{s}\sin ksd - t\sin ktd, \tag{A.2.14}$$

$$K_{33} = K_{11}, \tag{A.2.15}$$

$$K_{34} = \frac{t^2-3}{1+t^2}(1-\cos ksd\cos ktd) + \frac{t^2-1-2s^2t^2}{st(1+t^2)}\sin ksd\sin ktd, \tag{A.2.16}$$

$$K_{44} = K_{22}. \tag{A.2.17}$$

and the corresponding half-space rock stiffness matrix is

$$K^{\mathrm{R}}_{\text{P-SV}}(\omega) = kG^{*\mathrm{R}}\begin{bmatrix} \dfrac{\mathrm{i}\,s(1+t^2)}{1+st} & 2-\dfrac{1+t^2}{1+st} \\ 2-\dfrac{1+t^2}{1+st} & \dfrac{\mathrm{i}\,t(1+t^2)}{1+st} \end{bmatrix}. \tag{A.2.18}$$

A.3 Peak Factor in Prediction of Structural Peak Response

Let $f(t)$ represent a stationary process with zero mean and the one-side power spectral density (PSD) function $G_f(\omega)$, the maximum absolute value of the process over duration T is defined as

$$f_{\max,T}(t) = \max\left|f(t)\right|,\ 0 < t < T. \tag{A.3.1}$$

The mean and standard deviation of $f_{\max,T}(t)$ can be obtained from the model by Der Kiureghian (1980) as

$$\mu_{\max,f} = \left[\sqrt{2\ln(\nu_e T)} + \frac{0.5722}{\sqrt{2\ln(\nu_e T)}}\right]\sigma_f, \tag{A.3.2}$$

$$\sigma_{\max,f}=\begin{cases}\left[\dfrac{1.2}{\sqrt{2\ln(\nu_e T)}}-\dfrac{5.4}{13+(2\ln(\nu_e T))^{3.2}}\right]\sigma_f, & \nu_e T>2.1,\\ 0.65\sigma_f, & \nu_e T\leqslant 2.1,\end{cases} \tag{A.3.3}$$

in which σ_f is the standard deviation of process $f(t)$, and ν_e is given by

$$\nu_e=\begin{cases}\left(1.63q^{0.45}-0.38\right)\nu, & q<0.69,\\ \nu, & q\geqslant 0.69,\end{cases} \tag{A.3.4}$$

where

$$q=\sqrt{1-\frac{\lambda_1^2}{\lambda_0\lambda_2}},\quad \nu=\frac{1}{\pi}\sqrt{\frac{\lambda_2}{\lambda_0}}, \tag{A.3.5}$$

and

$$\lambda_m=\int_0^\infty \omega^m G_f(\omega)\mathrm{d}\omega,\quad m=0,1,2, \tag{A.3.6}$$

where λ_m is the mth moment of PSD $G_f(\omega)$.

The peak factor model in equations (A.3.2) and (A.3.3) not only provides accurate predictive result but is also more appropriate to be used in the earthquake engineering.

A.4 Polynomial and Trigonometric Basis Functions

The ith normalized polynomial basis function $\Phi_i(x)$ over the interval $[a,b]$ is given by

$$\Phi_i(x)=\frac{\psi_i\left(\frac{2x}{b-a}-\frac{b+a}{b-a}\right)}{\eta_i},\quad \eta_i=\sqrt{\int_a^b \psi_i^2\left(\frac{2x}{b-a}-\frac{b+a}{b-a}\right)\mathrm{d}x}, \tag{A.4.1}$$

where $\psi_i(\cdot)$ is the Legendre polynomial, up to $P=(N_p-1)$th degree, over interval $[-1,1]$ as

$$\psi_0=1,\quad \psi_1=x,\ \ \ldots,\ \ \psi_i=\frac{2i-1}{i}x\psi_{i-1}-\frac{i-1}{i}\psi_{i-2},\ i=2,3,\ldots,P. \tag{A.4.2}$$

The trigonometric basis functions, up to $T=(N_p-1)/2$ harmonics, on the interval $[a,b]$ are

$$\Phi_0=1,\ldots,\Phi_{2i-1}=\cos\left(\frac{2i\pi x}{b-a}-\frac{i\pi(b+a)}{b-a}\right),\Phi_{2i}=\sin\left(\frac{2i\pi x}{b-a}-\frac{i\pi(b+a)}{b-a}\right),\quad i=1,2,\ldots,T. \tag{A.4.3}$$